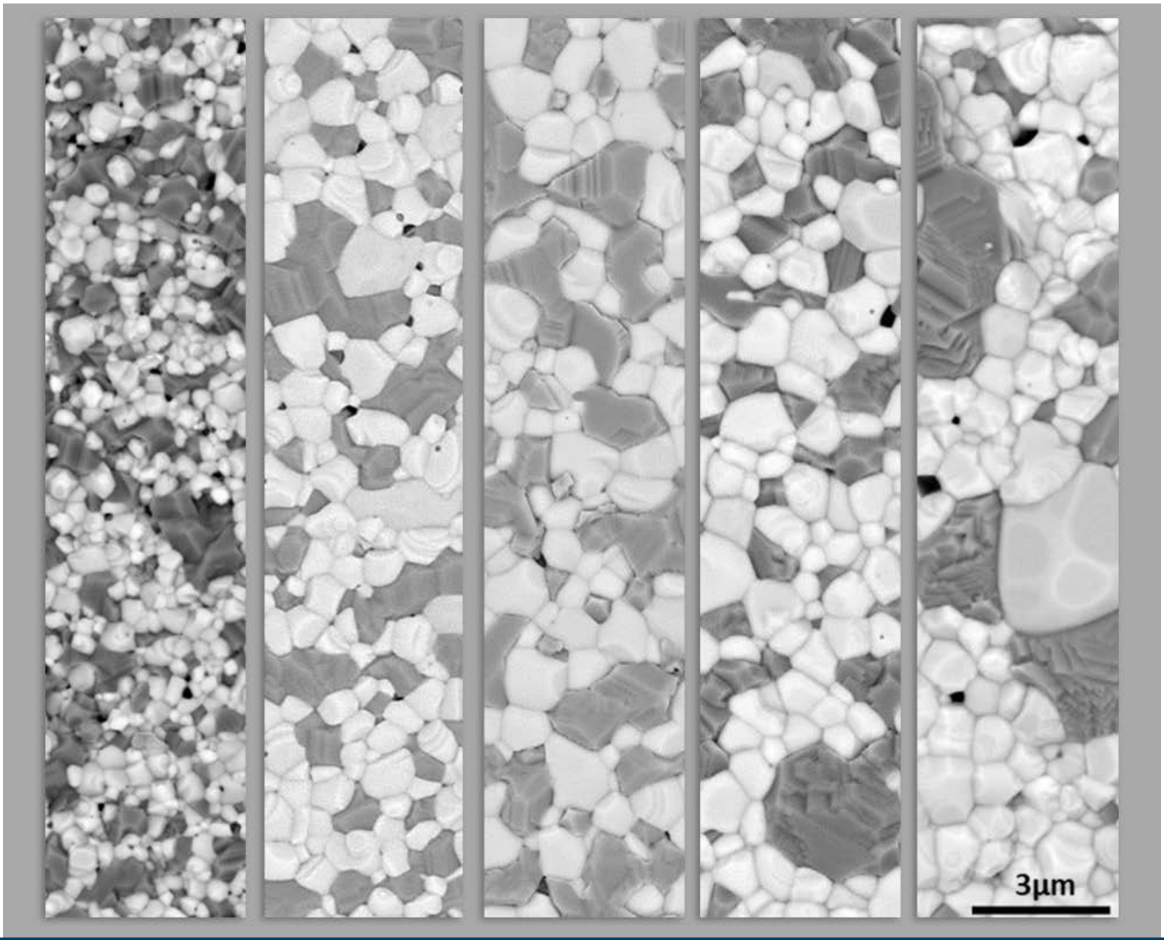

Ceria-based composites for application in Oxygen transport membranes

Liudmila Fischer

Energie & Umwelt / Energy & Environment
Band / Volume 621
ISBN 978-3-95806-739-4

UNIVERSITY
OF TWENTE.

JÜLICH
Forschungszentrum

Schriften des Forschungszentrums Jülich
Reihe Energie & Umwelt / Energy & Environment Band / Volume 621

Forschungszentrum Jülich GmbH
Institut für Energie- und Klimaforschung (IEK)
Werkstoffsynthese und Herstellungsverfahren (IEK-1)

Ceria-based composites for application in Oxygen transport membranes

Liudmila Fischer

Schriften des Forschungszentrums Jülich
Reihe Energie & Umwelt / Energy & Environment Band / Volume 621

ISSN 1866-1793 ISBN 978-3-95806-739-4

Bibliografische Information der Deutschen Nationalbibliothek.
Die Deutsche Nationalbibliothek verzeichnet diese Publikation in der
Deutschen Nationalbibliografie; detaillierte Bibliografische Daten
sind im Internet über http://dnb.d-nb.de abrufbar.

Herausgeber und Vertrieb: Forschungszentrum Jülich GmbH
Zentralbibliothek, Verlag
52425 Jülich
Tel.: +49 2461 61-5368
Fax: +49 2461 61-6103
zb-publikation@fz-juelich.de
www.fz-juelich.de/zb

Umschlaggestaltung: Grafische Medien, Forschungszentrum Jülich GmbH

Druck: Grafische Medien, Forschungszentrum Jülich GmbH

Schriften des Forschungszentrums Jülich
Reihe Energie & Umwelt / Energy & Environment, Band / Volume 621

Diss. Twente, Univ., 2024

ISSN 1866-1793
ISBN 978-3-95806-739-4

Vollständig frei verfügbar über das Publikationsportal des Forschungszentrums Jülich (JuSER)
unter www.fz-juelich.de/zb/openaccess.

Content

SUMMARY

Among the gas membrane separation technologies, inorganic dense membranes, like oxygen transport membranes (OTMs), are regarded as one of the most potential and promising methods and gain considerable attention over the past decades. OTMs represent an energy-efficient and economical alternative to conventional cryogenic air separation for producing pure oxygen for oxyfuel combustion technologies as they provide high oxygen selectivity in a single-step process. OTMs require high permeability as well as chemical and mechanical stability under harsh ambient conditions, like CO_2- or SO_x - containing atmospheres. Mixed ionic-electronic conductors (MIEC) are applied mostly as materials for OTMs. Compared to diverse single-phase materials, dual-phase composite materials, i.e., pure ionic-conductor $Ce_{0.8}Gd_{0.2}O_{2-\delta}$ (CGO20) and electronic-conductor $FeCo_2O_4$ (FCO), may potentially fulfil these requirements completely. The transport properties of the MIEC system are closely related to the composition and conducting properties of the individual phases in the composite, as well as microstructure features, such as density, porosity, grain size, and the presence of defects. Therefore, the objective of this work is to determine the relationship between the composition as well as the morphology of the permeation properties in the fluorite-spinel ceramic composite.

Chapter 1 introduces the fundamental concept of a membrane reactor with integrated OTM, where the main process of oxygen separation takes place. It describes the basis of the oxygen transport mechanisms in the membrane addressing the charge carriers' transport in the bulk and surface of the Mixed Ionic-Electronic Conductors (MIEC). Moreover, conventional single-phase and dual-phase materials used for OTM and the components for the dual-phase composite material, investigated in this study, are outlined.

As the first step in this work, a potential best-case scenario of the oxygen flux for ceria-based composite materials under perfect conditions without any limitations is defined in **Chapter 1.** An oxygen flux of 1 ml/cm^2 min is considered to be the technically relevant minimum flux requirement. By varying the parameters, such as membrane thickness and partial pressure, the temperature-related permeance level for the dual-phase composite can be estimated. Although a technically relevant minimum flux requirement (1 ml/cm^2 min) cannot be achieved in reality, the studied material system

of $Ce_{0.8}Gd_{0.2}O_{2-\delta}$ -$FeCo_2O_4$ (CGO20-FCO) can be evaluated in the context of potential application conditions at intermediate temperatures (<850°C).

Chapter 2 reports the optimization of the sintering profile for the CGO20-FCO composite aiming towards improved microstructural features and transport properties. The characterizations reveal the multi-phase composite structure with the fluorite CGO20 structure, two spinel types: inverse iron-rich and normal cobalt-rich, and emerged $Gd_{0.85}Ce_{0.15}Fe_{0.75}Co_{0.25}O_3$ (GCFCO) phase with perovskite structure, independent of the dwelling time. The presence of the high-temperature CoO phase is found only for the long dwelling time (100 h), which is the result of incomplete oxidization. An additional step in a cooling cycle at 850°C helps to facilitate the oxidization of CoO and to get rid of this phase, resulting in the stable Co_3O_4 phase. The morphological properties, such as density, grain size, and porosity are strongly dependent on the dwelling time at 1200°C for the 60CGO20-FCO composite.

Permeation properties of the basic composite (100-x) wt. % CGO20 – x wt.% FCO with $10 \leq x \leq 40$ are studied in **Chapter 3.** The permeance maximum is found for the 80:20 wt.% ratio at 850°C. At the low FCO fraction (<25 wt.%) in the composite, a sufficient percolation with the targeted 30 vol.% of the electronic (e)-conducting phase is achieved, thanks to phase interaction and formation to the perovskite phase. This emerged donor-doped $GdFeO_3$ phase contributes to the electronic conductivity providing additional paths for the charge carriers. Utilizing the empirical models for the fluorite and spinel phases the composition of the newly formed perovskite phase could be estimated in relation to the different amounts of spinel in the initial powder mixture. Furthermore, this GCFCO phase was synthesized separately and exploited as an electron-conducting phase and added to the commercially available CGO20. This approach reveals a dual-phase structure after sintering, which is expected to be more chemically stable compared to FCO in particular at low p_{O2}.

In **Chapters 4 and 5** the designing of the composite by varying the electron-conductor and ion-conductor is performed. First, the $Fe_{3-x}Co_xO_4$ spinel system with x= 0, 1, and 3 was investigated and was compared to x=2, regarding the morphological and permeation properties. In the absence of one of the cations (iron or cobalt), a significant drop in oxygen permeance as well as limited stability is observed. Moreover, in the cobalt-free composite, no phase interaction takes place, resulting in a dual-phase composite, whereas in iron-free the emerged $Gd_5Fe_3O_{12}$ with the garnet structure is formed, which conducting properties are not as good as by GCFCO. The best performance was found for the composites with x=1 and 2 in $Fe_{3-x}Co_xO_4$, where both cations are present, due to the formation of the GCFCO phase. Thus, the FCO and F2CO are the most attractive candidates from the $Fe_{3-x}Co_xO_4$ spinel system for OTM.

As alternative ion conductors from the material system $Ce_{1-x}RE_xO_{2-\delta}$ (where RE= Gd or Sm and x= 0.1 or 0.2) were investigated, namely $Ce_{0.9}Gd_{0.1}O_{2-\delta}$ (CGO10) and $Ce_{0.8}Sm_{0.2}O_{2-\delta}$ (CSO20) were selected and analysed in **Chapter 5**. Both composite rows exhibit the dense (~95%) close-packed microstructure with fine grain size 0.5-0.7 µm. A type of fluorite plays a crucial role, emphasizing the importance of the dopant fraction in the fluorite. So CGO10-based composite reveals the dual-phase structure, without phase interaction, due to a lack of gadolinium for the perovskite phase formation. Along the grain boundaries segregation of the gadolinium, iron, and cobalt is found, which role in the percolation process is still not fully understood and needs to be further investigated. For composites with reduced FCO fraction (<25 wt.%) the microstructure features are crucial, in particular volume fraction and the grain size of the individual phases. The morphology determines ionic and electronic contiguity and hence the permeance performance of the composite. As a result, the maximum oxygen flux j_{O2} of 0.28 and 0.14 ml/cm^2 min was found at 1000°C and 850°C respectively in the 1 mm thick membrane of 80CGO10-FCO composites.

The CSO20-based composite reveals similar morphological properties to the CGO20-based composite, with a multi-phase structure and quite similar grain size. Composite 80CSO20-FCO reaches the oxygen flux maximum of 0.26 and 0.12 at 1000°C and 850°C, respectively, which is slightly improved compared to the CGO20-based composite.

Chapter 6 focuses on the reduction of the thickness in the bulk pellets from 2 mm to 0.4 mm since the thin dense membranes generally exhibit significantly enhanced oxygen flux. The bare and surface-modified membranes were analysed using Wagner`s model. This L_c value was estimated by utilizing the modified Wagner’s equation, underlying that the LSCF coating is proven to be effective to overcome the surface limitation in the CGO20-FCO composite, especially at low temperatures.

It was postulated that the reaction of incorporation and extrapolation are different on the feed and sweep sides, so the investigation of the surface modification was performed. The segregation of the spinel phase at one side of the membrane is indicated, which possibly can act as a block for the continuous e- and ion- paths without coating.

At high temperatures (950-1000°C) the difference in the one- or two- side activation is insignificant, showing that even in a bare membrane the transport process is governed by bulk diffusion. By lowering temperatures, the surface kinetics influence gets more pronounced. Surface modification by applying the $La_{0.6}Sr_{0.4}Co_{0.2}Fe_{0.8}O_{3-\delta}$ (LSCF) layer is important to overcome the surface limitations and focus on bulk transport at low temperatures (<850°C).

The step-by-step procedure for the development of asymmetric configuration for the 60 CGO20-FCO is described in **Chapter 7.** Each manufacturing step, including slurry formulation for both layers, heat treatment, and post-processing faced some challenges. The microstructural defects, mechanical instability, and density issues were addressed to their nature and discussed in detail. Finally, careful analysis and the possible ways to overcome the problems are given to ensure sufficient mechanical stability and simultaneously transport properties of the asymmetric membrane.

Chapter 8 summarizes all obtained results, reflects overall findings, and further determines a direction for future research. It shows that the promising dual-phase composite with a dominating fluorite structure can provide the necessary stability and permeation performance for application in membrane reactors. The formation of an emerged $GdFeO_3$ perovskite phase with traces of cerium and cobalt has been proven by XRD, SEM, and TEM investigations, which effectively contributes to electronic transport. This phase is determined as a pure electronic conductor and, thus, can be used as a potential electron-conducting phase mixed with the commercially available $Ce_{0.8}Gd_{0.2}O_{2-\delta}$ for the development of the thin supported membrane. Finally, the test of the obtained membranes in the membrane reactor in aggressive atmospheres is required to evaluate the membrane stability and permeance performance.

SAMENVATTING

Van alle scheidingstechnologieën met gasmembranen worden anorganische dichte membranen, zoals zuurstoftransportmembranen (OTM's), beschouwd als een van de meest potentiële en veelbelovende methoden. OTM's vormen een energie-efficiënt en economisch alternatief voor conventionele cryogene luchtscheiding voor de productie van zuivere zuurstof bij oxyfuelverbranding, aangezien ze een hoge zuurstofselectiviteit bieden in een eenstapsproces. OTM's vereisen een hoge permeabiliteit en chemische en mechanische stabiliteit onder moeilijke operatie condities, zoals CO_2- of SO_x-houdende atmosferen. Gemengde ionisch-elektronische geleiders (MIEC) worden meestal toegepast als materialen voor OTM's. Vergeleken met diverse enkelfasige materialen kunnen composietmaterialen met twee fasen, d.w.z. zuivere ionengeleider $Ce_{0.8}Gd_{0.2}O_{2-\delta}$ (CGO20) en elektronische geleider $FeCo_2O_4$ (FCO), mogelijk volledig aan deze vereisten voldoen. De transporteigenschappen van het MIEC systeem zijn nauw verbonden met de samenstelling en de geleidende eigenschappen van de individuele fasen in het composiet, evenals met de microstructuurkenmerken, zoals dichtheid, porositeit, korrelgrootte en de aanwezigheid van defecten. Daarom is het doel van dit werk het bepalen van de relatie tussen de samenstelling en de morfologie van de permeatie-eigenschappen in de fluoriet-spinel keramische composiet.

Hoofdstuk 1 introduceert het fundamentele concept van een membraanreactor met geïntegreerde OTM, waar het belangrijkste proces van zuurstofscheiding plaatsvindt. Het beschrijft de basis van de zuurstoftransportmechanismen in het membraan, waarbij het transport van ladingsdragers in de bulk en aan het oppervlak van de Gemengde Ionisch-Elektronische Geleiders (MIEC) aan de orde komt. Bovendien worden conventionele enkelfasige en tweefasige materialen die worden gebruikt voor OTM en de componenten voor het tweefasige composietmateriaal dat in deze studie wordt onderzocht, geschetst.

Als eerste stap in dit werk is een potentieel bestcasescenario van de zuurstofflux voor composietmaterialen op basis van ceria onder perfecte omstandigheden zonder beperkingen gedefinieerd in **Hoofdstuk 1**. Een zuurstofflux van 1 ml/cm^2 min wordt beschouwd als de technisch relevante minimale vereiste flux. Door de parameters, zoals membraandikte en partiële druk, te variëren kan het temperatuurgerelateerde

permeantieniveau voor de composiet met twee fasen worden geschat. Hoewel een technisch relevante minimale fluxvereiste (1 ml/cm^2 min) in werkelijkheid niet kan worden bereikt, kan het bestudeerde materiaalsysteem van $Ce_{0.8}Gd_{0.2}O_{2-\delta}$ -$FeCo_2O_4$ (CGO20-FCO) worden geëvalueerd in de context van potentiële toepassingsomstandigheden bij middelhoge temperaturen (<850°C).

Hoofdstuk 2 beschrijft de optimalisatie van het sinterprofiel voor de CGO20-FCO composiet met als doel verbeterde microstructurele eigenschappen en transporteigenschappen. De karakteriseringen onthullen de meerfasige composietstructuur met de fluoriet CGO20-structuur, twee spineltypen: omgekeerd ijzer-rijk en normaal kobalt-rijk, en naar voren gekomen $Gd_{0.85}Ce_{0.15}Fe_{0.75}Co_{0.25}O_3$ (GCFCO) fase met perovskietstructuur, onafhankelijk van de verblijftijd. De aanwezigheid van CoO bij hoge temperatuur wordt alleen gevonden bij de lange verblijftijd (100 uur), wat het resultaat is van onvolledige oxidatie. Een extra stap in een koelcyclus bij 850 °C helpt om de oxidatie van CoO te vergemakkelijken en deze fase kwijt te raken, wat resulteert in de stabiele Co_3O_4-fase. De morfologische eigenschappen, zoals dichtheid, korrelgrootte en porositeit zijn sterk afhankelijk van de verblijftijd bij 1200°C voor de 60CGO20-FCO composiet.

Permeatie-eigenschappen van het basiscomposiet (100-x) wt. % CGO20 - x wt.% FCO met $10 \leq x \leq 40$ worden bestudeerd in **Hoofdstuk 3**. Het permeantiemaximum wordt gevonden voor de verhouding 80:20 bij 850°C. Bij de lage FCO-fractie (<25 wt.%) in het composiet wordt voldoende percolatie met de beoogde 30 vol.% van de e-geleidende fase bereikt, dankzij fase-interactie en vorming naar de perovskietfase. Deze opgekomen donor-gedoteerde $GdFeO_3$ fase draagt bij aan de elektronische geleidbaarheid en biedt extra paden voor de ladingsdragers. Met behulp van de empirische modellen voor de fluoriet- en spinelfasen kon de samenstelling van de nieuw gevormde perovskietfase worden geschat in relatie tot de verschillende hoeveelheden spinel in het oorspronkelijke poedermengsel. Bovendien werd deze GCFCO-fase apart gesynthetiseerd en geëxploiteerd als een electronen (e)-geleidende fase, en toegevoegd aan het commercieel beschikbare CGO20. Deze benadering onthult een tweefasenstructuur na sinteren, die naar verwachting chemisch stabieler is in vergelijking met FCO, in het bijzonder bij lage p_{O2}.

In Hoofdstuk 4 en 5 wordt het ontwerp van het composiet uitgevoerd door de e-geleider en ionengeleider te variëren. Eerst werd het $Fe_{3-x}Co_xO_4$-spinelsysteem met x= 0, 1 en 3 onderzocht en vergeleken met x=2 wat betreft morfologische en permeatie-eigenschappen. Bij afwezigheid van een van de kationen (ijzer of kobalt) werd een significante daling in zuurstofpermeantie en een beperkte stabiliteit waargenomen. Bovendien vindt er in het kobalt -vrije composiet geen fase-interactie plaats, wat resulteert in een composiet met twee fasen, terwijl in ijzer -vrij het ontstane $Gd_5Fe_3O_{12}$ met de „garnet“ structuur wordt gevormd, waarvan de geleidende eigenschappen niet zo goed zijn als bij GCFCO. De beste prestaties werden gevonden voor de composieten met x=1 en 2 in $Fe_{3-x}Co_xO_4$, waar beide kationen aanwezig zijn, door de vorming van de GCFCO-fase. FCO en F2CO zijn dus de meest aantrekkelijke kandidaten van het $Fe_{3-x}Co_xO_4$ spinelsysteem voor OTM.

Als alternatieve ionengeleiders van het materiaalsysteem $Ce_{1-x}RE_xO_{2-\delta}$ (waarbij RE= Gd of Sm en x= 0.1 of 0.2) werd onderzocht, namelijk $Ce_{0.9}Gd_{0.1}O_{2-\delta}$ (CGO10) en $Ce_{0.8}Sm_{0.2}O_{2-}$ (CSO20) werden geselecteerd en geanalyseerd in **Hoofdstuk 5**. Beide samengestelde rijen vertonen de dichte (~95%) gesloten microstructuur met een fijne korrelgrootte van 0.5-0.7 µm. Het type fluoriet speelt een cruciale rol en benadrukt het belang van de doteringsfractie in het fluoriet. De composiet op basis van CGO10 vertoont dus een tweefasige structuur, zonder fase-interactie, door een gebrek aan gadolinium voor de vorming van de perovskietfase. Langs de korrelgrenzen wordt segregatie van gadolinium, ijzer en kobalt gevonden, waarvan de rol in het percolatieproces nog niet volledig wordt begrepen en verder moet worden onderzocht. Voor composieten met een gereduceerde FCO fractie (<25 wt.%) zijn de microstructuurkenmerken cruciaal, in het bijzonder de volumefractie en de korrelgrootte van de individuele fasen. De morfologie bepaalt de ionische en elektronische contiguïteit en dus de permeantieprestaties van het composiet. Als resultaat werd het maximum van de zuurstofflux j_{O2} van 0.28 en 0.14 ml/cm^2 min gevonden bij respectievelijk 1000°C en 850°C in de 80CGO10-FCO composieten. De composiet op basis van CSO20 vertoont vergelijkbare morfologische eigenschappen als de composiet op basis van CGO20, met een meerfasenstructuur en een behoorlijke korrelgrootte. Composiet 80CSO20-FCO bereikt het maximum van de zuurstofflux van 0.26 en 0.12 bij respectievelijk 1000°C en 850°C, wat iets beter is vergeleken met composiet op basis van CGO20.

Hoofdstuk 6 richt zich op de vermindering van de dikte in de bulkmembranen van 2 mm naar 0.4 mm omdat de dunne dichte membranen over het algemeen een aanzienlijk grotere zuurstofflux vertonen. De kale en oppervlaktegemodificeerde membranen werden geanalyseerd met behulp van het model van Wagner. Deze L_c-waarde werd geschat met behulp van de gewijzigde vergelijking van Wagner, wat erop wijst dat de LSCF-coating effectief blijkt te zijn om de oppervlaktebeperking in het CGO20-FCO-composiet te overwinnen, vooral bij lage temperaturen. Er werd verondersteld dat de reactie van incorporatie en extrapolatie verschillend zijn aan de voedings- en veegzijde, dus werd de oppervlaktemodificatie onderzocht. De segregatie van de spinelfase aan één zijde van het membraan is aangegeven, wat mogelijk als een blokkade kan werken voor de continue e- en ionpaden zonder coating. Bij hoge temperaturen (950-1000°C) is het verschil in activering aan één of twee zijden verwaarloosbaar, wat aantoont dat zelfs in een kaal membraan het transportproces wordt beheerst door bulkdiffusie. Bij lagere temperaturen wordt de invloed van de oppervlaktekinetiek sterker. Oppervlaktemodificatie door toepassing van de $La_{0.6}Sr_{0.4}Co_{0.2}Fe_{0.8}O_{3-\delta}$ (LSCF) laag is belangrijk om de oppervlaktebeperkingen te overwinnen en te focussen op bulktransport bij lage temperaturen (<850°C).

De stapsgewijze procedure voor de ontwikkeling van de asymmetrische configuratie voor de 60CGO20-FCO wordt beschreven in **Hoofdstuk 7**. Elke productiestap, inclusief slurryformulering voor beide lagen, warmtebehandeling en nabewerking, had te maken met een aantal uitdagingen. De microstructurele defecten, mechanische instabiliteit en dichtheidsproblemen werden naar hun aard aangepakt en in detail besproken. Tot slot worden een zorgvuldige analyse en de mogelijke manieren om de problemen op te lossen gegeven om voldoende mechanische stabiliteit en tegelijkertijd transporteigenschappen van het asymmetrische membraan te garanderen.

Hoofdstuk 8 vat alle verkregen resultaten samen en geeft de algemene bevindingen weer, en bepaalt verder de richting voor toekomstig onderzoek. Het toont aan dat het veelbelovende dual-phase composiet met dominante fluorietstructuur de nodige stabiliteit en permeatieprestaties kan leveren voor toepassing in membraanreactoren. De vorming van een opkomende $GdFeO_3$ perovskietfase met sporen van cerium en kobalt is aangetoond door XRD-, SEM- en TEM-onderzoeken, die effectief bijdraagt aan het elektronische transport. Deze fase wordt bepaald als een zuivere elektronische geleider en kan dus worden gebruikt als een potentiële elektronische geleidende fase gemengd met het commercieel beschikbare $Ce_{0.8}Gd_{0.2}O_{2-\delta}$ voor de ontwikkeling van het dun ondersteunde membraan. Tot slot moeten de verkregen membranen getest worden in de membraanreactor in agressieve atmosferen om de stabiliteit van het membraan en de permeantieprestaties te evalueren.

Abbreviations

Materials

$Ce_{0.8}Gd_{0.2}O_{2-\delta}$	CGO20
$Ce_{0.9}Gd_{0.1}O_{2-\delta}$	CGO10
$Ce_{0.8}Sm_{0.2}O_{2-\delta}$	CSO20
$Fe_{3-x}Co_xO_4$	F3-xCxO
Fe_2CoO_4	F2CO
$FeCo_2O_4$	FCO
$Gd_{0.85}Ce_{0.15}Fe_{0.75}Co_{0.25}O_3$	GCFCO
$La_{0.6}Sr_{0.4}Co_{0.2}Fe_{0.8}O_{3-\delta}$	LSCF
$Ba_{0.5}Sr_{0.5}Co_{0.8}Fe_{0.2}O_{3-\delta}$	BSCF

Abbreviations

CMR	Catalytic Membrane Reactor
OTM	Oxygen Transport Membrane
MIEC	Mixed Ionic and Electronic Conductivity
TPB	Triple Phase Boundary
XRD	X-ray Diffraction
SEM	Scanning Electron Microscopy
EDS	Energy Dispersive X-ray Spectroscopy
STEM-HAADF	Scanning Transmission Electron Microscopy High Angle Annular Dark Field
TEM	Transmission Electron Microscopy
RE	Rare- Earth
FCC	Face-centered Cubic

Symbols

R	Gas Constant (8.314 J.mol^{-1}.K^{-1})
F	Faraday´s Constant (96 485.309 C/mol)
N_A	Avogadro Constant (6.02214076×10^{23} mol^{-1})
j	Flux (ml.cm^{-2}.min^{-1})
L	Thickness (cm)
T	Temperature (K or °C)

σ	Conductivity (S.cm$_{-1}$)
p'	Partial Pressure (bar)
k_s	Surface Exchange Coefficient (cm. s^{-1})
D_s	Diffusion Coefficient (cm^2.s^{-1})
L_c	Characteristic Thickness (cm)
c	Concentration (mol.cm^3)
m	Mass (g)
ρ	Density (g.cm^3)
E_{A}	Activation Energy (kJ.mol^{-1})

Chapter 1

1. Introduction

1.1 Technologies for oxygen separation

Oxygen is one of the most used chemicals in the world, accounting for about ¼ of the world market of industrial gases [1,2] and it is deployed in many industrial areas (combustion processes, steel industry, health care, chemical processes). The use of pure oxygen or oxygen-enriched air offers a variety of technical applications compared to the use of air with considerable technological, economic, and ecological advantages. For example, the use of oxygen in combustion processes leads to emissions reduction and an increase in efficiency. Accordingly, the interest lies in producing pure oxygen as cost-effectively as possible [3,4].

Nowadays pure oxygen is mainly produced on a large scale by cryogenic distillation. This method separates the oxygen from the gases by using the difference in the boiling temperatures of oxygen and nitrogen [5]. Since the boiling points of oxygen and nitrogen are very close to each other (-183 and -196°C for oxygen and nitrogen respectively) and because of the very low operating temperature, the separation of oxygen and nitrogen is complex and energy-intensive (energy demand of *ca.* 225 kW h ton^{-1}) [2]. New technologies should be introduced to maintain the effectiveness of production and simultaneously reduce CO_x emissions. Hence, the continuously expanding demand for oxygen evokes interest in developing new methods for oxygen production, such as membrane technologies. Oxygen permeable ceramic membranes were found as a reliable alternative to conventional processes, helping to reduce production costs by as much as 35 % compared to cryogenic distillation [3,4]. The methods based on inorganic dense membranes, including oxygen-permeable ceramic membranes are regarded as a potential and promising methods among the gas membrane separation technologies and gain considerable attention over the past decades [6]. The oxygen transport membranes can be integrated into a chemical reactor device – catalytic membrane reactor (CMR), which has attracted considerable attention from scientists and engineers in different fields [7].

The CMR enables simultaneously two processes in a single step: the separation process through the membrane and the chemical reaction at one or both sides of the membrane. The permeable membrane serves as a selective barrier, allowing only specific molecules to pass the membrane, whereas others are blocked [8]. This combination of the separation and reaction processes creates synergies between them. The technical concept exhibits a lot of advantages, such as lower pollution, green and sustainable chemistry, less energy consumption, and improved performance in terms of selectivity and separation. Furthermore, the membrane reactor can be applied for different tasks regarding the desired product, i.e., hydrogen, syngas (mixture of H_2 and CO), higher hydrocarbons (C_{2+} -hydrocarbons, ethane, ethylene), methane (CH_4), ammonia (NH_3), or different process [9]. There are known different types of membrane reactors addressing its concepts (extractor, contractor, and distributor concept) or configuration (disc/flat sheet, tubular and hollow fibres) [7,8].

Depending on the type of reaction and operating conditions in CMR, different membrane materials, such as metal, polymers, and ceramics can be used. Moreover, the CMR could be classified regarding membrane type, which is designed to be selective for certain charge carriers, i.e., oxygen ions or protons, while retaining others. For example, the membrane reactor with mixed ion-electron conducting membranes and mixed proton-electron conducting membranes are shown schematically in Figure 1.1 [8].

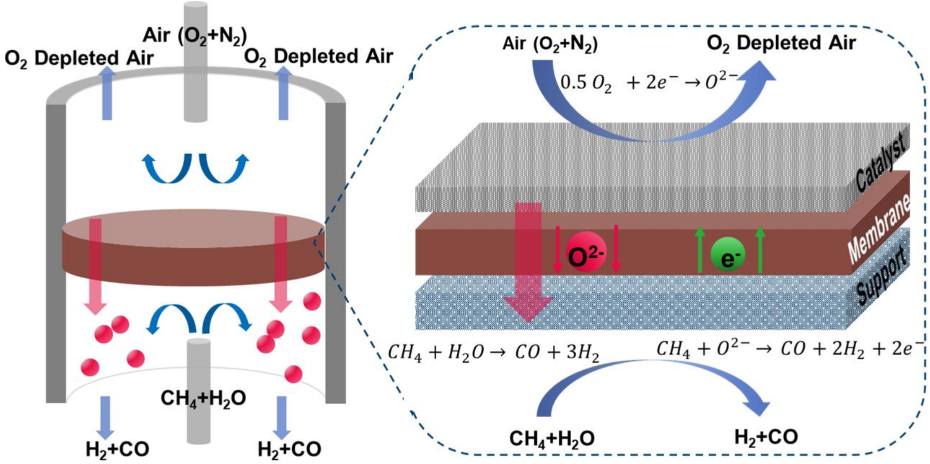

Figure 1.1 Reactions for oxidative coupling of methane with a mixed ion-electron conducting membrane

The properties of the material for the permeable membrane are crucial for the effective separation process, where some reactants or reaction products diffuse through the membrane material, separating it from the mixture. That is why many researchers focus on the development of these ceramic materials, improving their chemical and mechanical properties. These materials could be used for the production of pure oxygen by means of an oxygen transport membrane (OTM).

As an example, the oxyfuel process realization employing the OTM and this is one way for the utilization of carbon capture and storage technologies [10]. The technology with OTM is less energy intensive [2,11] and provides many economic and environmental benefits, such as the capability to realize the efficiency of oxygen production with high oxygen quality, due to high oxygen selectivity, which is in ideal case almost 100 % (>99.999%) [2,12]. The oxygen transport membrane technology can offer a sufficient and economically beneficial solution for different oxygen-intensive industrial sectors such as production of non-ferrous metallurgy, steel, cement, and glass, where heating can be done by the oxyfuel combustion process. The implementation of the membrane oxygen separation technology is done by means of dense mixed ionic-electronic ceramic conducting membranes (MIEC) [2,13], which are commonly made of both types of conductors: ionic and electronic conductors.

1.2 Mixed Ionic Electronic conductors (MIEC)

As it is already mentioned, there are known two types of mixed conductors: single and dual (multi-)-phase for the application as a bulk material for OTM.

1.2.1 Single-phase MIEC

Single-phase OTM can be represented as various structures such as perovskite (ABO_3) or fluorites (AO_2), brownmillerites ($A_2B_2O_5$), and pyrochlores ($A_2B_2O_7$) name a few, which conduct oxygen ions through their crystal lattice [2,10,13,14]. Due to high ionic conductivity, the perovskite and fluorite structures are the most studied. Unlike fluorite, perovskite provides simultaneously sufficient electronic conductivity at targeted conditions, thus it makes perovskite more attractive. The perovskite single-phase materials typically have cubic symmetry and can be described with the ABO_3 formula, the structure is shown in Figure 1.2. To enable ionic conductivity in a single-phase material, it is necessary to introduce some oxygen vacancies by partial substitution of the A-site cation with a lower oxidized one [15]. At the B site, there is always a cation with variable valence. Typically, metals such as Fe or Co are good candidates for the B site and provide high hole or electronic conduction to the composite. The $La_{0.6}Sr_{0.4}Co_{0.2}Fe_{0.8}O_{3-\delta}$ (LSCF) and $Ba_{0.5}Sr_{0.5}Co_{0.8}Fe_{0.2}O_{3-\delta}$ (BSCF) single-phase mixed conductors show exceptional permeability at experimental conditions [16–25], however, all of them suffer from poor chemical and thermal stability [26–34].

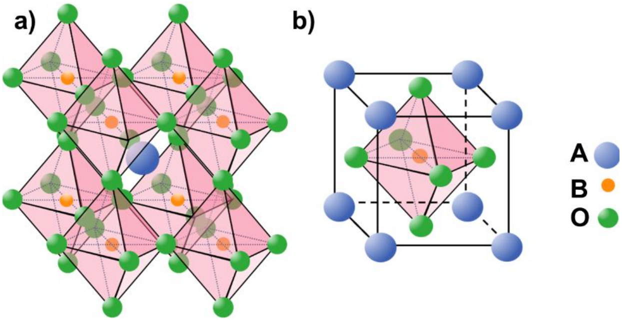

Figure 1.2 a) A cation b) B cation as an individual centre in ideal cubic perovskite structure ABO_3

Moreover, the application of the operating conditions, such as flue gases containing SO_x and CO_x, is quite questionable for single-phase materials, due to possible irreversible reactions i.e., carbonating reaction [35,36].

1.2.2 Dual-phase MIEC

The dual-phase materials have been intensively investigated in order to overcome single phase limitations and yield a chemically and mechanically stable composite. Both phases in the material coexist and provide a continuous network, contributing to the different types of the transport. As a rule, the ionic conductor serves as a continuous phase and the electronic conductor is uniformly dispersed, but networked in the whole membrane volume, hence facilitating oxygen permeation. This dual- or multiphase membrane concept gives rise to additional opportunities in the selection of materials and fabrication methods for the oxygen transport membranes, and thus it is an interesting alternative to the known conventional materials. The typical example is the combination of the fluorite and spinel phases as ion- and electron-conducting phases, respectively. Both phases should meet some requirements regarding stability and provide sufficient compatibility with each other. The dual-phase materials offer higher stability in acidic atmospheres than single-phase ones, however, the permeation performance could be further improved [37–39].

The permeation process through the ceramic membrane is implemented via ionic and electronic conductance, which should be realized in the separate phases. The presence of both phases is key to ensuring good percolation, providing connected ways for both types of charge carriers, the constant oxygen flux, and thus, the sufficient performance of the composite [40–42]. Since the electron conductivity is generally higher compared to the ionic one, the ion-conducting phase should be as high as possible, while the electron-conducting phase amount is as low as possible to form an interconnected network of continuous pathways for electrons and ions. This means that the concentrations of the individual phases should be above the percolating threshold, which is generally reported to be 30 vol. % [43,44].

1.3 Basic transport principle in Oxygen Transport Membranes (OTM)

1.3.1 Membrane configuration

Nowadays there are two known types of oxygen transport membranes (OTM) referring to their configuration. The asymmetric OTM performs better than the symmetric ones. The asymmetric membrane assembly, consisting of the LSCF catalytic activation layer, and a dense membrane layer applied on the porous support to ensure mechanical stability is shown schematically in Figure 1.3. There are two known variations of asymmetric membranes: with support at the oxygen-rich or with support at the oxygen-lean sides [21,45,46].

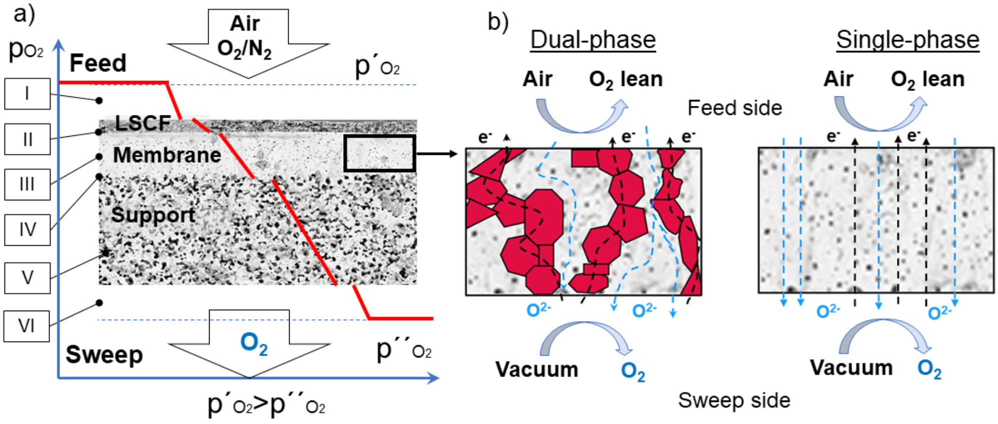

Figure 1.3 a) Schematic representation of the rate-limiting steps in MIEC material over the partial pressure b) Zoom-in of the dense layer with two different MIEC types: dual- and single-phase one (red filled grains are representing the electron-conducting phase, the remainder is the ion-conducting phase)

The OTM consists of the MIEC, which enables the transport of oxygen ions in the material via oxygen vacancies, whereas electrons move via polaron transport in the crystal lattice, hence resulting in a pure oxygen flux. The partial pressure gradient over the membrane serves as the driving force for oxygen transport. It provides ion diffusion and helps with the oxygen surface exchange, where O_2 molecules leave the gas phase and assimilate into oxygen vacancies in the mixed conducting layers. Such membranes found application mostly at temperatures over 600°C since the ion diffusion process is temperature dependent and it is rate-limiting.

Oxygen transport is a quite complex process and involves several transport mechanisms, which can be rate-limiting and can hinder transport in some way, hence can be considered as resistances (see Figure 1.3a).

These resistances correspond to

- The lattice diffusion in the bulk membrane, where oxygen ions diffuse through the solid membrane via vacancies or other defects under a pressure gradient between the feed and permeate side (zone III), while the electrons move in opposite directions to maintain electrical neutrality.
- Two surface exchange reactions, where the oxygen molecules ionize and dissociate to oxygen ions (zone II)

  $$\frac{1}{2}O_2 + V_{\ddot{O}} \rightarrow O_O^x + 2h^{\cdot}$$

  and oxygen ions associate with oxygen molecules (zone IV) according to equations 1 and 2.

  $$O_O^x + 2h^{\cdot} \rightarrow \frac{1}{2}O_2 + V_{\ddot{O}}$$

- Concentration polarization in the gas phases (zone I and VI)
- Pores in the porous support (zone V) [47].

The dependence on the oxygen partial pressure at the zone boundaries is varied from step to step [16]. Mass transfer of the gaseous O_2 to the surface of the membrane occurs at the high-pressure side, going through the bulk membrane and support accompanying the pressure loss and finishes at the low partial-pressure side [48]. Compared to the transport mechanisms in the bulk membrane and surface exchange the resistance of gas phase polarisation (zone I and VI) is often negligible [49,50]. The transport processes in zones III, II, and IV should be taken into account, thus they are explained further in detail.

1.3.2 Surface modification

Oxygen transport in MIEC membranes needs good ionic and electronic conductivity. The presence of both ionic and electronic continuous paths is key for good performance during the oxygen permeation process. Figure 1.3b shows the two types of MIEC materials and transport paths for the electrons and ions. In the single phase MIEC, the whole surface area participates in the transport process, enabling the almost obstacle-free movement of electrons and ions. In the dual- or multi-phase membranes, however, only part of the surface takes part in the charge carrier transport process. Thus, the concentrations of ionic and electron-conducting phases should be above the percolating threshold, which is usually assumed to be 30 vol.% [43,44]. However, in real conditions, interconnectivity between particles is far from ideal and only part of the surface sufficiently contributes to the oxygen exchange process [51]. The surface exchange process at low temperatures is a rate-limiting factor in dual- or multi-phase membranes compared to single-phase due to randomly distributed phases, as shown in Figure 1.3b. To form an effective percolation network in the composite the interface involving the gas phase, electronic conductor (electron holes), and ionic conductor (oxygen vacancies) is required. This interface is known as the triple-phase boundary (TPB). Generally, the amount of the triple-phase boundaries in the composite is very small [52]. The TPB and the potential electron and ion paths in dual-phase material are schematically represented in Figure 1.4.

Dissociation and reduction processes take place on the surface, followed by the diffusion process of O2 ions in the bulk. Released electrons need to be transported to the high partial pressure side. Significantly enhanced transport of charge carriers and hence the permeation in dual-phase materials can be reached by applying a catalytic activation layer (for our material is LSCF) either on one or both sides of the membrane, as reported elsewhere [52–56]. In this case, the potential triple-phase boundaries can be prolonged by a coating of MIEC with a conducting porous activation layer, which facilitates the oxygen incorporation over the entire membrane surface and gives the possibility of electron distribution to the ion-conducting phase.

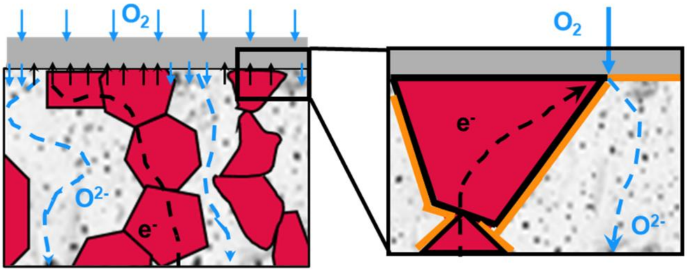

Figure 1.4 Schematic representation of the TPB in the dual-phase material, (red filled grains are the electron conducting phase, the orange open grains are the ion-conducting phase)

1.3.3 Transport in Bulk

If transport in the bulk membrane itself is assumed to be free from surface limitations, the oxygen permeation process in dense membranes can be described by a widely accepted model developed according to Wagner's theory and written as a standard Wagner´s equation [57]:

$$j_{O2} = \frac{RT}{16F^2} \cdot \overline{\sigma_{amb}} \cdot \frac{1}{L} \cdot ln \frac{p'_{O2}}{p''_{O2}}$$ **Equation 1.1**

With σ_{amb} ambipolar conductivity is a function of the electronic σ_e and σ_{ion}ionic of one material. In the case of the compound, the ambipolar conductivity is different and should be corrected.

$$\sigma_{amb} = \frac{\sigma_i \sigma_e}{\sigma_i + \sigma_e}$$ **Equation 1.2**

And

$$\sigma_{ion} = \frac{c_o D_s z_o^2 F^2}{RT}$$ **Equation 1.3**

Where oxygen anions are characterized by D_s - self-diffusion coefficient with the valence charge z_o= -2, other constants have the usual meaning. The c_o is the volume concentration of oxygen anions at equilibrium and k_s is the surface exchange coefficient, derived from the data of ^{18}O-^{16}O isotopic exchange. Generally, bulk diffusion is the lattice diffusion in oxides and involves some point defects such as vacancies, interstitial atoms, and others [49,58]. Transport in the bulk corresponds to oxygen ion diffusion from the high partial pressure side to the low pressure, while electrons move in the opposite direction to maintain electrical neutrality as schematically illustrated in Figure 1.3b.

1.3.4 Transport in Surface

At both oxygen-reach and oxygen-lean sides the MIEC undergoes the row of surface exchange reactions: oxygen adsorption, dissociation, and charge transfer (Figure 1.5). The overall surface exchange reaction can be limited by them. So, in Zone II at the high-oxygen partial pressure side, the row of reaction steps enables the oxygen surface exchange process: oxygen reduction, dissociation and incorporation into the oxide lattice.

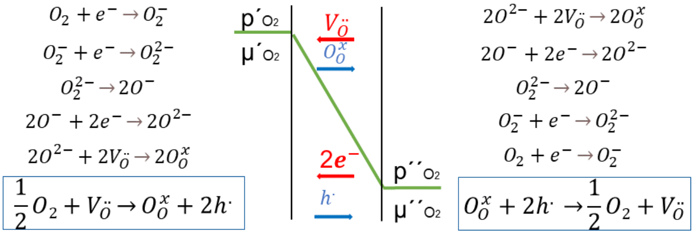

Figure 1.5 Principal overview of the ion transport through dense ion-electronic conducting membrane inclusive the reactions oxygen reduction, dissociation and incorporation into the oxide lattice at the one side and oxidation, association, and desorption of oxygen molecules on the other side of membrane

These reactions happen to occur only in the triple phase boundary, where air, ionic, and electronic conducting phases provide molecular oxygen O_2, oxygen vacancies $V_{\ddot{O}}$, and electrons e^- respectively.

It is also assumed that the same reaction takes place in the opposite direction [51,59], so in Zone IV at the low partial pressure side, all listed reactions occur in the opposite order, starting with the oxidation, association, and desorption of oxygen molecules. From Wagner´s equation, it can be concluded that the oxygen flux is inversely proportional to the thickness of the membrane. Based on this the performance of the membrane can be managed and the dominating transport mechanism is determined. In the MIEC with large thicknesses, bulk diffusion is dominant over surface exchange mechanisms. Interface reactions, on the other hand, are quite limiting in the case of a very thin membrane. However, both contribute equally to the resulting oxygen flux through the membrane at a certain thickness. This parameter is introduced as characteristic thickness L_c for the membranes under mixed controlled kinetics:

$$L_c = \frac{\mathrm{RT}}{16F^2} \cdot \overline{\sigma_{amb}} \cdot \frac{1}{j_{ex}^{o}}$$

Equation 1.4

In conditions near to equilibrium (steady state) and absence of the oxygen potential gradients the oxygen exchange is represented as:

$$j_{O2} = -j_{ex}^{o} \cdot \frac{\nabla \mu_{O2}^{int}}{RT}$$ **Equation 1.5**

Where j_{ex}^{o} is the balanced exchange rate on both membrane surfaces and can be found as $j_{ex}^{o} = \frac{1}{4} \cdot k_s \cdot c_o$. The value $\nabla \mu_{O2}^{int}$ is the gas-solid interface chemical potential gradient. Using all these values is modified into [51]:

$$\boldsymbol{j_{O2} = \frac{RT}{16F^2} \cdot \frac{\sigma_i \sigma_e}{\sigma_i + \sigma_e} \cdot \frac{1}{L + 2L_c} \cdot ln \frac{p'_{O2}}{p''_{O2}}}$$ **Equation 1.6**

Based on the knowledge that most MIEC are predominantly electronic conductors the Nernst-Einstein relationship according to Equation 1.3. After all this modification and introduction of these parameters, Equation 1.4 can be rewritten as:

$$L_c = \frac{D_s}{k_s}$$ **Equation 1.7**

According to the inverse relationship between these two parameters in Wagner´s equation, the reduction of the membrane thickness leads to an increase in oxygen flux, however, it is valid only until a certain value. Lc value is temperature dependent and by utilising the Arrhenius relation could be express as:

$$L_c(\mathrm{T}) = \frac{D_s}{k_s} = \frac{D_{s0} \cdot exp(-\frac{E_{A,D}}{RT})}{k_{s0} \cdot exp(-\frac{E_{A,k}}{RT})} = L_{c,0} \cdot exp(-\frac{E_A}{RT})$$ **Equation 1.8**

1.4 Material selection

Dual- and multi-phase material development focus is the design of the material with the optimized composition, and phase fractions resulting in a connected network for the realization of ionic and electronic transport. As already mentioned, to sustain a sufficient percolating network for both types of particles, the separate phase should be carefully chosen regarding connectivity and compatibility, to produce a reliable mixed-conducting composite. Moreover, these materials should provide sufficient quality, namely the conducting properties, thermal, phase, and chemical stability, and mechanical properties. Since many requirements need to be fulfilled at the same time, the selection of the components for the composite material is a very critical point.

Nowadays, the composites of acceptor-doped ceria in combination with mixed or electronic conducting materials are under close attention and have been recently intensively investigated for application at the intermediate temperature range (600-850°C) [2,10,13,60–62].

1.4.1 Electron-conducting materials

There are two relevant types of electron conductors for the OTM application for selected conditions: perovskite and spinel type electron conductors. An easy control of the composition, structure, valence, and morphology has made the spinels suitable in various reactions [63]. The spinel is generally known as a pure electron conductor, while the perovskite material, i.e., BSCF or LSCF, exhibits predominantly electronic conductivity with low ionic conductivity [64]. The principal difference is in the paths for the oxygen ions since the perovskite is also able to conduct oxygen ions and electrons as shown in Figure 1.6.

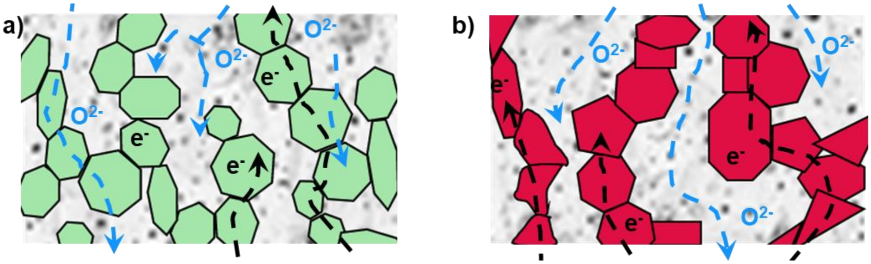

Figure 1.6 Possible electron and ion transport ways in dual-phase composite a) ionic and mixed conductor b) ionic and pure electron conductor

Spinels with a general formula ABO_4 and cubic structure attracted attention as a suitable electron conductor. There are various known spinels for the composite material. To name a few $NiFeO_4$, $Mn_{1.5}Co_{1.5}O_4$, and $Fe_{3-x}Co_xO_4$ systems [63,65–68]. The O-ions form an FCC lattice, while the 1/8 tetrahedral sites and ½ octahedral sites are taken by metal atoms. In other words inside a big FCC O-ion lattice the two types of cubic building units, filling all 8 octants are presented as illustrated in Figure 1.7.

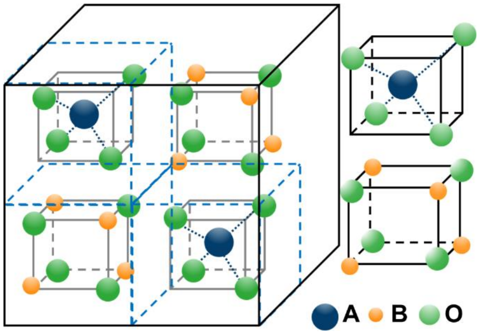

Figure 1.7 Spinel crystal structure (AB_2O_4)

For the current work as an electron-conducting phase, the spinel system $Fe_{3-x}Co_xO_4$ with various x is of particular interest. This system is intensively investigated and showed quite comparable functional properties, conducting properties as well as stability, especially at reducing atmospheres [62,66,68–70]. With respect to the Fe-Co phase diagram, several members of that system were mixed with ion-conducting materials, resulting in forming of dual- or multi-phase ceramic composites and reported somewhere [40,61,62]. The Fe fraction in the spinel phase and the whole dual-phase system has an impact on electronic conductivity [42,71]. Furthermore, it is found that the influence of the Fe/Co ratio in the spinel phase is significant in the context of the phase interaction at the sintering temperature, revealing different final microstructure.

1.4.2 Ion-conducting material

The fluorite-type crystal structure is considered to be the most conventional fast oxide-ion conducting material [2,72,73]. can be described by the AO_2 formula, where A is tetravalent cations. Principally anions are placed in eight tetrahedral sites and the cations occupy face-cantered positions in cubic unit cells. The ceria-based oxides with RE -dopant are a good ion-conducting phase for the dual-phase composite, benefiting from the oxygen vacancies generation by doping. The majority of defects in ceria materials are oxygen vacancies, which amount is closely related to dopant content. Furthermore, the oxygen vacancies define the final conductivity, which can be described as:

$$RE_2O_3 \rightarrow 2RE_{Ce}^{'} + 3O_O^x + V_{\ddot{O}}$$

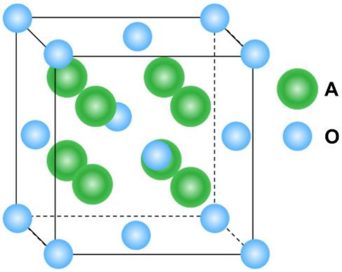

Figure 1.8 The fluorite type crystal structure, green spheres are O^{2-} oxygen ion sites and blue spheres are A^{4+} cation sites

The RE-doped ceria system occupies a central position among the fluorite materials and is intensively investigated for application as OTM [2,74,75]. Pure ceria has limited ionic conductivity [76], however, with the addition of a dopant, the conductivity is significantly improved [77–80]. Chemical expansion is expected, due to the introduction of oxygen vacancies, which start to expand the lattice [81]. Recent modelling and experimental efforts showed a high level of conductivity of RE-doped materials, depending on the type of dopant [2,78]. Many works have been devoted to correlating the dopant type and its amount with the final conducting and structural properties [79,82–84]. The highest conductivity was found for Nd, Sm, and Gd in the range between 10 and 20 mol.% [77,78], where only the fluorite structure is present [85–87]. Since Nd is reported to be a quite rare and critical element [88], two types of dopants have been tested in this work: Gd and Sm. A new approach regarding co-doping of ceria with samarium and gadolinium was published recently, aiming to lower the activation energy and further improve the structural as well as conductive properties [89–91].

1.4.3 Selected Composite

The recent years of OTM development show that dual-phase ceria-dominated materials have more potential for oxygen separation than perovskite membranes. So, the fluorite-spinel composite system has been developed as a promising candidate material. As an ion conductor, the $Ce_{1-x}RE_xO_{2-\delta}$ (where RE= Gd or Sm and x= 0.1 or 0.2) was selected due to good chemical stability [60,70,75,92–97] and excellent ion-conducting properties (~0.075-0.1 $S{\cdot}cm^{-1}$) [65,70,98,99]. To select a suitable electron-conduction material the following requirements should be fulfilled:

- Enhanced electronic conductivity (~0.85-19 $S{\cdot}cm^{-1}$) of the single phase [64]

- Comparable conductivity to achieve sufficient ambipolar conductivity of the compound. [12]
- Similar expansion coefficients to prevent the cracks and other defect formation and propagation, due to increased residual stresses [96]
- Stability in the aggressive atmospheres [66].

So, the various electron conductors of $Fe_xCo_{3-x}O_4$ ($0 < x < 3$) spinel systems are found to be most suitable and promising for the targeted application. Moreover, these spinels act as a sintering agent for doped-ceria, reducing sintering temperature and increasing the density of the final material [70,71,100,101]. In the current work, the fluorite-spinel composite with various ion- and electron conductors was systematically investigated in the context of the microstructure features and the transport properties. For the future upscale the cost-efficient solid-state reaction with subsequent one-step sintering was utilized for the dual-phase membrane fabrication [102].

1.5 Scope of the thesis

Oxygen Transport Membrane (OTM) used for oxygen separation from the air or other oxygen-containing gas mixtures is a widely studied topic in the oxyfuel combustion process nowadays. The technology with OTM provides many economic and environmental benefits, such as the capability to realize the efficiency of oxygen production with high oxygen quality and simultaneously reduce the cost of production compared to the other processes. Dual-phase materials for the OTM exhibit great potential, due to high stability under harsh conditions. The combination of a fluorite material as an ion-conducting phase with a spinel as an electron conductor is one of the most promising candidates for OTM. The in-depth understanding of the multi-phase nature of the composite membranes based on $Ce_{0.8}Gd_{0.2}O_{2-\delta}$ (CGO20) and $FeCo_2O_4$ (FCO) synthesized by solid-state reactive sintering (SSRS) is the main goal of this work. The fluorite-spinel system is intensively investigated and gives a possibility to obtain a high permeable membrane material with sufficient stability. The dual-phase materials development is aiming to minimize the amount of the electron conducting phase and simultaneously have no loss in the percolation of this phase and thus the permeation performance. A potential performance estimation for the chosen CGO20-FCO system in perfect conditions is done, revealing that the permeation potential is sufficiently high for its deployment in membrane reactors.

As an initial step, a “best-case estimation” of the oxygen flux should be performed in order to investigate the applicability and potential performance of a CGO-based dual-phase composite system, which is discussed in the final part of **Chapter 1**. Assuming the perfect conditions without any surface limitations and/or porous support influence for the asymmetric configuration. Oxygen flux of 1 ml/cm^2 min is considered to be the technically relevant minimum flux requirement, and by varying the thickness and partial pressure parameters it could be estimated temperature-related permeance level for the dual-phase composite. Even if the “best case" cannot technically be achieved in reality, the chosen composite can be evaluated in the context of potential application conditions.

Chapter 2 is devoted to the optimization of the sintering profile for dual- / multi-phase composites. The chosen sintering temperature is 1200°C for all studied composites, many studies have been done on the temperature influence on the microstructure features of the dual- and multi-phase composites, namely the grain and pore size, relative density, and porosity. However, the effect of the dwelling time has not been systematically investigated for the CGO20-FCO system so far. Thus, the dwelling time was varied between 0 and 100 h at 1200°C. The cooling rate is also critical, especially for the spinel phase, where the residual Co/Fe monoxide phase can be eliminated by optimization of the cooling process. The suitable sintering profile with sufficient dwelling time was defined and will be further utilized for the upscaling for OTM production.

The investigation of the basic CGO20-FCO composite with FCO fraction from 10 to 40 wt.% is discussed in **Chapter 3**. The microstructure features including the structural properties and fraction of each phase were analysed via TEM, SEM, and XRD with Rietveld refinement. Utilizing the empirical models for the fluorite and spinel phases the composition of the newly formed donor-doped $GdFeO_3$ phase could be estimated in relation to the different amounts of spinel in the initial powder mixture. Sufficient percolation can be reached even at the low amount of nominal FCO in composite (<25 wt.%), thanks to phase interaction and the formation of an emerged phase. Maximum permeation is observed for the 80 wt.% CGO20 with 20wt. % FCO combination at 850°C. Moreover, the CGO20-based composite with GCFCO as an electronic conductor, reveals indeed dual-phase morphology and significantly enhanced permeation.

The design of the dual-phase composite system and explanation of the ion- and electron-conducting phase choice, based on the microstructure and performance is discussed in **Chapter 4 and Chapter 5.**

The Fe/Co ratio in the multi– and dual-phase composite material, coming from the spinel phase is crucial for the determination of the final morphology and permeation of materials. The systematic study of the effect of the Fe/Co ratio of $Fe_xCo_{3-x}O_4$ ($0<x<3$) in CGO20-FCO composite is performed in **Chapter 4**. The phase interaction, third phase formation, fraction, and lattice parameter of each phase after phase interaction, as well as morphology, including grain size and porosity, are discussed. Fe/Co ratio affects the third phase quality, resulting in either the donor-doped $GdFeO_3$ or $Gd_5Fe_3O_{12}$. It was postulated importance of the both cations' presence in the fluorite-spinel composite system, to ensure sufficient percolation.

Chapter 5 focuses on the selection of the ion-conducting phase $Ce_{1-x}RE_xO_{2-\delta}$ with a different type of dopant (RE= Gd or Sm) as well as the amount of this dopant (x= *0.1 or*

0.2) in the fluorite structure, followed by a discussion of its effect on the final morphology of the ceria-based material. Due to the different conductivity of Sm- and Gd-doped ceria, the final permeation performance is different in investigated composites. The amount of dopant in the initial ceria-based composite system has an impact on the final microstructure, resulting in dual- or multi-phase morphology The correlation between the volume fraction of the electronic-conducting phases, microstructure, and permeance of CGO20 and CSO20 composites is discussed.

The optimized material was then utilized to prepare a membrane with an asymmetric configuration in order to decrease the thickness of the dense layer but ensure a stable structure for the potential application in harsh conditions. **Chapter 6** compares the permeation performance of dense CGO20-FCO multi-phase membranes with varying thicknesses from 0.4 to 2 mm. The impact of surface exchange kinetics is analysed and quantified in terms of the different bulk membrane thicknesses. The experimental data of bare and coated membranes was compared with Wagner´s equation and the modified one, which considers the L_c value of transition thickness from bulk-limited permeation to surface exchange-limited one. The L_c characteristic thickness and specific oxygen flux were estimated, as a function of the temperature in the range of 700-1000°C. The L_c value seems to be almost constant for both types of membranes at high temperatures, while at low temperatures the L_c differs significantly for coated and uncoated samples. Furthermore, the effects of the surface-exchange kinetics on the oxygen-permeation properties have been studied in terms of surface modification. The importance of the catalytic layer application has been analysed in detail, regarding the rate-limiting mechanisms. The impact of the sample configuration with the application of a catalytic activation layer on either one or both sides of the membrane on the final oxygen flux is discussed.

The chosen dual-phase composite system (60 wt. % CGO20 - 40 wt.% FCO), is developed into an asymmetric membrane configuration by a sequential tape-casting process described in **Chapter 7**. The quality analysis of the green tape as well as the sintered samples was continuously performed, to recognize and overcome potential problems. Additionally, the discussion of the occurrence of bulk and surface defects, addressing their nature and possible solution to improve the tape quality, is done. To get a defect-free thin membrane with a mechanically stable support structure further optimization steps are required, such as the process of slurry optimization, in particular the variation of the additives. Further, the sintering profile was adjusted by varying the temperature to get a well-densified and stable microstructure of the composite membrane.

A summary of the scientific contribution of this work and the conclusions for the development and application of the CGO20-FCO composite system for the OTM is given in **Chapter 8**. This part also gives perspectives for future development of the multi-phase CGO20-FCO composite material for application in an OTM based membrane reactor, including stability tests under harsh conditions.

1.6 Best-case performance of ceria-based composite

Due to complexity of the selected composite system in context of the various phase interactions and other factors, as an initial step of the material investigation the prediction of the “best-case performance” addressed to permeance is done.

Current analysis is the part of the published work [2].

As a first step to investigate the applicability and potential performance of a dual-phase composite system, a “best-case estimation” of the oxygen flux should be made. Even if the “best-case scenario” cannot technically be achieved, this approach has the benefit to assess if the selected dual-phase composite can in theory reach the performance required by the targeted application.

An example of such an estimation for a dual-phase OTM is described below. As “best case situation” it is assumed that the Wagner equation (Equation 2) is valid in the entire parameter range *i.e.,* neglecting surface exchange limitation as well as any impact of porous supports required for thin membranes.

Dual-phase OTMs typically show permeation rate limitations by the ionic conductivity. Therefore, a maximum portion of the ionic conductor is beneficial. In consequence, a best-case situation exists if the (hypothetical) dual-phase membrane consists only of the ion conducting phase, and assuming an infinite electronic conductivity. In this case the ambipolar conductivity equals the ionic one.

As ion conducting phase 20 mol% Gd-doped ceria (CGO20) is chosen as an example due to its high ionic conductivity at intermediate temperatures, *i.e.* 500–600 °C [103]. The targeted permeation rate value (benchmark) considered the technical relevant minimum flux requirement by the OTM community varies from 1 to 10 ml cm^{-2} min^{-1} [104,105].

Using reported data for CGO20 ($\sigma^{410\ °C}{}_{ionic} = 8,15 \times 10^{-4}$ S cm^{-1}; $E_a = 70$ kJ mol^{-1}) [79], the upper bound of the oxygen permeation rate can be calculated according to Equation 2 [2] considering the thickness L, the absolute temperature T, and the driving force $Ln\frac{p_{O2}^{feed,}}{p_{O2}^{permeate}}$ as parameters. Here, p' (corresponding to $p_{O2}{}^{feed}$) is fixed to air at ambient pressure, *i.e.,* $p' = 0.21$ bar. For p'' (corresponding to $p_{O2}{}^{permeate}$) two concentrations are chosen arbitrarily, *i.e.,* $p'' = 0.005$ bar mimicking typical oxygen permeation tests using air and inert gas (Ar or He) as feed and sweep gases, respectively and $p'' = 10^{-15}$ bar exemplarily for membrane reactor applications.

In Figure 1.9 the dependency of the oxygen flux on pressure gradient, thickness and operating temperature is illustrated in an Arrhenius plot. The orange line represents the hypothetical oxygen flux across a 1 mm thick membrane lab operated in a 0.21/0.005 partial pressure gradient. It should be noticed that both thickness and pressure gradient are the most common test conditions reported, as shown in Table 1 [2].

The reduction of the membrane thickness to 50 µm leads to significant improvement of the hypothetical oxygen flux as illustrated by a shift along the *Y*-direction (green line). The same tendency occurs by reduction of the sweep side partial pressure from 0.005 bar to 10^{-15} bar (brown line). As expected, the highest fluxes can be achieved with a thin membrane operated at high driving force (violet line). In these hypothetical cases the "best-case estimation" equals the benchmark performance of 1 ml cm^{-2} min^{-1} already at temperatures above 470 °C.

For comparison, Figure 1.9 also shows experimental data of 1 mm thick membrane pellets (single phase perovskite $La_{0.6}Sr_{0.4}Co_{0.2}Fe_{0.8}O_{3-\delta}$ (LSCF) and CGO20-based surface activated dual-phase composite). The experimental data were driving force normalized to $p'' = 0.005$ bar (an average value of O_2 concentration measured by mass spectrometry during the permeation test). At 1000 °C, LSCF comes close to the benchmark (coincidently equal to the upper bound of CGO) and utilizing thin supported membranes it is reported that it can easily exceed the benchmark value at temperatures above 800 °C [21,106]. However, due to a relatively high activation energy, LSCF reaches only 2.5% of the upper bound of CGO at 650 °C. The second material (black squares, Figure 1.9), a CGO-based composite using $FeCo_2O_4$ spinel as second phase (CGO–FCO) [53,60], shows significant lower activation energy. Below 800 °C a better performance compared to LSCF, reaching approx. 30% of the upper bound at 650 °C, can be observed. Please note, that this specific membrane is given here as an example for illustration, and the authors consider it as one out of many applicable composites. However, the benefit of CGO20-based dual-phase membranes in comparison to single-phase perovskites at lower temperature is considered to be systematic.

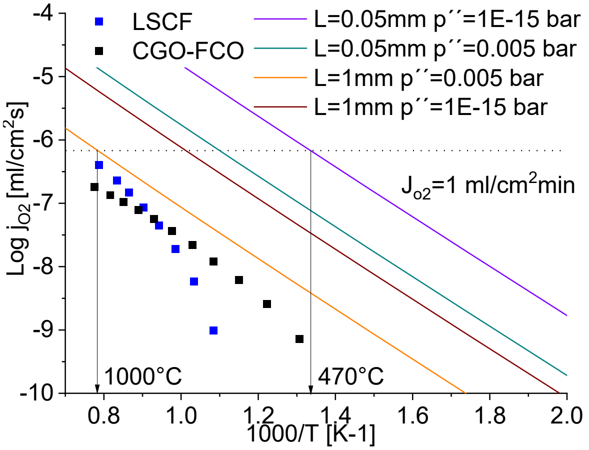

Figure 1.9 The modelling of best-case performance of CGO20 for L = 0.05 and 1 mm, p''_{O2}= 0.005 and 10^{-15} bar, dashed line represents oxygen flux of 1 ml cm^{-2} min^{-1} as well as experimental data of LSCF and CGO–FCO 1 mm thick pellets.

While for thicker membranes, *i.e.,* 1 mm, the experimentally measured performance and the “best case estimations” are in reasonable agreement, large discrepancies can be found for thinner membranes. As example, the experimental data for an 11 µm thin supported CGO–FCO composite membrane (prepared by tape casting) is shown in Figure 1.10. While the measured performance exceeds the benchmark at higher temperatures, the gap between the respective upper bound (orange coloured line) and experimental values increases significantly. Moreover, the activation energy drastically increases below 900 °C. This is strongly indicating surface exchange limitations, as discussed in Sub-section 1.3.3 [2]. In particular the surface activation of the membrane support interface, a place which is not easily accessible for catalyst integration, seems performance limiting. In consequence, an advanced activation using a Ce/Pr-based catalyst infiltrated into the support as well as a porous composite top-coating was carried out. A clear performance improvement at intermediate temperatures (Figure 1.10, green square symbols) was achieved, but nevertheless there is obviously still dramatic need for optimization.

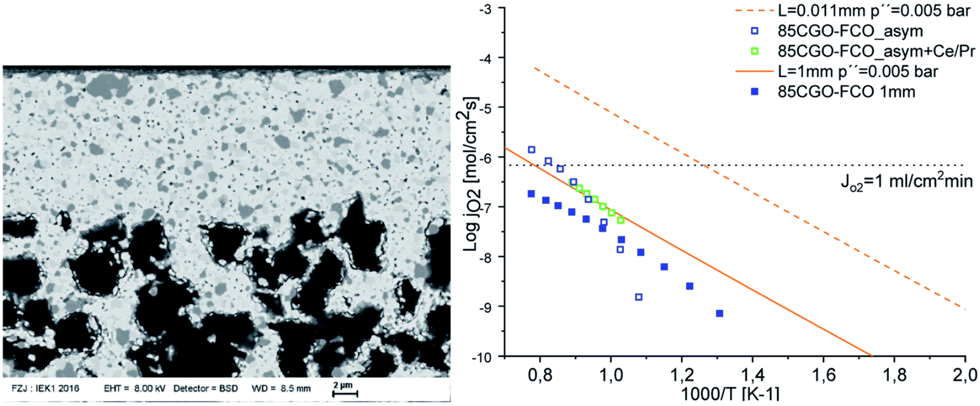

Figure 1.10 Left: 11 µm thin asymmetric membrane made of $Ce_{0.8}Gd_{0.2}O_{2-\delta}$–$FeCo_2O_4$ composite (CGO–FCO) right: performance of asymmetric CGO–FCO with porous LSCF top-coating as well as advanced surface activation using $(Ce,Tb)O_2$–$NiFe_2O_4$ composite porous top coating and a Ce/Pr-based catalyst infiltrated into both top coating and porous CGO–FCO support.

References

1. Emsley, J. *Nature's building blocks*: *An A - Z guide to the elements*; Oxford University Press: Oxford, 2002.

2. Kiebach, R.; Pirou, S.; Martinez Aguilera, L.; Haugen, A.B.; Kaiser, A.; Hendriksen, P.V.; Balaguer, M.; García-Fayos, J.; Serra, J.M.; Schulze-Küppers, F.*; et al.* A review on dual-phase oxygen transport membranes: from fundamentals to commercial deployment. *J. Mater. Chem. A* **2022**, *10*, 2152–2195.

3. Smart, S.; Lin, C.X.C.; Ding, L.; Thambimuthu, K.; Diniz da Costa, J.C. Ceramic membranes for gas processing in coal gasification. *Energy Environ. Sci.* **2010**, *3*, 268.

4. Leo, A.; Liu, S.; Costa, J.C.D.d. Development of mixed conducting membranes for clean coal energy delivery. *International Journal of Greenhouse Gas Control* **2009**, *3*, 357–367.

5. Allam, R.J. Improved oxygen production technologies. *Energy Procedia* **2009**, *1*, 461–470.

6. Garcia-Fayos, J.; Serra, J.M.; Luiten-Olieman, M.W.; Meulenberg, W.A. Gas separation ceramic membranes. In *Advanced Ceramics for Energy Conversion and Storage*: Elsevier, 2020, pp. 321–385.

7. Dong, X.; Jin, W.; Xu, N.; Li, K. Dense ceramic catalytic membranes and membrane reactors for energy and environmental applications. *Chemical communications (Cambridge, England)* **2011**, *47*, 10886–10902.

8. Deibert, W.; Ivanova, M.E.; Baumann, S.; Guillon, O.; Meulenberg, W.A. Ion-conducting ceramic membrane reactors for high-temperature applications. *Journal of Membrane Science* **2017**, *543*, 79–97.

9. Tan, X.; Li, K. *Inorganic Membrane Reactors*; John Wiley & Sons, Ltd: Chichester, UK, 2014.

10. Bai, W.; Feng, J.; Luo, C.; Zhang, P.; Wang, H.; Yang, Y.; Zhao, Y.; Fan, H. A comprehensive review on oxygen transport membranes: Development history, current status, and future directions. *International Journal of Hydrogen Energy* **2021**, *46*, 36257–36290.

11. Sunarso, J.; Baumann, S.; Serra, J.M.; Meulenberg, W.A.; Liu, S.; Lin, Y.S.; Diniz da Costa, J.C. Mixed ionic–electronic conducting (MIEC) ceramic-based membranes for oxygen separation. *Journal of Membrane Science* **2008**, *320*, 13–41.

12. Zhu, X.; Yang, W. *Mixed Conducting Ceramic Membranes*; Springer Berlin Heidelberg: Berlin, Heidelberg, 2017.

13. Chen, G.; Feldhoff, A.; Weidenkaff, A.; Li, C.; Liu, S.; Zhu, X.; Sunarso, J.; Huang, K.; Wu, X.-Y.; Ghoniem, A.F.*; et al.* Roadmap for Sustainable Mixed Ionic-Electronic Conducting Membranes. *Adv Funct Materials* **2022**, *32*.

14. Arratibel Plazaola, A.; Cruellas Labella, A.; Liu, Y.; Badiola Porras, N.; Pacheco Tanaka, D.; Sint Annaland, M.; Gallucci, F. Mixed Ionic-Electronic Conducting Membranes (MIEC) for Their Application in Membrane Reactors: A Review. *Processes* **2019**, *7*, 128.

15. Zhang, K.; Sunarso, J.; Shao, Z.; Zhou, W.; Sun, C.; Wang, S.; Liu, S. Research progress and materials selection guidelines on mixed conducting perovskite-type ceramic membranes for oxygen production. *RSC Adv.* **2011**, *1*, 1661.

16. Baumann, S.; Serra, J.M.; Lobera, M.P.; Escolástico, S.; Schulze-Küppers, F.; Meulenberg, W.A. Ultrahigh oxygen permeation flux through supported Ba0.5Sr0.5Co0.8Fe0.2O3−δ membranes. *Journal of Membrane Science* **2011**, *377*, 198–205.

17. Hoffmann, R.; Pippardt, U.; Kriegel, R. Impact of sintering temperature on permeation and long-term development of support structure and stability for asymmetric oxygen transporting BSCF membranes. *Journal of Membrane Science* **2019**, *581*, 270–282.

18. Shao, Z. Investigation of the permeation behavior and stability of a $Ba_{0.5}Sr_{0.5}Co_{0.8}Fe_{0.2}O_{3-\delta}$ oxygen membrane. *Journal of Membrane Science* **2000**, *172*, 177–188.

19. Shao, Z.; Xiong, G.; Dong, H.; Yang, W.; Lin, L. Synthesis, oxygen permeation study and membrane performance of a Ba0.5Sr0.5Co0.8Fe0.2O3−δ oxygen-permeable dense ceramic reactor for partial oxidation of methane to syngas. *Separation and Purification Technology* **2001**, *25*, 97–116.

20. Wang, H.; Cong, Y.; Yang, W. Oxygen permeation study in a tubular Ba0.5Sr0.5Co0.8Fe0.2O3-δ oxygen permeable membrane. *Journal of Membrane Science* **2002**, *210*, 259–271.

21. Serra, J.M.; Garcia-Fayos, J.; Baumann, S.; Schulze-Küppers, F.; Meulenberg, W.A. Oxygen permeation through tape-cast asymmetric all-La0.6Sr0.4Co0.2Fe0.8O3−δ membranes. *Journal of Membrane Science* **2013**, *447*, 297–305.

22. Lane, J. Oxygen transport in La0.6Sr0.4Co0.2Fe0.8O3−δ. *Solid State Ionics* **1999**, *121*, 201–208.

23. Tan, X.; Wang, Z.; Liu, H.; Liu, S. Enhancement of oxygen permeation through $La_{0.6}Sr_{0.4}Co_{0.2}Fe_{0.8}O_{3-\delta}$ hollow fibre membranes by surface modifications. *Journal of Membrane Science* **2008**, *324*, 128–135.

24. Teraoka, Y.; Zhang, H.-M.; Furukawa, S.; Yamazoe, N. OXYGEN PERMEATION THROUGH PEROVSKITE-TYPE OXIDES. *Chem. Lett.* **1985**, *14*, 1743–1746.

25. Zhao, J.; Pang, Y.; Su, C.; Jiang, S.; Ge, L. Toward High Performance Mixed Ionic and Electronic Conducting Perovskite-Based Oxygen Permeable Membranes: An Overview of Strategies and Rationales. *Energy Fuels* **2023**, *37*, 7042–7061.

26. Waindich, A.; Möbius, A.; Müller, M. Corrosion of $Ba_{1-x}Sr_xCo_{1-y}FeyO_{3-\delta}$ and $La_{0.3}Ba_{0.7}Co_{0.2}Fe_{0.8}O_{3-\delta}$ materials for oxygen separating membranes under Oxycoal conditions. *Journal of Membrane Science* **2009**, *337*, 182–187.

27. Gao, J.; Li, L.; Yin, Z.; Zhang, J.; Lu, S.; Tan, X. Poisoning effect of SO_2 on the oxygen permeation behavior of $La_{0.6}Sr_{0.4}Co_{0.2}Fe_{0.8}O_{3-\delta}$ perovskite hollow fiber membranes. *Journal of Membrane Science* **2014**, *455*, 341–348.

28. Ramirez-Reina, T.; Santos, J.L.; García-Moncada, N.; Ivanova, S.; Odriozola, J.A. Development of Robust Mixed-Conducting Membranes with High Permeability and Stability. In *Perovskites and Related Mixed Oxides*; Granger, P., Parvulescu, V.I., Prellier, W., Eds.: Wiley-VCH Verlag GmbH & Co. KGaA: Weinheim, Germany, 2016, pp. 719–738.

29. Engels, S.; Markus, T.; Modigell, M.; Singheiser, L. Oxygen permeation and stability investigations on MIEC membrane materials under operating conditions for power plant processes. *Journal of Membrane Science* **2011**, *370*, 58–69.

30. Schulz, M.; Kriegel, R.; Kämpfer, A. Assessment of CO_2 stability and oxygen flux of oxygen permeable membranes. *Journal of Membrane Science* **2011**, *378*, 10–17.

31. Tan, X.; Liu, N.; Meng, B.; Sunarso, J.; Zhang, K.; Liu, S. Oxygen permeation behavior of $La_{0.6}Sr_{0.4}Co_{0.8}Fe_{0.2}O_3$ hollow fibre membranes with highly concentrated CO_2 exposure. *Journal of Membrane Science* **2012**, *389*, 216–222.

32. Mueller, D.N.; Souza, R.A. de; Weirich, T.E.; Roehrens, D.; Mayer, J.; Martin, M. A kinetic study of the decomposition of the cubic perovskite-type oxide $Ba_xSr_{1-x}Co_{0.8}Fe_{0.2}O_{3-\delta}$

(BSCF) (x = 0.1 and 0.5). *Physical chemistry chemical physics : PCCP* **2010**, *12*, 10320–10328.

33. Yi, J.; Schroeder, M. High temperature degradation of $Ba_{0.5}Sr_{0.5}Co_{0.8}Fe_{0.2}O_{3-\delta}$ membranes in atmospheres containing concentrated carbon dioxide. *Journal of Membrane Science* **2011**, *378*, 163–170.

34. Matras, D.; Vamvakeros, A.; Jacques, S.D.M.; Middelkoop, V.; Vaughan, G.; Agote Aran, M.; Cernik, R.J.; Beale, A.M. In situ X-ray diffraction computed tomography studies examining the thermal and chemical stabilities of working $Ba_{0.5}Sr_{0.5}Co_{0.8}Fe_{0.2}O_{3-\delta}$ membranes during oxidative coupling of methane. *Physical chemistry chemical physics : PCCP* **2020**, *22*, 18964–18975.

35. ARNOLD, M.; WANG, H.; FELDHOFF, A. Influence of CO_2 on the oxygen permeation performance and the microstructure of perovskite-type $(Ba_{0.5}Sr_{0.5})(Co_{0.8}Fe_{0.2})O_{3-\delta}$ membranes. *Journal of Membrane Science* **2007**, *293*, 44–52.

36. Benson, S.J.; Waller, D.; Kilner, J.A. Degradation of $La_{0.6}Sr_{0.4}Fe_{0.8}Co_{0.2}O_{3-\delta}$ in Carbon Dioxide and Water Atmospheres. *J. Electrochem. Soc.* **1999**, *146*, 1305–1309.

37. Joo, J.H.; Yun, K.S.; Yoo, C.-Y.; Yu, J.H. Novel oxygen transport membranes with tunable segmented structures. *J. Mater. Chem. A* **2014**, *2*, 8174–8178.

38. Yun, K.S.; Yoo, C.-Y.; Yoon, S.-G.; Yu, J.H.; Joo, J.H. Chemically and thermo-mechanically stable LSM–YSZ segmented oxygen permeable ceramic membrane. *Journal of Membrane Science* **2015**, *486*, 222–228.

39. Zhang, K.; Shao, Z.; Li, C.; Liu, S. Novel CO_2 -tolerant ion-transporting ceramic membranes with an external short circuit for oxygen separation at intermediate temperatures. *Energy Environ. Sci.* **2012**, *5*, 5257–5264.

40. Fischer, L.; Neuhaus, K.; Schmidt, C.; Ran, K.; Behr, P.; Baumann, S.; Mayer, J.; Meulenberg, W.A. Phase formation and performance of solid state reactive sintered $Ce_{0.8}Gd_{0.2}O_{2-\delta}$ -$FeCo_2O_4$ composites. *J. Mater. Chem. A* **2022**, *10*, 2412–2420.

41. Zeng, F.; Baumann, S.; Malzbender, J.; Nijmeijer, A.; Winnubst, L.; Guillon, O.; Schwaiger, R.; Meulenberg, W.A. Enhancing oxygen permeation of solid-state reactive sintered $Ce_{0.8}Gd_{0.2}O_2$-$FeCo_2O_4$ composite by optimizing the powder preparation method. *Journal of Membrane Science* **2021**, *628*, 119248.

42. Fischer, L.; Ran, K.; Schmidt, C.; Neuhaus, K.; Baumann, S.; Behr, P.; Mayer, J.; Bouwmeester, H.J.M.; Nijmeijer, A.; Guillon, O.*; et al.* Role of Fe/Co Ratio in Dual Phase $Ce_{0.8}Gd_{0.2}O_{2-}$ -$Fe_{3-x}Co_xO_4$ Composites for Oxygen Separation. *Membranes* **2023**, *13*.

43. Zhu, X.; Yang, W. Composite membrane based on ionic conductor and mixed conductor for oxygen permeation. *AIChE J.* **2008**, *54*, 665–672.

44. Lorenz, C.D.; Ziff, R.M. Precise determination of the critical percolation threshold for the three-dimensional “Swiss cheese” model using a growth algorithm. *The Journal of Chemical Physics* **2001**, *114*, 3659–3661.

45. Niehoff, P.; Baumann, S.; Schulze-Küppers, F.; Bradley, R.S.; Shapiro, I.; Meulenberg, W.A.; Withers, P.J.; Vaßen, R. Oxygen transport through supported Ba0.5Sr0.5Co0.8Fe0.2O3−δ membranes. *Separation and Purification Technology* **2014**, *121*, 60–67.

46. Chang, X.; Zhang, C.; Dong, X.; Yang, C.; Jin, W.; Xu, N. Experimental and modeling study of oxygen permeation modes for asymmetric mixed-conducting membranes. *Journal of Membrane Science* **2008**, *322*, 429–435.

47. Schulze-Küppers, F.; Baumann, S.; Meulenberg, W.A.; Bouwmeester, H. Influence of support layer resistance on oxygen fluxes through asymmetric membranes based on perovskite-type oxides SrTi1-Fe O3-. *Journal of Membrane Science* **2020**, *596*, 117704.

48. Lemes-Rachadel, P.; Garcia, G.S.; Machado, R.A.F.; Hotza, D.; Costa, J.C.D.d. Current developments of mixed conducting membranes on porous substrates. *Journal of Membrane Science* **2014**, *17*, 242–249.

49. Liu, Y.; Tan, X.; Li, K. Mixed Conducting Ceramics for Catalytic Membrane Processing. *Catalysis Reviews* **2006**, *48*, 145–198.

50. Xu, S.J.; Thomson, W.J. Oxygen permeation rates through ion-conducting perovskite membranes. *Chemical Engineering Science* **1999**, *54*, 3839–3850.

51. Bouwmeester, H.; Burggraaf, A.J. Chapter 10 Dense ceramic membranes for oxygen separation **1996**, *4*, 435–528.

52. Joo, J.H.; Yun, K.S.; Lee, Y.; Jung, J.; Yoo, C.-Y.; Yu, J.H. Dramatically Enhanced Oxygen Fluxes in Fluorite-Rich Dual-Phase Membrane by Surface Modification. *Chem. Mater.* **2014**, *26*, 4387–4394.

53. Ramasamy, M.; Baumann, S.; Palisaitis, J.; Schulze-Küppers, F.; Balaguer, M.; Kim, D.; Meulenberg, W.A.; Mayer, J.; Bhave, R.; Guillon, O.*; et al.* Influence of Microstructure and Surface Activation of Dual-Phase Membrane $Ce_{0.8}Gd_{0.2}O_{2-\delta}$-$FeCo_2O_4$ on Oxygen Permeation. *J. Am. Ceram. Soc.* **2016**, *99*, 349–355.

54. Na, B.T.; Park, J.H.; Park, J.H.; Yu, J.H.; Joo, J.H. Elucidation of the Oxygen Surface Kinetics in a Coated Dual-Phase Membrane for Enhancing Oxygen Permeation Flux. *ACS applied materials & interfaces* **2017**, *9*, 19917–19924.

55. Kwon, Y.; Na, B.T.; Park, J.H.; Yun, K.S.; Hong, S.K.; Yu, J.H.; Joo, J.H. Guidelines for selecting coating materials for a high oxygen permeation flux in a fluorite-rich dual-phase membrane. *Journal of Membrane Science* **2017**, *535*, 200–207.

56. Cheng, S.; Huang, H.; Ovtar, S.; Simonsen, S.B.; Chen, M.; Zhang, W.; Søgaard, M.; Kaiser, A.; Hendriksen, P.V.; Chen, C. High-Performance Microchanneled Asymmetric

Gd(0.1)Ce(0.9)O(1.95-δ)-La(0.6)Sr(0.4)FeO(3-δ)-Based Membranes for Oxygen Separation. *ACS applied materials & interfaces* **2016**, *8*, 4548–4560.

57. *The CRC handbook of solid state electrochemistry*; CRC Press: Boca Raton, Fla., 1997.

58. Lin, Y.-S.; Wang, W.; Han, J. Oxygen permeation through thin mixed-conducting solid oxide membranes. *AIChE J.* **1994**, *40*, 786–798.

59. Bouwmeester, H.; Kruidhof, H.; Burggraaf, A.J. Importance of the surface exchange kinetics as rate limiting step in oxygen permeation through mixed-conducting oxides. *Solid State Ionics* **1994**, *72*, 185–194.

60. Ramasamy, M.; Persoon, E.S.; Baumann, S.; Schroeder, M.; Schulze-Küppers, F.; Görtz, D.; Bhave, R.; Bram, M.; Meulenberg, W.A. Structural and chemical stability of high performance $Ce_{0.8}Gd_{0.2}O_{2-\delta}$-$FeCo_2O_4$ dual phase oxygen transport membranes. *Journal of Membrane Science* **2017**, *544*, 278–286.

61. Zeng, F. *Mechanical reliability and oxygen permeation of $Ce_{0.8}Gd_{0.2}O_{2-\delta}$-$FeCo_2O_4$ dual-phase composite*; University of Twente: Enschede, 2021.

62. Ramasamy, M. *Dual Phase Oxygen Transport Membrane for Efficient Oxyfuel Combustion*; Forschungszentrum Jülich GmbH, 2016.

63. Zhao, Q.; Yan, Z.; Chen, C.; Chen, J. Spinels: Controlled Preparation, Oxygen Reduction/Evolution Reaction Application, and Beyond. *Chemical reviews* **2017**, *117*, 10121–10211.

64. Kiefer, T. *Entwicklung neuer Schutz- und Kontaktierungsschichten für Hochtemperatur-Brennstoffzellen*; Forschungszentrum, Zentralbibliothek: Jülich, 2008.

65. Takamura, H.; Kawai, M.; Okumura, K.; Kamegawa, A.; Okada, M. Preparation and Oxygen Permeability of Gd-Doped Ceria and Spinel-Type Ferrite Composites. *MRS Proc.* **2002**, *756*.

66. Bahlawane, N.; Ngamou, P.H.T.; Vannier, V.; Kottke, T.; Heberle, J.; Kohse-Höinghaus, K. Tailoring the properties and the reactivity of the spinel cobalt oxide. *Physical chemistry chemical physics : PCCP* **2009**, *11*, 9224–9232.

67. Takamura, H.; Koshino, Y.; Kamegawa, A.; Okada, M. Electrode and oxygen permeation properties of (Ce, Sm)O_2–MFe_2O_4 composite thin films (M=Co and Mn). *Solid State Ionics* **2006**, *177*, 2185–2189.

68. Zhang, T. Iron oxide as an effective sintering aid and a grain boundary scavenger for ceria-based electrolytes. *Solid State Ionics* **2004**, *167*, 203–207.

69. Ferreira, T.; Waerenborgh, J.C.; Mendonça, M.; Nunes, M.R.; Costa, F.M. Structural and morphological characterization of $FeCo_2O_4$ and $CoFe_2O_4$ spinels prepared by a coprecipitation method. *Solid State Sciences* **2003**, *5*, 383–392.

70. Ji, Y.; Kilner, J.; Carolan, M. Electrical conductivity and oxygen transfer in gadolinia-doped ceria (CGO)–$Co_3O_{4-\delta}$ composites. *Journal of the European Ceramic Society* **2004**, *24*, 3613–3616.

71. Buchheit, A.; Teßmer, B.; Ran, K.; Mayer, J.; Wiemhöfer, H.-D.; Neuhaus, K. The Impact of Fe Addition on the Electronic Conductivity of Gadolinium Doped Ceria. *ECS J. Solid State Sci. Technol.* **2019**, *8*, P41-P50.

72. Malavasi, L.; Fisher, C.A.J.; Islam, M.S. Oxide-ion and proton conducting electrolyte materials for clean energy applications: structural and mechanistic features. *Chemical Society reviews* **2010**, *39*, 4370–4387.

73. Vernoux, P.; Lizarraga, L.; Tsampas, M.N.; Sapountzi, F.M.; Lucas-Consuegra, A. de; Valverde, J.-L.; Souentie, S.; Vayenas, C.G.; Tsiplakides, D.; Balomenou, S.*; et al.* Ionically conducting ceramics as active catalyst supports. *Chemical reviews* **2013**, *113*, 8192–8260.

74. Artini, C. Rare-Earth-Doped Ceria Systems and Their Performance as Solid Electrolytes: A Puzzling Tangle of Structural Issues at the Average and Local Scale. *Inorganic chemistry* **2018**, *57*, 13047–13062.

75. Kharton, V.V.; Kovalevsky, A.V.; Viskup, A.P.; Figueiredo, F.M.; Yaremchenko, A.A.; Naumovich, E.N.; Marques, F.M.B. Oxygen Permeability of $Ce_{0.8}Gd_{0.2}O_{2-\delta}$ $La_{0.7}Sr_{0.3}MnO_{3-\delta}$ Composite Membranes. *J. Electrochem. Soc.* **2000**, *147*, 2814.

76. PANHANS, M.; BLUMENTHAL, R. A thermodynamic and electrical conductivity study of nonstoichiometric cerium dioxide. *Solid State Ionics* **1993**, *60*, 279–298.

77. Koettgen, J.; Martin, M. The ionic conductivity of Sm-doped ceria. *J. Am. Ceram. Soc.* **2020**, *103*, 3776–3787.

78. Koettgen, J.; Grieshammer, S.; Hein, P.; Grope, B.O.H.; Nakayama, M.; Martin, M. Understanding the ionic conductivity maximum in doped ceria: trapping and blocking. *Physical chemistry chemical physics : PCCP* **2018**, *20*, 14291–14321.

79. Kharton, V.V.; Figueiredo, F.M.; Navarro, L.; Naumovich, E.N.; Kovalevsky, A.V.; Yaremchenko, A.A.; Viskup, A.P.; Carneiro, A.; Marques, F.M.B.; Frade, J.R. Ceria-based materials for solid oxide fuel cells. *J Mater Sci* **2001**, *36*, 1105–1117.

80. Presto, S.; Artini, C.; Pani, M.; Carnasciali, M.M.; Massardo, S.; Viviani, M. Ionic conductivity and local structural features in $Ce_{1-x}Sm_xO_{2-x/2}$. *Physical chemistry chemical physics : PCCP* **2018**, *20*, 28338–28345.

81. Duncan, K.L.; Wang, Y.; Bishop, S.R.; Ebrahimi, F.; Wachsman, E.D. Role of Point Defects in the Physical Properties of Fluorite Oxides. *J. Am. Ceram. Soc.* **2006**, *89*, 3162–3166.

82. MOGENSEN, M. Physical, chemical and electrochemical properties of pure and doped ceria. *Solid State Ionics* **2000**, *129*, 63–94.

83. Artini, C.; Costa, G.A.; Pani, M.; Lausi, A.; Plaisier, J. Structural characterization of the CeO2/Gd2O3 mixed system by synchrotron X-ray diffraction. *Journal of Solid State Chemistry* **2012**, *190*, 24–28.

84. Coduri, M.; Checchia, S.; Longhi, M.; Ceresoli, D.; Scavini, M. Rare Earth Doped Ceria: The Complex Connection Between Structure and Properties. *Frontiers in chemistry* **2018**, *6*, 526.

85. Artini, C.; Pani, M.; Carnasciali, M.M.; Buscaglia, M.T.; Plaisier, J.R.; Costa, G.A. Structural features of Sm- and Gd-doped ceria studied by synchrotron X-ray diffraction and μ-Raman spectroscopy. *Inorganic chemistry* **2015**, *54*, 4126–4137.

86. Artini, C.; Carnasciali, M.M.; Viviani, M.; Presto, S.; Plaisier, J.R.; Costa, G.A.; Pani, M. Structural properties of Sm-doped ceria electrolytes at the fuel cell operating temperatures. *Solid State Ionics* **2018**, *315*, 85–91.

87. Artini, C.; Pani, M.; Carnasciali, M.M.; Plaisier, J.R.; Costa, G.A. Lu-, Sm-, and Gd-Doped Ceria: A Comparative Approach to Their Structural Properties. *Inorganic chemistry* **2016**, *55*, 10567–10579.

88. Gielen, D. and M. Lyons. Critical Materials For The Energy Transition: Rare Earth elements, *2022*.

89. Artini, C.; Viviani, M.; Presto, S.; Massardo, S.; Carnasciali, M.M.; Gigli, L.; Pani, M. Correlations between structure, microstructure and ionic conductivity in (Gd,Sm)-doped ceria. *Physical chemistry chemical physics : PCCP* **2022**, *24*, 23622–23633.

90. Coles-Aldridge, A.V.; Baker, R.T. Ionic conductivity in multiply substituted ceria-based electrolytes. *Solid State Ionics* **2018**, *316*, 9–19.

91. Kilner, J.A. Defects and Conductivity in Ceria-based Oxides. *Chem. Lett.* **2008**, *37*, 1012–1015.

92. Luo, H.; Efimov, K.; Jiang, H.; Feldhoff, A.; Wang, H.; Caro, J. CO2-stable and cobalt-free dual-phase membrane for oxygen separation. *Angewandte Chemie (International ed. in English)* **2011**, *50*, 759–763.

93. Luo, H.; Jiang, H.; Efimov, K.; Liang, F.; Wang, H.; Caro, J. CO_2 -Tolerant Oxygen-Permeable Fe_2O_3 -$Ce_{0.9}Gd_{0.1}O_{2-\delta}$ Dual Phase Membranes. *Ind. Eng. Chem. Res.* **2011**, *50*, 13508–13517.

94. Cheng, H.; Zhang, N.; Xiong, X.; Lu, X.; Zhao, H.; Li, S.; Zhou, Z. Synthesis, Oxygen Permeation, and CO_2 -Tolerance Properties of $Ce_{0.8}Gd_{0.2}O_{2-\delta}$ –$Ba_{0.95}La_{0.05}Fe_{1-x}Nb_xO_{3-\delta}$ Dual-Phase Membranes. *ACS Sustainable Chem. Eng.* **2015**, *3*, 1982–1992.

95. Kim, S.K.; Shin, M.J.; Rufner, J.; van Benthem, K.; Yu, J.H.; Kim, S. $Sr_{0.95}Fe_{0.5}Co_{0.5}O_{3-\delta}$–$Ce_{0.9}Gd_{0.1}O_{2-\delta}$ dual-phase membrane: Oxygen permeability, phase stability, and chemical compatibility. *Journal of Membrane Science* **2014**, *462*, 153–159.

96. Samson, A.J.; Søgaard, M.; Vang Hendriksen, P. (Ce,Gd)O_2−-based dual phase membranes for oxygen separation. *Journal of Membrane Science* **2014**, *470*, 178–188.

97. Nigge, U. Composites of $Ce_{0.8}Gd_{0.2}O_{2-\delta}$ and $Gd_{0.7}Ca_{0.3}CoO_{3-\delta}$ as oxygen permeable membranes for exhaust gas sensors. *Solid State Ionics* **2002**, *146*, 163–174.

98. Wang, S. Electrical and Ionic Conductivity of Gd-Doped Ceria. *Proc. Vol.* **1999**, *1999-19*, 193–200.

99. Joo, J.H.; Park, G.S.; Yoo, C.-Y.; Yu, J.H. Contribution of the surface exchange kinetics to the oxygen transport properties in $Ce_{0.9}Gd_{0.1}O_{2-\delta}$–$La_{0.6}Sr_{0.4}Co_{0.2}Fe_{0.8}O_{3-\delta}$ dual-phase membrane. *Solid State Ionics* **2013**, *253*, 64–69.

100. Pikalova, E.Y.; Demina, A.N.; Demin, A.K.; Murashkina, A.A.; Sopernikov, V.E.; Esina, N.O. Effect of doping with Co_2O_3, TiO_2, Fe_2O_3, and Mn_2O_3 on the properties of $Ce_{0.8}Gd_{0.2}O_{2-\delta}$. *Inorg Mater* **2007**, *43*, 735–742.

101. Tsipis, E.V.; Waerenborgh, J.C.; Kharton, V.V. Grain-boundary states in solid oxide electrolyte ceramics processed using iron oxide sintering aids: a Mössbauer spectroscopy study. *J Solid State Electrochem* **2017**, *21*, 2965–2974.

102. Cousin, P. Ross, R.A. Preparation of mixed oxides: a review. *Mater. Sci. Eng., AMaterials Science & Engineering, A: Structural Materials: Properties, Microstructures and Processing* **1990**, 119–125.

103. Kilner, J.A.; Burriel, M. Materials for Intermediate-Temperature Solid-Oxide Fuel Cells. *Annu. Rev. Mater. Res.* **2014**, *44*, 365–393.

104. Bredesen R., Sogge J. *A Technical and Economic Assessment of Membrane Reactors for Hydrogen and Syngas Production*, 1996.

105. den Exter M. J. , Haije W. G. , Vente J. F. *Inorganic Membranes for Energy and Environmental Applications*, 2009.

106. Schulze-Küppers, F.; Baumann, S.; Tietz, F.; Bouwmeester, H.; Meulenberg, W.A. Towards the fabrication of $La_{0.98-x}Sr_xCo_{0.2}Fe_{0.8}O_{3-\delta}$ perovskite-type oxygen transport membranes. *Journal of the European Ceramic Society* **2014**, *34*, 3741–3748.

Chapter 2

2. Impact of the sintering parameter on the microstructural and transport properties of 60 wt. % $Ce_{0.8}Gd_{0.2}O_{2-\delta}$ – 40 wt. % $FeCo_2O_4$ composites

Abstract

The dual-phase composite 60 wt. % $Ce_{0.8}Gd_{0.2}O_{2-\delta}$ - 40 wt. % $FeCo_2O_4$ (60CGO20-FCO) shows to be an excellent Oxygen Transport Membrane (OTM) with sufficient stability and oxygen permeance. To achieve a mechanically and chemically stable composite material an optimised microstructure should be designed. In general, the modification of the sintering profile is a classical way of microstructure optimization as well as optimization of the functional properties of ceramic materials. Moreover, optimization of the sintering program would be beneficial to minimize the increase in porosity and achieve maximum densification with minimum pore and grain growth during sintering. Thus, the chosen 60CGO20-FCO composite has been subjected to different heat treatments to determine its impact on the main morphology characteristics, such as grain size, pore size, relative density, and porosity. The dwell time was varied between 0 and 100 hours at 1200°C and seems to have an influence on the fraction of the resulting phases, revealing the formation of a high-temperature CoO phase after 100 hours. In other samples fired for 0 - 50 hours at 1200°C fluorite, spinel, and perovskite phases are prevailing. To eliminate the undesired CoO phase the cooling rate has been varied. The results reveal that the 5-hour dwell time at 1200 °C is the most suitable one for the chosen composite material, resulting in a sufficiently dense membrane with well-distributed phases, and can be further utilized for scaling up OTM production.

This Chapter is submitted for publication to Materials Advances Journal in December 2023

2.1 Introduction

Recently the development of ceramic dual-phase materials for Oxygen Transport Membranes (OTM) attracts much attention in the scientific community as mixed ionic-electronic conductors (MIEC) are very promising for gas separation [1–5] at elevated temperatures and have the potential for improving performance and reducing the cost of several industrial processes [6,7]. MIEC materials can be used for oxygen separation from mixed gases, such as air. The oxygen separation process can include exposure to flue gases containing CO_2, SO_x, dust, and steam [8–10]. Nowadays, dense dual- and multiphase composite materials with separate ionic and electronic conductors are among the most promising and efficient materials regarding stability for application in membrane reactors [11–16]. However, these material systems are quite complex and affected by many factors, such as sintering temperature and dwell time. Thus, because of the complexity of this composite system a systematic study of the microstructure-related features is required.

Rare earth doped ceria with the fluorite structure showed to be an excellent ion-conductor [17–19], in particular for application at temperatures <850°C [20,21]. The $Fe_xCo_{3-x}O_4$ ($0 < x < 3$) spinel system is found to be most suitable and promising for the targeted application due to its stability in aggressive atmospheres and good electronic conductivity [22–24]. The fluorite-spinel composite $Ce_{0.8}Gd_{0.2}O_{2-\delta}$-$FeCo_2O_4$ (CGO20-FCO) is a suitable example of such a material, providing a stable structure and sufficient oxygen permeability [25,26]. The presence of both phases is key to ensure good percolation, which leads to a stable oxygen flux, and sufficient performance of the composite [14,15]. This means that the concentrations of the individual phases should be above the percolating threshold, which is generally reported as 30 vol. % [27,28]. Under ideal conditions, all selected phases should stay separate and not interact during the heat treatment. However, recent studies reported the formation of an additional emerged orthorhombic phase of the $GdFeO_3$-type after phase interaction [13,14,29–31]. This phase contributes effectively to electronic conductivity [11,14,31].

Generally, to ensure a stable and functional dual- or multi-phase material for long-term gas separation processes, the quality of the connectivity and compatibility of the two phases is crucial. Hence, a defect-free membrane with optimized phase morphology should be targeted. Under real conditions, interface between particles is imperfect and can depend on different factors, such as powder particle size, synthesis and sintering parameters. The control of the microstructure via modification of the heat treatment plays an important role in the solid-state sintering process and defines the properties of the material, such as density, strength, and transport features [18,32–34].

In general, a temperature range of 1100-1500 °C is used to prepare the dual- and multiphase composites for the OTM [18,33–35]. At lower temperatures, a lack of densification can be expected, and one may obtain a material with poor mechanical properties. A temperature up to 1600 °C is necessary to yield a dense functional single phase ceria membrane [36]. However, the addition of the other oxides (i.e. Fe_2O_3) as sintering aids can lower the sintering temperature and reach sufficient densification of the dual-phase material [37]. For the CGO20-FCO system, the optimal sintering temperature is 1200 °C. Above 1300 °C undesired effects, such as increased grain growth, can be observed, which in turn can affect the mechanical and transport properties of the material in negative way [32,38]. Grain growth is a known phenomenon in ceria-based materials at elevated temperatures [39,40]. The effect of the temperature on the CGO20-FCO composite materials is already investigated in the context of phase interaction [33,41–44].

However, some questions related to the phase interaction as well as the morphology of the CGO20-FCO dual-phase composite are still open. When is the phase interaction completed in the CGO20-FCO composite, considering the complexity of this system? Is there an influence of the cooling rate on the phase composition? What is the dwell time requirement for the densification and pore removal processes at 1200 °C for the studied MIEC materials? To clarify all these aspects the correlation between the dwell time and phase interaction, final morphology, and permeation performance should be investigated.

The current study aims to present detailed characterization of the 60CGO20-FCO composites, including the quantification of all phase constituent volume fractions, grain and pore size, and density as well as the porosity, and reveal the relationships between the microstructure features with the applied heat treatment and cooling methods. Furthermore, comparatively little research has been conducted on the effect of the dwell time on the morphology features and the permeation performance of the CGO20-FCO composite, which will be presented here.

2.2 Experimental

2.2.1 Sample preparation

$Ce_{0.8}Gd_{0.2}O_{2-\delta}$ (CGO20) (Cerpotech, >99%, Tiller, Norway), Fe_2O_3 (FO) (Merck, 99 %) and Co_3O_4 (CO) (Merck, 99 %) powders used for the experiments were synthesized by the Solid-State Reactive Sintering method (SSRS). Fe_2O_3 and Co_3O_4 were mixed in a Fe: Co 1:2 ratio, resulting in spinel $FeCo_2O_4$ (FCO), which was added to commercially available Gd-doped ceria. Respective amounts of powders were weighed to create $Ce_{0.8}Gd_{0.2}O_{2-\delta}$ - $FeCo_2O_4$ (CGO20-FCO) compositions with wt. % - ratios of 60:40 and 80:20. The powder mixtures were ball milled in polyethylene bottles over 48 h using zirconia balls on a roller bench at a speed of 175 rpm. After drying for 48 h in ambient air at 70 °C, powder mixtures were pressed using a uniaxial press in disc-shaped membranes in a 20-mm stainless steel die and then sintered at 1200 °C for different dwell times in air with a heating rate of 5 K min^{-1} as listed in Table 2.1. At this sintering temperature, the spinel partially reduces into a high-temperature monoxide phase with a rock salt structure. To ensure complete reoxidation of the high-temperature Co/Fe-monoxide phase to a spinel phase that is stable at operating temperatures (600-1000 °C), a slow rate of 0.5 K min^{-1} between 900 and 800 °C was implemented in the cooling step. This rate was chosen by referring to [45,46] .

Table 2.1 Selected dwelling time (t, h) at 1200°C for the investigated composites

Composite	0	0.16	0.5	1	5	20	50	100
60:40 CGO20-FCO	√	√	√	√	√	√	√	√
80:20 CGO20-FCO					√			√

After the sintering step, all samples were ground to 1 mm thick discs in two steps, by applying SiC papers with different grits from P 800 to P 1200 (by WS FLEX 18C). The surface of the membrane can contribute to the oxygen exchange process in an important, though more limited way. Modifying the surface by applying a catalytic layer is required to maximize surface area, participating in the process, and minimize all possible surface limitations. On both sides of the discs, a porous $La_{0.58}Sr_{0.4}Co_{0.2}Fe_{0.8}O_{3-\delta}$ (LSCF) catalytic activation layer with a thickness of 5 μm was applied using a screen-printing technique. The resulting discs were then calcined in the furnace at 1100 °C for 5 hours.

The impact of the cooling method on the microstructural properties of the 60CGO20-FCO composite sintered at 1200 °C for 100 h was performed and used heat treatment parameters are listed in Table 2.2.

Table 2.2 Heat treatment and cooling methods of the 60CGO20-FCO composites sintered at 1200°C

Heat treatment and cooling method	Named further
Sintered at 1200 °C for 5 h and cooled with standard 0.5 K min^{-1} between 900 and 800 °C in the furnace	*5h*
Sintered at 1200 °C for 100 h and held additionally at 850 °C for 100h then cooled in the furnace with 0.5 K min^{-1} between 900 - 800 °C	*Slow*
Sintered at 1200 °C for 100 h and cooled with standard 0.5 K min^{-1} between 900 and 800 °C in the furnace	*Standard*
Sintered at 1200 °C for 100 h and cooled freely in the air outside the furnace	*Fast*
Sintered at 1200 °C for 100 h and quenched in water	*Quenching*

2.2.2 Characterization methods

Crystal structure

The crystal structure of the materials was determined using an X-ray diffraction (XRD) diffractometer D4 ENDEAVOR (Bruker, Karlsruhe, Germany). The diffraction angle was chosen in the range of 2θ from 10° to 80°, with increments of 0.02° for 2θ and 0.75 seconds of measurement time per step. Analysis of the measured data was performed with X'Pert HighScore (PANalytical B.V., version 3.0.5) software. Phase quantifications and associated crystal structure analyses were carried out by Rietveld refinement using the software Profex (Version 4.2.2) software. A low error Rwp was held <4 % for all samples, which also indicates a good fitting. The errors of each fit were calculated individually and are reported in Table 2.3.

Microscopy

Scanning Electron Microscopy (SEM) and Energy Dispersive X-ray Spectroscopy (EDS) were used to study the morphology of the prepared materials. SEM images were taken with a Zeiss Ultra 55 and a Zeiss Semini SEM 450 (Carl Zeiss NTS GmbH, German) at different magnifications. The electronic conductivity of samples was enhanced by sputter deposition of a thin platinum layer prior to the measurement.

Further image analysis-based method was conducted via ImageJ software on all composite samples including ~1000 grains utilizing so-called isodata threshold method [47], which helped to estimate the average grain size of all phases as well as area fraction of pores. However, the limited number of characterized grains/pores might induce large inaccuracy in the grain size and pore size calculations.

For Transmission Electron Microscopy (TEM) analysis, all specimens were cut from composite pellets by focused ion beam (FIB) milling using an FEI Strata 400 system with a gallium ion beam. Further thinning and cleaning was performed using an argon ion beam in a Fischione Nanomill 1040 at beam energies of 900 eV and 500 eV. TEM and energy-filtered TEM (EFTEM) imaging was performed using an FEI Tecnai F20 at 200 kV. For high-resolution high-angle annular dark-field (HAADF) imaging and Energy-dispersive X-ray spectroscopy (EDS) chemical mapping an FEI Titan G2 80-200 ChemiSTEM microscope equipped with an high brightness field emission (XFEG) gun and a probe Cs corrector was used [48].

Oxygen permeation measurements

All composite materials were subjected to oxygen permeation experiments. The experimental setup consisted of a vertical quartz glass housing, where the membrane pellets were sealed with two gold rings with an inner diameter of 13 mm. The separation of the oxygen from ambient air fed with 250 mlN min^{-1} was performed in a temperature range between 650 °C and 1000 °C. As a sweep gas argon was used with 50 mlN min^{-1} flow rate using mass flow controllers (Bronkhorst, Germany). A mass spectrometer (Omnistar, Pfeiffer Vacuum GmbH, Germany) was used to detect concentrations of oxygen and nitrogen in the permeate gas, i.e., oxygen enriched argon. With the help of the measured nitrogen concentration in the argon sweep gas, air leakage through either membrane or the sealing was calculated according to

$$j_{O_2} = F_{Ar}\left(\frac{X_{O_2} - \frac{1}{4}X_{N_2}}{1 - X_{O_2} - X_{N_2}}\right)\frac{1}{A_{mem}} \qquad \textbf{Equation 2.1}$$

Here F_{Ar} is argon flow rate, *i.e.,* 50 ml_N min^{-1}, X_{O2} and X_{N2} the oxygen and nitrogen concentration in the permeate gas, respectively. The membrane area available for permeation is A_{mem}=1.33 mm^2. The factor $\frac{1}{4}$ reflects the O_2/N_2 ratio in the air feed assuming that the leak is not gas selective.

Since the oxygen partial pressure in the permeate gas is temperature dependent, the driving force for permeation is not constant during the measurement. Additionally, the sample thickness deviation after the grinding process was ±8 % from the target thickness of 1 mm. Therefore, the permeance, i.e., driving force normalized permeation rate, normalized to the reference thickness L_0 = 1 mm is calculated assuming Wagner´s behaviour using

$$Permeance = \frac{j_{O_2}}{ln\frac{p_{O_2}^{'}}{p_{O_2}^{''}}}\frac{L_{mem}}{L_0}$$ **Equation 2.2**

Here, $p_{O_2}^{'}$ and $p_{O_2}^{''}$ are the oxygen partial pressures in the retentate and permeate gas, respectively, and L_{mem} is the actual membrane thickness. The overall experimental error is assumed to be ±10 %, which is well accepted in the literature.

2.3 Results and discussion

Based on the realization of the complex but important microstructures of dual-phase oxygen transport membranes, the standard composite 60CGO20-FCO was subjected to sintering at 1200 °C for different dwell times and further analysed to clarify the connection between the dwell time and phase interaction, morphology as well as permeation.

2.3.1 Microstructure analysis

60CGO20-FCO at 1200°C for different dwelling time

The resulting XRD pattern of each as-sintered sample and before heat treatment is shown in Figure 2.1. The as-pressed pellet showed the presence of the three starting oxides: Fe_2O_3, Co_3O_4, and 20 mol. % Gd-doped ceria.

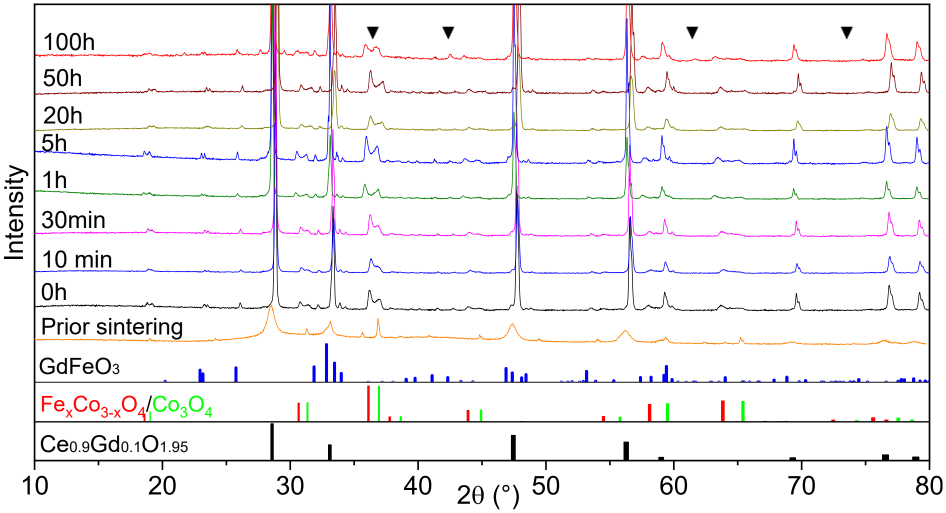

Figure 2.1 The XRD patterns of the 60CGO20-FCO composite sintered at 1200 °C with various dwell times, including an unsintered pellet. CoO rock salt phase peaks are marked as a triangle. At the bottom, reference reflections are shown for the perovskite in blue, spinel in red and green, and fluorite in black

In all sintered samples the final microstructure consists of three phases after phase interaction: a cubic fluorite structure with space group *Fm3m*, a donor-doped orthorhombic $GdFeO_3$ (GCFCO) perovskite structure with space group *Pnma*, and Fe/Co rich phases with a cubic spinel structure with space group *Fm3m*. This is in agreement with [44] since the formation of the Fe-Co spinel in CGO20-FCO composite starts at 900 °C and perovskite at 1050 °C. An exception is the 100 hours sintered pellet, where an additional CoO rock salt phase with space group *Fm3m* was observed, which is a result of incomplete re-oxidization during cooling. This has already been observed in earlier research [26,45,49,50]. The CoO phase is difficult to distinguish in the XRD patterns since they can hardly be separated from the GCFCO and Co_3O_4 patterns, however, several peaks are marked are assigned to the CoO phase in Figure 2.1. Moreover, with respect to the Fe-Co oxide phase diagram [46], a coexistence of the two spinel phases is detected in all samples: the nominal and inverse spinel. According to the Fe-Co phase diagram, which shows that the $FeCo_2O_4$ spinel is only stable in a narrow temperature range [51], it can be concluded that Fe-rich spinel is likely the $CoFe_2O_4$ structure in the final microstructure.

Table 2.3 Lattice parameter (a) and fraction (F) of the phases after quantification by Rietveld refinement analyses of the 60CGO-FCO composites sintered at 1200 °C

	CGO(Fluorite), *Fm3m*		**FCO (Spinel), *Fd3m***		**Co_3O_4(Spinel), *Fd3m***		**GCFCO (Perovskite), *Pnma***				**CoO *Fm-3m***
t	F, wt.%	a=b=c, Å	F wt.%	a=b=c, Å	F, wt.%	a=b=c, Å	F, wt.%	Lattice parameter, Å a	b	c	F, wt.%
CGO20	100.0	5.424[3]	-	-	-	-	-	-	-	-	-
0 h	53.9[3]	5.417[1]	17.7[3]	8.286[3]	20.3[6]	8.146[0]	8.1[6]	5.336[3]	5.609[4]	7.652[6]	-
0.16h	55.4[5]	5.417[3]	17.6[3]	8.297[1]	19.6[6]	8.146[3]	7.5[9]	5.333	5.606[1]	7.641[3]	-
0.5h	54.5[4]	5.419[9]	17.3[6]	8.297[7]	19.6[2]	8.146[2]	8.6[3]	5.337[3]	5.609[2]	7.652[7]	-
1h	53.1[3]	5.419[2]	23.1[7]	8.280[6]	15.3[3]	8.146[0]	8.5[7]	5.337[1]	5.610[2]	7.654[8]	-
5h	52.1[2]	5.418[5]	22.3[1]	8.287[3]	16.6[0]	8.125[1]	9.0[3]	5.336[3]	5.608[6]	7.639[7]	-
20h	53.6[3]	5.417[3]	15.7[0]	8.298[3]	22.1[2]	8.140[3]	8.5[3]	5.339[0]	5.611[5]	7.649[8]	-
50h	52.3[4]	5.416[8]	18.1[6]	8.309[2]	20.0[9]	8.138[8]	9.7[5]	5.337[6]	5.612[3]	7.653[3]	-
100h	54.7[3]	5.417[2]	17.1[3]	8.330[3]	17.4[7]	8.161[3]	7.9[3]	5.341[7]	5.618[5]	7.635[3]	2.8[9]

Further Rietveld refinement quantified the composition of the dual-phase composites, which are listed in Table 2.3. The unit-cell parameters of the pure phases are known from the literature $a_{(FeCo2O4)}$=0.8244 nm, $a_{(Fe2CoO4)}$=0.8385 nm [24,51,52], $a_{(Co3O4)}$=0.8142 nm [52,53] and $a_{(CGO20)}$=0.54209 nm [54,55]. The lattice parameter of CGO20 used in our composite before phase interaction was a=0.54246 nm and it was found to decrease by the addition of the spinel resulting in $a_{(CGO20)}$ =0.5418±0.0001 nm. It can be concluded that the fluorite phase contains 10 mol.% of Gd, instead 20 mol.%, due to phase interaction and formation of a GCFCO emerged phase, which is in accordance with previously published work [11,56]. There was no remarkable change in CGO lattice parameter along the whole investigated time range. The influence of the dwell time on the lattice parameter seems to be stronger for the inverse and normal spinel phases.

The weight fraction of the fluorite remains almost unchanged, revealing a slightly lower amount for samples >1 hour dwell time, compared to <1 hour. The amount of GCFCO also remains almost constant in the range of 8.5±1 wt.%, regardless of the dwell time. The $GdFeO_3$-based perovskite phase that is formed during the sintering process can be considered as a pure electron conductor according to *Ramasamy, Fischer et al* [11,14], and its contribution leads to an increase in the amount of total electron conducting phase, that in turn takes place at the expense of the of ion-conducting phases. All studied samples were subjected to the analysis described in *Fischer et al.* [14], and the resulting volume fraction of individual phases was estimated and graphically represented in Figure 2.2b.

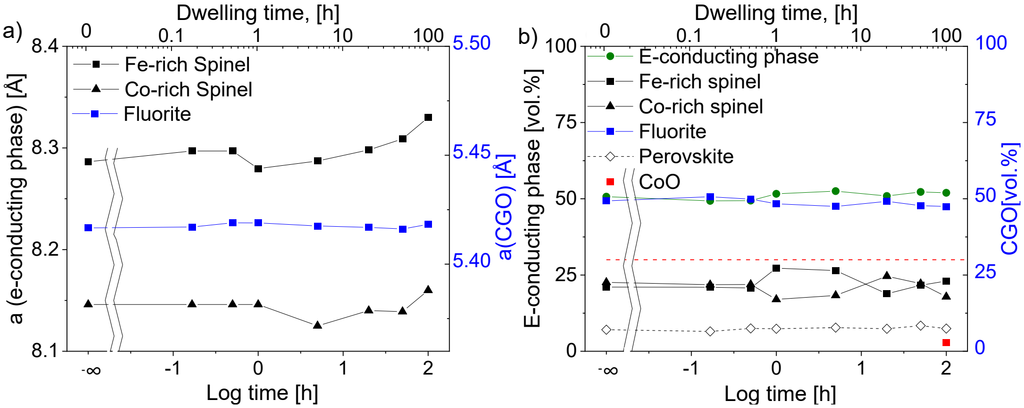

Figure 2.2 a) Lattice parameter and b) volume fraction of observed phases in 60CGO20-FCO composites sintered at 1200 °C (solid lines are a guide to the eye)

The percolation threshold of 30 vol. % (shown as a red dashed line in Figure 2.2b) has been achieved for all samples: the sum of volume fraction of all present electron conducting phases (spinels and perovskite) shown in green lays in the range of 50.5±1 vol. %. That explains the relatively high oxygen flux for the composites. The amount of additional CoO phase is ~2.8 vol. % in a 100 hours fired sample, which likely contributes to electronic conductivity, too [56]. Due to the long dwell time the amount of CoO is increased within the composite, which in turn has not enough time for its complete reoxidation to a spinel phase.

Back scattered electron (BSE) SEM images of the surface in Figure 2.3 reveal the distribution of the phases in samples fired at 1200 °C for various dwell times, including fluorite, spinel, and perovskite grains distinguished by different grey scales. It is known, that an emerging GCFCO phase appears at 1050 °C [44]. In all studied samples fired at 1200 °C the perovskite phase is fully formed as indicated in light grey, dark spinel grains possess a rather uneven grain size, being coarsely distributed among white CGO grains.

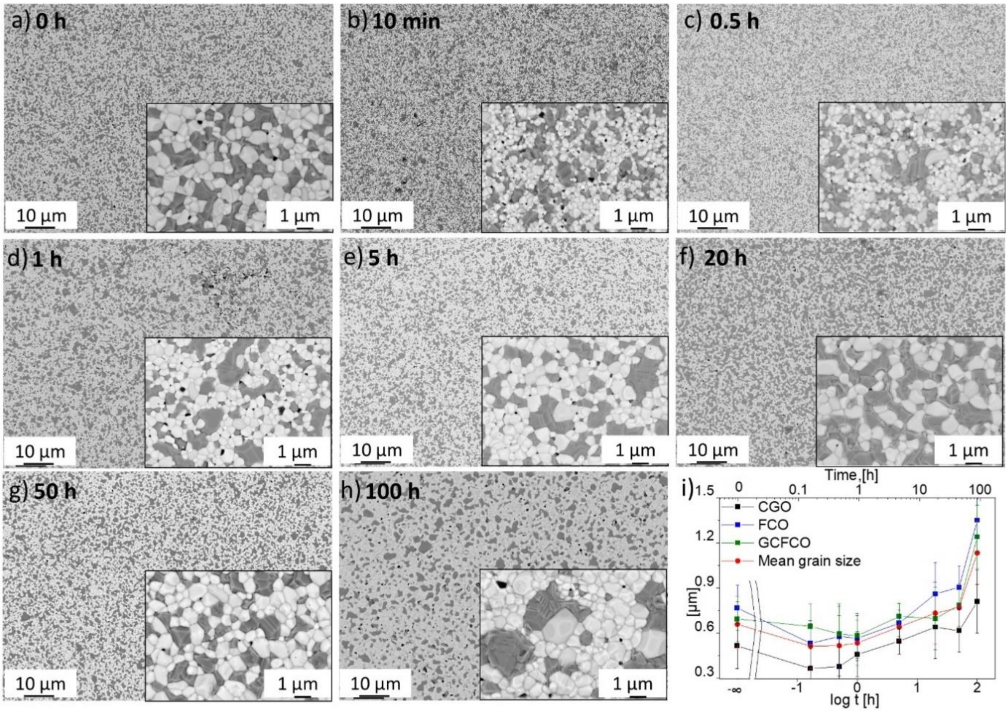

Figure 2.3 a-h) BSE-images of 60CGO20-FCO surface morphology of the samples sintered at 1200 °C with two magnifications i) Graph of grain size of individual phases as a function of the dwell time (solid lines are a guide to the eye)

Generally, there are two stages of grain growth. The initial coarsening stage is between room temperature and the sintering temperature. During this stage coarsening can be responsible for grain growth, but not a conventional boundary migration. Since the grain boundaries are possibly pinned by the open pore channels in as-pressed sample. At this stage, the density of the sample is quite low, but the particle rearrangement and surface diffusion can lead to some grain growth. After reaching the sintering temperature at the typical density above 90 % the second stage of grain growth begins, where grain boundary migration via a diffusion process is likely to be dominating mechanism [57]. The grains grow rapidly, and pores become closed and isolated, leading also to the pore coarsening. Densification, grain, and pore growth are the three main processes that occur during sintering in the ceramic composite [44].

Grain and pore size

The first visual analysis of the surface morphology by SEM reveals that an increase in dwell time occurring across the dwell time range of 0-1 h results in a surface with rather small grain size. Between 5-100 hours, the surface is quite plain and smooth with enlarged grains. The grain size of each phase as well as the pore size and area fraction of pores were analysed by an image analysis-based method with ImageJ software for all samples[47,58].

In the not single-phase composites, the uniform distribution of the one phase in the uniformly packed matrix of the second phase is required [57]. Our powder mixture consists of more than one solid prior firing process, so the grain growth is probably limited because of the second phase in the grain boundaries. Thus, in the investigated composite, the grain growth is not homogeneous and depends on the type of grains; spinel grains are slightly larger compared to the fluorite and perovskite grains.

The mean grain size of the four phases increases with increasing dwell time, as displayed in Figure 2.3i. Below 1 hour, the grain growth is less pronounced, with an almost constant value of 0.57 µm, followed by a gradual increase in the grain size to 0.77 µm at 50 hours. Then a drastic increase can be seen at doubling the dwell time, resulting in the largest grain size of 1.13 µm at 100 h. In general, the sintering process involves the competition of both main processes: coarsening and densification and probably depends on the dwell time at 1200°C. It is likely that grain growth is the dominant process for the samples sintered for 50 and 100 h, while below 50 h other processes are dominant. The increased grain size in ceramic materials might lead to enhanced crack formation and poor mechanical properties [59].

Figure 2.4 shows the grain and pore size, density, and porosity as a function of isothermal holding time. Three well-defined regions can be identified concerning the dominating process as a function of time. Densification is usually driven by pore agglomeration and pore-removing processes. When the grain growth is faster compared to pore growth, which naturally accompanies the grain growth, the material undergoes densification. For the analysis, the pore/grain ratio was introduced and its change describes coarsening and densification, which also helps to distinguish the regimes along the time range [38].

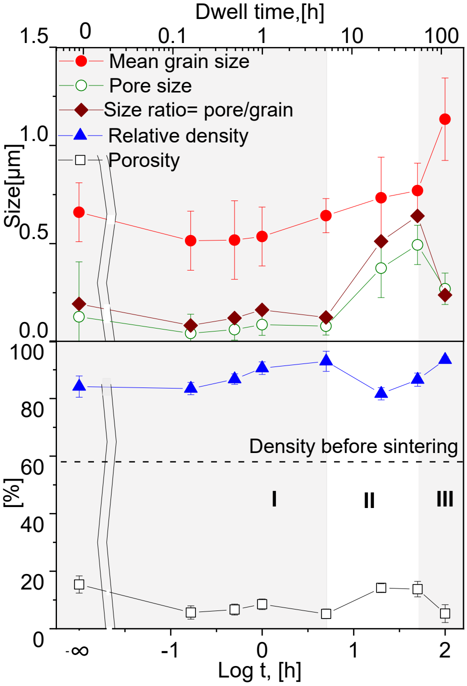

Figure 2.4 a) Estimated relative density and porosity over the dwell time; b) Average grain, pore size and the pore/grain ratio dependency on the dwell time in the 60CGO20-FCO composites sintered at 1200 °C (solid lines are a guide to the eye)

Density

An increase in density with an accompanying moderate grain growth is known for Gd-doped ceria during the first step of densification [60]. Sintering at 1200 °C for dwell times between 0 and 100 hours led to a densification level between 82 and 93 % of the theoretical density. It is clear that all samples undergo some densification process already at the heating phase, as the 0 h sintered sample shows a relative density > 80 %. In our case the samples held isothermally for less than 5 hours showed densification as the dominant process (I). The relative density of the samples gradually increases until a maximum of 93 % at 5 h. Between 5 and 50 hours grain and pore growth develop concurrently with slight pore growth domination, where possibly de-densification occurs resulting in a relative density reduction (II) (similar to [41]). At 100 hours again a decrease in densification is observed (III). This suggests that a sufficient dwell time for the 60CGO20-FCO composite at 1200 °C is 5 hours, where a fast and effective densification process takes place. Since the relationships between relative density and grain size are not linear, the densification processes and grain growth likely proceed via different diffusion routes in surface and volume, possibly due to the large difference in E_a of these diffusion mechanisms [61].

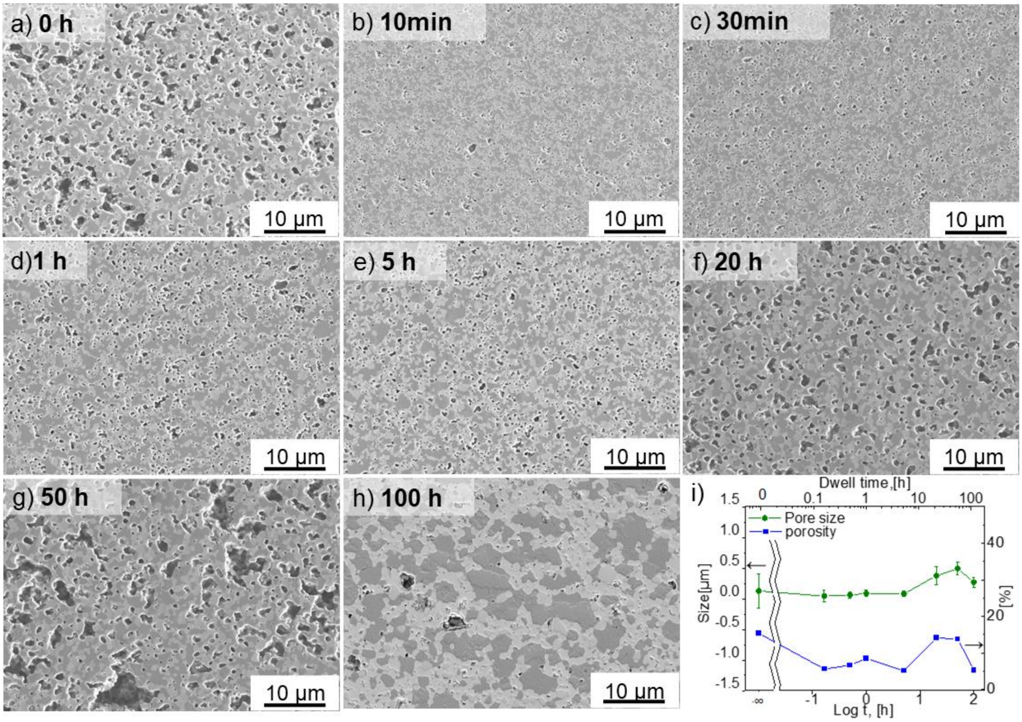

Figure 2.5 a-f) SE-images of cross-section 60CGO20-FCO composite sintered at 1200 °C for different dwell time i) pore size and porosity as a function of the dwell time (solid lines are a guide to the eye)

The density of the 20 h and 50 h-fired samples rapidly decreased to a minimum (82 % of the theoretical density) at 20 hours, where probably the de-densification phenomenon occurs. The observed loss in the density of the dual-phase composite could be attributed to a loss of weight as a result of oxygen gas production, with a reduction of Ce^{4+} to Ce^{3+} in the fluorite phase. In the spinel phase, the reduction of iron and cobalt also leads to a release of oxygen and the formation of a rock salt phase, which increases pore volume and size at elevated temperature [62].

Porosity

Porosity is also affected by various dwell times, as pore growth is related to both aforementioned processes during sintering: grain growth and densification. The surface images with higher magnification in Figure 2.3 display an intergranular porosity in all samples. The intragranular porosity level is relatively low for all samples, which is advantageous and gives a possibility to remove pores during the final stage of sintering for this composite. The surface image analysis is, however, incomplete since it cannot reveal distribution in the bulk, due to the “skin” layer formed on the surface. The cross-section images in Figure 2.5 a-i illustrate the dependency of the pore size and pore distribution on the dwell time in the bulk. The pore growth, migration and accumulation in connection with the dwell time are shown. There are many trapped pores along grain boundaries and in interior of the individual grains in the investigated samples.

The porosity of the samples has been estimated from the SEM images via ImageJ software [47], while the relative density was estimated geometrically. The resulting values are in agreement and depicted in Figure 2.4. The porosity lies between 5-6 % for all samples, except peaks at 0 h, 20 h, and 50 h, with 15 %, 13 %, and 14 % respectively.

All samples fired below 5 hours exhibit a slightly higher level of open porosity with a homogeneous distribution of pores, corresponding to a densification ratio of 84-90 %. Pores are also present in samples fired for >5 h, however, most of them are closed and large, which could be due to the clustering of the pores: the longer sample was held in the furnace, the more pores were united into larger ones, building a connected network. The grain size difference, comprehensive stress on pores, and surface tension drive pore growth in ceramic materials [38,61]. For dwell times between 0 and 50 hours pores are thermodynamically stable, so the grain growth process takes place via mass transport, and thus densification occurs. At dwell times >50 hours the pores are possibly unstable and hence both grain growth and pore removal can be observed, similar as was observed elsewhere [38]. With a dwell time below 5 hours there is no significant influence on the pore size, it remains almost constant (0.1 µm) and afterwards increases up to 0.5 µm at 50 h dwell time, followed by shrinkage of the pore size to 0.27 µm at 100 h dwell time. Such behaviour points out that by reaching 1200 °C the process of pore clustering starts from 5 h dwell time, with simultaneous loss in material density. Based on the analysis, three main regions corresponding to the governing process can be distinguished: densification, pore-growth, and drastic grain growth, as shown in Figure 2.4.

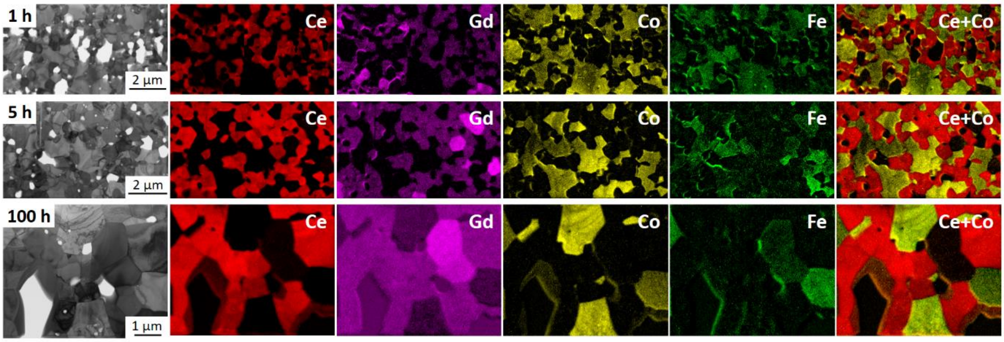

Figure 2.6 Energy-filtered TEM (EFTEM) analysis of 60CGO20-FCO composite sintered at 1200°C for 1 h, 5 h and 100 h, identifying three main phases: Gd-doped ceria (red), Fe/Co-oxide (green) and the $GdFeO_3$-based perovskite (bright magenta)

Fluorite, spinel, and orthorhombic perovskite phases are homogeneously distributed in three samples sintered for 1, 5, and 100 hours at 1200 °C as identified by TEM (EFTEM) analysis shown in Figure 2.6. According to the EFTEM elemental mapping, the Fe and Co maps show a non-uniform distribution in the spinel phase, which can be subdivided into two spinel types: a normal Co-rich and an inverse Fe-rich spinel, which is in agreement with the fact that two spinel phases coexist in the composite after the phase interaction, regardless of the dwell time. The high-temperature CoO grains are seen on the elemental map of a 100 hours fired sample. Grains are mostly situated nearby the Co-rich spinel phases, while Fe-rich spinel phases are neighbours to GCFCO-like grains.

Further electron diffraction analysis performed on samples sintered for 1 and 100 hours only in the 100 hours sintered sample, as shown exemplarily in Figure 2.7. Together with the element mapping, the crystal structure fitting the best with our experimental results is the rock salt phase with the cubic structure. All observed CoO grains are contiguous to the spinel grains, namely cobalt-rich ones, and do not form any connected network for potential transport. CoO is the product of the Co_3O_4 reduction and this transformation starts already at 400 °C [63,64]. At sintering temperature (1200 °C) CoO and Co_3O_4 are in equilibrium according to the phase diagram [46]. However, below approx. 950 °C a coexistence of Co_3O_4 and FCO is thermodynamically favoured. Please note, that Co_3O_4 here refers to the crystal structure and that Fe is partly substituting Co. Since the Fe/Co-ratio in both Co_3O_4 and FCO varies with temperature, rearranging of the cations must occur during the cooling process, which obviously is not completed in this composite [63,64].

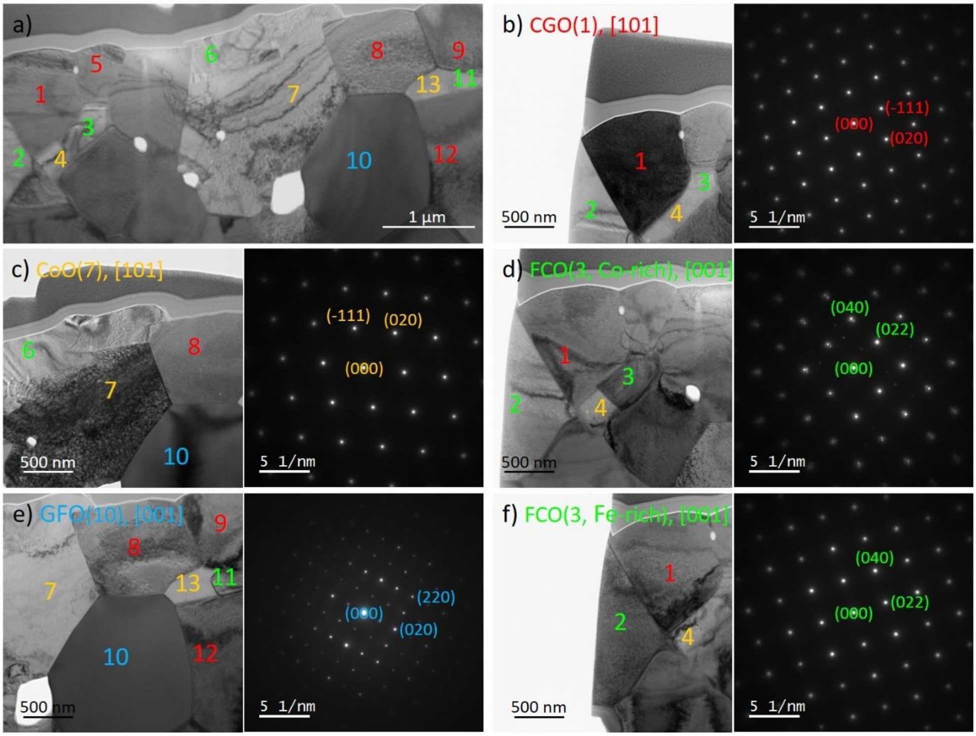

Figure 2.7 Diffraction analysis of the 60CGO20-FCO composite sintered at 1200 °C for 100 h, a) overview of investigated sample with fluorite (red), Fe/Co spinel (green), perovskite (blue) and rock salt (orange) phases, b-f) individual analysis of each grain

2.3.2 Cooling method

Since CoO is the product of incomplete reduction of the spinel phase, some further investigation was performed to study the connection of cooling conditions with the remaining monoxide fraction. Four 100 hours sintered samples were cooled differently and analysed by XRD and Rietveld refinement. Prior to describing the results of the microstructural characterization of the 100 h sintered samples, it is important to clarify the terminology which is summarised in Table 2.2 in experimental section. The *Slow* cooling sintering program includes an additional step at 850 °C for 100 h; *Fast* cooling is the program, where the sample was taken out of the furnace after 100 hours sintering and cooled in ambient air, and *Quenching* is the sample quenched in water at room temperature after holding it for 100 hours at 1200 °C.

SEM analysis in Figure 2.8 shows rather large islands of the spinel phase within the microstructure and unevenly large grains of a GCFCO emerged phase in all investigated samples sintered for 100 h with different cooling cycles. In all 100 hours fired pellets the grains are closely packed and uniformly distributed. The samples are free of cracks or any other visual defects. The difference in the phase distribution is minor for all 100 h sintered samples as well as the average grain size, which is in the range of 1.2 ± 0.1 µm for all samples.

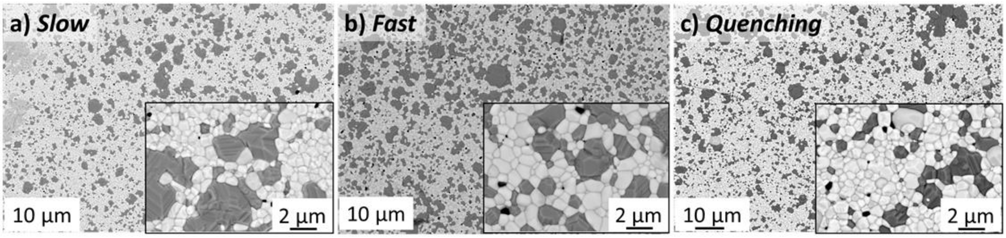

Figure 2.8 Surface morphology of 60CGO20-FCO subjected to different heat treatment in the furnace at a) 1200 °C for 100 h and subsequent 850 °C for 100 h with standard cooling; b) 1200 °C for 100 h with free cooling in air c) 1200 °C for 100 h with quenching in water

All samples sintered for 100 hours show a low level of porosity (1-5.5 %) with quite small pores (0.1-0.2 µm). There is no significant influence of the cooling method on the pore size, see Figure 2.9. The sample with an additional step at 850 °C for 100 h has slightly larger pores and grains, but, however, a significantly lower level of porosity (~1 %) compared to other samples, resulting in a slightly improved relative density of 94.8 %, while others have ~92-93 %.

The porosity has been estimated from the SEM images via image analysis, while the relative density was estimated geometrically from the dimensions and weight of the as-sintered pellets. Moreover, the limited number of characterized images might however induce inaccuracy in the porosity calculations. The character of the pores is also slightly different. All 100 h fired samples contain both types of pores intergranular and intragranular (predominantly located in the spinel phase), while the pellet with the 850 °C dwell step contains pores located along the grain boundaries. Due to slow diffusion kinetics the removal of the pores in the grain core is almost impossible, while the reduction of the pores along the grain boundary is still possible via grain boundary diffusion at the latter sintering stage. Hence this additional step helps to eliminate pores in the grain core and along the grain boundaries, improving the quality of the final microstructure.

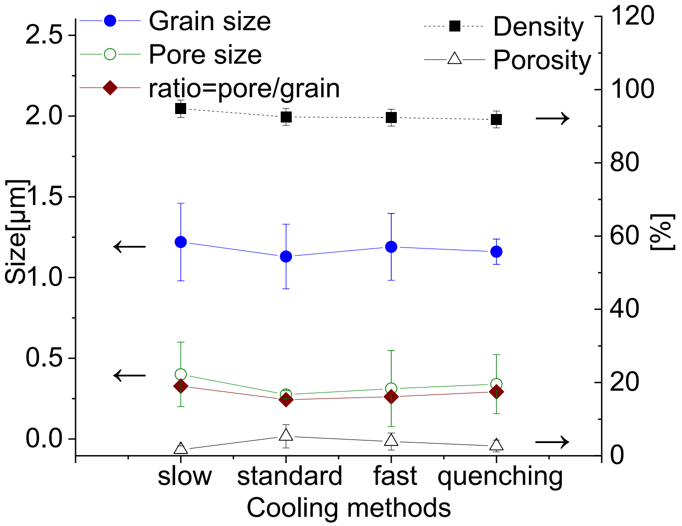

Figure 2.9 Grain, pore size, relative density and porosity of the 100 h sintered samples cooled differently (solid lines are a guide to the eye)

According to the Fe-Co-O phase diagram [45,46], the partial reduction of the spinel into a high-temperature Co/Fe monoxide phase with a rock salt structure can occur at 1200 °C sintering temperature [11,65]. In the Co-O phase, the most thermodynamically stable phases are the cubic CoO and Co_3O_4 oxides and the transition between these two oxides is reversible [63,64,66]. A slow rate of 0.5 K min^{-1} between 900 and 800 °C was implemented in the cooling cycle to ensure its complete reoxidation to a spinel phase that is stable at target operating temperatures (600-1000 °C). Generally, this slow cooling helps the reoxidation process and Co/Fe monoxide is no more detectable (<1 wt. %), as can be seen for the sample sintered for 5 hours. The resulting XRD patterns are shown in Figure 2.10. The CoO peaks were observed in the 100 hours fired samples subjected to quenching, cooling in ambient air, and the standard cooling program. Additionally, in the *Slow* cooling program, Co monoxide is completely oxidized and only fluorite, spinel, and perovskite phases are present, which is almost identical to the 5 hours sintered sample. Thus, this additional step in the sintering program helps to eliminate this high-temperature CoO phase and preserve normal and inverse spinel structures.

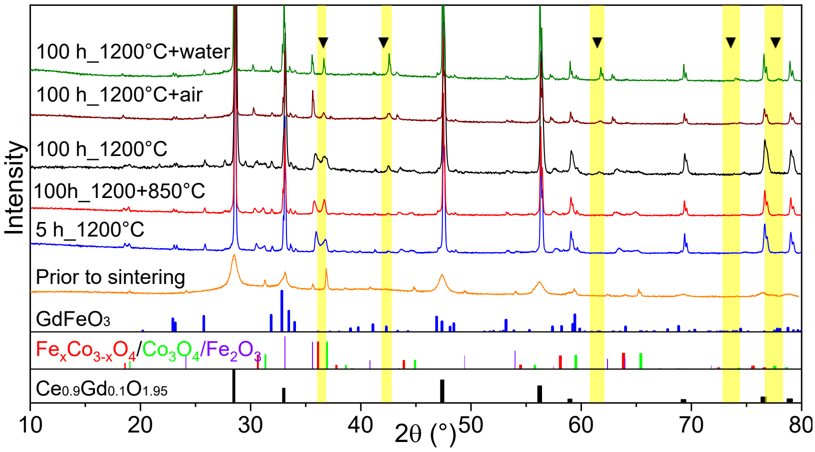

Figure 2.10 XRD patterns of 60CGO20-FCO composite subjected to different heat treatment and cooling methods. At the bottom, reference reflections are shown for the perovskite in blue, spinel in red and green, and fluorite in black

XRD and Rietveld refinement of the surface and bulk of each sample shows a small difference in the amount of fluorite phase. In the electron-conducting phases, however, the difference is more significant across the sintered pellet. While a higher amount of GCFCO can be found in the bulk, the spinel amount is higher on the surface. The Rietveld refinement confirmed the presence of the CoO in all samples fired for 100 h, except the sample cooled slowly as depicted in Figure 2.11.

In this pellet, only 0.2 vol. % and 0.5 vol. % of the monoxide was estimated on the surface and in the bulk, respectively, which is below the detection limit and thus will further be neglected. As expected, the maximum CoO fraction is found in the quenched sample and the fast cooled pellets, followed by the sample subjected to standard cooling in the furnace. The oxidation process of CoO on the surface and in the bulk encompasses different reactions and strongly depends on the diffusion paths [66]. The volume fraction of CoO in the bulk is higher compared to that on the surface in pellets cooled slow, standard, and fast, as shown in Figure 2.11b. Due to lack of diffusion time for the CoO oxidation reaction, a certain amount of CoO remains unoxidized in the bulk.

The rock salt phase itself was probably completely oxidized into Co_3O_4 during the slow cooling process, due to free access to the oxygen in the air [45]. In contrast, the quenched sample, where the oxidation process was terminated after 100 hours, contains a higher amount of the CoO on the surface, compared to that in the bulk.

These results again support the theory that too drastic cooling gives no time for the reaction in the CoO-Co_3O_4 system, ending up in the high amount of 20 vol.% of residual high-temperature CoO in the surface skin layer. The amount of the Co_3O_4 phase is strongly affected by heat treatment and the fraction of the rock salt: the amount of CoO increases, while Co_3O_4 decreases. Based on our observation, the rearranging of the ions happens in the cooling phase until the high-temperature phase is completely oxidized. Hence, slow cooling with an additional step is required in the sintering profile, to control the phase transformation and final morphology of the dual- or multi-phase composite.

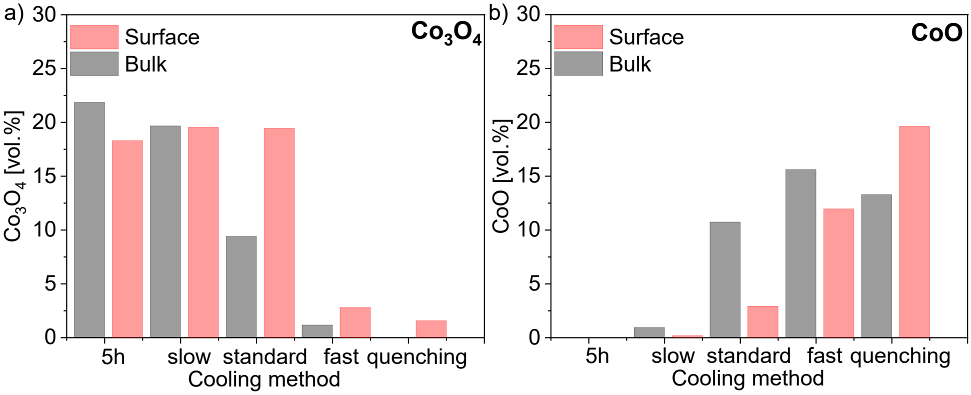

Figure 2.11 Volume fraction of 60CGO20-FCO composite subjected different heat treatment and cooling methods in a) Co_3O_4 and b) CoO amount comparison in the bulk and surface

The fluorite lattice parameter remains constant independent of the cooling cycle. While the fluorite and CoO lattice parameter is almost identical for all samples in the bulk and surface, the spinel lattice parameter shows some differences, pointing out a clear trend, as shown in Figure 2.12.

An increase in the cooling rate leads to an increase in the lattice parameter for the iron-rich spinel and a slight increase in the cobalt-rich spinel phases, which can be attributed to the oxidation reactions upon the cooling process [67]. The larger lattice parameter indicates a higher iron content in the Fe-Co spinel phase according to Vegard's law, hence by an increase in the cooling rate an increase of the iron-rich spinel fraction in the bulk is observed with a maximum in the quenched sample. This can be explained by the difference of the cations' mobility [68]. Cobalt cations are diffusing faster so they are migrating to the surface forming CoO or/and Co_3O_4 resulting in an increase of the Co-containing phases at the surface (Figure 2.12b). In consequence, the Fe-containing phases (FCO and GCFCO) are more present in the bulk and increase with a faster cooling rate.

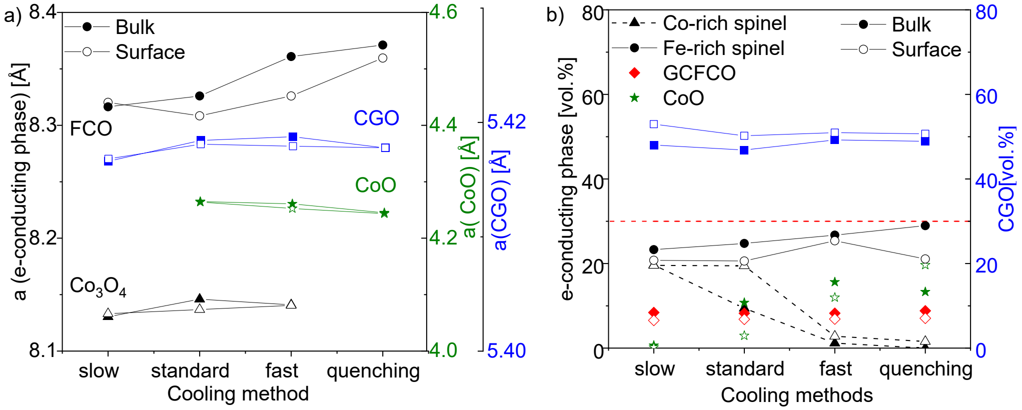

Figure 2.12 a) Lattice parameter difference and b) volume fraction of spinels and CGO in the bulk and surface (solid lines are a guide to the eye)

2.3.3 Functional properties

The temperature-dependent oxygen permeation of the composites with nominal 60CGO20-FCO sintered at 1200 °C for different times below 1 h and above 1 h are shown along with their activation energies in Figure 2.13 a and b, respectively. At short dwell time (<1 hour) all Arrhenius plots of the examined composites show a kink at 880 °C indicating a change in the rate limiting process. At 1 and 5 hours, dwell time the change in activation energy is at lower temperature, i.e., 800 °C, and much less pronounced. It completely disappears at longer dwell times ≥ 20 hours. Typically, in OTM this behaviour is ascribed to a change from bulk diffusion limitation at high temperature to surface exchange limitation at lower temperature. At high temperatures (>800 °C) the permeation rates for all examined composite membranes are almost identical with E_a in the range of 61-76 kJ/mol, which indeed can be attributed to the bulk transport, i.e. the ionic conductivity of the fluorite ($E_{a\ CGO20}$=72 kJ/mol [54,69]). The lower E_a of ~ 55 kJ/mol for the 0 h sintered sample might be due to insufficient sintering and increased porosity impeding electronic conductivity. At low temperatures (650-800 °C) E_a is much higher 112-117 kJ/mol for short dwell time (<1 hour), indicating rate limitations due to surface exchange kinetics although all membranes were coated with porous LSCF activation layers on both sides.

The resulting oxygen permeances of the coated membranes are mostly within the estimated experimental error of ± 10 %. Along the time range between 0 and 5 h dwell time, there is a very slight increase in permeation until 1 hour followed by a slight decrease until 50 hours dwell time. But, at 100 h dwell time a sharp increase in oxygen permeation is observed with the maximum of j_{O2}=0.13 ml/cm^2*min at 950 °C, Figure 2.14, which correlates with the grain growth shown in Figure 2.4.

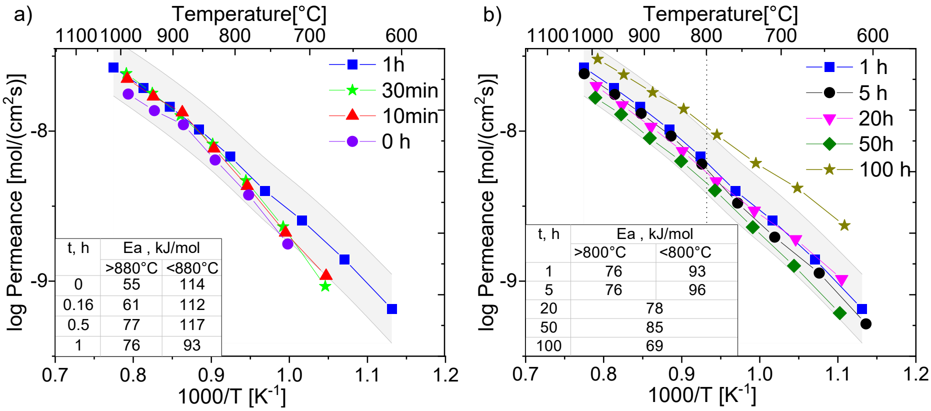

a)

t, h	Ea , kJ/mol	
	>880°C	<880°C
0	55	114
0.16	61	112
0.5	77	117
1	76	93

b)

t, h	Ea , kJ/mol	
	>800°C	<800°C
1	76	93
5	76	96
20	78	
50	85	
100	69	

Figure 2.13 Arrhenius-type plots of oxygen flux density of the 60CGO20-FCO composite sintered at 1200 °C for a) 0, 1 h and 10, 30 min b) 1, 5, 20, 50 and 100 h (solid lines are a guide to the eye)

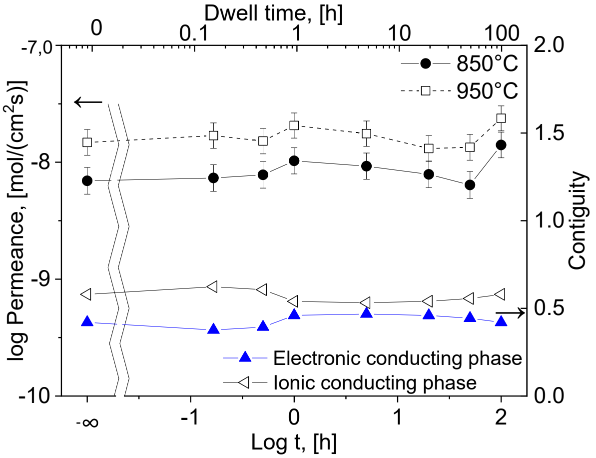

Figure 2.14 Permeation and contiguity of the phases in the 60CGO20-FCO composite sintered at 1200 °C with activation energy of the permeation depending on the dwelling time (solid lines are a guide to the eye)

The main challenge of the dual- and multiphase materials design is maximizing the ionic conducting volume without losing too much electronic conduction determined by the electronic conductivity of the selected phases as well as continuous percolation paths for the transport. While percolation is considering solely the volume fractions, the “contiguity” was introduced in [70,71] additionally accounting for the grain sizes of the individual phases. It can be expressed as the fraction of the total interconnected surface area of one phase shared with particles of the same phase and helps to estimate percolation and conducting properties within the dual-phase OTM composite [72]. Therefore, the contiguity of both the ionic conducting phase as well as the sum of electronic conducting phases was determined and shown in Figure 2.14.

$$C_i + C_e = 1$$ **Equation 2.3**

$$V_i + V_e = 1$$ **Equation 2.4**

$$C_i = \frac{V_i * R}{V_i * R + V_e}$$ **Equation 2.5**

with $R = \frac{d_e}{d_i}$, V_i and V_e are the volume fraction of the ionic- and electron-conducting phases, respectively.

Indeed, the contiguity of electron conducting phase for the short dwell times is lower compared to higher dwell times, Figure 2.14, which might be due to not fully sintered phases. However, it cannot explain the high permeance after 100 hours sintering, where the contiguity remains stable compared to 1-5 hours sintering.

The permeation of all composites at 850 °C with respect to the electron-conducting phase volume fraction is shown in Figure 2.15. Among the various dwell times, the best results are found for the 100-h sintered sample of 60:40 ratio, which shows a stable dense microstructure with large grains and a low level of porosity. The large grains size is favourable in this case because less grain boundaries are involved, which typically act as barrier for the transport of charged carriers in particular ions [13].

Although the oxygen permeance of the 100 h fired sample is the best among the differently sintered multiphase 60CGO20-FCO samples, comparison of the performance with other composite variations [14] shows the importance of the microstructure design. In general, the oxygen flux comparison of 60:40 with 80:20 fluorite: spinel weight ratio (Figure 2.16), sintered at 1200 °C for 5 hours shows, that the reduction of the electron conducting phase volume effectively helps to improve permeation performance, reaching maximum j_{O2}=0.12 and 0.22 ml/cm^2*min for the 80 wt. % CGO20 in composite at 850 °C and 1000 °C respectively.

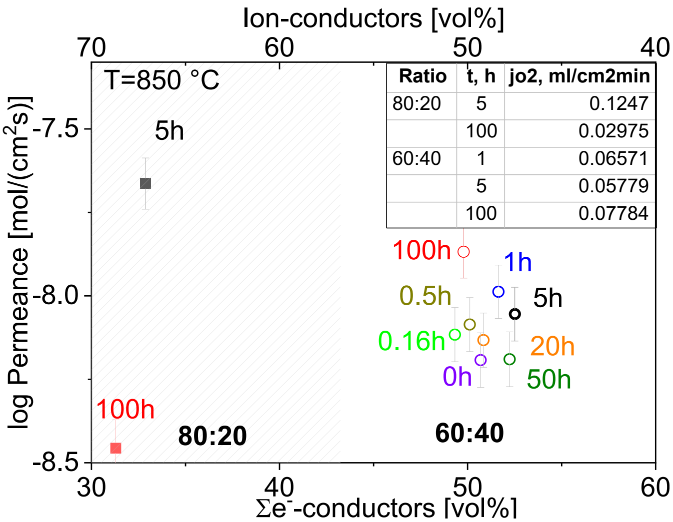

Ratio	t, h	jo2, ml/cm2min
80:20	5	0.1247
	100	0.02975
60:40	1	0.06571
	5	0.05779
	100	0.07784

Figure 2.15 Comparison of the final permeation performance permeance of CGO20-FCO composite with ratio 60:40 and 80:20 sintered with various dwelling time depending on the volume fraction of e−-conducting phases

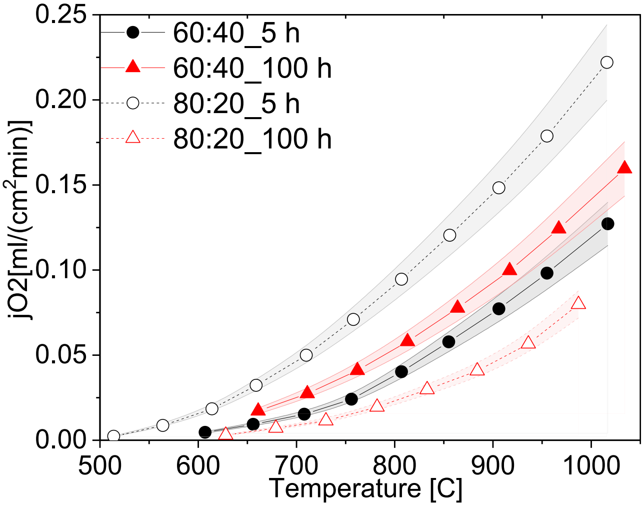

Figure 2.16 Oxygen permeation rates of the ceria-based materials with 60:40 and 80:20 ratios sintered at 5 and 100h (solid lines are a guide to the eye)

Interestingly, the 80CGO20-FCO fired for 100 hours showed a drastic drop in the oxygen flux. While in a 60:40 ratio, the amount of e-conducting phase is sufficient to provide continuous paths, regardless of the grain size, in 80:20 the large grains with a size of approx. 1.1 µm possibly lead to the insulation of the electron-conducting phase. Obviously, the coarser microstructure leads to lower electronic contiguity and overall percolation. In this case, the lower number of grain boundaries plays only a minor role.

2.4. Conclusions

Dual-phase dense 60 wt.% $Ce_{0.8}Gd_{0.2}O_{2-\delta}$ - 40 wt.% $FeCo_2O_4$ membranes were successfully synthesized by solid-state reactive sintering with one-step thermal processing at 1200 °C using commercially available $Ce_{0.8}Gd_{0.2}O_{2-\delta}$, Co_3O_4 and Fe_2O_3 as raw materials. The influence of the sintering parameters was systematically studied by varying the dwelling time and cooling methods.

It was found that already at 0 h dwell time, the phase interaction was completed, and all phases were present: fluorite, spinel, and perovskite. All samples sintered <1 h dwell time, however, reveal insufficient densification, i.e., high porosity and not connected matrix of the phases. That emphasizes that a longer dwell time is required to obtain a close-packed and uniformly distributed microstructure. The 100 hours sintered sample shows the best permeation performance with j_{O2}= 0.078 ml/cm^2*min at 850 °C thanks to the improved microstructure with enlarged grains. However, the implementation of such conditions is not reasonable for future scale-up towards potential commercialization, due to very long dwell time. Although the 80:20 composite sintered for 100 h has a similar grain size, its performance is very poor. Apparently, the isolation of the minor phase (electron-conducting phase) occurs, which negatively affects the percolation and hence oxygen flux.

The influence of the sintering profile on the microstructural features such as grain size distribution, pore volume and size, as well as density were discussed. The initial mix of the oxides undergoes some modification during the sintering process and results in a multi-phase microstructure with the coexistence of fluorite, perovskite, and two spinel types, except the 100 hours fired pellets, where an additional high-temperature CoO phase is observed. The grain growth as well as pore growth are dependent on the dwell time. The mean grain size increased moderately from 0.57-0.77 µm between 1 and 50 hours dwell time and reached its maximum of 1.13 µm in a 100 h fired sample. The relative density maximum of 93 and 94 % were obtained for the 5 and 100 h sintered samples. The de-densification phenomenon is observed for the 20 and 50-h sintered samples, where intensive grain and pore growth occurs simultaneously.

TEM analysis indicated a few CoO grains located next to Co_3O_4 spinel grains in the 100 h fired sample. In this case, residual high-temperature CoO is identified due to the long dwell time, where a higher amount of CoO is formed and does not have enough time to re-oxidize during cooling completely. The control of the cooling rate can thus govern the process of the Co rearranging between the Co_3O_4 and CoO phases until the equilibrium is reached. Moreover, it was observed that slow cooling with an additional step for 100 hours at 850 °C helps to eliminate the CoO phase and preserve the desired fluorite, spinel, and perovskite phase mixture. This emphasizes the importance of the slow cooling for the Fe-Co spinel within our composite system.

Among all chosen conditions, the intermediate time of 5 hours at 1200 °C sintering temperature is the most suitable for the CGO20-FCO multi-phase composite showing good structure-related properties with optimised grain size and low porosity and oxygen permeation with oxygen flux of j_{O2}= 0.06 ml/cm^2*min at 850 °C. Moreover, a cooling rate of 0.5 K min^{-1} between 900 and 800 °C is sufficient to re-oxidize the CoO phase to get the desired spinel structure.

References

1. Sunarso, J.; Baumann, S.; Serra, J.M.; Meulenberg, W.A.; Liu, S.; Lin, Y.S.; Diniz da Costa, J.C. Mixed ionic–electronic conducting (MIEC) ceramic-based membranes for oxygen separation. *Journal of Membrane Science* **2008**, *320*, 13–41.
2. Kiebach, R.; Pirou, S.; Martinez Aguilera, L.; Haugen, A.B.; Kaiser, A.; Hendriksen, P.V.; Balaguer, M.; García-Fayos, J.; Serra, J.M.; Schulze-Küppers, F.*; et al.* A review on dual-phase oxygen transport membranes: from fundamentals to commercial deployment. *J. Mater. Chem. A* **2022**, *10*, 2152–2195.
3. Chen, G.; Feldhoff, A.; Weidenkaff, A.; Li, C.; Liu, S.; Zhu, X.; Sunarso, J.; Huang, K.; Wu, X.-Y.; Ghoniem, A.F.*; et al.* Roadmap for Sustainable Mixed Ionic-Electronic Conducting Membranes. *Adv Funct Materials* **2022**, *32*.
4. Bai, W.; Feng, J.; Luo, C.; Zhang, P.; Wang, H.; Yang, Y.; Zhao, Y.; Fan, H. A comprehensive review on oxygen transport membranes: Development history, current status, and future directions. *International Journal of Hydrogen Energy* **2021**, *46*, 36257–36290.
5. Zhao, J.; Pang, Y.; Su, C.; Jiang, S.; Ge, L. Toward High Performance Mixed Ionic and Electronic Conducting Perovskite-Based Oxygen Permeable Membranes: An Overview of Strategies and Rationales. *Energy Fuels* **2023**, *37*, 7042–7061.
6. Leo, A.; Liu, S.; Costa, J.C.D.d. Development of mixed conducting membranes for clean coal energy delivery. *International Journal of Greenhouse Gas Control* **2009**, *3*, 357–367.
7. Smart, S.; Lin, C.X.C.; Ding, L.; Thambimuthu, K.; Diniz da Costa, J.C. Ceramic membranes for gas processing in coal gasification. *Energy Environ. Sci.* **2010**, *3*, 268.
8. Balaguer, M.; García-Fayos, J.; Solís, C.; Serra, J.M. Fast Oxygen Separation Through SO_2- and CO_2-Stable Dual-Phase Membrane Based on $NiFe_2O_4$ –$Ce_{0.8}Tb_{0.2}O_{2-\delta}$. *Chem. Mater.* **2013**, *25*, 4986–4993.

9. Garcia-Fayos, J.; Balaguer, M.; Baumann, S.; Serra, J.M. Dual-phase membrane based on $LaCo_{0.2}Ni_{0.4}Fe_{0.4}O_{3-x}$-$Ce_{0.8}Gd_{0.2}O_{2-\delta}$ composition for oxygen permeation under CO_2/SO_2-rich gas environments. *Journal of Membrane Science* **2018**, *548*, 117–124.

10. Takamura, H.; Okumura, K.; Koshino, Y.; Kamegawa, A.; Okada, M. Oxygen Permeation Properties of Ceria-Ferrite-Based Composites. *J Electroceram* **2004**, *13*, 613–618.

11. Ramasamy, M. *Dual Phase Oxygen Transport Membrane for Efficient Oxyfuel Combustion*; Forschungszentrum Jülich GmbH, 2016.

12. Fang, W.; Liang, F.; Cao, Z.; Steinbach, F.; Feldhoff, A. A mixed ionic and electronic conducting dual-phase membrane with high oxygen permeability. *Angewandte Chemie (International ed. in English)* **2015**, *54*, 4847–4850.

13. Lin, Y.; Fang, S.; Su, D.; Brinkman, K.S.; Chen, F. Enhancing grain boundary ionic conductivity in mixed ionic-electronic conductors. *Nature communications* **2015**, *6*, 6824.

14. Fischer, L.; Neuhaus, K.; Schmidt, C.; Ran, K.; Behr, P.; Baumann, S.; Mayer, J.; Meulenberg, W.A. Phase formation and performance of solid state reactive sintered $Ce_{0.8}Gd_{0.2}O_{2-\delta}$-$FeCo_2O_4$ composites. *J. Mater. Chem. A* **2022**, *10*, 2412–2420.

15. Zeng, F.; Baumann, S.; Malzbender, J.; Nijmeijer, A.; Winnubst, L.; Guillon, O.; Schwaiger, R.; Meulenberg, W.A. Enhancing oxygen permeation of solid-state reactive sintered $Ce_{0.8}Gd_{0.2}O_{2-\delta}$-$FeCo_2O_4$composite by optimizing the powder preparation method. *Journal of Membrane Science* **2021**, *628*, 119248.

16. Arratibel Plazaola, A.; Cruellas Labella, A.; Liu, Y.; Badiola Porras, N.; Pacheco Tanaka, D.; Sint Annaland, M.; Gallucci, F. Mixed Ionic-Electronic Conducting Membranes (MIEC) for Their Application in Membrane Reactors: A Review. *Processes* **2019**, *7*, 128.

17. Coduri, M.; Checchia, S.; Longhi, M.; Ceresoli, D.; Scavini, M. Rare Earth Doped Ceria: The Complex Connection Between Structure and Properties. *Frontiers in chemistry* **2018**, *6*, 526.

18. Joo, J.H.; Yun, K.S.; Lee, Y.; Jung, J.; Yoo, C.-Y.; Yu, J.H. Dramatically Enhanced Oxygen Fluxes in Fluorite-Rich Dual-Phase Membrane by Surface Modification. *Chem. Mater.* **2014**, *26*, 4387–4394.

19. Presto, S.; Artini, C.; Pani, M.; Carnasciali, M.M.; Massardo, S.; Viviani, M. Ionic conductivity and local structural features in $Ce_{1-x}Sm_xO_{2-x/2}$. *Physical chemistry chemical physics : PCCP* **2018**, *20*, 28338–28345.

20. Kilner, J.A.; Burriel, M. Materials for Intermediate-Temperature Solid-Oxide Fuel Cells. *Annu. Rev. Mater. Res.* **2014**, *44*, 365–393.

21. Koettgen, J.; Grieshammer, S.; Hein, P.; Grope, B.O.H.; Nakayama, M.; Martin, M. Understanding the ionic conductivity maximum in doped ceria: trapping and blocking. *Physical chemistry chemical physics : PCCP* **2018**, *20*, 14291–14321.

22. Kiefer, T. *Entwicklung neuer Schutz- und Kontaktierungsschichten für Hochtemperatur-Brennstoffzellen*; Forschungszentrum, Zentralbibliothek: Jülich, 2008.

23. Samson, A.J.; Søgaard, M.; Vang Hendriksen, P. $(Ce,Gd)O_2$−-based dual phase membranes for oxygen separation. *Journal of Membrane Science* **2014**, *470*, 178–188.

24. Bahlawane, N.; Ngamou, P.H.T.; Vannier, V.; Kottke, T.; Heberle, J.; Kohse-Höinghaus, K. Tailoring the properties and the reactivity of the spinel cobalt oxide. *Physical chemistry chemical physics : PCCP* **2009**, *11*, 9224–9232.

25. Ramasamy, M.; Persoon, E.S.; Baumann, S.; Schroeder, M.; Schulze-Küppers, F.; Görtz, D.; Bhave, R.; Bram, M.; Meulenberg, W.A. Structural and chemical stability of high performance $Ce_{0.8}Gd_{0.2}O_{2-\delta}$-$FeCo_2O_4$ dual phase oxygen transport membranes. *Journal of Membrane Science* **2017**, *544*, 278–286.

26. Fischer, L.; Ran, K.; Schmidt, C.; Neuhaus, K.; Baumann, S.; Behr, P.; Mayer, J.; Bouwmeester, H.J.M.; Nijmeijer, A.; Guillon, O.*; et al.* Role of Fe/Co Ratio in Dual Phase $Ce_{0.8}Gd_{0.2}O_{2-}$-$Fe_{3-x}Co_xO_4$ Composites for Oxygen Separation. *Membranes* **2023**, *13*.

27. Zhu, X.; Yang, W. Composite membrane based on ionic conductor and mixed conductor for oxygen permeation. *AIChE J.* **2008**, *54*, 665–672.

28. Lorenz, C.D.; Ziff, R.M. Precise determination of the critical percolation threshold for the three-dimensional “Swiss cheese” model using a growth algorithm. *The Journal of Chemical Physics* **2001**, *114*, 3659–3661.

29. Ge, M.; Huang, X.; Yan, H.; Gursoy, D.; Meng, Y.; Zhang, J.; Ghose, S.; Chiu, W.K.S.; Brinkman, K.S.; Chu, Y.S. Three-dimensional imaging of grain boundaries via quantitative fluorescence X-ray tomography analysis. *Commun Mater* **2022**, *3*.

30. Zhang, Z.; Zhou, W.; Chen, Y.; Chen, D.; Chen, J.; Liu, S.; Jin, W.; Shao, Z. Novel Approach for Developing Dual-Phase Ceramic Membranes for Oxygen Separation through Beneficial Phase Reaction. *ACS applied materials & interfaces* **2015**, *7*, 22918–22926.

31. Ran, K.; Zeng, F.; Fischer, L.; Baumann, S.; Meulenberg, W.A.; Neuhaus, K.; Mayer, J. The in situ generated emerging phase inside dual phase oxygen transport membranes. *Acta Materialia* **2022**, *234*, 118034.

32. Yasuda, K.; Uemura, K.; Shiota, T. Sintering and mechanical properties of gadolinium-doped ceria ceramics. *J. Phys.: Conf. Ser.* **2012**, *339*, 12006.

33. Raju, K.; Kim, S.; Hyung, C.J.; Yu, J.H.; Seong, Y.-H.; Kim, S.-H.; Han, I.-S. Optimal sintering temperature for Ce0.9Gd0.1O2−δ–La0.6Sr0.4Co0.2Fe0.8O3–δ composites evaluated through their microstructural, mechanical and elastic properties. *Ceramics International* **2019**, *45*, 1460–1463.

34. Joo, J.H.; Park, G.S.; Yoo, C.-Y.; Yu, J.H. Contribution of the surface exchange kinetics to the oxygen transport properties in $Ce_{0.9}Gd_{0.1}O_{2-\delta}$ –$La_{0.6}Sr_{0.4}Co_{0.2}Fe_{0.8}O_{3-\delta}$ dual-phase membrane. *Solid State Ionics* **2013**, *253*, 64–69.

35. Li, Q.; Zhu, X.; He, Y.; Cong, Y.; Yang, W. Effects of sintering temperature on properties of dual-phase oxygen permeable membranes. *Journal of Membrane Science* **2011**, *367*, 134–140.

36. Kharton, V.V. Oxygen transport in $Ce_{0.8}Gd_{0.2}O_{2-\delta}$-based composite membranes. *Solid State Ionics* **2003**, *160*, 247–258.

37. Luo, H.; Jiang, H.; Efimov, K.; Liang, F.; Wang, H.; Caro, J. CO_2 -Tolerant Oxygen-Permeable Fe_2O_3 -$Ce_{0.9}Gd_{0.1}O_{2-\delta}$ Dual Phase Membranes. *Ind. Eng. Chem. Res.* **2011**, *50*, 13508–13517.

38. Shi, J.-L.; Deguchi, Y.; Sakabe, Y. Relation between grain growth, densification and surface diffusion in solid state sintering—a direct observation. *J Mater Sci* **2005**, *40*, 5711–5719.

39. Lee, K.-T.; Kim, D.-K.; Park, J.-H.; Shon, I.-J. Effect of Fe_2O_3 on properties and densification of $Ce_{0.8}Gd_{0.2}O_{2-\delta}$ by PCAS. *Ceramics International* **2009**, *35*, 1345–1351.

40. Zhang, T.; Hing, P.; Huang, H.; KILNER, J. Sintering and grain growth of CoO-doped CeO 2 ceramics. *Journal of the European Ceramic Society* **2002**, *22*, 27–34.

41. Gil, V.; Tartaj, J.; Moure, C.; Durán, P. Sintering, microstructural development, and electrical properties of gadolinia-doped ceria electrolyte with bismuth oxide as a sintering aid. *Journal of the European Ceramic Society* **2006**, *26*, 3161–3171.

42. Zhang, T.; Hing, P.; Huang, H.; KILNER, J. Densification, microstructure and grain growth in the CeO2–Fe2O3 system (0⩽Fe/Ce⩽20%). *Journal of the European Ceramic Society* **2001**, *21*, 2221–2228.

43. Jud, E.; HUWILER, C.B.; Gauckler, L.J. Grain Growth of Micron-Sized Grains in Undoped and Cobalt Oxide Doped Ceria Solid Solutions. *Nippon Seramikkusu Kyokai gakujutsu ronbunshi* **2006**, *114*, 963–969.

44. Zeng, F.; Malzbender, J.; Baumann, S.; Nijmeijer, A.; Winnubst, L.; Ziegner, M.; Guillon, O.; Schwaiger, R.; Meulenberg, W.A. Optimization of sintering conditions for improved microstructural and mechanical properties of dense $Ce_{0.8}Gd_{0.2}O_{2-\delta}$-$FeCo_2O_4$oxygen transport membranes. *Journal of the European Ceramic Society* **2021**, *41*, 509–516.

45. Murray, P.J.; late) J.W. Linnett, (Mössbauer studies in the spinel system coxfe3−xo4. *Journal of Physics and Chemistry of Solids* **1976**, *37*, 619–624.

46. Hansson, A.N.; Linderoth, S.; Mogensen, M.; Somers, M.A. X-ray diffraction investigation of phase stability in the Co–Cr–O and the Fe–Co–Cr–O systems in air at 1323K. *Journal of Alloys and Compounds* **2005**, *402*, 194–200.

47. Picture Thresholding Using an Iterative Selection Method. *IEEE Trans. Syst., Man, Cybern.* **1978**, *8*, 630–632.

48. Kovács, A.; Schierholz, R.; Tillmann, K. FEI Titan G2 80-200 CREWLEY. *JLSRF* **2016**, *2*.

49. Zeng, F.; Malzbender, J.; Baumann, S.; Zhou, W.; Ziegner, M.; Nijmeijer, A.; Guillon, O.; Schwaiger, R.; Albert Meulenberg, W. Mechanical reliability of $Ce_{0.8}Gd_{0.2}O_{2-\delta}$-$FeCo_2O_4$ dual phase membranes synthesized by one-step solid-state reaction. *J. Am. Ceram. Soc.* **2021**, *104*, 1814–1830.

50. Fischer, L.; Ran, K.; Schmidt, C.; Neuhaus, K.; Baumann, S.; Behr, P.; Mayer, J.; Bouwmeester, H.J.; Nijmeijer, A.; Guillon, O.*; et al.* Lanthanide element variation in rare earth doped ceria – FeCo2O4 dual phase oxygen transport membranes. *Open Ceramics* **2024**, *17*, 100519.

51. Ferreira, T.; Waerenborgh, J.C.; Mendonça, M.; Nunes, M.R.; Costa, F.M. Structural and morphological characterization of $FeCo_2O_4$ and $CoFe_2O_4$ spinels prepared by a coprecipitation method. *Solid State Sciences* **2003**, *5*, 383–392.

52. Brik, M.G.; Suchocki, A.; Kamińska, A. Lattice parameters and stability of the spinel compounds in relation to the ionic radii and electronegativities of constituting chemical elements. *Inorganic chemistry* **2014**, *53*, 5088–5099.

53. Ji, Y.; Kilner, J.; Carolan, M. Electrical conductivity and oxygen transfer in gadolinia-doped ceria (CGO)–$Co_3O_{4-\delta}$ composites. *Journal of the European Ceramic Society* **2004**, *24*, 3613–3616.

54. Kharton, V.V.; Figueiredo, F.M.; Navarro, L.; Naumovich, E.N.; Kovalevsky, A.V.; Yaremchenko, A.A.; Viskup, A.P.; Carneiro, A.; Marques, F.M.B.; Frade, J.R. Ceria-based materials for solid oxide fuel cells. *J Mater Sci* **2001**, *36*, 1105–1117.

55. Artini, C.; Pani, M.; Carnasciali, M.M.; Plaisier, J.R.; Costa, G.A. Lu-, Sm-, and Gd-Doped Ceria: A Comparative Approach to Their Structural Properties. *Inorganic chemistry* **2016**, *55*, 10567–10579.

56. Zeng, F. *Mechanical reliability and oxygen permeation of* $Ce_{0.8}Gd_{0.2}O_{2-\delta}$-$FeCo_2O_4$ *dual-phase composite*; University of Twente: Enschede, 2021.

57. Rahaman, M.N. *Ceramic Processing and Sintering*; CRC Press, 2017.

58. Schneider, C.A.; Rasband, W.S.; Eliceiri, K.W. NIH Image to ImageJ: 25 years of image analysis. *Nature methods* **2012**, *9*, 671–675.

59. Stawarczyk, B.; Ozcan, M.; Hallmann, L.; Ender, A.; Mehl, A.; Hämmerlet, C.H.F. The effect of zirconia sintering temperature on flexural strength, grain size, and contrast ratio. *Clinical oral investigations* **2013**, *17*, 269–274.

60. Pérez-Coll, D.; Sánchez-López, E.; Mather, G.C. Influence of porosity on the bulk and grain-boundary electrical properties of Gd-doped ceria. *Solid State Ionics* **2010**, *181*, 1033–1042.

61. Shi, J.L. Relation Between Coarsening and Densification in Solid-state Sintering of Ceramics: Experimental Test on Superfine Zirconia Powder Compacts. *J. Mater. Res.* **1999**, *14*, 1389–1397.

62. Schulze-Küppers, F.; Baumann, S.; Tietz, F.; Bouwmeester, H.; Meulenberg, W.A. Towards the fabrication of $La_{0.98-x}Sr_xCo_{0.2}Fe_{0.8}O_{3-\delta}$ perovskite-type oxygen transport membranes. *Journal of the European Ceramic Society* **2014**, *34*, 3741–3748.

63. Chen, X.; van Gog, H.; van Huis, M.A. Transformation of Co_3O_4 nanoparticles to CoO monitored by in situ TEM and predicted ferromagnetism at the Co_3O_4/CoO interface from first principles. *Journal of materials chemistry. C* **2021**, *9*, 5662–5675.

64. Kong, F.-C.; Li, Y.-F.; Shang, C.; Liu, Z.-P. Stability and Phase Transition of Cobalt Oxide Phases by Machine Learning Global Potential Energy Surface. *J. Phys. Chem. C* **2019**, *123*, 17539–17547.

65. Zeng, F.; Baumann, S.; Malzbender, J.; Nijmeijer, A.; Winnubst, L.; Guillon, O.; Schwaiger, R.; Meulenberg, W.A. Enhancing oxygen permeation of solid-state reactive sintered $Ce_{0.8}Gd_{0.2}O_2$-$FeCo_2O_4$ composite by optimizing the powder preparation method. *Journal of Membrane Science* **2021**, *628*, 119248.

66. Żyła, M.; Smoła, G.; Knapik, A.; Rysz, J.; Sitarz, M.; Grzesik, Z. The formation of the Co_3O_4 cobalt oxide within CoO substrate. *Corrosion Science* **2016**, *112*, 536–541.

67. Kaczmarska, A.; Grzesik, Z.; Mrowec, S. On the Defect Structure and Transport Properties of Co_3O_4 Spinel Oxide. *High Temperature Materials and Processes* **2012**, *31*, 371–379.

68. FUHSING, L.; TINKLER, S.; DIEKMANN, R. Point defects and cation tracer diffusion in $(Co_xFe_{1-x})_{3-\delta}O_4$ spinels. *Solid State Ionics* **1993**, *62*, 39–52.

69. Kharton, V.V.; Shaula, A.L.; Naumovich, E.N.; Vyshatko, N.P.; Marozau, I.P.; Viskup, A.P.; Marques, F.M.B. Ionic Transport in $Gd_3Fe_5O_{12}$- and $Y_3Fe_5O_{12}$-Based Garnets. *J. Electrochem. Soc.* **2003**, *150*, J33.

70. Gurland, J.; Brown University. Division of Engineering; United States. Office of Ordnance Research. *The Measurement of Grain Contiguity in Two-phase Alloys*; Division of Engineering, Brown University, 1957.

71. Fan, Z.; Miodownik, A.P.; Tsakiropoulos, P. Microstructural characterisation of two phase materials. *Materials Science and Technology* **1993**, *9*, 1094–1100.

72. Zeng, F.; Malzbender, J.; Baumann, S.; Krüger, M.; Winnubst, L.; Guillon, O.; Meulenberg, W.A. Phase and microstructural characterizations for $Ce_{0.8}Gd_{0.2}O_{2-\delta}$-$FeCo_2O_4$ dual phase oxygen transport membranes. *Journal of the European Ceramic Society* **2020**, *40*, 5646–5652.

Chapter 3

3. Phase formation and performance of solid state reactive sintered $Ce_{0.8}Gd_{0.2}O_{2-\delta}$ - $FeCo_2O_4$ composites

Abstract

Reactive sintering of dual phase composites for use as oxygen transport membranes is a promising method enabling lower sintering temperatures as well as low-cost raw materials. $Ce_{0.8}Gd_{0.2}O_{2-\delta}$–$FeCo_2O_4$ composites with different nominal weight ratios from 60 : 40 to 90 : 10 are processed by reactive sintering of commercial $Ce_{0.8}Gd_{0.2}O_{2-\delta}$, Fe_2O_3, and Co_3O_4 powders. The phases formed in situ during sintering are investigated qualitatively and quantitatively by means of XRD and Rietveld refinement as well as transmission electron microscopy. Besides gadolinia-doped ceria, two Fe/Co-spinel phases are in equilibrium in agreement with the phase diagram. Moreover, a donor-doped $GdFeO_3$-based perovskite (Gd,Ce)(Fe,Co)O_3 showing electronic conductivity is formed. Due to these intense phase reactions, the composition of each individual phase is assessed for all composites and their functional properties are discussed. The oxygen permeation performances of the composites are measured including their dependence on temperature and the potential limiting steps are discussed. The results reveal that the phase reactions support the formation of the desired mixed ionic electronic conductivity achieving percolation at low nominal spinel contents. The specific microstructure plays an extremely important role in the membrane performance and, thus, special attention should be paid to this in future research about dual phase membranes.

This Chapter has been published as: Fischer, L.; Neuhaus, K.; Schmidt, C.; Ran, K.; Behr, P.; Baumann, S.; Mayer, J.; Meulenberg, W.A. Phase formation and performance of solid state reactive sintered $Ce_{0.8}Gd_{0.2}O_{2-\delta}$-$FeCo_2O_4$ composites. *J. Mater. Chem. A* **2022**, *10*, 2412–2420, DOI: https://doi.org/10.1039/D1TA05695F

3.1 Introduction

The development of ceramic dual-phase materials for Oxygen Transport Membranes (OTMs) has attracted much attention in the scientific world. These mixed ionic-electronic conductors (MIECs) are operated at elevated temperatures, i.e. 700–900 °C, and have the potential for improving the performance and reducing the cost of several industrial gas separation processes due to high energy efficiency [1,2]. If the membrane separates two gas phases with different oxygen partial pressures p_{O2}, oxygen molecules will be reduced to oxygen ions at the surface of the high p_{O2}-side taking up in sum four electrons. The ions diffuse through the membrane to the low p_{O2}-side where they recombine to form oxygen molecules releasing the electrons again. These electrons transfer back to the high p_{O2}-side simultaneously due to the MIEC character of the membrane material [3]. However, classical single phase MIEC materials, mainly perovskites, suffer from stability issues under operating conditions. Therefore, composite membranes, a combination of both ion and electron conducting ceramic phases, have attracted major interest in recent years [4–8]. Such composites provide the major advantage that two inherently stable materials can be selected provided that their properties such as conductivities, thermal expansion behaviour, and inertness match well. The phase mixture in the composite has to provide separate but continuous pathways for both oxygen ions and electrons and, thus, a percolation of the phases is required. The number of excellent oxygen ion conductors is limited mainly to doped zirconia or ceria, whereby Gd-doped ceria (CGO) shows the highest ionic conductivity in particular at lower temperatures [9]. In contrast, there is a lot of choice of ceramic electronic conductors, which typically crystallize in perovskite or spinel structure both consisting of transition metal elements typically providing electron hole conductivity via small polaron hopping [10–15].

Normally, phases are selected that do not react with each other during sintering and operation in order to maintain these conductive pathways. Recent studies, however, revealed that CGO mixed with Fe/Co-spinel ($Fe_{3-x}Co_xO_4$) forms an additional orthorhombic perovskite phase during sintering, which even improved the overall performance [16–18]. It turned out that the perovskite phase is $GdFeO_3$-based with Ce and Co on the A-site and B-site, respectively. The Ce^{4+} substituting Gd^{3+} acts as a donor and, thus, electronic conductivity is introduced [19–22].

This orthorhombic perovskite phase is quite stable and forms distinct grains rather than being a grain boundary phase as speculated in the literature [10]. Obviously, the perovskite phase does not have significant negative effects on the ion- or electron-conducting pathways, i.e., ambipolar conductivity. Obviously, this unintended formation of the perovskite phase is not undesired and in contrast might even have positive effects. Lin et al. [17] hypothesized an increase in ionic conductivity of the ceria phase due to the extraction of Gd, which otherwise would be segregated at the ceria–ceria grain boundaries resulting in ion transport blocking space charge layers. The maximum performance was observed at a low nominal spinel concentration of 15 wt.%, [19] which is well below 30 vol% often referred to as the percolation threshold. However, percolation is affected by many factors [23] in particular in real microstructures. Considering uncorrelated equal-sized spheres in the so-called “swiss-cheese” model the percolation limit is calculated to be 28.95 vol% [24]. Therefore, 30 vol% appears to be a useful guideline although it does not represent a sharp limit. Certain percolating paths can occur well below that. Nevertheless, sufficient electronic conduction requires enough “strong” paths with certain conductivity. On the other hand, the perovskite formation takes place at the expense of the ceria volume fraction reducing oxygen ion conductance, which is considered rate limiting, and increasing the volume fraction of the electronic conducting phases compared to the nominal composition.

Therefore, in order to better understand the influence of the several phases formed during solid state reactive sintering, various nominal combinations of $Ce_{0.8}Gd_{0.2}O_{2-\delta}$ (CGO) and $FeCo_2O_4$ (FCO) are investigated in this work. The resulting phase mixtures are analysed qualitatively and quantitatively based on X-ray diffraction and Rietveld refinement, respectively. Individual phase compositions are determined and their influence on the functional properties, i.e., conductivity and oxygen permeance, is discussed.

3.2 Experimental

3.2.1 Sample preparation

$Ce_{0.8}Gd_{0.2}O_{2-\delta}$ (CGO), Fe_2O_3 and Co_3O_4 powders were used for the Solid-State Reactive Sintering (SSRS) process. Respective amounts of powders were weighed for nominal CGO-$FeCo_2O_4$ compositions with wt.%-ratios of 60 : 40, 65 : 35, 70 : 30, 75 : 25, 80 : 20, 85 : 15 and 90 : 10. The powder mixtures were ball milled in ethanol for 48 h on a roller bench with 175 rpm. After drying in ambient air at 70° the powder mixtures were pressed with a uniaxial press in disc-shaped membranes with d = 20 mm. The discs were sintered with a heating rate of 5 K min^{-1} to 1200 °C and a dwell time of 5 hours. At sintering temperature, the spinel partially reduces into a high temperature monoxide phase with rock salt structure. Therefore, a slow rate of 0.5 K min^{-1} between 900 and 800 °C is implemented in the cooling cycle in order to ensure complete reoxidation of the high temperature Co/Fe-monoxide phase to the spinel phase stable at operating temperatures according to the $Fe_{3-x}Co_xO_4$ phase diagram [16].

The sintered discs were ground to approx. 1 mm thickness in 2 steps (by WS FLEX 18C) with SiC papers of P 800 and P 1200 grit, respectively. Subsequently, porous LSCF ($La_{0.58}Sr_{0.4}Co_{0.2}Fe_{0.8}O_{3-\delta}$) catalytic activation layers with a thickness of approx. 5 µm were applied via screen printing on both sides of the discs and calcined at 1100 °C for 5 hours.

Single-phase powders of spinel as well as the resulting perovskite, i.e. $Gd_{0.85}Ce_{0.15}Fe_{0.75}Co_{0.25}O_3$, were synthesized by gelation and complexation of an aqueous solution of metal nitrates known as the Pechini-method [25].

3.2.2 Characterization methods

The crystal structures are determined via X-ray diffraction (XRD) using a D4 ENDEAVOR (Bruker, Germany). The diffraction angle is varied in the range of 10° to 80° 2θ with increments of 0.02° 2θ and 0.75 seconds of measurement time per step. Measured data were analysed with help of the program package X'Pert HighScore (PANalytical B.V., version 3.0.5). Crystal structure analysis and associated phase quantifications were carried out by Rietveld refinement using the software Profex (Version 4.2.2). The errors of each fitting are calculated individually and given in Table 3.1.

Microscopy

The morphology of the materials is analysed by Scanning Electron Microscopy (SEM) and Energy Dispersive X-ray Spectroscopy (EDS). The SEM images with different magnifications are taken with Zeiss Ultra 55 and Zeiss Supra 50 VP1 (Carl Zeiss NTS GmbH, Germany) equipment. The electronic conductivity of the samples was enhanced by sputter deposition of a thin platinum layer prior to the analysis.

TEM specimens were cut from the CGO-FCO pellets by focused ion beam (FIB) milling using an FEI Strata 400 system with a Ga ion beam. Further thinning and cleaning were performed with an Ar ion beam in a Fischione Nanomill 1040 at 900 eV and 500 eV beam energy respectively. TEM, energy-filtered TEM imaging and electron diffraction were performed using an FEI Tecnai F20 at 200 kV. High-resolution high-angle annular dark-field (HAADF) imaging was conducted with an FEI Titan G2 80-200 ChemiSTEM microscope equipped with an XFEG and a probe Cs corrector [26].

Table 3.1 Lattice parameter and weight fraction F of the phases of the CGO-FCO composites with a nominal FCO content of 10–40 wt.% sintered at 1200 °C for 5 h. The space groups of the phases are given in the headline. Numbers in square brackets give the calculated uncertainty of the last digit

	Fluorite (CGO), *Fm3m*		**Fe-rich spinel *Fd3m***		**Co-rich spinel *Fd3m***		**GCFCO (Perovskite), *Pnma***			
FCO [wt.%]	**F [wt.%]**	**a = b = c [Å]**	**F [wt.%]**	**a = b = c [Å]**	**F [wt.%]**	**a = b = c [Å]**	**F [wt.%]**	**Lattice parameter [Å]**		
								a	b	c
10	82.1[3]	5.4213[5]	0	—	7.1[3]	8.1309[2]	10.7 [2]	5.3370[3]	5.6121[4]	7.6467[8]
15	73.5[3]	5.4215[5]	7.8[2]	8.2483[8]	5.1[2]	8.1321[3]	13.6[2]	5.3376[4]	5.6147[5]	7.6492[8]
20	69.4[3]	5.4221[4]	4.2[2]	8.2426[9]	14.5[2]	8.1795[2]	11.9[2]	5.3421[4]	5.6191[4]	7.6583[7]
25	62.5[3]	5.4227[5]	9.2[2]	8.3032[8]	13.3[2]	8.1436[2]	12.9[2]	5.3404[3]	5.6163[4]	7.6549[7]
30	61.3[3]	5.4220[4]	15.5[2]	8.2994[8]	11.8[2]	8.1490[2]	11.4[2]	5.3399[3]	5.6141[5]	7.6576[8]
35	56.3[3]	5.4201[4]	16.4[2]	8.2967[8]	17.0[2]	8.1580[2]	10.3[2]	5.3409[3]	5.6121[4]	7.6368[8]
40	51.7[3]	5.4211[5]	20.3[2]	8.2966[9]	18.2[2]	8.1461[3]	9.8[2]	5.3395[3]	5.6121[4]	7.6410[8]

Electrical conductivity

The total conductivity of the single-phase perovskite samples was determined by an analysis of temperature dependent impedance spectra using a Novotherm HT 1200 frequency analyser. The samples were coated with a Pt resinate paste (RP 070107, Heraeus GmbH, Germany) and Pt sheet contacts were attached at both sides of the sample. The samples were measured in air. An AC voltage peak-to-peak amplitude of 40 mV was applied for all measurements. As the electronic conductivity of all composites was very high, no splitting in separate contributions from the grain bulk and grain boundary was possible, and only a straight line (ohmic resistor) was visible in the Nyquist plots. The temperature dependent electronic conductivity of the composites was measured using a DC measurement setup (Keithley 2600B): the top of the sample pellet was in contact with a Pt micro contact with a diameter of about 200–400 nm and the bottom was in contact with a Pt sheet. Additionally, Pt resinate paste (RP 070107, Heraeus GmbH) was applied on the sheet to reduce the contact resistance. The exact size of the micro contact was determined by measuring its imprint on the sample after the measurements using light microscopy and comparing it with light microscopy images of the contact itself.

In order to distinguish the oxygen partial pressure dependent electronic conductivity contribution from the total conductivity, Hebb–Wagner measurements [27,28] were conducted. The Pt micro contact described above was additionally surrounded by a gas tight encapsulation (IP 041 glass paste by Heraeus GmbH), using the same measurement setup as for the standard DC measurements. The experimental error of both methods is ±5%.

Oxygen permeation measurements

The oxygen permeation experiments were performed in a vertical quartz glass housing, where the membranes were sealed with two gold rings with an inner diameter of 13 mm. The separation of the oxygen from ambient air fed with 250 $\mathrm{ml_N\ min^{-1}}$ was performed between approx. 650 °C and 1000 °C by using argon as a sweep gas with 50 $\mathrm{ml_N\ min^{-1}}$ flow rate using mass flow controllers (Bronkhorst, Germany). The oxygen and nitrogen concentration in the permeate gas, i.e., oxygen enriched argon, was detected with a mass spectrometer (Omnistar, Pfeiffer Vacuum GmbH, Germany). With help of the measured nitrogen concentration air leakage through the membrane or the sealing is considered using

$$j_{O_2} = F_{Ar}\left(\frac{X_{O_2} - \frac{1}{4}X_{N_2}}{1 - X_{O_2} - X_{N_2}}\right)\frac{1}{A_{mem}} \qquad \textbf{Equation 3.1}$$

with F_{Ar} being the argon flow rate, i.e., 50 $\mathrm{ml_N\ min^{-1}}$, X_{O2} and X_{N2} the oxygen and nitrogen concentration in the permeate gas, respectively, and A_{mem} the open membrane area, i.e., 1.33 $\mathrm{mm^2}$. The factor $\frac{1}{4}$ reflects the O_2/N_2 ratio in the air feed assuming that the leak is not gas selective.

Since the oxygen partial pressure in the permeate gas is temperature dependent, the driving force of the permeation rate is not constant during the measurement. Moreover, the sample thickness after grinding has a deviation from the target, i.e., 1 mm, of ±8%. Therefore, the permeance, i.e., driving force normalized permeation rate, normalized to the reference thickness L_0 = 1 mm is calculated assuming Wagner behaviour using

$$Permeance = \frac{j_{O_2}}{ln\frac{p_{O_2}^{'}}{p_{O_2}^{''}}}\frac{L_{mem}}{L_0} \qquad \textbf{Equation 3.2}$$

With $p_{O_2}^{'}$ and $p_{O_2}^{''}$ being the oxygen partial pressures in the retentate and permeate gas, respectively, and L_{mem} the actual membrane thickness.

The overall experimental error cannot be calculated precisely. It is assumed to be ±10%, which is well accepted in the literature.

3.3 Results and discussion

3.3.1 Microstructure

The phase identification has been performed via XRD. All samples consist of ceria ($Ce_{0.8}Gd_{0.2}O_{2-δ}$) and spinel-type ($FeCo_2O_4$) phases with the additional orthorhombic perovskite structure $GdFeO_3$ as expected without the formation of any other phases, Figure 3.1. The change in the spinel fraction in the composite is evident by the decrease of the intensities of the corresponding reflections in the XRD patterns in the region of $35 \leq 2θ \leq 38°$. Moreover, reflection splitting is visible revealing two coexisting spinel phases in accordance with the phase diagram [16].

The phases are homogeneously distributed as indicated in Figure 3.2. The three crystallographic phases are confirmed as fluorite ($Ce_{1-x}Gd_xO_2$), spinel ($Fe_{3-x}Co_xO_4$) and perovskite ($GdFeO_3$) and exemplarily shown by the HAADF images in Figure 3.3 for the 60 : 40 CGO-FCO composites. The weight fractions and lattice parameters of each phase were determined by Rietveld refinement as shown in Table 3.1. In agreement with the phase diagram of the $Fe_xCo_{3-x}O_4$ system two types of spinels are present in the range of $0.65 \leq Fe \leq 1.07$, i.e., Co-rich (normal spinel) and Fe-rich (inverse spinel). Indeed, both spinels are detected for all composites except 90 : 10

proportion, in which only of the Co-rich normal spinel is found. The resulting weight fraction of each phase is plotted versus the nominal spinel content in Figure 3.4.

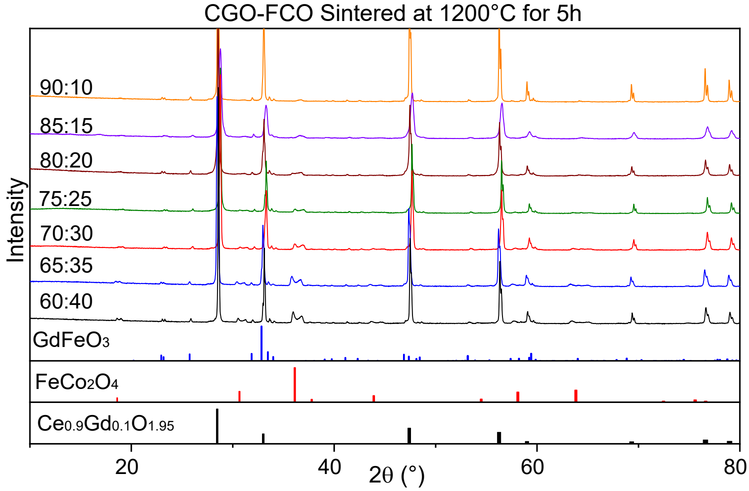

Figure 3.1 XRD patterns of the CGO-FCO composites in a row with various FCO contents sintered at 1200 °C for 5 h. At the bottom, reference reflections are shown for the perovskite (01-072-9909) in blue, spinel (01-074-3417) in red, and fluorite (01-075-0161) in black. ICCD numbers are given in brackets.

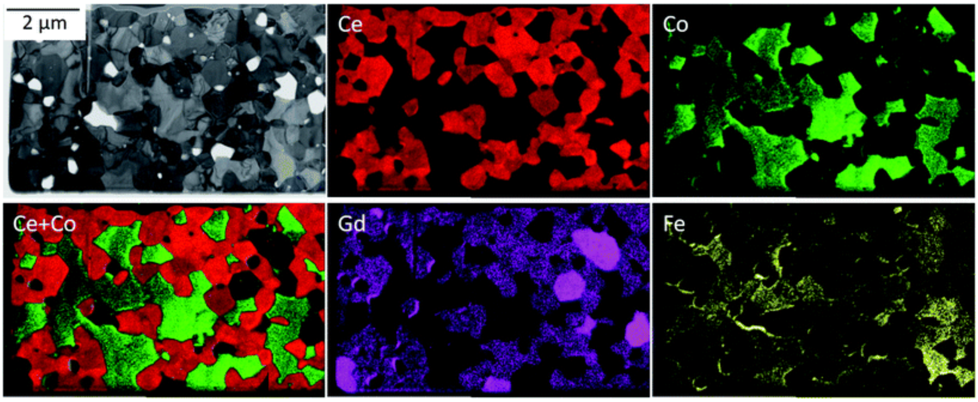

Figure 3.2 Energy-filtered TEM (EFTEM) analysis identifying three main phases: Gd-doped ceria (red), Fe/Co-oxide (green) and the GdFeO3-based perovskite (bright magenta)

As expected, the CGO weight fraction after sintering steadily decreases with increasing nominal FCO content in the primary powder mixture, whereas the weight fraction of both spinel phases increases. In contrast, the perovskite phase weight fraction remains relatively constant in the range of 11 ± 2% for all composites. However, due to the intense phase interactions the chemical compositions of the respective phases change, which is reflected by a change in lattice parameters in Table 3.1.

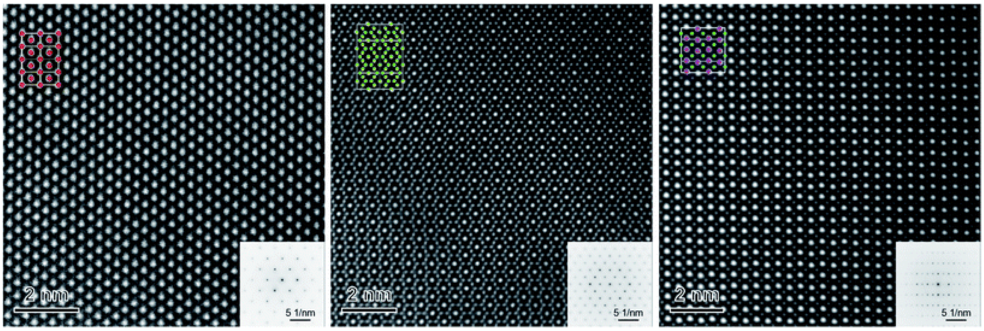

Figure 3.3 High-resolution HAADF images of single grains of CGO (left), FCO (middle) and GCFCO (right) recorded along the [101], [101] and [110] zone axis, respectively. Upper left/lower right insets are the corresponding structural models/diffraction patterns measured in the TEM mode. Oxygen is not shown

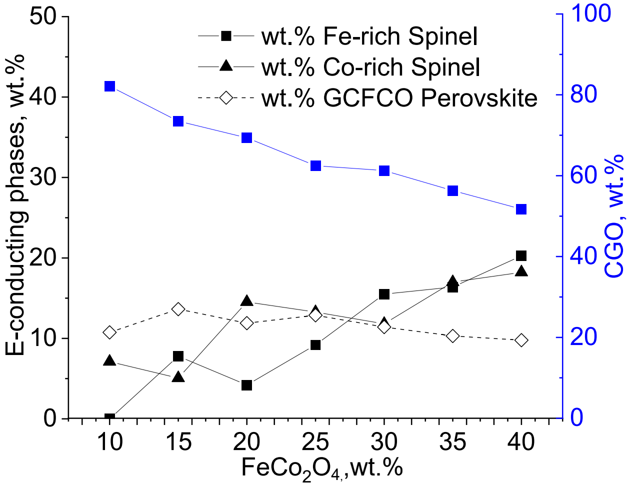

Figure 3.4 Weight fraction of detected phases in the CGO-FCO composites sintered at 1200 °C for 5 h according to Table 3.1

3.3.2 Phase composition

The exact chemical composition of the different phases in the sintered composite is not accessible with methods such as EDS. Therefore, lattice parameters are used to determine the chemical composition of all detected phases after sintering.

Spinel and fluorite phases

The spinel system $Fe_xCo_{3-x}O_4$ with Fd3m structure can be well analysed with the help of Vegard's law [29]. According to this rule of mixtures the linear relationship between the Fe-content and lattice parameter is given in that binary solid solution. The resulting Fe-content in the spinel phases is listed in Table 3.2. In contrast, the fluorite structure of $Ce_{1-x}Gd_xO_{2-x/2}$ does not obey Vegard's law [30] although there is a nearly linear relationship between the lattice parameter and Gd-content x in the region of interest, i.e. $x \leq 0.2$.

Table 3.2 Fe- and Gd-content in spinel and fluorite phases, respectively, after reactive sintering

Nominal spinel content [wt.%]	x in $Co_{3-x}Fe_xO_4$ Fe-rich spinel	x in $Co_{3-x}Fe_xO_4$ Co-rich spinel	x in $Ce_{2-x}Gd_xO_{2-d}$
10	-	0.14	0.15
15	0.97	0.15	0.152
20	0.92	0.48	0.162
25	1.34	0.23	0.17
30	1.32	0.27	0.16
35	1.30	0.33	0.13
40	1.30	0.25	0.146

Hong and Virkar [31] derived an equation for the lattice parameter of doped ceria considering the ionic radii of the different components

$$a = \frac{4}{\sqrt{3}} \times \left[x r_M + (1-x) r_{Ce} + (1-0.25x) r_o + 0.25 x r_{Vo}\right] \times 0.9971 \qquad \textbf{Equation 3.3}$$

where x is the concentration of the dopant in pure CeO_2, here Gd, so $r_M = r_{Gd} = 0.1053$ nm, $r_{Ce} = 0.097$ nm is the radius of the cerium ion, $r_o = 0.138$ nm and $r_{Vo} = 0.1164$ is the radius of the oxygen ion and vacancy, respectively. The resulting Gd-content x is listed in Table 3.2.

The $Gd_{1-x}Ce_xFe_{1-y}Co_yO_3$ system is much less investigated and, thus, the determination of the perovskite composition from the lattice parameter is not reliable. Therefore, it is calculated assuming a constant mass of the respective cations, i.e., no significant evaporation or similar effects occur during sintering. A mass balance is done using cation stoichiometry used for the synthesis and the calculated amount and composition of spinels and fluorite after sintering, Table 3.3.

Table 3.3 Calculated composition of the $Gd_{1-x}Ce_xFe_{1-y}Co_yO_3$ perovskite phase after reactive sintering

Nominal spinel content [wt.%]	Gd	Ce	Fe	Co
10	0.61	0.39	0.68	0.33
15	0.58	0.42	0.69	0.31
20	0.50	0.50	0.58	0.42
25	0.43	0.57	0.42	0.58
30	0.52	0.48	0.42	0.58
35	0.75	0.25	0.41	0.59
40	0.63	0.37	0.45	0.55

Perovskite phase

3.3.3 Composite composition

With knowledge of the composition and weight fraction of the individual phases the actual volume fractions of those coexisting phases can be calculated. The required densities of the different phases are calculated for each composite individually using

$$\frac{M_F Z N_A}{V_e}$$ **Equation 3.4**

with M_f being the molecular weight of one formula unit according to Table 3.2 and Table 3.3, Z the number of formula units per unit cell, N_A the Avogadro constant, and V_c the unit cell volume according to the lattice parameters given in Table 3.1.

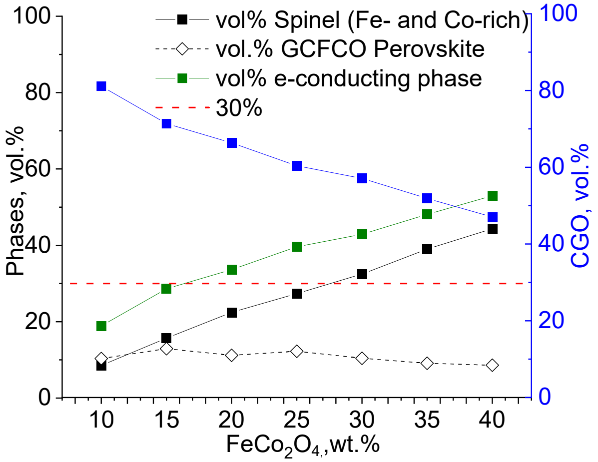

Figure 3.5 Volume fraction of detected phases in the CGO-FCO composites sintered at 1200 °C for 5 h.

The average densities in g cm^{-3} are 5.55 ± 0.064, 5.89 ± 0.041, 7.22 ± 0.005, and 7.39 ± 0.059 for the Fe-rich spinel, Co-rich spinel, fluorite, and perovskite, respectively, revealing only gradual changes of the density with composition. Figure 3.5 shows the volume fraction of the fluorite, perovskite and spinel phases versus the nominal weight fraction of FCO in the initial powder mixture. Indeed, there is a linear dependence of the total spinel amount, which exceeds the percolation threshold, i.e., 30 vol%, above 30 wt.% nominal FCO content. Since the perovskite phase contributes to the electronic conductivity the cumulative volume fraction of all electronic conducting phases is plotted, too. This volume fraction already exceeds the percolation threshold >15 wt.% nominal spinel content. This explains the excellent performance of the composite at low nominal FCO contents. Nevertheless, even below that threshold significant oxygen permeation can be measured down to 10% nominal spinel content, i.e., 18 vol% electronic conducting phases.

3.3.4 Performance

Individual phases

The phase changes during reactive sintering need to be considered to assess the composite performance. For $Ce_{1-x}Gd_xO_{2-x/2}$ it is well known that the ionic conductivity is hardly affected for 0.1 ≤ x ≤ 0.2. This is confirmed by own measurements of different CGO powders, Figure 3.6.

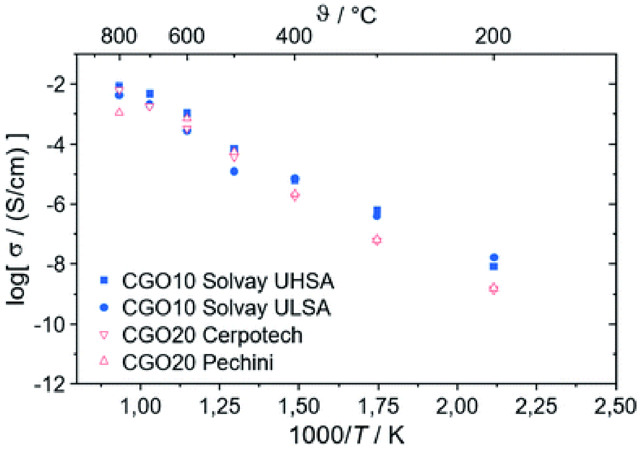

Figure 3.6 Ionic conductivity of CGO with 10 and 20 mol% Gd-substitution, respectively. The experimental error is ±5%

In contrast, the chemical composition of the electronic conducting phases determines their conductivities. Two spinels are synthesized exemplarily, i.e., Fe_2CoO_4 and

$FeCo_2O_4$. Figure 3.7 shows that the Fe-richer spinel shows lower conductivity. According to Table 3.2, the maximum Fe-content in the spinel phases is 1.34, well below that of Fe_2CoO_4 and, thus, the electronic conductivity can be regarded as sufficiently high. In the perovskite system single phase $Gd_{0.85}Ce_{0.15}Fe_{0.75}Co_{0.25}O_3$ (GCFCO) shows very similar conductivity, Figure 3.7. Hebb–Wagner measurements of the electronic partial conductivities with variable p_{O2} of this perovskite (exemplarily shown for p_{O2} = 0.21 bar as open symbols in Figure 3.7) showed a similar dimension like the total conductivities from impedance spectroscopy. In addition, oxygen permeation was negligible, i.e., below the detection limit, revealing that the chosen GCFCO is a pure electronic conductor and does not possess significant oxygen non-stoichiometry, i.e., $\delta \approx 0$. Moreover, Hebb–Wagner measurements down to $p_{O2} = 10^{-10}$ bar did not show any change of transport mechanisms indicating that the non-stoichiometry remains close to zero in that p_{O2}-range.

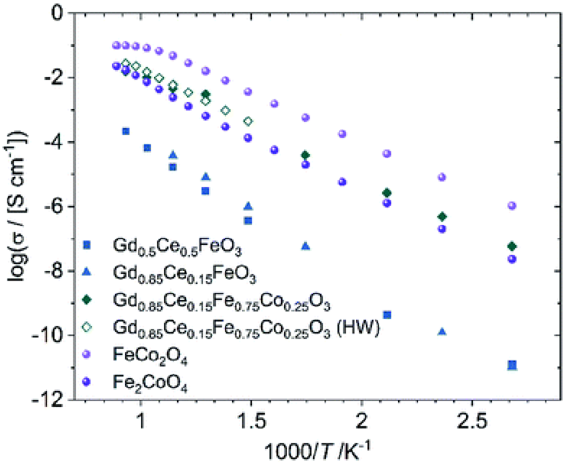

Figure 3.7 Electronic conductivity of phases identified in the composite. The legend gives nominal compositions, because some samples are not single phase. The experimental error is ±5%.

Co-free perovskites, in contrast, show very low conductivities. However, these materials did not show phase purity, but additional phases such as Gd-doped ceria, magnetite, and $Gd_3Fe_5O_{12}$, which are not present in the composites. Apparently, Co substitution on the B-site of $GdFeO_3$ supports perovskite phase formation. Ce substitution on the A-site acts as the donor and enables electronic conductivity. The $GdFeO_3$-based perovskites detected in the composites show Co- and Ce-substitution of 31–59% at the B-site and 25–57% at the A-site, respectively, Table 3.3. Therefore, those phases are considered as good electronic conductors.

Composites

The composites show good performance, Figure 3.8, as expected from previous reports [19]. For better comparison the oxygen permeance is normalized to the membrane thickness according to Equation 3.2. As a result, the activation energy E_A of the permeance is equal to that of the ambipolar conductivity. Data from Figure 3.8 reveal an E_A of 60–80 kJ mol^{-1} indicating that the ionic conductivity of the ceria phase is rate limiting. Only for the composite with nominal composition 90 : 10 wt.% E_A = 101 kJ mol^{-1} indicating a change in the rate limiting process probably due to the lack of electronic conductivity.

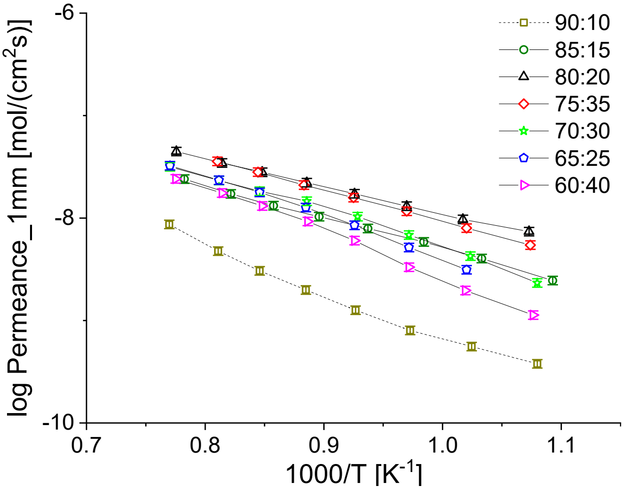

Figure 3.8 Arrhenius plot of the permeance of CGO-FCO composites normalized to a thickness of 1 mm. Error bars represent ± 10% of the measured values.

Figure 3.9 shows a comparison of this work with previously reported data on composites of the same nominal compositions, but differently synthesized, i.e. by the Pechini method, [19] a sol–gel technique starting from an aqueous precursor solution. The permeance follows the same systematic process. However, the Pechini synthesized composites show higher performance for low FCO-contents. This might be attributed to the typically finer microstructure with highly homogeneous cation distribution achieved by the sol–gel synthesis. Even if there are some percolating paths, these need to be “strong” enough to ensure sufficient electronic conduction. The comparison of microstructures (Figure 3.10) indicates similarly small ceria grains in the sub-micron range and slightly coarser spinel agglomerates for SSRS compared to that obtained by the Pechini method and, thus, no drastic difference. Unfortunately, quantification is not possible due to the low differences in grey scale contrast between the several phases.

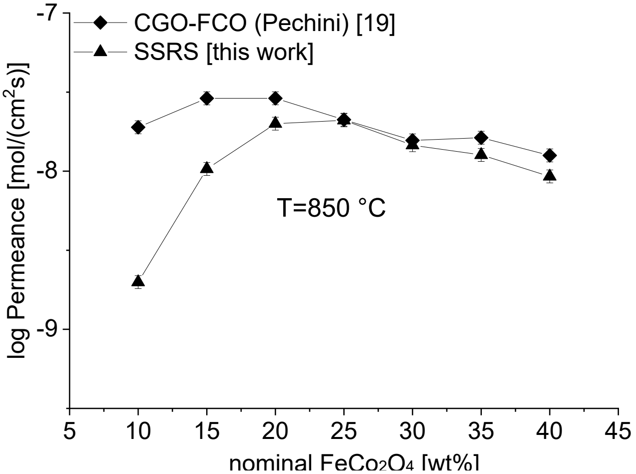

Figure 3.9 Permeance of differently synthesized composites depending on the nominal FCO-content. Error bars represent ± 10% of the measured values.

But, as analysed above the phase interactions during sintering lead to an increase in electronic conducting phases. However, this takes place at the expense of the ceria content, i.e., ionic conducting volume, which is rate limiting and thus not desired. Figure 3.11 shows the permeance versus the volume fraction of the sum of electronic conducting phases. In comparison to the CGO-FCO series CGO-GCFCO composites were synthesized using commercially available CGO and pre-synthesized $Gd_{0.85}Ce_{0.15}Fe_{0.75}Co_{0.25}O_3$. In this case no phase interactions during sintering are observed and, thus, indeed dual phase membranes are achieved. At low and high e^--conductor content, respectively, the permeance is quite similar. Above 40 vol% an identical behaviour can be expected because the ionic conductivity, i.e., ceria content, is the rate limiting factor. Around 30 vol% of e^--conductor content the SSRS CGO-FCO series shows higher performance over the CGO-GCFCO series. This, again, reveals the importance of the phase distribution, i.e., microstructure, inside the composite close to the percolation threshold. It seems to be even more important than the phase itself, in this case perovskite or spinel, or actually both together, as long as the electronic conductivity of these individual phases is sufficiently high.

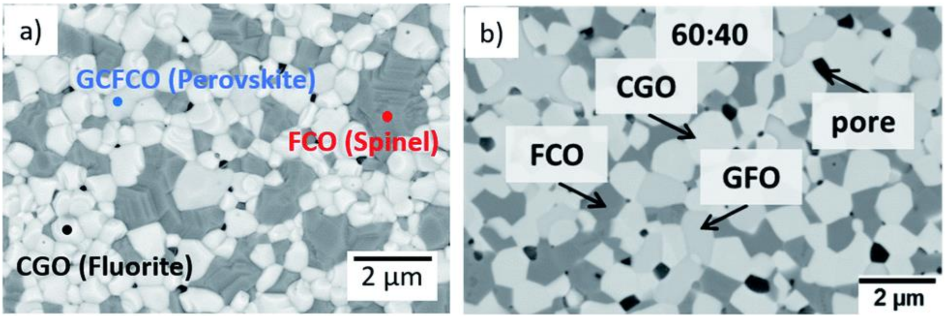

Figure 3.10 Microstructure of a sintered 60 : 40 CGO-FCO composite (a) synthesized by SSRS (SEM of surface, this work) and (b) synthesized by the Pechini method previously (SEM cross-section. Reproduced with permission. [19] Copyright 2017, Elsevier).

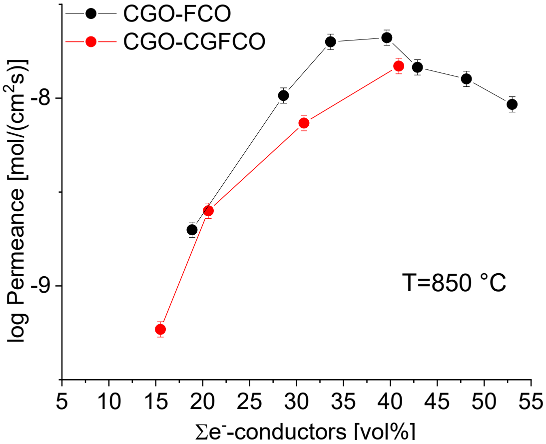

Figure 3.11 Permeance of CGO-FCO and CGO-GCFCO composites depending on the volume fraction of e−-conducting phases. Error bars represent ±10% of the measured values.

3.4 Conclusions

MIEC composites with nominal composition $Ce_{0.8}Gd_{0.2}O_{2-\delta}$ (CGO) – $FeCo_2O_4$ (FCO) can be successfully synthesized by the cost-efficient solid state reactive sintering (SSRS) technique using commercial powders of CGO as well as Fe_2O_3 and Co_3O_4. During sintering several phase interactions occur resulting in a mixture of four phases after sintering, i.e., CGO, two Fe/Co-spinel phases and a $GdFeO_3$-based perovskite. The composition of the individual phases depends on the nominal CGO-FCO ratio defining the mixture of the raw powders. Nevertheless, their functional characteristics, i.e., ionic or electronic conductivity, remain. For the perovskite formation during reactive sintering approx. 5 mol% of Gd is extracted from the initial CGO, which does not affect its ionic conductivity significantly. But the ceria volume fraction is reduced and, thus the ion conducting pathways. The two spinel phases are in equilibrium according to the $Fe_{3-x}Co_xO_4$ phase diagram and provide electronic conductivity, just like the perovskite $Gd_{1-x}Ce_xFe_{1-y}Co_yO_3$, which is a donor doped $GdFeO_3$ and, thus, a pure electronic conductor with a similar conductivity to the spinel. Consequently, the electronic conducting volume fraction is increased.

In MIEC composites typically the ionic conductivity is rate limiting provided that sufficient electronic conduction is achieved, which is a combination of the electronic conductivity of the selected phase(s) and the presence of sufficient percolating paths. This represents a typical optimization task, i.e., maximizing the ionic conducting volume without losing percolation of the electronic conduction.

In comparison to a two-phase system without reactive sintering made from pre-synthesized CGO and GCFCO ($Gd_{0.85}Ce_{0.15}Fe_{0.75}Co_{0.25}O_3$) the CGO-FCO SSRS shows higher performance close to 30 vol% of the electronic conducting phases, which is often considered as the percolation threshold. The phase interactions during SSRS obviously help achieving significant percolation of electronic conductors at high ceria content enhancing ambipolar conductivity compared to the CGO-GCFCO series solid state sintered without phase reactions. In the Pechini synthesized CGO-FCO series reported previously comparable phase interactions as in SSRS series occur. Even higher performance at the same nominal composition close to that percolation threshold was found, which might be attributed to the finer particles synthesized by the Pechini method. Moreover, the potential role of grain boundaries needs more attention. These results reveal the importance of tailoring the microstructure of composite membranes by materials engineering, which seems to be even more important compared to the investigation of more and more novel material mixtures.

Summarizing, SSRS of CGO-FCO is an attractive route – even though slightly less performing compared to the Pechini synthesized variant – due to its suitability for industrialization using cheap and abundant oxides. Further developments should concentrate on tailoring the resulting microstructure closing the gap with the Pechini synthesized composites.

Nevertheless, the in situ formed perovskite system (GdCe) (FeCo)O_3 represents an interesting alternative candidate as an electronic conductor in ceria-based composite membranes. It is expected to provide higher chemical stability compared to FCO in particular at lower p_{O2}. Moreover, there might be a chance to introduce oxygen non-stoichiometry, which would lead to mixed conductivity supporting ionic transport and facilitating surface exchange not investigated here. Therefore, the GCFCO system should be further investigated.

References

1. Deibert, W.; Ivanova, M.E.; Baumann, S.; Guillon, O.; Meulenberg, W.A. Ion-conducting ceramic membrane reactors for high-temperature applications. *Journal of Membrane Science* **2017**, *543*, 79–97.
2. Arratibel Plazaola, A.; Cruellas Labella, A.; Liu, Y.; Badiola Porras, N.; Pacheco Tanaka, D.; Sint Annaland, M.; Gallucci, F. Mixed Ionic-Electronic Conducting Membranes (MIEC) for Their Application in Membrane Reactors: A Review. *Processes* **2019**, *7*, 128.
3. Sunarso, J.; Baumann, S.; Serra, J.M.; Meulenberg, W.A.; Liu, S.; Lin, Y.S.; Diniz da Costa, J.C. Mixed ionic–electronic conducting (MIEC) ceramic-based membranes for oxygen separation. *Journal of Membrane Science* **2008**, *320*, 13–41.
4. Balaguer, M.; García-Fayos, J.; Solís, C.; Serra, J.M. Fast Oxygen Separation Through SO_2- and CO_2-Stable Dual-Phase Membrane Based on $NiFe_2O_4$–$Ce_{0.8}Tb_{0.2}O_{2-\delta}$. *Chem. Mater.* **2013**, *25*, 4986–4993.
5. Cheng, H.; Zhang, N.; Xiong, X.; Lu, X.; Zhao, H.; Li, S.; Zhou, Z. Synthesis, Oxygen Permeation, and CO_2-Tolerance Properties of $Ce_{0.8}Gd_{0.2}O_{2-\delta}$–$Ba_{0.95}La_{0.05}Fe_{1-x}Nb_xO_{3-\delta}$ Dual-Phase Membranes. *ACS Sustainable Chem. Eng.* **2015**, *3*, 1982–1992.
6. Luo, H.; Klande, T.; Cao, Z.; Liang, F.; Wang, H.; Caro, J. A CO 2 -stable reduction-tolerant Nd-containing dual phase membrane for oxyfuel CO 2 capture. *J. Mater. Chem. A* **2014**, *2*, 7780–7787.

7. Cheng, S.; Søgaard, M.; Han, L.; Zhang, W.; Chen, M.; Kaiser, A.; Hendriksen, P.V. A novel CO_2- and SO_2-tolerant dual phase composite membrane for oxygen separation. *Chemical communications (Cambridge, England)* **2015**, *51*, 7140–7143.

8. Garcia-Fayos, J.; Balaguer, M.; Serra, J.M. Dual-Phase Oxygen Transport Membranes for Stable Operation in Environments Containing Carbon Dioxide and Sulfur Dioxide. *ChemSusChem* **2015**, *8*, 4242–4249.

9. Kilner, J.A.; Burriel, M. Materials for Intermediate-Temperature Solid-Oxide Fuel Cells. *Annu. Rev. Mater. Res.* **2014**, *44*, 365–393.

10. Takamura, H.; Kobayashi, T.; Kasahara, T.; Kamegawa, A.; Okada, M. Oxygen permeation and methane reforming properties of ceria-based composite membranes. *Journal of Alloys and Compounds* **2006**, *408-412*, 1084–1089.

11. Luo, H.; Jiang, H.; Efimov, K.; Liang, F.; Wang, H.; Caro, J. CO_2 -Tolerant Oxygen-Permeable Fe_2O_3 -$Ce_{0.9}Gd_{0.1}O_{2-\delta}$ Dual Phase Membranes. *Ind. Eng. Chem. Res.* **2011**, *50*, 13508–13517.

12. Fang, W.; Liang, F.; Cao, Z.; Steinbach, F.; Feldhoff, A. A mixed ionic and electronic conducting dual-phase membrane with high oxygen permeability. *Angewandte Chemie (International ed. in English)* **2015**, *54*, 4847–4850.

13. Pippardt, U. , Böer, , J., Ch. Bollert, Hoffmann, A., Heidenreich,M., Kriegel,R. , Schulz,M., Simon, A. Performance and Stability of Mixed Conducting Composite Membranes Based on Substituted Ceria. *Journal of Ceramic Science and Technology* **2014**, 309–316.

14. Garcia-Fayos, J.; Vert, V.B.; Balaguer, M.; Solís, C.; Gaudillere, C.; Serra, J.M. Oxygen transport membranes in a biomass/coal combined strategy for reducing CO 2 emissions: Permeation study of selected membranes under different CO 2 -rich atmospheres. *Catalysis Today* **2015**, *257*, 221–228.

15. He, Y.; Shi, L.; Wu, F.; Xie, W.; Wang, S.; Yan, D.; Liu, P.; Li, M.-R.; Caro, J.; Luo, H. A novel dual phase membrane 40 wt% Nd 0.6 Sr 0.4 CoO 3−δ –60 wt% Ce 0.9 Nd 0.1 O 2−δ : design, synthesis and properties. *J. Mater. Chem. A* **2018**, *6*, 84–92.

16. Ramasamy, M.; Baumann, S.; Palisaitis, J.; Schulze-Küppers, F.; Balaguer, M.; Kim, D.; Meulenberg, W.A.; Mayer, J.; Bhave, R.; Guillon, O.*; et al.* Influence of Microstructure and Surface Activation of Dual-Phase Membrane $Ce_{0.8}Gd_{0.2}O_{2-\delta}$ -$FeCo_2O_4$ on Oxygen Permeation. *J. Am. Ceram. Soc.* **2016**, *99*, 349–355.

17. Lin, Y.; Fang, S.; Su, D.; Brinkman, K.S.; Chen, F. Enhancing grain boundary ionic conductivity in mixed ionic-electronic conductors. *Nature communications* **2015**, *6*, 6824.

18. Zhang, Z.; Zhou, W.; Chen, Y.; Chen, D.; Chen, J.; Liu, S.; Jin, W.; Shao, Z. Novel Approach for Developing Dual-Phase Ceramic Membranes for Oxygen Separation through Beneficial Phase Reaction. *ACS applied materials & interfaces* **2015**, *7*, 22918–22926.

19. Ramasamy, M.; Persoon, E.S.; Baumann, S.; Schroeder, M.; Schulze-Küppers, F.; Görtz, D.; Bhave, R.; Bram, M.; Meulenberg, W.A. Structural and chemical stability of high performance $Ce_{0.8}Gd_{0.2}O_{2-\delta}$-$FeCo_2O_4$ dual phase oxygen transport membranes. *Journal of Membrane Science* **2017**, *544*, 278–286.

20. Zeng, F.; Malzbender, J.; Baumann, S.; Nijmeijer, A.; Winnubst, L.; Ziegner, M.; Guillon, O.; Schwaiger, R.; Meulenberg, W.A. Optimization of sintering conditions for improved microstructural and mechanical properties of dense $Ce_{0.8}Gd_{0.2}O_{2-\delta}$-$FeCo_2O_4$oxygen transport membranes. *Journal of the European Ceramic Society* **2021**, *41*, 509–516.

21. Zeng, F.; Malzbender, J.; Baumann, S.; Krüger, M.; Winnubst, L.; Guillon, O.; Meulenberg, W.A. Phase and microstructural characterizations for $Ce_{0.8}Gd_{0.2}O_{2-\delta}$-$FeCo_2O_4$ dual phase oxygen transport membranes. *Journal of the European Ceramic Society* **2020**, *40*, 5646–5652.

22. Zeng, F.; Baumann, S.; Malzbender, J.; Nijmeijer, A.; Winnubst, L.; Guillon, O.; Schwaiger, R.; Meulenberg, W.A. Enhancing oxygen permeation of solid-state reactive sintered $Ce_{0.8}Gd_{0.2}O_2$-$FeCo_2O_4$ composite by optimizing the powder preparation method. *Journal of Membrane Science* **2021**, *628*, 119248.

23. van der Marck, S.C. Percolation thresholds and universal formulas. *Phys. Rev. E* **1997**, *55*, 1514–1517.

24. Lorenz, C.D.; Ziff, R.M. Precise determination of the critical percolation threshold for the three-dimensional "Swiss cheese" model using a growth algorithm. *The Journal of Chemical Physics* **2001**, *114*, 3659–3661.

25. Schmale, K.; Grünebaum, M.; Janssen, M.; Baumann, S.; Schulze-Küppers, F.; Wiemhöfer, H.-D. Electronic conductivity of $Ce_{0.8}Gd_{0.2-x}Pr_xO_{2-\delta}$ and influence of added CoO. *phys. stat. sol. (b)* **2011**, *248*, 314–322.

26. Kovács, A.; Schierholz, R.; Tillmann, K. FEI Titan G2 80-200 CREWLEY. *JLSRF* **2016**, *2*.

27. Buchheit, A.; Teßmer, B.; Ran, K.; Mayer, J.; Wiemhöfer, H.-D.; Neuhaus, K. The Impact of Fe Addition on the Electronic Conductivity of Gadolinium Doped Ceria. *ECS J. Solid State Sci. Technol.* **2019**, *8*, P41-P50.

28. Neuhaus, K.; Dolle, R.; Wiemhöfer, H.-D. Assessment of the Effect of Transition Metal Oxide Addition on the Conductivity of Commercial Gd-Doped Ceria. *J. Electrochem. Soc.* **2018**, *165*, F533-F542.

29. Bahlawane, N.; Ngamou, P.H.T.; Vannier, V.; Kottke, T.; Heberle, J.; Kohse-Höinghaus, K. Tailoring the properties and the reactivity of the spinel cobalt oxide. *Physical chemistry chemical physics : PCCP* **2009**, *11*, 9224–9232.

30. Artini, C.; Pani, M.; Carnasciali, M.M.; Plaisier, J.R.; Costa, G.A. Lu-, Sm-, and Gd-Doped Ceria: A Comparative Approach to Their Structural Properties. *Inorganic chemistry* **2016**, *55*, 10567–10579.

31. Hong, S.J.; Virkar, A.V. Lattice Parameters and Densities of Rare-Earth Oxide Doped Ceria Electrolytes. *J. Am. Ceram. Soc.* **1995**, *78*, 433–439.

Chapter 4

4. Role of Fe/Co ratio in dual phase $Ce_{0.8}Gd_{0.2}O_{2-\delta}$ - $FeCo_2O_4$ composites for oxygen separation

Abstract

Dual-phase membranes are increasingly attracting attention as a solution for developing stable oxygen permeation membranes. $Ce_{0.8}Gd_{0.2}O_{2-\delta}$ - $Fe_{3-x}Co_xO_4$ (CGO-F(3-x)CxO) composites are one group of promising candidates. This study aims to understand the effect of the Fe/Co-ratio, i.e., x= 0, 1, 2, and 3 in $Fe_{3-x}Co_xO_4$, on microstructure evolution and performance of the composite. The samples were prepared using the solid-state reactive sintering method (SSRS) to induce phase interactions, which determines the final composite microstructure. The Fe/Co ratio in the spinel structure was found to be a crucial factor in determining phase evolution, microstructure and permeation of the material. Microstructure analysis showed that all iron-free composites had a dual-phase structure after sintering. In contrast, iron-containing composites formed additional phases with a spinel or garnet structure which likely contributed to electronic conductivity. The presence of both cations resulted in better performance than that of pure iron or cobalt oxides. This demonstrated that both types of cations were necessary to form a composite structure, which then allowed sufficient percolation of robust electronic and ionic conducting pathways. The maximum oxygen flux is j_{O2} =0.16 and 0.11 ml/cm^2*s at 1000°C and 850°C respectively of the 85CGO-FC2O composite, which is comparable oxygen permeation flux reported previously.

This Chapter has been published as : Fischer, L.; Ran, K.; Schmidt, C.; Neuhaus, K.; Baumann, S.; Behr, P.; Mayer, J.; Bouwmeester, H.J.M.; Nijmeijer, A.; Guillon, O. Meulenberg, W.A.*; et al.* Role of Fe/Co Ratio in Dual Phase $Ce_{0.8}Gd_{0.2}O_{2-\delta}$-$FeCo_2O_4$ Composites for Oxygen Separation. *Membranes* **2023**, *13*, DOI: https://doi.org/10.3390/membranes13050482

4.1 Introduction

Oxygen separation using oxygen transport membranes (OTMs) is a good alternative to cryogenic air separation for producing pure oxygen in oxyfuel combustion. These ceramic membranes are more economically beneficial than other known gas separation methods, consume less power, and produce high quality oxygen in a single step process. Therefore there is increasing interest in the development and application of OTMs for industrial processes, e.g., for oxyfuel combustion and syngas production [1,2]. Mixed ionic-electronic conducting materials (MIEC) can be used for oxygen separation from air or the oxygen separation process can include exposure to flue gases containing CO_2, SO_x, dust, and steam [3–5]. In general, oxygen transport in dual- and multiphase membranes is implemented by using both ionic and electronic conducting phases. The presence of both of these phases is key to ensure good percolation and thus performance of the material. This means that the concentrations of individual phase should be above the percolating threshold, which is generally reported as 30 vol. %. For dual-phase material the ionic conductivity is normally the rate-limiting property. Accordingly, the main target in this field is to enable the reduction of the electron conducting phase without negatively affecting the final percolation properties of the material. Moreover, these materials should be sufficiently stable at the operating conditions, e.g., in flue gases at high temperatures and with an oxygen partial pressure gradient [6] Since the fluorite: spinel ratio has a significant influence on performance [7] the 85:15 combination is chosen, based on the previous investigations of the $Ce_{0.8}Gd_{0.2}O_{2-\delta}$ - $FeCo_2O_4$ (CGO-FC2O) multi-phase material [8,9]. Additionally, as a reference, the 60:40 ratio is used, which is very common in literature due to the high amount of the electron-conducting phase avoiding any problems with percolation. To produce a reliable, mixed-conducting composite, the quality of the connectivity and compatibility of the two phases is crucial. Under real conditions, interconnectivity between particles is imperfect and can be dependent on many different factors. In addition, the surface can also contribute to the oxygen exchange process in an important, though more limited way [10,11]. Modifying the surface by applying a catalytic layer is required to maximize surface area and to eliminate all possible surface limitations.

Composites of acceptor-doped ceria in combination with electronic conducting materials are of great interest and have recently been widely investigated in the intermediate temperature range (600-850°C) [2,4,12–16]. For the electron conducting material, oxides from aliovalent transition metals in particular iron and cobalt are well studied. This includes perovskites revealing dependence on the microstructure, phase constituents, conducting properties as well as permeation performance [17–19]. Furthermore, the spinel system $Fe_{3-x}Co_xO_4$ with x= 0, 1, 2, and 3 is of particular interest [20]. The mixed Fe-Co spinel structure is reported to have higher thermal stability compared to the normal Co_3O_4 spinel, illustrating that Fe substitution affects positively thermal stability and stability at reducing atmospheres, which is advantageous for the potential application in membrane reaction. The functional properties of the pure $Fe_{3-x}Co_xO_4$ system have been well reported [20–27] and several members of that system were mixed with doped ceria forming dual- or multi-phase composites.

The solubility of the end member Co_3O_4 (CO) in CGO is less than 1 %, and higher concentrations lead to Co_3O_4 segregation. With addition of >5 mol % of Co_3O_4 to the ceria, Co_3O_4 remains as a separate phase after sample preparation and sintering processes and leads to an improved electrical conductivity. It has also been reported that a three-dimensional interconnection of the phases in a dual-composite forms only when the amount of cobalt oxide exceeds 10 mol %. Adding Co_3O_4 also increases the surface exchange coefficient effectively, increasing the connected transport pathways [27,28].

The addition of the other end member Fe_2O_3 (FO) often is used as a sintering aid for sample densification and, in some cases, can even reduce the sintering temperature by 100-150°C [22,29,30]. When added to the CGO, iron oxide also has a positive effect on the total conductivity of CGO [22]. The presence of the iron in the CGO matrix reduces the lattice parameter of CGO [31]. The solubility of Fe_2O_3 in ceria reported in the literature ranges from 1 to 2 %, which may be due to variations in preparation methods and operating temperatures [22,30,32]. It was also reported that the addition of FO to CGO increases the grain boundary and total conductivity of the material. High conductivity is expected due to the possible formation of a Schottky type potential barrier at the grain boundaries within the high temperature range. This can enhance electron transport along the grain boundaries but at the same time be an obstacle for ionic transport across them [33]. It also increases the density of materials and leads to grain growth [29,34].

The addition of $FeCo_2O$ [8,35] and Fe_2CoO [15,36] has been also been published revealing significant phase interactions at sintering temperature. However, a systematic study of the role of Fe/Co-ratio on phase evolution and permeation performance is missing, amongst others because different fractions of ionic and electronic conducting phases in the composites were investigated.

Since the phase evolution in the composite CGO-FC2O (x=2 in $Fe_{3-x}Co_xO_4$) has been previously investigated in detail [33], three more members from the system $Fe_{3-x}Co_xO_4$ with x=0, 1, and 3, will be discussed here., i.e., Fe_2O_3, Fe_2CoO_4 (F2CO) and Co_3O_4. Based on the previous work, nominal ceria/spinel ratios of 60:40 wt.% and 85:15 wt.% were selected, respectively, for microstructural and performance analyses. In the former case (60:40) good percolation of the electronic pathways is given, while the latter (85:15) is close to the percolation threshold.

4.2 Materials and Methods

4.2.1 Sample preparation

$Ce_{0.8}Gd_{0.2}O_{2-\delta}$ (CGO) (Cerpotech, >99 %), Fe_2O_3 (FO) (Merck, 99 %) and Co_3O_4 (CO) (Merck, 99 %) powders used for the experiments were synthesized by the Solid-State Reactive Sintering method (SSRS). Fe_2O_3 and Co_3O_4 were mixed, so Fe:Co in a 2:1 ratio, resulting in spinel Fe_2CoO_4 (x=1), which was added to commercially available ceria. Respective amounts of powders were weighed to create CGO-F2CO compositions with wt. % -ratios of 60:40, 80:20, and 85:15. Cobalt-free and iron-free composites were performed with ratios of 60:40 and 85:15. Over 48 h the powder mixtures were ball milled in polyethylene bottles using zirconia balls on a roller bench at a speed of 175 rpm. After drying for 48 h in ambient air at 70° C, powder mixtures were pressed using a uniaxial press in disc-shaped membranes with d=20 mm and then sintered at 1200°C for 5 h in air with a heating rate of 5 K min-1. At this sintering temperature the spinel partially reduces into a high temperature monoxide phase with a rock salt structure. To ensure complete reoxidation of the high temperature Co/Fe-monoxide phase to a spinel phase that is stable at operating temperatures (600-1000°C), a slow rate of 0.5 K min^{-1} between 900 and 800 °C was implemented in the cooling cycle. This rate was determined by referring to the $Fe_{3-x}Co_xO_4$ phase diagram. After the sintering step all samples were ground down to 1 mm thick discs in 2 steps, applying SiC merge papers with different grits from P 800 to P 1200 (by WS FLEX 18C). On both sides of the discs a porous $La_{0.58}Sr_{0.4}Co_{0.2}Fe_{0.8}O_{3-\delta}$ (LSCF) catalytic activation layer with a thickness of 5 µm was applied using a screen-printing technique. Discs were then calcined in the oven at 1100 °C for 5 hours.

4. 2.2 Characterization methods

Crystal structure

Crystal structure was determined using the X-ray diffraction (XRD) diffractometer D4 ENDEAVOR (Bruker, Karlsruhe, Germany). Diffraction angle was chosen in the range of 2θ from 10° to 80°, with increments of 0.02° for 2θ and 0.75 seconds of measurement time per step. Analysis of the measured data was performed with X'Pert HighScore (PANalytical B.V., version 3.0.5) software. Phase quantifications and associated crystal structure analyses were carried out by Rietveld refinement using (Version 4.2.2) software. The errors of each fit were calculated individually and are reported in Table 4.1, -2 and -3.

Table 4.1 Lattice parameter and fraction (F) of the phases after quantification by Rietveld refinement analyses of the CGO-CO composites sintered at 1200°C for 5 h

FCO, %	**CGO(Fluorite)**		**Co_3O_4(Spinel)**	
	F, wt.%	a=b=c, Å	F, wt.%	a=b=c, Å
0	100.00	5.4246[0]	0	-
15	83.50[5]	5.4249[0]	16.50[5]	8.0808[5]
40	-	-	-	-

Table 4.2 Lattice parameter and fraction (F) of the phases after quantification by Rietveld refinement analyses of the CGO-FO composites sintered at 1200°C for 5 h

FCO,wt.%	**CGO (Fluorite)**		**$Gd_3Fe_5O_{12}$**		**Fe_2O_3**		
	F, wt.%	a=b=c, Å	F wt.%	a=b=c, Å	F, wt.%	Lattice parameter, Å	
						a=b	c
0	100.00	5.4246[0]	0	-	0	-	-
15	74.30[3]	5.4154[5]	20.75[2]	12.47[2]	4.96[2]	5.0351[4]	13.7358
40	55.00[3]	5.4155[4]	15.33[2]	12.47[2]	30.7[3]	5.0366[6]	13.7359

Table 4.3 Lattice parameter and fraction (F) of the phases after quantification by Rietveld refinement analyses of the CGO-F2CO composites sintered at 1200°C for 5 h

FCO, wt.%	**CGO(Fluorite)**		**F2CO (Spinel)**		**CGFCO (Perovskite)**			
	F, wt.%	a=b=c, Å	F, wt.%	a=b=c, Å	F, wt.%	Lattice parameter, Å		
						a	b	c
0	100.00	5.4246[0]	0	-	0	-	-	-
15	74.00[1]	5.4185[1]	13.50[1]	8.3688[2]	12.30[2]	5.3429[8]	5.6099[1]	7.658[1]
20	69.00[2]	5.4181[8]	18.90[1]	8.3699[1]	12.00[1]	5.3433[8]	5.6097[1]	7.662[5]
40	51.60[1]	5.4179[4]	37.40[9]	8.3835[1]	11.00[9]	5.3485[2]	5.6103[5]	7.669[3]

Microscopy

Scanning Electron Microscopy (SEM) and Energy Dispersive X-ray Spectroscopy (EDXS) were used to obtain material morphology. SEM images were taken with a Zeiss Ultra 55 and a Zeiss Supra 50 VP1 (Carl Zeiss NTS GmbH, German) SEM at different magnifications. The electronic conductivity of samples was enhanced by sputter deposition of a thin platinum layer prior to measurement.

For the Transmission Electron Microscopy (TEM) analysis, all specimens were cut from composite pellets by focused ion beam (FIB) milling using an FEI Strata 400 system with a Gallium ion beam. Further thinning and cleaning were performed using an Argon ion beam in a Fischione Nanomill 1040 at beam energies of 900 eV and 500 eV. TEM and energy-filtered TEM (EFTEM) imaging were performed using an FEI Tecnai F20 at 200 kV. For high-resolution high-angle annular dark-field (HAADF) imaging and EDXS chemical mapping an FEI Titan G2 80-200 ChemiSTEM microscope equipped with an XFEG and a probe Cs corrector was used [37].

Electrical conductivity

The total conductivity of the single-phase perovskite samples was determined by analysing the temperature-dependent impedance spectra with the help of a Novotherm HT 1200 frequency analyser. All samples were coated with a Pt resinate paste (RP 070107, Heraeus GmbH, Germany) and on both sides of the sample Pt sheet contacts were attached and measured in air. For all measurements an AC voltage peak-to-peak amplitude of 40 mV was applied. As the electronic conductivity of both spinels was very high, no division into separate contributions from the grain bulk and grain boundary was visible. Nyquist plots instead only showed a straight line (ohmic contribution from electron conducting phase).

The temperature-dependent electrical (total) conductivity of the composites, which was also dominated by the electron conductivity of the electron conducting phase, was measured using a DC measurement setup (Keithley 2600B): the top of the sample pellet was in contact with a Pt microcontact with a diameter of about 400 nm and the bottom was in contact with a Pt sheet. Additionally, Pt resinate paste (RP 070107, Heraeus GmbH) was applied to the sheet to reduce contact resistance. By using light microscopy to measure the imprint on the sample, the exact size of the micro-contact was determined. This was then compared to light microscopy images of the contact itself.

Oxygen permeation measurements

The oxygen permeation tests of all materials were performed in a vertical quartz glass housing, where the composite membranes were sealed with two gold rings with inner diameters of 13 mm. The separation of the oxygen from ambient air fed with 250 mlN min^{-1} was performed between 650 °C and 1000 °C. Argon was used as a sweep gas with a 50 mlN min^{-1} flow rate using mass flow controllers (Bronkhorst, Germany). A mass spectrometer (Omnistar, Pfeiffer Vacuum GmbH, Germany) detected the oxygen and nitrogen concentrations, in the permeate gas, i.e., oxygen enriched argon. Using the measured nitrogen concentration, the air leakage through either the membrane or the sealing was determined according to:

$$j_{O_2} = F_{Ar}\left(\frac{X_{O_2} - \frac{1}{4}X_{N_2}}{1 - X_{O_2} - X_{N_2}}\right)\frac{1}{A_{mem}}$$ **Equation 4.1**

with F_{Ar} being the argon flow rate, (50 mlN min^{-1}), X_{O2} and X_{N2} the oxygen and nitrogen concentration in the permeate gas, respectively, and A_{mem} the open membrane area (1.33 mm^2). The factor 1/4 reflects the O_2/N_2 ratio in the air feed, assuming that the leak is not gas selective.

The driving force of the permeation rate was not constant during the measurement, since the oxygen partial pressure in the permeate gas is temperature dependent. Additionally, the thickness of the discs after grinding deviates ±8% from the target thickness of 1 mm. Consequently, the driving force normalized permeation rate, also referred to as permeance, was normalized to the reference thickness L_0 = 1 mm and was calculated assuming Wagner behaviour using following equation

$$Permeance = \frac{j_{O_2}}{ln\frac{p'_{O_2}}{p''_{O_2}}}\frac{L_{mem}}{L_0}$$ **Equation 4.2**

Here, p'_{O_2} and $p''_{O_2}$are the oxygen partial pressures in the retentate and permeate gas, respectively, and L_{mem} is the actual membrane thickness. While the overall experimental error cannot be calculated precisely, it is assumed to be ±10%, which is well accepted in the literature.

4.3 Results and discussion

4.3.1 Microstructure evolution

The spinel system $Fe_{3-x}Co_xO_4$ with the *Fd3m* structure was analysed according to the $Fe_{3-x}Co_xO_4$ phase diagram illustrated in Fe-Co phase diagramm from [38]. There are generally considered to be two known spinel types, iron-rich and cobalt-rich. The difference between the two spinel structures is the distribution of divalent and trivalent cations. To preserve the *Fd3m* symmetry in the normal spinel structure, divalent cations (Co^{2+}) occupy all tetrahedral A sites, while all octahedral B sites are occupied by trivalent cations (Fe^{3+}). This is in contrast to the inverse spinel structure, where the A sites as well as 50 % of the B sites are occupied by trivalent cations, the remaining 50 % of the B sites contain divalent cations [39–41]. Thus the normal and inverse spinel structures can be expressed as AB_2O_4 and $B(AB)O_4$ respectively [42]. There are three spinel regions on the Fe-Co phase diagram. Where concentrations of iron-doping are low, the Co_3O_4-like structure is found. This has a normal spinel structure. At high iron-doping concentrations ($x \geq 1.2$) conditions are favourable for the Fe_3O_4-like structure, which has an inverse spinel. In this case only one spinel phase (inverse spinel) can be observed in the composite whose lattice parameter increases with the amount of incorporated iron. Pure Fe_3O_4 exists only at 1300 °C in accordance with the Fe-Co phase diagram. In the intermediate range ($0.65 \leq x \leq 1.07$) coexistence of both spinel types is possible with clear predominance of the inverse spinel structure [20]. This section may be divided by subheadings. It should provide a concise and precise description of the experimental results, their interpretation, as well as the experimental conclusions that can be drawn.

Fe-free composites (x=3 in $Fe_{3-x}Co_xO_4$)

Two iron-free composites with 60:40 and 85:15 ratios were subjected to microstructural and performance analyses (abbreviated later as 60CGO-CO and 85CGO-CO). During the fabrication and sintering steps several problems appeared. The first sintering attempt under standard conditions of 1200°C for 5 h, resulted in all 60CGO-CO samples breaking and/or showing visual cracks as shown in Figure 4.1. This may have been due to the formation of an additional rock salt phase at 1200°C, which is a known phenomenon in dual-phase materials [43]. In such a phase transformation, the volume expansion may cause the sample to crack. Macroscopic fractures were not observed for 85CGO-CO samples, but all samples had insufficient gas tightness.

Modifying the sintering programme to reduce the sintering temperature to 1100 °C with a 0.5 K/min cooling rate helped to reduce cracking, as according to the phase diagram, it helps the transformation of CoO_x to Co_3O. However, it was still not possible to produce samples with sufficient gas-tightness for the permeation tests.

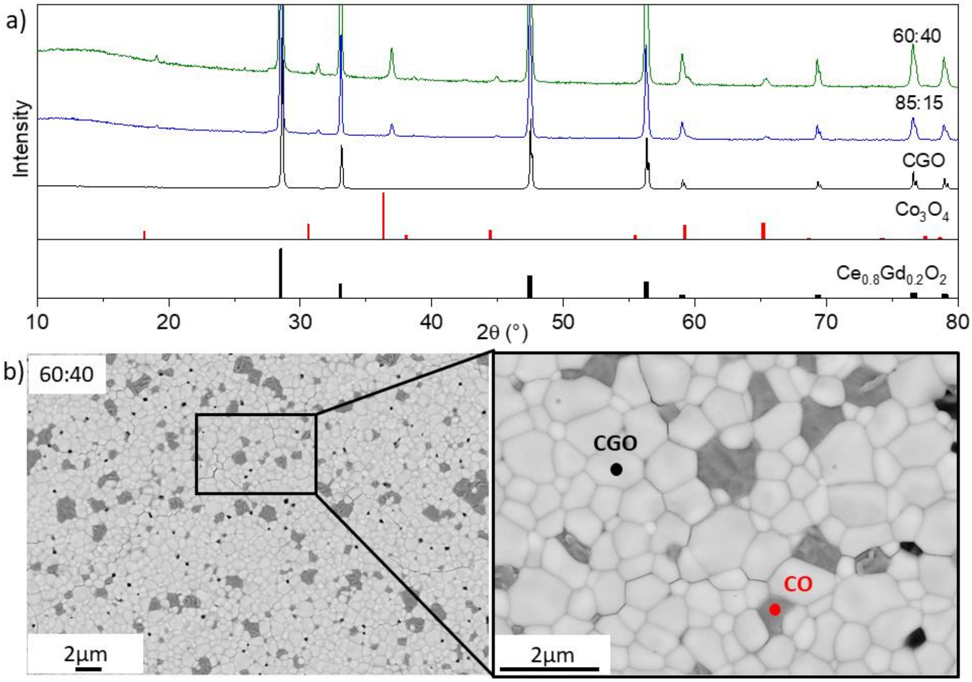

Figure 4.1 a) The XRD patterns of CGO-CO materials sintered at 1200°C for 5 h and single-phase CGO sintered at 1400°C for 5 h as well as peak positions of phases, b) SEM image of CGO-CO morphology of the samples sintered at 1200°C for 5h

SEM analysis shows a mixture of the two phases in both composites, ceria (white) and cobalt oxide (dark grey). A mean grain size of 0.68 μm can be estimated for both phases from the SEM. In the 60:40 composite, intergranular cracks were detected along the grain boundaries, primarily between CGO-CGO grains, as can be seen in Figure 4.1b. The reason for the cracks is likely to be the internal stress resulting from either thermal expansion or the difference in chemical expansion of some localized CGO grains during sintering [43]. The character of the cracks in the 85:15 composite was slightly different. While fewer cracks were observed, they were found both along the grain boundaries as well as within the CGO grains.

Due to the low solubility of cobalt oxide (<1 %), $Co_3O_{4-\delta}$ was found as a separate phase in the samples [27,28]. It was also thermodynamically unfavourable to get gadolinium ions from the fluorite structure (CGO) and move them into the ABO_3 phase structure at sintering temperature. Thus, perovskite $Gd^{3+}Co^{3+}O_3$ phase formation is likely not possible at 1200°C sintering temperature and instead only cobalt oxide is produced. The amount of added CO (15 and 40 wt. %) did not have much effect on grain size and phase distribution.

The presence of two phases was also confirmed by XRD analysis: CGO with cubic fluorite-type structure and Co_3O_4 with cubic spinel structure as shown in Figure 4.1a. With further Rietveld refinement, the main phase characteristics were analysed. Weight percentages and lattice parameters for this series of composites are listed in Table 4.1. The CGO lattice parameter remained almost unchanged with the addition of CO to the acceptor-doped ceria, illustrating no phase interaction.

Other sintering attempts of the CGO-CO samples failed. Since most of the 60CGO-CO samples were broken at the fabrication stage, and most permeation tests were not successful, the composite was not used in further analyses.

Co-Free Composite (x = 0 in $Fe_{3-x}Co_xO_4$)

Similarly, two cobalt-free composites with 60:40 and 85:15 ratios were fabricated and subjected to microstructure analyses. The room-temperature XRD patterns revealed the presence of three main phases in both cobalt-free composites CGO-FO: CGO with a cubic fluorite structure, Fe_2O_3 with a rhombohedral structure, and cubic $Gd_3Fe_5O_{12}$ (GCFO), as shown in Figure 4.2a.

Subsequent Rietveld refinement shows that, among these composites, the third phase accounted for 15–20 wt.%, listed in Table 4.2. The lattice parameter of CGO was reduced by 0.17% after addition of Fe_2O_3 to the acceptor-doped ceria, probably due to the substitution of smaller Fe^{3+} ions for Ce^{4+} in the fluorite matrix.

The XRD results were confirmed by SEM analysis, where three phases with a mean grain size of 0.5 μm were observed, as shown in Figure 4.2b: FO (dark grey), GCFO (light grey), and CGO (white). There were no visual defects or cracks after the sintering process.

In contrast to CO, the addition of FO to the nominal composite leads to a phase interaction during sintering at 1200°C and the formation of a third phase $Gd_3Fe_5O_{12}$.

This is called gadolinium iron garnet, has a cubic structure, and is in the space group *Ia3d*, with respect to the Fe-Co phase diagram [44]. According to the literature the solubility of iron oxides is a bit higher than Co_3O_4, which likely provides better compatibility with the phases in the CGO-FO composite. As a result, a $Gd_3Fe_5O_{12}$-based phase is formed, consisting of gadolinium cations from the fluorite phase as well as iron cations from the Fe_2O_3 phase. It is also likely that this phase contains traces of cerium cations on the A site. The third phase remains in the range of 15-20 wt. % and seems to be greatly affected by the amount of the FO in the nominal composite: the more FO the less $Gd_3Fe_5O_{12}$ phase is formed. This tertiary phase was also observed and mentioned by Lin et al., who claimed that it had low conductivity compared to the perovskite-like structure [15]. According to these observations it can be concluded that the presence of iron cations in the composite is a necessary condition to form a tertiary phase during the sintering process, namely a cerium doped $Gd_3Fe_5O_{12}$ phase in a CGO-FO composite.

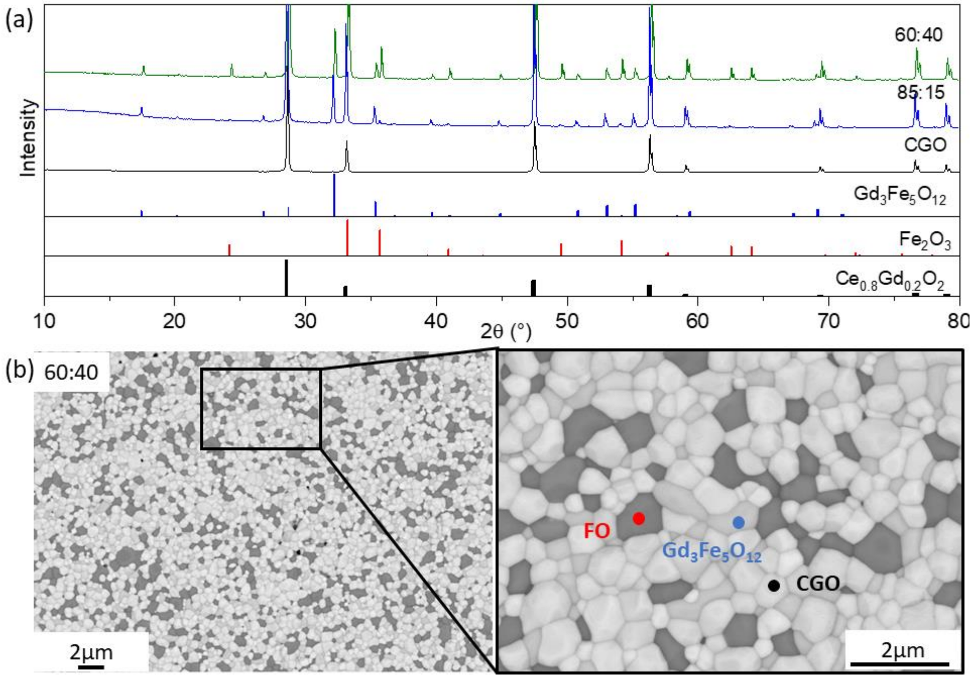

Figure 4.2 a) The XRD patterns of the cobalt-free CGO-FO materials with 60:40 (green) and 85:15 (blue) ratios sintered at 1200 °C for 5 h and single-phase CGO (black) sintered at 1400 °C for 5 h as well as peak positions of phases. (b) SEM image of CGO-FO morphology of the sample sintered at 1200 °C for 5 h.

When comparing the fraction of the electron conducting phases in these composites with the permeation threshold, some assumptions were made. Since the exact composition and conducting properties of $Gd_3Fe_5O_{12}$ were not clear, we could only assume that the $Gd_3Fe_5O_{12}$phase provided some electron conducting properties to support e-transport [44–46]. In this case it was clear that while the permeation threshold of 30 vol. % was not reached by the CGO-CO composite, the CGO-FO composite reached this threshold at 17 wt. % FO.

Iron Rich Spinel (x = 1 in $Fe_{3-x}Co_xO_4$)

After investigating the composites with CO and FO, it was interesting to see how the combination of these two oxides in different proportions affected the microstructure and transport properties of dual-phase composites. The first candidate mix of Fe_2O_3 and Co_3O_4, where Fe/Co held in a 1:2 ratio, resulting in a spinel $FeCo_2O_4$ (x=2) phase has been previously published [8]. Here Fe_2O_3 and Co_3O_4 with Fe/Co in a 2:1 ratio, resulting in a spinel Fe_2CoO_4 (x=1) phase was added into the ceria-based composite. In this study, three composite dual-phase membranes in combinations 60:40, 80:20 and 85:15 (abbreviated later as for example 60CGO-F2CO, etc.) were prepared using the SSRS method.

After investigating the composites with CO and FO, it was interesting to see how the combination of these two oxides in different proportions affected the microstructure and transport properties of dual-phase composites. The first candidate mix of Fe_2O_3 and Co_3O_4, where Fe/Co held in a 1:2 ratio, resulting in a spinel $FeCo_2O_4$ (x=2) phase has been previously published [8]. Here Fe_2O_3 and Co_3O_4 with Fe/Co in a 2:1 ratio, resulting in a spinel Fe_2CoO_4 (x=1) phase was added into the ceria-based composite. In this study, three composite dual-phase membranes in combinations 60:40, 80:20 and 85:15 (abbreviated later as for example 60CGO-F2CO, etc.) were prepared using the SSRS method.

During the sintering process, several phase interactions took place which resulted in a mixture of the three phases. X-ray diffraction in Figure 4.3 clearly confirmed that all materials from the CGO-F2CO row had the following phases: CGO with a cubic fluorite structure, F2CO with a cubic spinel structure, and $GdFeO_3$ with an orthorhombic perovskite structure. In the formation of the tertiary phase, approximately 10 % of the gadolinium is taken from CGO and successfully incorporated at the A sites in the ABO_3

structure [35]. For the B sites iron is more favourably incorporated compared to cobalt. This perovskite phase may contain the cerium as well as cobalt traces.

Although all three phases can be distinguished by their X-ray diffraction patterns, the intensities of the spinel and perovskite phase peaks change with respect to the amount of nominal F2CO in the initial composite. In the SEM images in Figure 4.3b, where contrast of various phases can be distinguished, in combination with the further EDX analysis fluorite (white), spinel (dark grey), and perovskite phases (light grey) are found. These results are in a good agreement with the XRD.

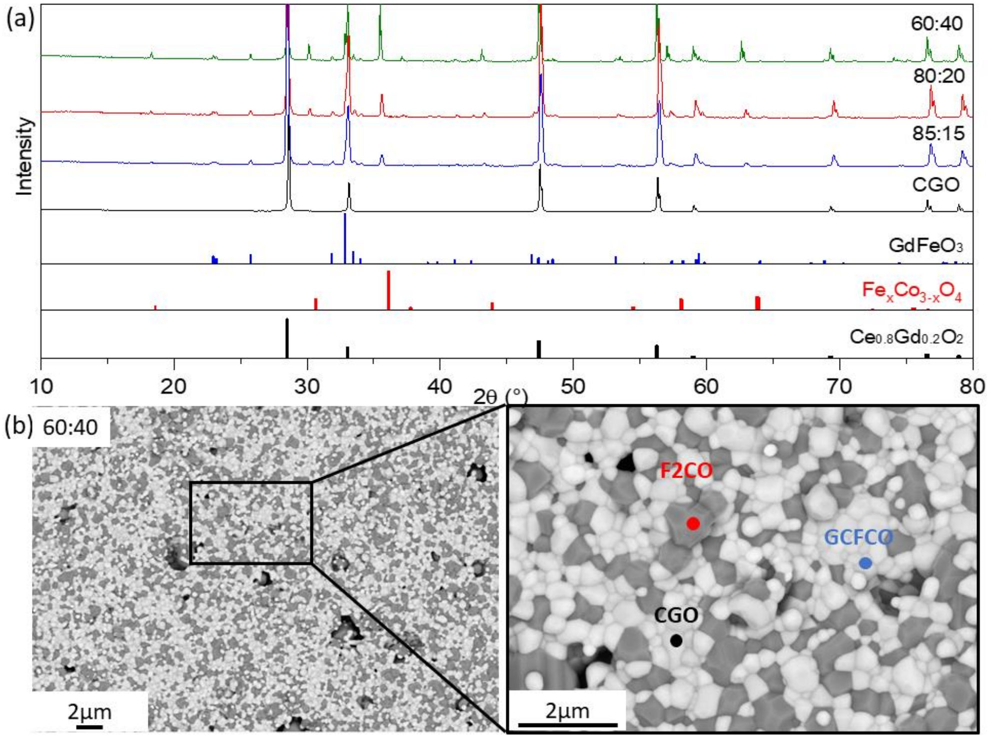

Figure 4.3 a) XRD patterns of the three CGO-F2CO composites with 60:40 (green), 80:20 (red) and 85:15 (blue) ratios sintered at 1200 °C for 5 h and single-phase CGO (black) sintered at 1400 °C for 5 h as well as peak positions of fluorite, spinel, and perovskite phases; (b) SEM image of the surface dual-phase composite 60CGO-F2CO. White is CGO, light grey is GFO, and black is F2CO.

Further Rietveld refinement quantified the composition of the dual-phase composites, which are listed in Table 4.3. In CGO-F2CO composite only one spinel type has been found. Similar to the CGO-FC2O (x=2) composite described in [8], the weight fraction of the fluorite phase decreased as F2CO increases in the initial powder mixture.

The amount of GCFCO remains constant in the range of 12±1 wt. %, regardless of the amount of F2CO in the nominal composite. Since the $GdFeO_3$-based perovskite that is formed can be distinguished as a pure electron conductor according to [8], the increase in the total electron conducting phase in the composite occurs at the expense of the number of ion-conducting phases, which is the rate limiting factor. The unit-cell parameters of the pure phases are known from literature Fe_2CoO_4 (0. 8385nm) [47] and CGO (0.54209 nm) [48]) and were measured before phase interaction. In our case there was no remarkable change after SSRS and the sintering steps for the dual-phase material fabrication (F2CO: 0.837 nm, CGO: 0.5418 nm), as indicated in Table 4.3. This indicated that we had an F2CO spinel structure in the composite after mixing the Fe_2O_3 and Co_3O_4 with Fe/Co in a 2:1 ratio.

Similar to the analysis performed on the CGO-FC2O (x=2) composite, described in [8], the compositions of the three individual phases were also estimated. The resulting volume fractions of each phase graphically represented in in Figure 4.4.

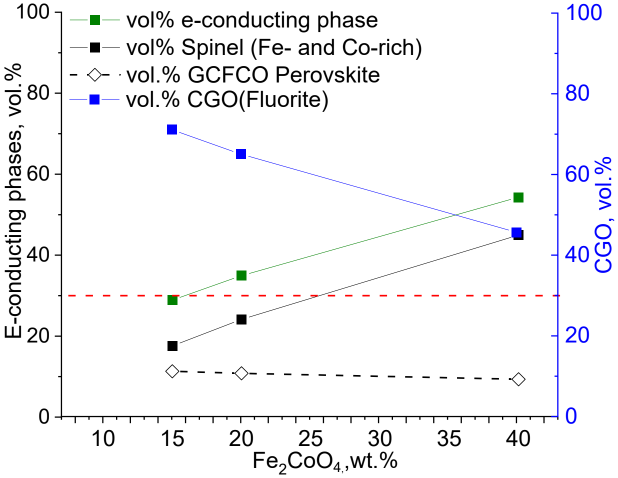

Figure 4.4 Volume fraction of detected phases in the CGO-F2CO composites

The percolation threshold of 30 vol.% (shown as a red dashed line in Figure) can be achieved at 25 wt.% of nominal F2CO in the composite (black line). Spinel and perovskite are responsible for e-transport, providing well-connected paths for the electrons in the material. The sum of the volume fraction of F2CO and GCFCO is shown in the graph in green. As can be seen that the threshold was reached already at 15 wt.% of the nominal F2CO in the composite material. This explains the relatively high oxygen flux for the CGO-F2CO (x = 1) composite material even at a low F2CO content (<20 wt.%).

Using TEM analysis, the presence of other phases was excluded. During the sintering process, the perovskite-like phase fraction was formed mostly between CGO grains, providing a well-connected network of the electron conducting phases and thus continuous pathways for electrons, which can be seen in Figure 6. The presence of this connected e-path helped to reach a sufficient percolation network in this composite and thus good oxygen flux.

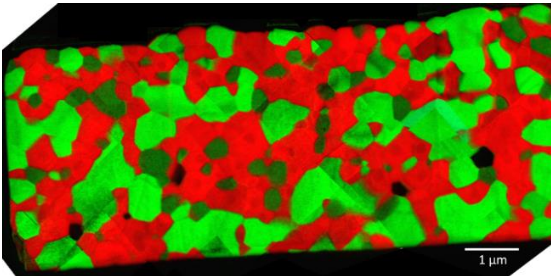

Figure 4.5 Distribution of the three phases: CGO (red), F2CO (light green) and GCFCO (dark green) in 60CGO-F2CO composite

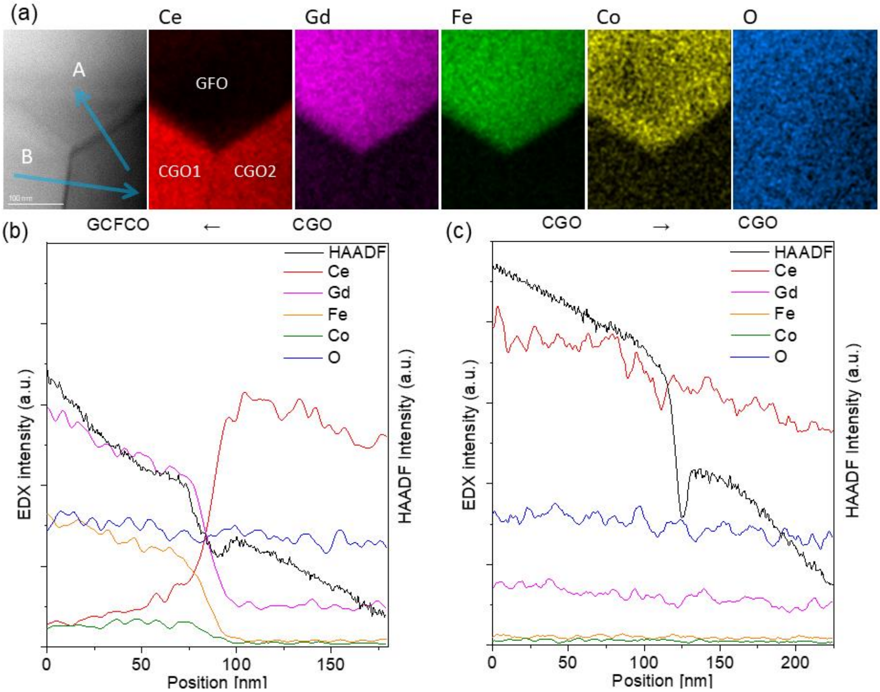

Figure 4.6 EDXS analysis of the grain boundaries. (a) The simultaneously acquired HAADF image and EDXS chemical mapping from Ce L, Gd L, Fe K, Co K and O K peak. (b) Line scans between CGO and GCFCO and (c) CGO and CGO grains

The HAADF image and EDXS chemical mapping in Figure 4.6a were recorded around a junction of two CGO grains and one GCFCO grain, where the two phases could be clearly separated based on the elemental maps.

As indicated by the arrow labelled as A, intensity profiles across the CGO2 and GCFCO were extracted and then plotted in Figure. All the elements smoothly transferred between the two phases, and no abrupt enrichment and/or depletion of any element was noticed.

Arrow B indicates the grain boundary between CGO1 and CGO2 grains, where also a smooth chemical transfer across the boundary can be observed.

In the CGO-F2CO composite, three different phases formed during the sintering process. This allowed the observation of six interface types, which resulted in different types of transport within the material. Interfaces between two spinel grains (F2CO-F2CO) and between spinel-orthorhombic (F2CO-GCFCO) as well as two orthorhombic (GCFCO-GCFCO) structures provided electronic transport, whereas CGO-CGO and CGO-GCFCO interfaces enhanced ionic transport.

Typical grain boundaries in the 60CGO-F2CO dual phase membranes are shown in Figure 4.7. All the grains are closely packed without any intergranular structures. Around the grain boundaries, the crystal structures of each grain are resolved down to the atomic scale, indicating no significant segregations or defects along the grain boundaries.

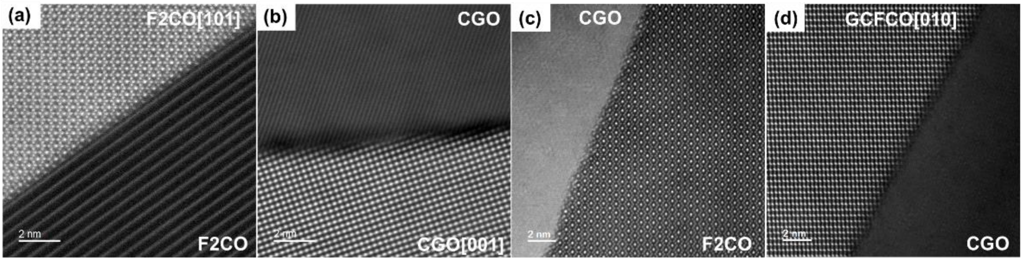

Figure 4.7 HAADF image of the grain boundary between different types of grains, (a) F2CO and F2CO, (b) CGO and CGO, (c) CGO and F2CO, and (d) CGO-GCFCO in the 60CGO-F2CO system

The influence of the Fe/Co ratio (x = 0–3) on the composite structure is investigated. The lattice parameter of pure CGO without phase interaction was 0.54246 nm and it was found to decrease after phase interaction due to Gd extraction (Table 4.1-3). The residual gadolinium content in CGO (Figure 4.8)) was calculated with help of the lattice parameter [8,49]. The iron-free composite (x = 3) reveals almost the same CGO lattice parameter compared to the pure CGO, because no phase interaction takes place. In contrast the pure Fe_2O_3 (x=0) extracts most gadolinium so that only approx. 5 mol% remain in the ceria, which reduces its ionic conductivity [50]. A mixture of iron and cobalt (x = 1 or 2) a plateau with approx. 10 mol% residual gadolinium is observed, which shows still high ionic conductivity [50].

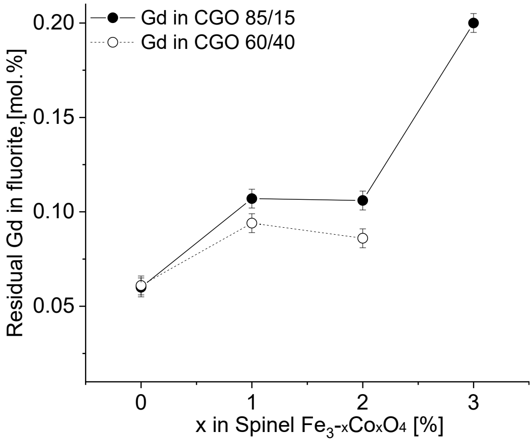

Figure 4.8 Residual gadolinium amount in fluorite dependent on Fe/Co ratio in CGO-based composites after sintering

The grain size of each phase as well as the pore size is analysed with ImageJ software on all samples [51] (Figure 4.9a). The spinel grains are slightly larger compared to the CGO and third phase, i.e., perovskite or garnet and all grain sizes slightly increase with increase in cobalt content x. The mean grain size value of the four composites is in the range of 0.48–0.68 µm.

The porosity (image analysis) does not vary significantly, which is in good agreement with the relative density values obtained geometrically (Figure 4.9b). The CGO-F2CO composite reveals a low number of larger pores, while CGO-FO has a higher number of pores with a small size << 1 µm. The highest densification > 91% relative densities was achieved with both F2CO and FC2O-added composites.

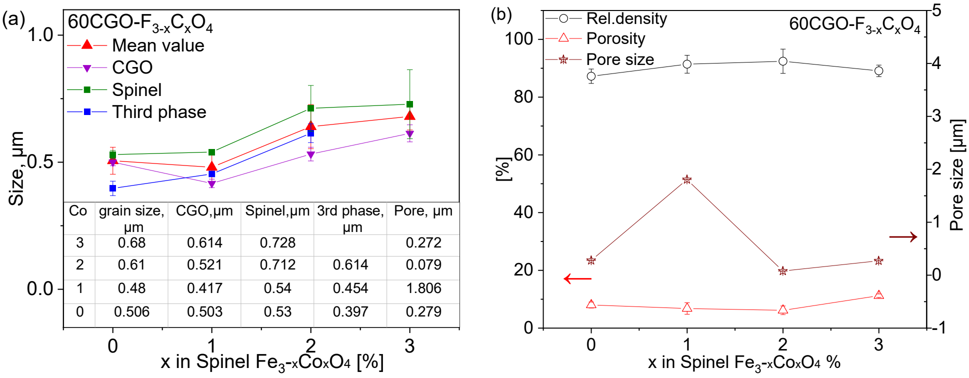

Co	grain size, µm	CGO,µm	Spinel,µm	3rd phase, µm	Pore, µm
3	0.68	0.614	0.728		0.272
2	0.61	0.521	0.712	0.614	0.079
1	0.48	0.417	0.54	0.454	1.806
0	0.506	0.503	0.53	0.397	0.279

Figure 4.9(a) The grain size and pore size dependency on the Fe/Co ratio in CGO20-based composite; (b) porosity and relative density dependency

4.3.2. Permeation of the Composites

Figure 4.10 shows the temperature-dependent oxygen permeation rates of the composites with nominal CGO-FCO wt.-ratio of 60:40 and 85:15, respectively. In case of 60:40, the amount of the electronic conductor is high enough to ensure good percolation and the ionic conductivity of the ceria is rate-limiting. In consequence, the composites with the spinel phases, i.e., x = 1 and x = 2, show identical oxygen flux (Figure 4.10a). In contrast, the composite with pure iron oxide, x = 0, shows significantly lower flux because the resulting phases after sintering, i.e., Fe_2O_3 (hematite with corundum structure) and $Gd_3Fe_5O_{12}$ (garnet structure) are known to have much lower electronic conductivity compared to the spinel and perovskite phases present in the other composites [15]. As described above, the composite with pure cobalt oxide, x=3, could not be prepared and measured successfully. with pure cobalt oxide, x = 3, could not be prepared and measured successfully.

The amount of electronic-conducting phases in the composites with 85:15 nominal wt.-ratio is around the percolation threshold as analysed above. Now, the choice of the electronic conducting phase(s) becomes relevant and, thus, the oxygen fluxes vary significantly (Figure 4.10b). Again, the pure iron oxide (x = 0) shows the lowest performance due to lack of electronic conductivity. In case of Co_3O_4 (x = 3), the electronic conductivity is known to be high. However, since no phase interactions occur, the volume fraction of Co_3O_4 is too low to enable sufficient electronic transport. In consequence, the ambipolar conductivity and, thus, permeance is limited, too. The total (i.e., electronic) conductivity of FC2O measured by impedance spectroscopy is higher compared to F2CO as shown in Figure 4.11, which is in accordance with literature [23]. Therefore, composites with FC2O (x = 2) show approx. 30% higher oxygen flux compared to that with F2CO (x = 1) at high temperatures. In addition, close to the percolation limit the phase distribution within the composite will have certain impact on its performance.

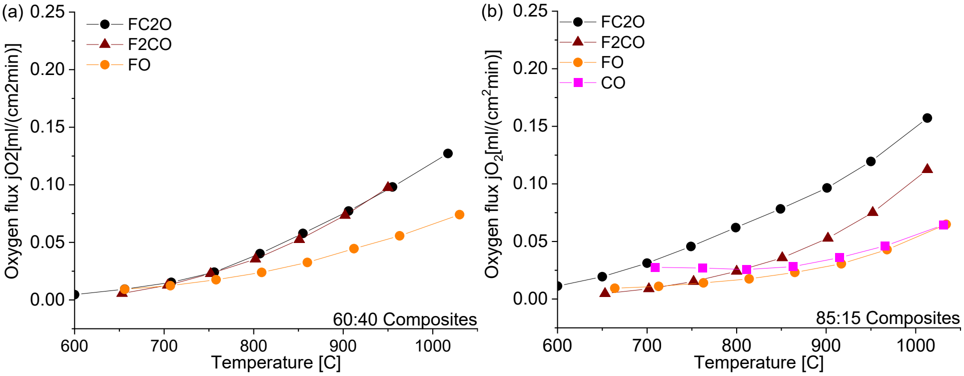

Figure 4.10 Oxygen permeation rates of the ceria-based materials for the (a) 60:40 and (b) 85:15 ratios

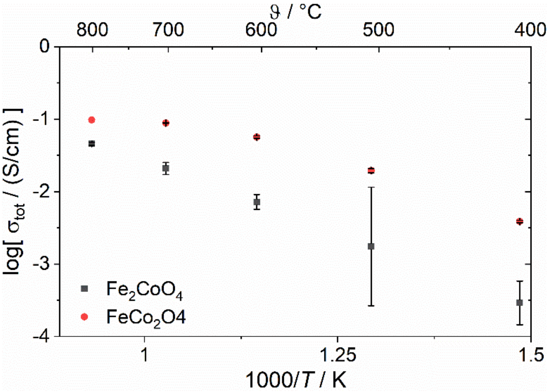

Figure 4.11 Total conductivity of spinel phases measured by impedance spectroscopy.

Permeance dependency on the electron conducting phase fraction of all studied composites is depicted in Figure 4.12. In summary, at high nominal spinel fraction in the composite, i.e., 40 wt.%, the Fe/Co-ratio in the spinel phase plays a minor role for the permeance (Figure 4.13), because the ionic conductivity of the ceria phase is rate-determining. Hence, an improvement in the composites’ permeance can only be achieved by developing better ion conductors rather than electron conductors. However, pure iron oxide crystallizes in corundum structure rather than spinel structure providing significantly lower electronic conductivity and, thus, permeance. Addition of cobalt stabilizes the spinel structure, but pure cobalt oxide leads to cracking due to severe phase changes during sintering cycles.

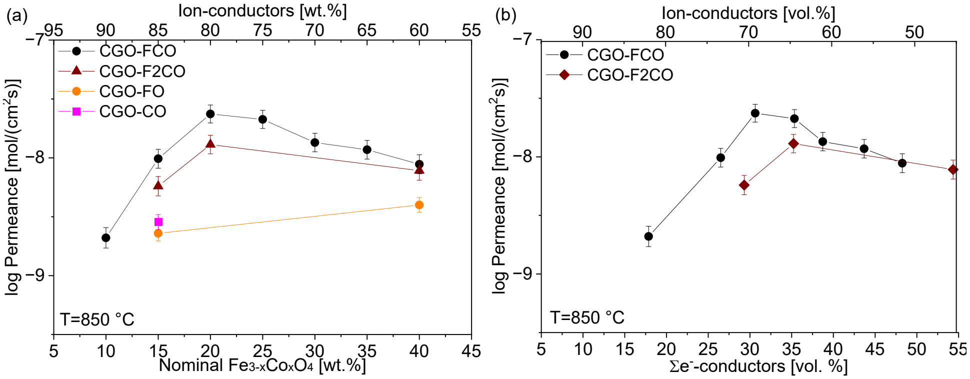

Figure 4.12 Permeance of the CGO-based composites depending on the $Fe_{3-x}Co_xO_4$ content in (a) weight percent and (b) volume percent

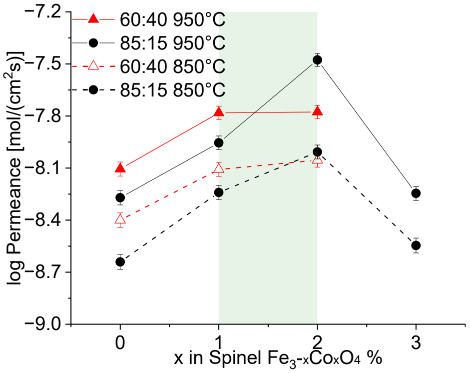

Figure 4.13 Dependency of the permeance on the cobalt amount in the composites with 60:40 and 85:15 ratios at T = 850 °C and 950 °C

At low nominal spinel fractions, i.e., 15 wt.%, the Fe/Co-ratio in the spinel phase plays a significant role in determining its electronic conductivity. Still pure iron oxide shows poor performance. Pure cobalt oxide on the other hand is below the percolation threshold and, thus, does not provide sufficient electronic pathways. An enhanced permeance can be achieved in ceria-based composites by both improving electronic conductivity of the second phase as well as optimization of the microstructure, i.e., phase distribution, in order to provide sufficient electronic pathways. The best composite in this study was nominally composed of 85 wt.% CGO and 15 wt.% FC2O.

Table 4.4 Comparison of the measured oxygen flux with the oxygen flux of the ceria-based dual-phase membranes reported in the literature.

Membrane Material	Weight Ratio	j_{O_2} (mL/min/cm^2)	T, (°C)	Thickness (mm)	Atmosphere	Synthesis	Coating	Ref.
$Ce_{0.8}Gd_{0.2}O_{2d}$–$FeCo_2O_4$	85:15	0.16	850	1	Air/Ar	one-pot	+	[24]
$Ce_{0.8}Gd_{0.2}O_{2d}$–$CoFe_2O_4$	60:40	0.1	850	1	Air/He	SSRS	+	[15]
$Ce_{0.9}Gd_{0.1}O_{2d}$–Fe_2O_3	60:40	0.06	900	0.5	Air/He	Pechini		[52]
$Ce_{0.8}Gd_{0.2}O_{2d}$–$CoFe_2O_4$	75:25	0.28	1000	1	Air/He	Pechini		[53]
$Ce_{0.8}Gd_{0.2}O_{2d}$–$FeCo_2O_4$	85:15	0.11	850	1	Air/Ar	SSRS	+	[35]
$Ce_{0.8}Gd_{0.2}O_{2d}$–Fe_2CoO_4	80:20	0.08	850	1	Air/Ar	SSRS	+	This work
$Ce_{0.8}Gd_{0.2}O_{2d}$–Fe_2CoO_4	80:20	0.16	1000	1	Air/Ar	SSRS	+	This work
$Ce_{0.8}Gd_{0.2}O_{2d}$–$FeCo_2O_4$	80:20	0.11	850	1	Air/Ar	SSRS	+	This work
$Ce_{0.8}Gd_{0.2}O_{2d}$–$FeCo_2O_4$	80:20	0.20	1000	1	Air/Ar	SSRS	+	This work

Direct comparison of published permeation data is in general difficult due to non-standardized sample geometry as well as measuring conditions. Nevertheless, the permeation rates of CGO-FCO composites investigated here are comparable to the literature data of other ceria-based membranes as shown in Table 4.4. This is expected because the permeation typically is limited by the ionic diffusion in the ceria phase in particular if percolation of both phases is guaranteed, e.g., commonly used 60:40 wt.%. The actual electronic conductivity of the second phase is of minor importance as long as it remains significantly higher compared to the ionic one. Therefore, increasing the amount of ceria is a straightforward strategy for enhancing permeation rates provided that sufficient electronic conduction is maintained. Thus, close to the percolation limit the microstructure as well as the actual electronic conductivity of the second phase becomes increasingly important.

4.4. Conclusions

MIEC composites based on commercially available $Ce_{0.8}Gd_{0.2}O_{2-\delta}$ powder in combination with spinel $Fe_{3-x}Co_xO_4$ (x = 0, 1, and 3) can be successfully synthesized using a cost-efficient solid state reactive sintering (SSRS) technique. During the sintering process, several phase interactions occur in CGO-FO (x = 0) and CGO-F2CO (x = 1) composites resulting in a mixture of three phases. For the cobalt-free composite, the CGO, FO, and the $Gd_3Fe_5O_{12}$ garnet structure have been indicated, while in CGO-F2CO fluorite CGO, Fe-rich spinel, and a $GdFeO_3$-based perovskite were detected. For x = 2 the spinel appears in two coexisting phases, which agrees with the phase diagram, while for x = 1 only one iron-rich spinel is indicated. In contrast, the composite CGO-CO (x = 3) has only two phases, CGO and Co_3O_4, and does not form a perovskite phase. In addition, it is difficult to produce crack-free samples of this composite. As a result, these iron-free and cobalt-free composites cannot be utilized as MIEC materials for use in an oxygen separation membrane.

A sufficient percolating network of ionic and electronic conducting phases in the investigated dual- (multi-)phase materials could only be achieved using both types of cations, iron and cobalt, fostering tertiary phase formation in the composite. This tertiary phase improved percolation and, accordingly, final permeance of material. Furthermore, the spinels Fe_2CoO_4 (x = 1) and $FeCo_2O_4$ (x = 2), made from Fe_3O_4 and Co_3O_4 in Fe/Co-proportions 2:1 and 1:2 respectively, provided adequate conductivity as a single phase. Consequently, the materials with $FeCo_2O_4$ (x = 2) and Fe_2CoO_4 (x = 1) remain the most attractive dual-phase materials for use as OTM. In the absence of one of the cations (iron or cobalt), a significant drop in oxygen permeance as well as limited stability is observed. The maximum oxygen flux is j_{O2} = 0.16 and 0.11 mL/cm^2*s at 1000 °C and 850 °C, respectively, of the CGO-FC2O composite, which is comparable oxygen permeation flux reported previously. The main challenge in the development of dual-phase materials remains in maximizing the amount of the ionic conducting phase without losing the percolation of the electronic conducting phase. Thus, the spinel system $Fe_{3-x}Co_xO_4$ ($1 < x < 2$) presents a particularly high potential for high- and intermediate-temperature applications in the MIEC materials, ensuring adequate thermal stability and microstructural as well as transport properties. However, while the mechanical properties in air in particular for the CGO-FC2O composite are thoroughly studied [16,25,43], application-oriented testing, e.g. of chemical expansion, for targeted operation conditions is required.

References

1. Sunarso, J.; Baumann, S.; Serra, J.M.; Meulenberg, W.A.; Liu, S.; Lin, Y.S.; Diniz da Costa, J.C. Mixed ionic–electronic conducting (MIEC) ceramic-based membranes for oxygen separation. *Journal of Membrane Science* **2008**, *320*, 13–41.
2. Kiebach, R.; Pirou, S.; Martinez Aguilera, L.; Haugen, A.B.; Kaiser, A.; Hendriksen, P.V.; Balaguer, M.; García-Fayos, J.; Serra, J.M.; Schulze-Küppers, F.*; et al.* A review on dual-phase oxygen transport membranes: from fundamentals to commercial deployment. *J. Mater. Chem. A* **2022**, *10*, 2152–2195.
3. Garcia-Fayos, J.; Balaguer, M.; Baumann, S.; Serra, J.M. Dual-phase membrane based on $LaCo_{0.2}Ni_{0.4}Fe_{0.4}O_{3-x}$-$Ce_{0.8}Gd_{0.2}O_{2-\delta}$ composition for oxygen permeation under CO_2/SO_2-rich gas environments. *Journal of Membrane Science* **2018**, *548*, 117–124.
4. Takamura, H.; Okumura, K.; Koshino, Y.; Kamegawa, A.; Okada, M. Oxygen Permeation Properties of Ceria-Ferrite-Based Composites. *J Electroceram* **2004**, *13*, 613–618.
5. Balaguer, M.; García-Fayos, J.; Solís, C.; Serra, J.M. Fast Oxygen Separation Through SO_2- and CO_2-Stable Dual-Phase Membrane Based on $NiFe_2O_4$ –$Ce_{0.8}Tb_{0.2}O_{2-\delta}$. *Chem. Mater.* **2013**, *25*, 4986–4993.
6. Czyperek, M.; Zapp, P.; Bouwmeester, H.; Modigell, M.; Peinemann, K.-V.; Voigt, I.; Meulenberg, W.A.; Singheiser, L.; Stöver, D. MEM-BRAIN gas separation membranes for zero-emission fossil power plants. *Energy Procedia* **2009**, *1*, 303–310.
7. Wang, S.; Shi, L.; Xie, Z.; He, Y.; Yan, D.; Li, M.-R.; Caro, J.; Luo, H. High-flux dual-phase percolation membrane for oxygen separation. *Journal of the European Ceramic Society* **2019**, *39*, 4882–4890.
8. Fischer, L.; Neuhaus, K.; Schmidt, C.; Ran, K.; Behr, P.; Baumann, S.; Mayer, J.; Meulenberg, W.A. Phase formation and performance of solid state reactive sintered $Ce_{0.8}Gd_{0.2}O_{2-\delta}$-$FeCo_2O_4$ composites. *J. Mater. Chem. A* **2022**, *10*, 2412–2420.
9. Ramasamy, M.; Baumann, S.; Opitz, A.; Iskandar, R.; Mayer, J.; Udomsilp, D.; Breuer, U.; Bram, M. Phase Interaction and Distribution in Mixed Ionic Electronic Conducting Ceria-Spinel Composites. In *Advances in Solid Oxide Fuel Cells and Electronic Ceramics II*; Kusnezoff, M., Bansal, N.P., Shimamura, K., Fukushima, M., Gyekenyesi, A., Eds.: John Wiley & Sons, Inc: Hoboken, NJ, USA, 2017, pp. 99–112.
10. Bouwmeester, H.; Burggraaf, A.J. Chapter 10 Dense ceramic membranes for oxygen separation **1996**, *4*, 435–528.
11. Joo, J.H.; Park, G.S.; Yoo, C.-Y.; Yu, J.H. Contribution of the surface exchange kinetics to the oxygen transport properties in $Ce_{0.9}Gd_{0.1}O_{2-\delta}$ –$La_{0.6}Sr_{0.4}Co_{0.2}Fe_{0.8}O_{3-\delta}$ dual-phase membrane. *Solid State Ionics* **2013**, *253*, 64–69.

12. Chen, G.; Feldhoff, A.; Weidenkaff, A.; Li, C.; Liu, S.; Zhu, X.; Sunarso, J.; Huang, K.; Wu, X.-Y.; Ghoniem, A.F.*; et al.* Roadmap for Sustainable Mixed Ionic-Electronic Conducting Membranes. *Adv Funct Materials* **2022**, *32*.

13. Bai, W.; Feng, J.; Luo, C.; Zhang, P.; Wang, H.; Yang, Y.; Zhao, Y.; Fan, H. A comprehensive review on oxygen transport membranes: Development history, current status, and future directions. *International Journal of Hydrogen Energy* **2021**, *46*, 36257–36290.

14. Ramasamy, M.; Persoon, E.S.; Baumann, S.; Schroeder, M.; Schulze-Küppers, F.; Görtz, D.; Bhave, R.; Bram, M.; Meulenberg, W.A. Structural and chemical stability of high performance $Ce_{0.8}Gd_{0.2}O_{2-\delta}$-$FeCo_2O_4$ dual phase oxygen transport membranes. *Journal of Membrane Science* **2017**, *544*, 278–286.

15. Lin, Y.; Fang, S.; Su, D.; Brinkman, K.S.; Chen, F. Enhancing grain boundary ionic conductivity in mixed ionic-electronic conductors. *Nature communications* **2015**, *6*, 6824.

16. Zeng, F.; Malzbender, J.; Baumann, S.; Schulze-Küppers, F.; Krüger, M.; Nijmeijer, A.; Guillon, O.; Meulenberg, W.A. Micromechanical Characterization of $Ce_{0.8}Gd_{0.2}O_{2-\delta}$–$FeCo_2O_4$ Dual Phase Oxygen Transport Membranes. *Adv. Eng. Mater.* **2020**, *22*, 1901558.

17. Wang, S.; Shi, L.; Boubeche, M.; Wang, H.; Xie, Z.; Tan, W.; He, Y.; Yan, D.; Luo, H. The effect of Fe/Co ratio on the structure and oxygen permeability of Ca-containing composite membranes. *Inorg. Chem. Front.* **2019**, *6*, 2885–2893.

18. Tong, J.; Yang, W.; Cai, R.; Zhu, B.; Xiong, G.; Lin, L. Investigation on the structure stability and oxygen permeability of titanium-doped perovskite-type oxides of $BaTi_{0.2}Co_xFe_{0.8-x}O_{3-\delta}$ (x=0.2–0.6). *Separation and Purification Technology* **2003**, *32*, 289–299.

19. Shao, Z.; Xiong, G.; Dong, H.; Yang, W.; Lin, L. Synthesis, oxygen permeation study and membrane performance of a Ba0.5Sr0.5Co0.8Fe0.2O3−δ oxygen-permeable dense ceramic reactor for partial oxidation of methane to syngas. *Separation and Purification Technology* **2001**, *25*, 97–116.

20. Bahlawane, N.; Ngamou, P.H.T.; Vannier, V.; Kottke, T.; Heberle, J.; Kohse-Höinghaus, K. Tailoring the properties and the reactivity of the spinel cobalt oxide. *Physical chemistry chemical physics : PCCP* **2009**, *11*, 9224–9232.

21. Ramasamy, M. *Dual Phase Oxygen Transport Membrane for Efficient Oxyfuel Combustion*; Forschungszentrum Jülich GmbH, 2016.

22. Zhang, T. Iron oxide as an effective sintering aid and a grain boundary scavenger for ceria-based electrolytes. *Solid State Ionics* **2004**, *167*, 203–207.

23. Kiefer, T. *Entwicklung neuer Schutz- und Kontaktierungsschichten für Hochtemperatur-Brennstoffzellen*; Forschungszentrum, Zentralbibliothek: Jülich, 2008.

24. Ramasamy, M.; Baumann, S.; Palisaitis, J.; Schulze-Küppers, F.; Balaguer, M.; Kim, D.; Meulenberg, W.A.; Mayer, J.; Bhave, R.; Guillon, O.*; et al.* Influence of Microstructure and

Surface Activation of Dual-Phase Membrane $Ce_{0.8}Gd_{0.2}O_{2-δ}$-$FeCo_2O_4$ on Oxygen Permeation. *J. Am. Ceram. Soc.* **2016**, *99*, 349–355.

25. Zeng, F.; Malzbender, J.; Baumann, S.; Nijmeijer, A.; Winnubst, L.; Ziegner, M.; Guillon, O.; Schwaiger, R.; Meulenberg, W.A. Optimization of sintering conditions for improved microstructural and mechanical properties of dense $Ce_{0.8}Gd_{0.2}O_{2-δ}$-$FeCo_2O_4$oxygen transport membranes. *Journal of the European Ceramic Society* **2021**, *41*, 509–516.

26. Ferreira, T.; Waerenborgh, J.C.; Mendonça, M.; Nunes, M.R.; Costa, F.M. Structural and morphological characterization of $FeCo_2O_4$ and $CoFe_2O_4$ spinels prepared by a coprecipitation method. *Solid State Sciences* **2003**, *5*, 383–392.

27. Ji, Y.; Kilner, J.; Carolan, M. Electrical conductivity and oxygen transfer in gadolinia-doped ceria (CGO)–$Co_3O_{4-δ}$ composites. *Journal of the European Ceramic Society* **2004**, *24*, 3613–3616.

28. Lewis, G. Effect of Co addition on the lattice parameter, electrical conductivity and sintering of gadolinia-doped ceria. *Solid State Ionics* **2002**, *152-153*, 567–573.

29. Zhang, T.; Hing, P.; Huang, H.; KILNER, J. Densification, microstructure and grain growth in the CeO2–Fe2O3 system (0⩽Fe/Ce⩽20%). *Journal of the European Ceramic Society* **2001**, *21*, 2221–2228.

30. Zheng, Y.; Zhou, M.; Ge, L.; Li, S.; Chen, H.; Guo, L. Effect of Fe2O3 on Sm-doped ceria system solid electrolyte for IT-SOFCs. *Journal of Alloys and Compounds* **2011**, *509*, 546–550.

31. Buchheit, A.; Teßmer, B.; Ran, K.; Mayer, J.; Wiemhöfer, H.-D.; Neuhaus, K. The Impact of Fe Addition on the Electronic Conductivity of Gadolinium Doped Ceria. *ECS J. Solid State Sci. Technol.* **2019**, *8*, P41-P50.

32. Matovic, B.; Dohcevic-Mitrovic, Z.; Radovic, M.; Brankovic, Z.; Brankovic, G.; Boskovic, S.; Popovic, Z.V. Synthesis and characterization of ceria based nanometric powders. *Journal of Power Sources* **2009**, *193*, 146–149.

33. Neuhaus, K.; Dolle, R.; Wiemhöfer, H.-D. The Effect of Transition Metal Oxide Addition on the Conductivity of Commercially Available Gd-Doped Ceria. *J. Electrochem. Soc.* **2020**, *167*, 44507.

34. Zhang, T. Preparation and mechanical properties of dense Ce0.8Gd0.2O2−δ ceramics. *Solid State Ionics* **2004**, *167*, 191–196.

35. Zeng, F.; Baumann, S.; Malzbender, J.; Nijmeijer, A.; Winnubst, L.; Guillon, O.; Schwaiger, R.; Meulenberg, W.A. Enhancing oxygen permeation of solid-state reactive sintered $Ce_{0.8}Gd_{0.2}O_2$-$FeCo_2O_4$ composite by optimizing the powder preparation method. *Journal of Membrane Science* **2021**, *628*, 119248.

36. Ge, M.; Huang, X.; Yan, H.; Gursoy, D.; Meng, Y.; Zhang, J.; Ghose, S.; Chiu, W.K.S.; Brinkman, K.S.; Chu, Y.S. Three-dimensional imaging of grain boundaries via quantitative fluorescence X-ray tomography analysis. *Commun Mater* **2022**, *3*.

37. Kovács, A.; Schierholz, R.; Tillmann, K. FEI Titan G2 80-200 CREWLEY. *JLSRF* **2016**, *2*.

38. Hansson, A.N.; Linderoth, S.; Mogensen, M.; Somers, M.A. X-ray diffraction investigation of phase stability in the Co–Cr–O and the Fe–Co–Cr–O systems in air at 1323K. *Journal of Alloys and Compounds* **2005**, *402*, 194–200.

39. Smith, P.A.; Spencer, C.D.; Stillwell, R.P. Co57 and Fe57 mössbauer studies of the spinels FeCo2O4 and Fe0.5Co2.5O4. *Journal of Physics and Chemistry of Solids* **1978**, *39*, 107–111.

40. Raval, Anand, Panchal, Nital, Jotania Rajshree. Structural properties and mictostructure of cobalt ferrite particles synthesized by a sol-gel autocombustion method. *Int. J. Mod. Phys. Conf. Ser.* **2013**, *22*, 558–563.

41. Fritsch, D.; Ederer, C. Epitaxial strain effects in the spinel ferrites CoFe2O4 and NiFe2O4 from first principles. *Phys. Rev. B* **2010**, *82*, 137.

42. Zhao, Q.; Yan, Z.; Chen, C.; Chen, J. Spinels: Controlled Preparation, Oxygen Reduction/Evolution Reaction Application, and Beyond. *Chemical reviews* **2017**, *117*, 10121–10211.

43. Zeng, F.; Malzbender, J.; Baumann, S.; Zhou, W.; Ziegner, M.; Nijmeijer, A.; Guillon, O.; Schwaiger, R.; Albert Meulenberg, W. Mechanical reliability of $Ce_{0.8}Gd_{0.2}O_{2-\delta}$ -FeCo $_2O_4$ dual phase membranes synthesized by one-step solid-state reaction. *J. Am. Ceram. Soc.* **2021**, *104*, 1814–1830.

44. Buscaglia, V. Growth of ternary oxides in the Gd2O3–Fe2O3 system. A diffusion couple study. *Solid State Ionics* **2002**, *146*, 257–271.

45. Kharton, V.V.; Shaula, A.L.; Naumovich, E.N.; Vyshatko, N.P.; Marozau, I.P.; Viskup, A.P.; Marques, F.M.B. Ionic Transport in $Gd_3Fe_5O_{12}$- and $Y_3Fe_5O_{12}$-Based Garnets. *J. Electrochem. Soc.* **2003**, *150*, J33.

46. Shaula, A.L.; Kharton, V.V.; Marques, F. Mixed conductivity of garnet phases based on gadolinium ferrite. *Journal of the European Ceramic Society* **2004**, *24*, 1309–1312.

47. Hou, Y.H.; Zhao, Y.J.; Liu, Z.W.; Yu, H.Y.; Zhong, X.C.; Qiu, W.Q.; Zeng, D.C.; Wen, L.S. Structural, electronic and magnetic properties of partially inverse spinel CoFe 2 O 4 : a first-principles study. *J Mater Sci* **2010**, *43*, 445003.

48. Kharton, V.V.; Kovalevsky, A.V.; Viskup, A.P.; Figueiredo, F.M.; Yaremchenko, A.A.; Naumovich, E.N.; Marques, F.M.B. Oxygen Permeability of $Ce_{0.8}Gd_{0.2}O_{2-\delta}$ $La_{0.7}Sr_{0.3}MnO_{3-\delta}$ Composite Membranes. *J. Electrochem. Soc.* **2000**, *147*, 2814.

49. Hong, S.J.; Virkar, A.V. Lattice Parameters and Densities of Rare-Earth Oxide Doped Ceria Electrolytes. *J. Am. Ceram. Soc.* **1995**, *78*, 433–439.

50. Koettgen, J.; Martin, M. The ionic conductivity of Sm-doped ceria. *J. Am. Ceram. Soc.* **2020**, *103*, 3776–3787.

51. Schneider, C.A.; Rasband, W.S.; Eliceiri, K.W. NIH Image to ImageJ: 25 years of image analysis. *Nature methods* **2012**, *9*, 671–675.

52. Luo, H.; Jiang, H.; Efimov, K.; Liang, F.; Wang, H.; Caro, J. CO_2 -Tolerant Oxygen-Permeable Fe_2O_3 -$Ce_{0.9}Gd_{0.1}O_{2-\delta}$ Dual Phase Membranes. *Ind. Eng. Chem. Res.* **2011**, *50*, 13508–13517.

53. Takamura, H.; Kawai, M.; Okumura, K.; Kamegawa, A.; Okada, M. Preparation and Oxygen Permeability of Gd-Doped Ceria and Spinel-Type Ferrite Composites. *MRS Proc.* **2002**, *756*.

Chapter 5

---

5. Lanthanide element variation in rare earth doped ceria – $FeCo_2O_4$ dual phase oxygen transport membranes

Abstract

The increased interest in dual-phase membrane materials for oxygen separation leads to the continuous optimization of their composition. Rare-earth doped ceria is a promising candidate as the ion-conducting phase in the membrane. Spinel-structured $FeCo_2O_4$ was investigated as an electronic conducting phase forming an additional electronic conducting perovskite-structured phase during sintering when combined with $Ce_{1-x}Ln_xO_{2-\delta}$. The influence of rare-earth lanthanide elements, i.e., Gd and Sm, as well as their concentration, i.e., x=0.1 and 0.2, on the final phase composition and microstructure as well as its related functional properties in particular oxygen permeation is analysed. 20 mol.% doping of either Gd or Sm reveals a multi-phase microstructure after sintering. Moreover, segregation of Gd/Sm, iron, and cobalt is found at the ceria-ceria grain boundaries in $Ce_{0.8}Sm_{0.2}O_{2-\delta}$- and $Ce_{0.9}Gd_{0.1}O_{2-\delta}$-based composites. In contrast, 10 mol.% Gd–doping leads to a dual-phase membrane material without the formation of any other phase. In all cases, the percolation threshold is reached at approx. 20 vol.% of the electron-conducting phase in the system leading to similar maximum permeation rates determined by the ionic conductivity of the ceria phase.

This Chapter has been published as: Fischer, L.; Ran, K.; Schmidt, C.; Neuhaus, K.; Baumann, S.; Behr, P.; Mayer, J.; Bouwmeester, H.J.M.; Nijmeijer, A.; Guillon, O. Meulenberg, W.A.*; et al.* 5. Lanthanide element variation in rare earth doped ceria – FeCo2O4 dual phase oxygen transport membranes. *Open Ceramics* **2023**, DOI: https://doi.org/10.1016/j.oceram.2023.100519

5.1 Introduction

Oxygen is an important gas for various technical applications such as combustion processes, partial oxidations in the chemical industry, or medical applications. Although oxygen is freely available in the air, its separation is a complex and energy-consuming process. Due to lower energy demand, ceramic membranes offer a good alternative to other known gas separation methods, such as cryogenic distillation, reducing operation costs and energy consumption [1–4]. These ceramic membranes consist of mixed ionic–electronic conducting (MIEC) oxides [5–7]. At high temperatures (typically 850-950°C), these MIECs show high oxygen permeation involving both oxygen ionic conductivity and electronic conductivity.

There are several known Oxygen transport membrane (OTM) materials with high oxygen flux, e.g., $Ba_{0.5}Sr_{0.5}Co_{0.8}Fe_{0.2}O_{3-\delta}$ and $La_{0.6}Sr_{0.4}Co_{0.2}Fe_{0.8}O_{3-\delta}$, [8–11]. However, these single-phase materials suffer from limited mechanical and chemical stability, especially under acidic (e.g. CO_2, SO_x) or reducing (e.g. H_2, CO) conditions, which makes them low performing in numerous industrial applications [12–17]. Therefore, dual-phase material systems, utilizing two inherently stable ionic- and electronic-conducting phases, have again attracted attention from the scientific community [1,5,6]. Nowadays, dual- and multiphase membranes with separate ionic and electronic conductors are among the most promising materials regarding stability for the application in membrane reactors [18].

The dual-phase $Ce_{0.8}Gd_{0.2}O_{2-\delta}$ –$FeCo_2O_4$ (CGO20-FCO) composite has been previously investigated in the context of the microstructure design and structural properties, mechanical properties as well as permeation performance and showed to be a good candidate for application in a membrane reactor at intermediate temperatures (<800°C) [19,20]. It was estimated that during the phase interaction, approximately 10 mol. % of gadolinium remains in the ion-conductive fluorite phase [21,22] the remainder is used for perovskite phase formation, which is an additional electron conductor. The ionic conductivity is still the limiting factor in this material, thus the investigated doping content of the rare earth-lanthanide element in t*he fluorite system* $Ce_{1-x}Ln_xO_{2-\delta}$ can be narrowed to a range of 10-20 mol.%, where the fluorite structure is stable [23,24]. Within the family of Ln-doped ceria, Gd- and Sm-doped systems are the most efficient, so the these doped ceria are the most prominent candidates due to their good chemical stability [25–29] and excellent ionic conductivities (~0.075-0.1 S·cm^{-1}) [30–35].

According to the literature, the ionic conductivities of 10 mol.% Gd-doped ceria (CGO10) or 20 mol% Sm-doped ceria (CSO20) are higher than the previously investigated CGO20 and, thus, are good candidates as ceria-FCO composites [36]. Comparison of the modelled conductivity of the rare-earth doped ceria at 500 °C reveals that the Sm-doped material has the highest ionic conductivity at approximately 10 mol.% of samarium [37]. In those calculations, apart from the acceptor dopant concentration also the interaction between dopant cations and mobile oxygen vacancies is taken into account [35,37]. Koettgen *et al.* [37] performed Kinetic Monte Carlo simulations (KMC) at 400°C, suggesting that 10 mol% Gd-doped ceria has a higher ionic conductivity compared to 20 mol.% Gd-doped ceria. This is assigned to a larger oxygen ion mobility in the CGO10 material, whereas the high ionic conductivity in CGO20 is reached due to the higher concentration of oxygen vacancies [38–40].

The computed ionic conductivity of neodymium and samarium doped ceria is even higher compared to the gadolinium doped ceria at 400 °C [35]. Neodymium on the other hand is regarded as critical within RE-elements mainly due to its importance in permanent magnets [41]. Therefore, it is not considered in this study.

The experimental data at 600°C shows that both, gadolinium and samarium doping, leads to a plateau in the total ionic conductivity between approximately 10-20 mol.% dopant, as discussed by Koettgen *et al.* [37]. That makes both dopants really attractive for the ceria materials. Moreover, the resulting permeation performance of a dual- or multi-phase composite membrane is not only dependent on the individual conductivities of the single phases, but bulk and grain boundary contributions to the conductivity could also be affected by e.g., phase interactions.

The grain boundaries in the doped-ceria ceramics can be highly resistive and serve as a barrier to oxygen ion transport across them. Avila Paredes *et al.* [42] reported that the activation energy E_a of the grain boundary conductivity decreases with decreasing dopant concentration in the fluorite. As a summary, the higher lattice conductivity and lower grain boundary resistance makes CGO10 more appropriate for application at intermediate temperatures [43]. Moreover 10 mol. % doped ceria shows better stability in reducing atmospheres compared to CGO20 [29,44].

Therefore, in this study we investigate the phase interactions of CGO10 and CSO20 with $FeCo_2O_4$ in comparison to formerly reported CGO20 [19]. Composite membranes were synthesized by solid state reactive sintering in varying weight ratios. The resulting phase composition and microstructure as well as functional properties are analysed and its relationships are discussed.

5.2 Experimental

5.2.1 Samples fabrication

Commercially available $Ce_{0.9}Gd_{0.1}O_{2-\delta}$ (CGO10) (Solvay), $Ce_{0.8}Sm_{0.2}O_{2-\delta}$ (CSO20) (Kceracell,), Fe_2O_3 (FO) (Merck, 99 %) and Co_3O_4 (CO) (Merck, 99 %) powders were synthesized by Solid-State Reactive Sintering method (SSRS). Respective amounts of powders were weighted for nominal CGO10-FCO and CSO20-FCO compositions with wt. % -ratios 60:40, 70:30, 80:20, 85:15, and 90:10. During 48 h the powder mixtures were ball-milled on a roller bench with a speed of 175 rpm. After drying in ambient air at 70° C for 48 h powder mixtures were pressed with a uniaxial press in disc-shaped membranes with d=20 mm and sintered at 1200°C for 5 h in air with the heating rate 5 K min^{-1}. At sintering temperature, the spinel partially reduces into a high-temperature monoxide phase with a rock salt structure. To ensure complete reoxidation of the high-temperature Co/Fe-monoxide phase to the spinel phase stable at operating temperatures according to the $Fe_{3-x}Co_xO_4$ phase diagram a slow rate of 0.5 K min^{-1} between 900 and 800°C is implemented in the cooling cycle. The membranes are considered to be sufficiently dense to exclude leakage since the leaked oxygen flux calculated from the nitrogen leak rate is low. After the sintering step, all samples were ground down to 1 mm-thick discs in 2 steps applying SiC merge papers with different grits from P 800 to P 1200 (by WS FLEX 18C). On both sides of the discs a porous $La_{0.58}Sr_{0.4}Co_{0.2}Fe_{0.8}O_{3-\delta}$ (LSCF) catalytic activation layer with a thickness of ~5 µm was applied via a screen-printing technique and the final membrane was calcined in an oven at 1100°C for 5 hours.

5.2.2 Characterization methods

Crystal structure

The X-ray diffraction (XRD) diffractometer D4 ENDEAVOR (Bruker, Germany) is exploited for crystal structure determination. The diffraction angle 2θ is in the range from 10° to 80°, with increments of 0.02° 2θ and 0.75 seconds of measurement time per step. Measured data is analysed with the help of the program package X'Pert HighScore (PANalytical B.V., version 3.0.5) software. Crystal structure analysis and associated phase quantifications were carried out by Rietveld refinement using the software Profex (Version 4.2.2). The errors of each fit are calculated individually and given in Table 5.1 and Table 5.2 and Table 5.3.

Microscopy

To obtain material morphology Scanning Electron Microscopy (SEM) and Energy Dispersive X-ray Spectroscopy (EDXS) were used. SEM images were taken with a Zeiss Ultra 55 and a Zeiss Supra 50 VP1 (Carl Zeiss NTS GmbH, German) SEM at different magnifications. The electronic conductivity of the samples was enhanced by sputter deposition of a thin platinum layer prior to the SEM measurement.

Further image analysis-based method was conducted via ImageJ software on all composite samples including ~1000 grains utilizing so-called isodata threshold method [45], which helped to estimate the average grain size of all phases as well as area fraction of pores. However, the limited number of characterized grains/pores might induce large inaccuracy in the grain size and pore size calculations.

The Transmission Electron Microscopy (TEM) characterization was also performed on both investigated materials. All specimens were cut from sintered composite pellets by Focused Ion Beam (FIB) milling using an FEI Strata 400 system with a gallium ion beam. Further thinning and cleaning was done by using an argon ion beam in a Fischione Nanomill 1040 at beam energies of 900 eV and 500 eV. TEM and energy-filtered TEM (EFTEM) imaging was performed using an FEI Tecnai F20 at 200 kV. The FEI Titan G2 80-200 ChemiSTEM microscope equipped with an XFEG and a probe Cs corrector was used in order to obtain high-resolution high-angle annular dark-field (HAADF) images and EDXS chemical mapping [46].

Electrical conductivity

The total conductivity of the single-phase fluorite samples was determined by analysing the temperature-dependent impedance spectra with the help of a Novotherm HT 1200 frequency analyzer. All samples were coated with a Pt resinate paste (RP 070107, Heraeus GmbH, Germany) and on both sides of the sample Pt sheet contacts were attached and measured in air. For all measurements an AC voltage peak-to-peak amplitude of 40 mV was applied. As the electronic conductivity of both spinels was very high, no division into separate contributions from the grain bulk and grain boundary was visible. Nyquist plots instead only showed a straight line (ohmic contribution from electron conducting phase).

Oxygen permeation measurements

All composite materials were subjected to oxygen permeation experiments. The experimental setup consisted of vertical quartz glass housing, where the membrane pellets were sealed with two gold rings with an inner diameter of 13 mm. The separation of the oxygen from ambient air fed with 250 ml_N min^{-1} was performed in a temperature range between 650°C and 1000°C. As a sweep gas argon was used with 50 ml_N min^{-1} flow rate using mass flow controllers (Bronkhorst, Germany). The mass spectrometer (Omnistar, Pfeiffer Vacuum GmbH, Germany) detected concentrations of oxygen and nitrogen in the permeate gas, i.e., oxygen enriched argon. With help of measured nitrogen concentration, air leakage through either membrane or the sealing was calculated according to

$$j_{O_2} = F_{Ar}\left(\frac{X_{O_2} - \frac{1}{4}X_{N_2}}{1 - X_{O_2} - X_{N_2}}\right)\frac{1}{A_{mem}} \qquad \textbf{Equation 5.1}$$

Here F_{Ar} is the argon flow rate, *i.e.,* 50 ml_N min^{-1}, X_{O2} and X_{N2} the oxygen and nitrogen concentration in the permeate gas, respectively, and open membrane area is A_{mem}=1.33 mm^2. The factor $\frac{1}{4}$ reflects the O_2/N_2 ratio in the air feed assuming that the leak is not gas selective.

Since the oxygen partial pressure in the permeate gas is temperature dependent, the driving force of the permeation rate is not constant during the measurement. Additionally, the sample thickness deviation after the grinding process was ±8 % from the target thickness of 1 mm. Consequently, the driving force normalized permeation rate, also referred to as permeance, was normalized to the reference thickness of L_0 = 1 mm and was calculated assuming Wagner behaviour using the following equation.

$$Permeance = \frac{j_{O_2}}{ln\frac{p'_{O_2}}{p''_{O_2}}}\frac{L_{mem}}{L_0} \qquad \textbf{Equation 5.2}$$

Here, p'_{O_2} and p''_{O_2} are the oxygen partial pressures in the retentate and permeate gas, respectively, and L_{mem} is the actual membrane thickness. The overall experimental error is assumed to be ±10 %, which is well accepted in the literature.

5.3 Results and discussion

5.3.1 Microstructure evolution

CSO20-FCO composite

Compositional and structural characterization is carried out for pellets with nominal composition of (100-x) wt.% $Ce_{0.8}Sm_{0.2}O_{1.9}$ (CSO20) and x wt.% $FeCo_2O_4$ (FCO), where 10 ≤ x ≤ 40. X-ray diffraction confirmed that during the sintering process, several phase interactions take place resulting in the mixture of three structures: CSO with a cubic fluorite structure, $Fe_{3-x}Co_xO_4$ with a cubic spinel structure, and $SmFeO_3$ with an orthorhombic perovskite structure as shown in Figure 5.1.

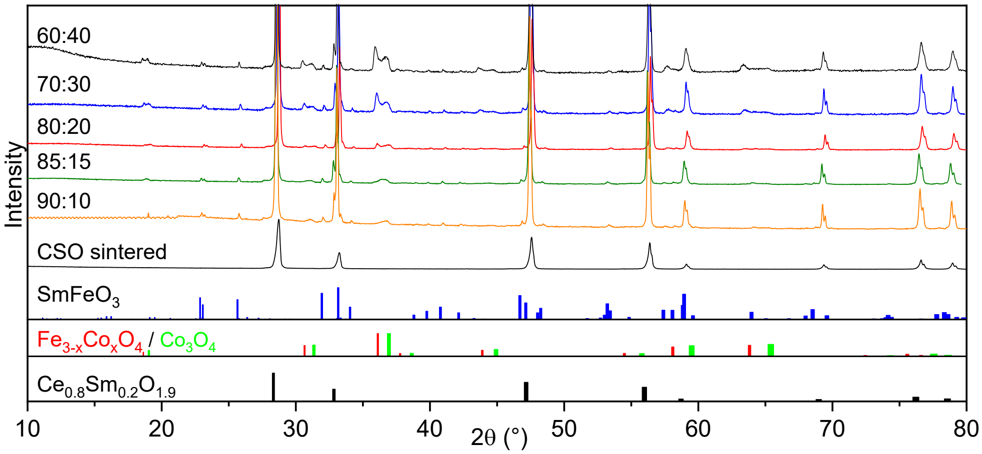

Figure 5.1 XRD pattern of CSO20-FCO composites and CSO20 single phase sintered at 1200°C for 5 h as well as three main defined phases

The intensities of the spinel reflections are increasing with the increase of the nominal FCO amount in the composite. This is an identical result compared to the 20 mol.% Gd-doped ceria (CGO20) composite, where the formation of the tertiary perovskite phase was also reported [19]. However, there are reports for the CSO20-based composite addressing to the third phase formation, depending on the type of added spinel and preparation methods [47,48]. Similarly to the CGO20-based composites and with respect to the Fe-Co oxide phase diagram: there are two spinel phases in equilibrium, i.e., iron-rich (inverse spinel) and cobalt-rich (normal spinel) [49]. Both are present in all CSO20-based composites, except for the 90:10 ratio, where only the normal spinel phase (Co_3O_4) is observed. Probably, most of the iron is consumed by the perovskite formation, so that the remaining Fe/Co-ratio decreases and only normal spinel forms accordingly.

Table 5.1 Lattice parameter and fraction (F) of the phases after quantification by Rietveld refinement analyses of the CSO20-FCO composites and single CSO phase sintered at 1200°C for 5 h

	CSO *Fd3m*		**FCO** *Fd3m*		**Co_3O_4** *Fd3m*		**CSFCO** *Pnma*			
FCO, wt.%	F, wt.%	a=b=c, Å	F wt.%	a=b=c, Å	F, wt.%	a=b=c, Å	F, wt.%	Lattice parameter, Å		
								a	b	c
0	100	5.4314[4]	-	-	-	-	-	-	-	-
10	80.24[3]	5.426[6]	0	#	10.95[6]	8.152[2]	8.81[7]	5.381[3]	5.597 [6]	7.691[4]
15	76.94[1]	5.425[4]	0.65[7]	8.312[4]	15.30[1]	8.174[3]	7.15[3]	5.385[4]	5.601[3]	7.696[6]
20	71.70[4]	5.425[7]	5.81[1]	8.312[5]	16.22[7]	8.156[1]	6.27[2]	5.385[4]	5.60 [1]	7.697[8]
30	63.46[9]	5.424 [5]	8.31[4]	8.312[2]	22.70[2]	8.182[5]	5.52[4]	5.383[7]	5.601[3]	7.698[1]
40	51.57[8]	5.421[9]	16.96[6]	8.298[8]	25.90[4]	8.149[1]	5.55[4]	5.378 [6]	5.598[8]	7.691[6]

Subsequent Rietveld refinement quantified the composition of CSO20-based composites, listed in Table 5.1. The lattice parameter of the CSO20 phase measured before phase interaction is a=5.4314 Å and decreases with increasing addition of FCO, as for CGO20-based composite [19]. Since the solubility of iron and cobalt in ceria is very limited (approx. 1-2 %) [50–53] this decrease in the lattice constant is accounted to the extraction of Sm from the ceria lattice forming the tertiary $SmFeO_3$-based perovskite phase during sintering (where Sm takes the A sites in the formed ABO_3 phase structure, while for the B sites iron cations are more favourable). In analogy to the CGO20 composite Ce and Co are partly occupying the A- and B-site, respectively, resulting in the formula $(SmCe)(FeCo)O_3$ (SCFCO).

The composition of individual phases is estimated via empirical models similarly to the analysis performed on the CGO20-FC2O composite, described in [19]. About 10 mol. % of Sm forms the tertiary phase during the sintering process, resulting in the residual 10 mol. % of Sm in CSO phase, what is similar to the CGO20-based composite.

SEM analysis shows the homogeneous distribution of these phases (Figure 5.2a). Three phases can be distinguished in different grey scale due to the material contrast (different average atom number) detecting back scattered electrons, Figure 5.2b. The image analysis, conducted on all CSO20-based samples including more than 1000 grains, revealed a mean grain size in the range of 0.5-0.85 μm.

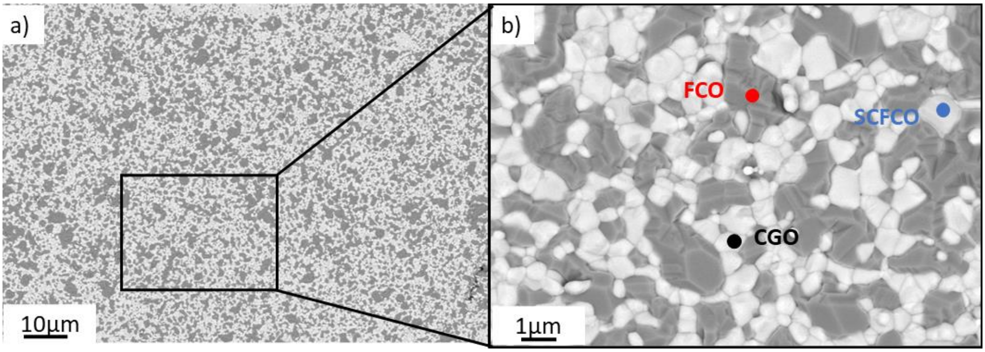

Figure 5.2 SEM image of the surface of 60CSO20-FCO sample sintered at 1200°C for 5 h with marked fluorite (light), spinel (black) grains, and perovskite (grey)

Further TEM analysis accompanied by energy-filtered (EFTEM) elemental mapping confirmed fluorite, spinel, and perovskite phases in all CSO20-FCO samples. The distribution of the three phases in the composite 60CSO20-FCO reveal a presence of perovskite grains. According to the EFTEM elemental mapping, the iron and cobalt show a non-uniform distribution in the FCO phase hence it can be subdivided into two spinel types: normal cobalt-rich and an inverse iron-rich spinel. This agrees well with the XRD analyses the phase diagram predicting two coexisting spinel phases.

The presence of the aforementioned three phases gives a feasibility to observe six interfaces, which might contribute to different types of transport within the composite material. The spinel and perovskite grains form a connected chain, which is responsible for the e-transport, while CGO grains enable ionic transport. The analysis of the interfaces by HAADF imaging is shown in Figure 5.3 for the 60CSO20-FCO composite. Most of the grain boundaries are clean without any visible defects or precipitations. Generally, defects and disordered features along the interfaces are not desired and quite unfavourable for any membrane materials, since they could strongly affect both types of conductivities. Thus, there are no barriers that significantly hinder or facilitate the transport of the oxygen ions or electrons/holes either via or across the grain boundaries. Figure 5.3c shows further EDX mapping in atomic scale, confirming that our results are fitting the best with the $SmFeO_3$-based perovskite, which indeed contains cerium and cobalt at the A- and B-site, respectively. The oxygen atoms are placed between the cation columns and are not visible by HAADF imaging, due to much smaller atomic number than cerium and samarium.

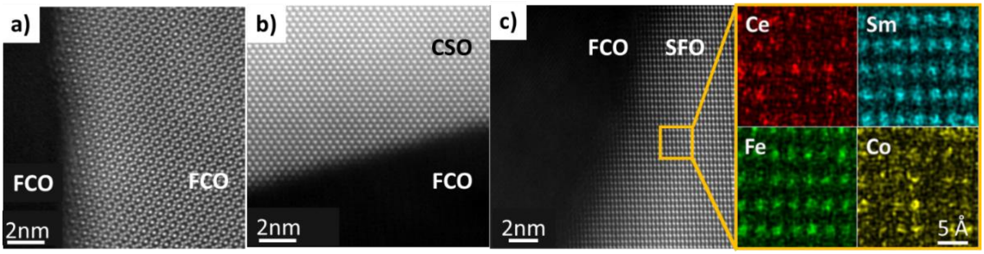

Figure 5.3 HAADF image of grain boundaries between phases in the 60CSO20-FCO system (a) FCO- FCO; (b) CSO-FCO; (c) FCO-SFO inclusive the EDX chemical mapping of perovskite grain along [010]

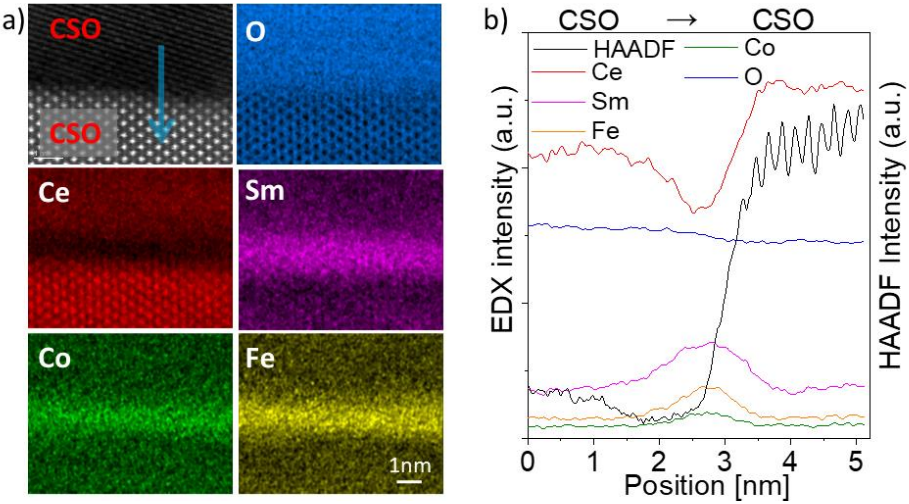

Figure 5.4 EDXS analysis of a ceria-ceria grain boundary in 60CSO20-FCO a) The simultaneously acquired HAADF image and EDXS chemical mapping from Ce L, Sm L, Fe K, Co K, and O K peak. b) Line scans between two fluorite grains marked as CSO grains based on the elemental maps

A closer look was taken to the ceria-ceria interface, Figure 5.4, at which often element segregation occurs [20]. Line scans along the blue arrow are plotted in Figure 5.4b A clear enrichment of samarium, iron and cobalt and a significant loss of cerium along the CSO-CSO grain boundary is visible. This has been already previously reported in similar CGO20-based membranes, where the $GdFeO_3$-phase is predominately surrounded by ceria grains [54]. Therefore, these segregations might be an early stage of the formation of an emerging perovskite-phase in both composites.

Similar, to the CGO an excess of oxygen vacancies and samarium is expected in the grain boundary core. As can be seen, the concentration of samarium is much higher along the grain boundaries than samarium concentration in the grain.

CGO10-FCO composite

Compositional and structural characterization is carried out for pellets with nominal composition of (1-x) wt.% CGO10 - x wt. % FCO, where 10 ≤ x ≤ 40. XRD patterns in Figure 5.5 confirmed the presence of a cubic fluorite phase, i.e., ceria, and cubic spinel-type phases, i.e., Co_3O_4 and $Fe_xCo_{3-x}O_4$. Again, there is a coexistence of the two spinel types in all CGO10-based composites. The increase of the spinel reflections in the region of 35≤2θ≤38° and approximately 63°2θ with increasing nominal spinel fraction in the initial composite can nicely be observed. However, no additional $GdFeO_3$ perovskite phase can be detected. In contrast to composites with CGO20 or CSO20, there is no phase interaction during the sintering process, thus indeed a dual-phase membrane material is achieved.

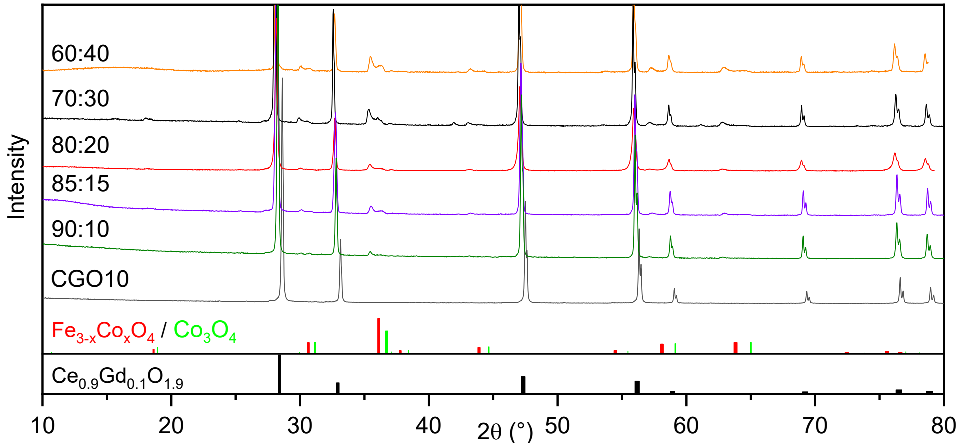

Figure 5.5 The XRD patterns of CGO10-FCO materials sintered at 1200°C for 5 h and single phase CGO10 as well as peak positions of phases

Further Rietveld refinement quantified the weight fractions of each phase as shown in Table 5.2. The resulting amount of fluorite fraction is reduced in each sintered composite compared to the nominal CGO10 content in the initial powder mixture. The lattice parameter of pure CGO10 measured in this work is 5.4172 Å agreeing well with literature reporting 5.418-5.42 Å [55,56]. In the composites, the lattice parameter of CGO10 is found to remain relatively constant after sintering confirming that no significant gadolinium extraction. For comparison in CGO20-based compounds the lattice parameter reduces by approx. 0.12±0.02%% due to the loss in gadolinium, which is consumed during the perovskite phase formation.

Table 5.2 Lattice parameter and fraction (F) of the phases after quantification by Rietveld refinement analyses of the CGO10-FCO composites and CGO10 singe phase sintered at 1200°C for 5 h

	CGO, *Fd3m*		FCO, *Fd3m*		Co_3O_4, *Fd3m*	
FCO, %	**F, wt.%**	**a=b=c, Å**	**F wt.%**	**a=b=c, Å**	**F, wt.%**	**a=b=c, Å**
0	100.0[0]	5.4172[7]	-	-	-	-
10	89.80[1]	5.4175[33	8.07[2]	8.3260[8]	2.14[9]	8.14562]
15	84.95[8]	5.4173[9]	7.62[2]	8.3063[1]	7.43[6]	8.1467[8]
20	79.04[2}]	5.4179[3]	14.12[2]	8.3031[6]	6.84[2]	8.1457[1]
30	69.18[1]	5.4176[3]	16.07[8]	8.3041[2]	14.75[9]	8.146[0]
40	58.51 [4]	5.4179[6]	22.53[3]	8.299[22]	18.29[2]	8.1351[1]

SEM analysis confirmed the presence of two phases in CGO10 -FCO composites: fluorite (light grains), and spinel (dark grains), without any other detectable phase. The grains are closely packed and uniformly distributed, exemplarily shown for 60:40 wt.%-ratio in Figure 5.6. The visual microstructure analysis of both surface and cross-section images via ImageJ software reveals the homogeneous distribution of the phases with a mean grain size of 0.5 µm. The spinel grains, in general, are larger than fluorite grains in both composites.

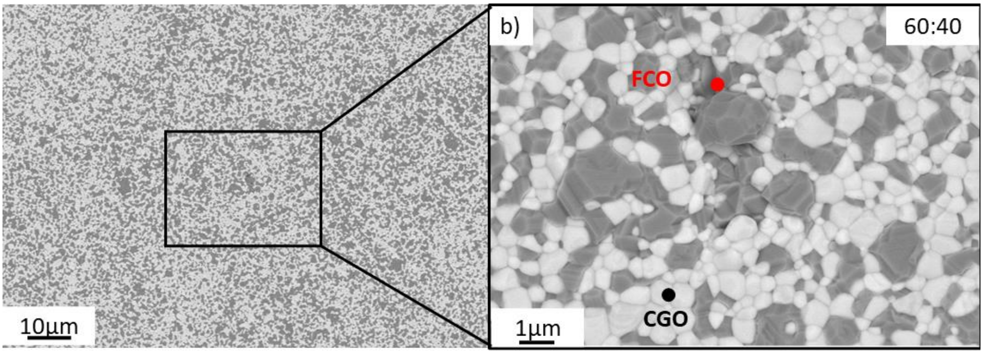

Figure 5.6 SEM image of 60CGO10-FCO sintered at 1200°C for 5h a) overview; b) detail with marked fluorite (light) and spinel (dark) grains

Image analysis was conducted on all samples of CGO10-, CGO20- and CSO20-based composites of both cross-section and surface images [57]. The average grain and pore sizes are given in Figure 5.7. The relationship between the dopant amount and grain size distribution in composites is seen by detailed analysis, included more than 2000 grains. The mean grain size of the two composites and reference CGO20-based composite is lying in the range of 0.5-0.68 µm and slightly increases with the higher dopant concentration. Both 20 mol.% doped composites reveal almost the same mean grain size, which is larger compared to 10 mol.% Gd-doped ceria. This result is logical since CGO10 powder was much finer, compared to 20 mol.% doped ceria. The grain growth is inhomogeneous in CGO20 and CSO20 composites, while in CGO10 composite all grains have similar size. In 20 mol.%-doped composite FCO grains are larger compared to the other phases, as can be seen in Figure 5.7a.

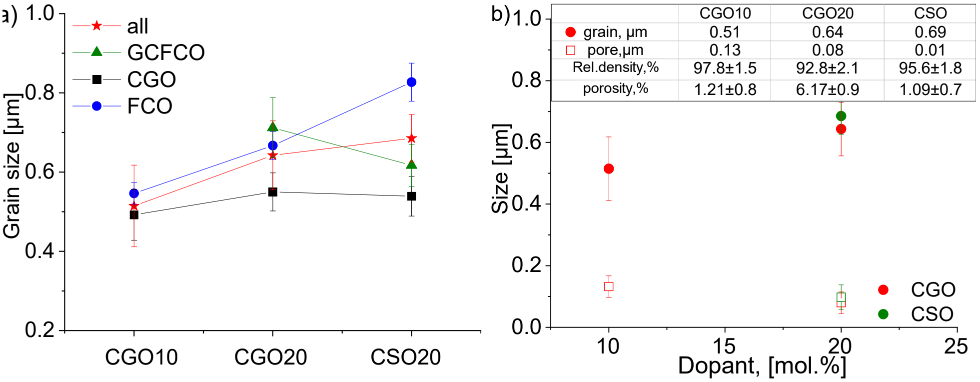

	CGO10	CGO20	CSO
● grain, µm	0.51	0.64	0.69
☐ pore,µm	0.13	0.08	0.01
Rel.density,%	97.8±1.5	92.8±2.1	95.6±1.8
porosity,%	1.21±0.8	6.17±0.9	1.09±0.7

Figure 5.7 a) Grain size of various phases in CGO10-, CGO20- and CSO20-based composites b) Grain and pore size relationship with the dopant fraction in the fluorite phase (solid lines for eye guidance only)

The porosity percentages have been estimated from the SEM images via image analysis, while the relative density was estimated geometrically from the dimensions and weight of the as-sintered pellets. The resulting values of both methods are well in agreement, Figure 5.7b. The dopant seems to have no significant effect on the grain and pore sizes, however the amount of the dopant (10 or 20 mol.%) seems to make a difference. Both CSO20 and CGO10-based composites reveal high level of relative density (>95-97 %) and correspondingly very low level of porosity (~ 1-2 %), these parameters are improved compared to the reference CGO20-FCO composite.

TEM analysis of the 10 and 20 mol. % Gd doped ceria composites reveal uniformly distributed element maps, as illustrated in Figure 5.8. Taking a closer look, a difference can be noticed in the Gd map: CGO10 has an evenly distributed intensity in composite, free of any tertiary phase, while the several grains are revealed with the higher gadolinium intensity in the CGO20-based sample, which confirms the presence of the perovskite phase in the microstructure.

The HAADF image and EDXS chemical mapping in Figure 5.9 contain a CGO GB in the 60CGO10-FCO composite G1 and G2. Both fluorite grains are randomly oriented. G1 appears brighter in the HAADF image as well as in the elemental maps most likely because it is closer to a zone axis compared to G2. As indicated by the blue arrow, intensity profiles across the grain boundary were extracted and plotted in Figure 5.9(b).

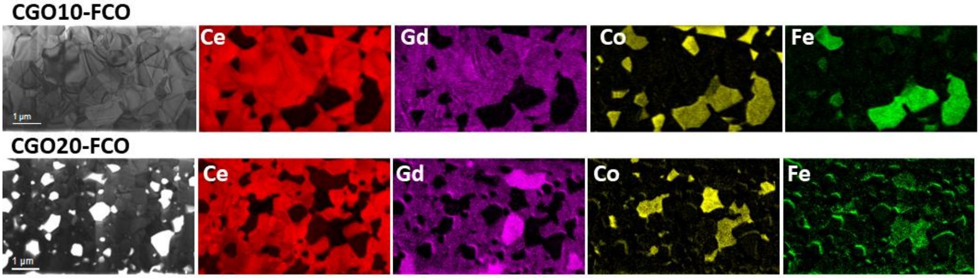

Figure 5.8 Elemental mapping by TEM and EFTEM images of the CGO10-FCO and CGO20- FCO with ratio 60:40

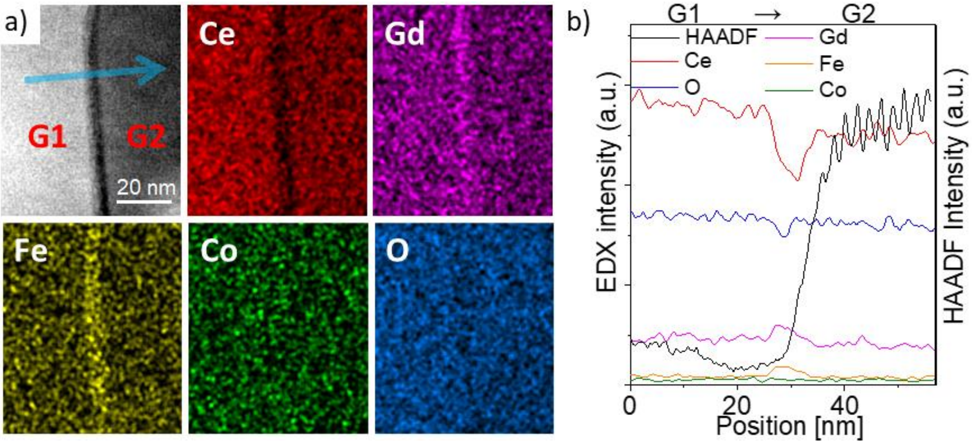

Figure 5.9 EDXS analysis of the grain boundaries a) The simultaneously acquired HAADF image and EDXS chemical mapping from Ce L, Gd L, Fe K, Co K, and O K peak. b) Line scans between two fluorite grains marked as G1 and G2 based on the elemental maps

Along the grain boundary, the enrichment of the gadolinium together with the migrated iron and cobalt was detected, while the Ce is significantly depleted. In addition, a slight depletion in oxygen, i.e., segregation of oxygen vacancies, can be observed. This is in agreement with literature about pure Gd-doped ceria, where excess of Gd^{3+} and depletion of oxygen ions in the grain boundary core appears, what can be also considered as an accumulation of the oxygen vacancies [54,58,59]. Compared to the

CGO20 and CSO20 composites, the segregation of the gadolinium in CGO10 composite is less pronounced, which can be attributed to the initial amount of the gadolinium in the fluorite [60]. Additionally, an excess of electrons near the grain boundary can be expected, as reported by Lei *et al*. [61].

The formed perovskite grains in the CGO20-FCO composites are mainly found between the fluorite grains [19,60]. In contrast, the initial gadolinium would be insufficient in CGO10-FCO, which possibly hinders the formation of a perovskite phase and often leaves iron and cobalt segregation along the fluorite-fluorite grain boundaries. Therefore, the segregation of iron and cobalt in the grain boundary of CGO10-based composites might also indicate a very initial stage of perovskite phase formation, which remains incomplete because of too low availability of gadolinium. Summarizing, in CGO10 the gadolinium appears very strongly bound in the ceria lattice, whereas the excess amount of gadolinium in CGO20 (as well as samarium in CSO20) can be extracted by Fe/Co-oxides forming the perovskite phase. The lattice parameter of pure CGO20 and CSO20 prior to phase interaction was 0.54246 nm and 0.54314 nm, respectively, and it was found to decrease after phase interaction due to Gd/Sm extraction.

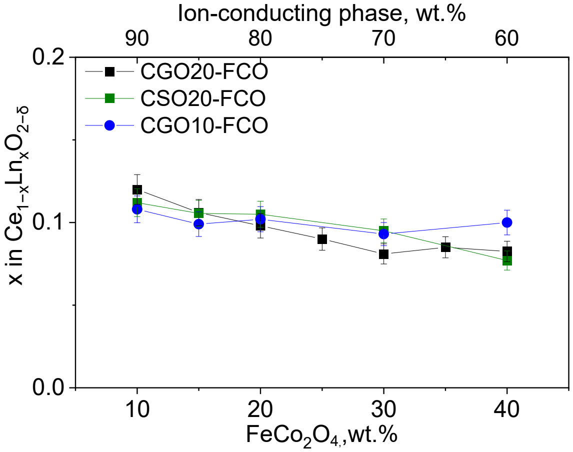

Figure 5.10 Gd/Sm content in the fluorite phase of all investigated composites (solid lines are a guide to the eye)

The residual doping content in the fluorite phase of the sintered composites was calculated from the lattice parameter, and shown in Figure 5.10 In the case of the CGO10-FCO composite, the amount of gadolinium is initially lower compared to the CGO20-FCO gadolinium content in the system. This shows the influence of the initial gadolinium content in the composite on the formation of the emerging perovskite phase. All composites end up at a dopant content of approx. 10 mol.% in the ceria phase.

5.3.2 Functional properties

Figure 5.11 shows the total conductivity of single-phase ceria materials performed by impedance spectroscopy in the temperature range of 400-800°C. The ionic conductivity of the investigated materials is dominating in the entire temperature range in air; thus, electronic conductivity can be considered negligible. At 500 C the Sm-doped material shows the highest total conductivity followed by CGO10 and CGO20 as predicted by Koettgen *et al.* [35,37]. At higher temperatures, however, these differences disappear, which was also reported earlier [62,63].

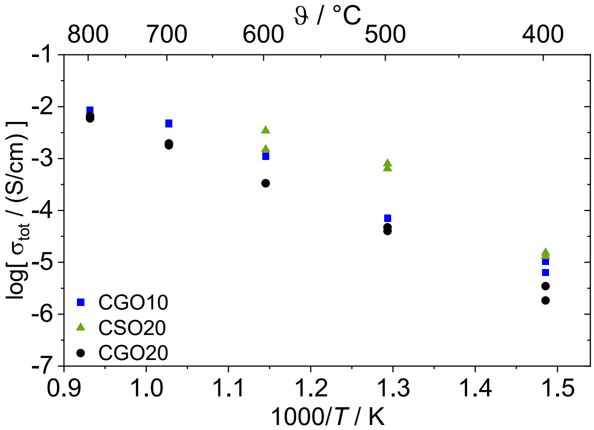

Figure 5.11 Ion (total) conductivity of CGO20, CGO10, and CSO20 measured by impedance spectroscopy in a temperature range of 400-800 °C. Data for CSO20 was only analysable in a temperature range below 600°C

Figure 5.12 a and b show the temperature dependent oxygen permeation rates and permeances of the composites with nominal fluorite-spinel wt.%-ratio of 60:40 and 80:20, respectively. The activation energies of thee composites agree well with those of the ionic conductivity of doped ceria reported in literature ($E_{a\ CGO10}$ = 60-66 kJ/mol [29,43,64], $E_{a\ CGO20}$=61-72 kJ/mol [29,43], $E_{a\ CSO20}$=74-94 kJ/mol [30,43,62,65]), it is concluded that the ionic transport is rate limiting. As a consequence, the permeation rate increases with increasing ceria content in the composite. The data was measured after the permeation has reached a steady state. The maximum permeation rates were obtained with the 80:20 ratio at 1020°C, i.e., 0.28, 0.26, and 0.22 ml/(cm^{2}min) for

CGO10, CSO20, and CGO20, respectively. At lower temperatures, the activation energies slightly increase, which can be ascribed to an increasing contribution of oxygen surface exchange to the overall transport. Therefore, despite the LSCF coating, surface exchange can no longer be neglected for al composites.

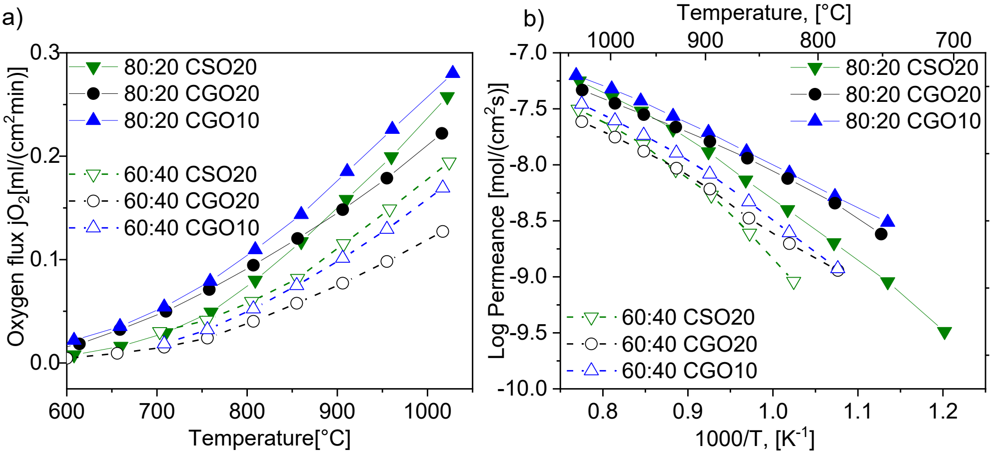

Figure 5.12 Temperature dependence a) of the oxygen permeation flux and b) of the permeance of the ceria-based composites with 60:40 and 80:20 ratios (solid and dashed lines are a guide to the eye)

Table 5.3 Activation energies E_a [kJ/mol] of the CGO10 and CSO20-based composites at temperatures >800°C

FCO wt.%	CSO20	CGO10	CGO20
10	103	102	101
15	76	66	74
20	79	68	58
25	-	-	60
30	78	75	62
35	-	-	80
40	95	74	80

The oxygen permeation of the three composites is evaluated as a function of the weight fraction of FCO (5 %-point-steps from 10-40 wt.%) at 850°C in Figure 5.13 (left). Principally the performance of all composites reveals similar behaviour along the investigated nominal FCO range. Starting from 40 wt. % FCO the permeance increases with decreasing FCO content, revealing that ionic conductance is the rate limiting process. A maximum permeance is found at approximately 20 wt. % nominal FCO for all three composites. A significant drop is seen in performance for all composites with 10 wt. % of FCO probably due to lack of percolation in the electron conducting phases. However, due to phase interactions during sintering, the nominal weight fractions do not represent the actual volume fraction of the ionic and electronic conducting phases, respectively. Therefore, volume fractions were calculated from Rietveld-refined XRD-patterns as described in [19].

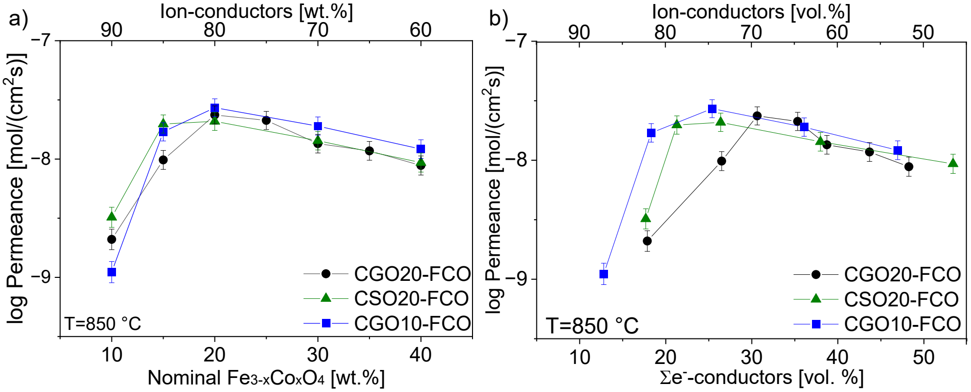

Figure 5.13 a) Permeance as a function of the nominal spinel amount for the CSO20-FCO, CGO20- and CGO10-FCO and synthesized by SSRS technique at 850°C; b) and as a function of the volume percentage of the electron conducting phase (solid lines are a guide to the eye)

Figure 5.13b shows that the maximum permeances of the different composites are achieved at very different volume fractions of electron conductors. This can be considered as percolation limit below which permeation decreases drastically due to the lack of electronic pathways. Obviously 20-30 vol.% of electronic conducting phases are required for sufficient percolation marked as red dashed lines in Figure 5.14, the percolation level varies with respect to the composite system [66,67]. Close to this percolation limit the permeance is presumably strongly dependent on the microstructure of the composite such as phase distribution and grain size. Moreover, the gadolinium, cobalt, and Iron enrichment along the grain boundaries might provide additional paths for the transport, affecting positively the percolation and final performance.

The better the compatibility, homogeneity, and uniformity of the phase distribution within the microstructure, the higher oxygen permeation is expected [68]. Similar results and the influence of components morphologies, such as grain size and morphology on performance are reported in [69], where it is concluded that a smaller grain size leads to a better percolation and, thus, oxygen permeation.

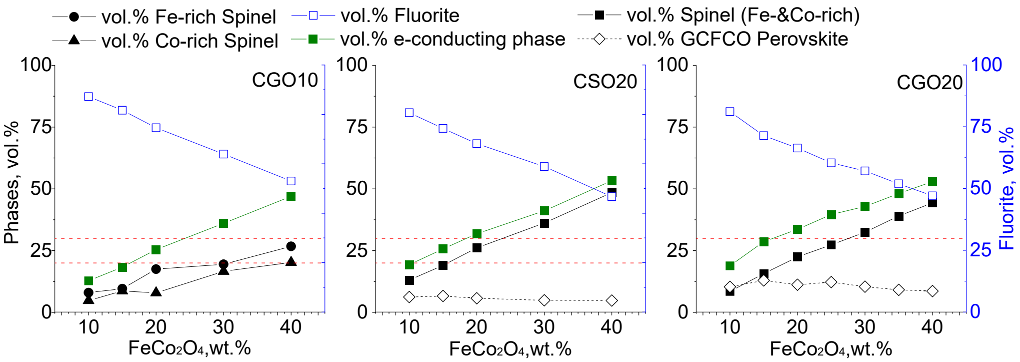

Figure 5.14 Volume fraction of detected phases in the CGO10-, CGO20- and CSO20-based composites. Red dashed lines represent the region of effective percolation achieving high permeation rates (solid lines are a guide to the eye)

Based on our observation the microstructure features play a crucial role for the low amount of the electron conducting phase in the composite, especially under 25 wt. % of the electron conducting phase in dual- and multi-phase composites. Now, the choice of the ion-conducting phase becomes relevant and strongly depends on the amount of the rare earth dopant. The dual-phase composite (10 mol.% of gadolinium) reveals no phase transformation, while in both 20 mol.%-doped materials, the phase transformation takes place, resulting in a multi-phase structure. Although the formed perovskite phase in CGO20 and CSO20 is a pure electron conductor and contributes to the electronic transport, its conductivity is still not as high as it is for the FCO spinels [19]. The presence of stronger electron-conductor FCO might be more effective, than the mix of the FCO and GCFCO in the composite. Moreover, the transport across grain boundaries between FCO-GCFCO might be not as fast as that for FCO-FCO grain boundaries. Hence, it also can affect the transport process for charged particles.

5.4 Conclusions

MIEC composites based on commercially available powders of $Ce_{0.9}Gd_{0.1}O_{2-\delta}$ (CGO10) and $Ce_{0.8}Sm_{0.2}O_{2-\delta}$ (CSO20) in combination with spinel $FeCo_2O_4$ can be successfully synthesized by the cost-efficient solid-state reactive sintering (SSRS) technique. As a result, dense (~95 %) dual- and multi-phase materials with fine microstructure (0.5-0.7 µm) are produced for potential application in OTM. During the sintering process, several phase interactions occur in the CSO20-FCO composite resulting in a multiphase MIEC system, i.e., a cubic fluorite CSO, a cubic Fe/Co-spinel, and a donor-doped $SmFeO_3$ perovskite. In contrast, the composite CGO10-FCO reveals only two phases, i.e., a fluorite CGO10 and a Fe/Co-spinel, without the formation of a tertiary phase, underlining the effect of the dopant amount (10 or 20 mol.%) in ceria. For both investigated in this study composites, there was coexistence of two spinel types an iron-rich and a cobalt-rich spinel, according to the Fe-Co-O phase diagram.

The detected enrichment of gadolinium or samarium, cobalt, and iron along grain boundaries impacts the electronic or/and ionic transport and might enhance the total conductivity of the composite, resulting in high oxygen permeation of the dual- and multi-phase composites. This Fe/Co accumulation together with pre-existing Gd/Sm segregation at the grain boundaries possibly acts as an initial state of the tertiary phase formation in 20 mol% doped ceria samples. However, in CGO10-based composites, the initial gadolinium fraction obviously is too low for the perovskite formation.

The main challenge of the dual-phase and multiphase materials design is maximizing the ionic conducting volume without losing the percolation of the electronic conduction. That’s why to ensure sufficient percolating networks both conditions should be fulfilled: high electronic conductivity of the selected phases and continuous percolation paths for the transport. Investigated materials reveal an oxygen flux of 0.23 and 0.2 ml/(cm^2min) at 950°C, for CGO10 and CSO20-based composites with 20 wt.% of FCO phase, respectively. Based on our findings, the microstructure plays a major role in the low electron conducting phase content (<25 vol.%) in the ceria-based composite, pointing out the importance of the phase distributions as well as the grain size of the presented phases. Thus, the CGO10-based composite has an advantage over the CGO20 and CSO20-based ones concerning the microstructure, resulting in higher oxygen permeance, particularly at low nominal FCO content. Microstructure-based modelling of the conductivity would be helpful in order to optimize the performance of such complex composite materials.

References

1. Bai, W.; Feng, J.; Luo, C.; Zhang, P.; Wang, H.; Yang, Y.; Zhao, Y.; Fan, H. A comprehensive review on oxygen transport membranes: Development history, current status, and future directions. *International Journal of Hydrogen Energy* **2021**, *46*, 36257–36290.
2. Dong, X.; Jin, W.; Xu, N.; Li, K. Dense ceramic catalytic membranes and membrane reactors for energy and environmental applications. *Chemical communications (Cambridge, England)* **2011**, *47*, 10886–10902.
3. Zhu, X.; Yang, W. Microstructural and Interfacial Designs of Oxygen-Permeable Membranes for Oxygen Separation and Reaction-Separation Coupling. *Advanced materials (Deerfield Beach, Fla.)* **2019**, *31*, e1902547.
4. Garcia-Fayos, J.; Serra, J.M.; Luiten-Olieman, M.W.; Meulenberg, W.A. Gas separation ceramic membranes. In *Advanced Ceramics for Energy Conversion and Storage*: Elsevier, 2020, pp. 321–385.
5. Chen, G.; Feldhoff, A.; Weidenkaff, A.; Li, C.; Liu, S.; Zhu, X.; Sunarso, J.; Huang, K.; Wu, X.-Y.; Ghoniem, A.F.*; et al.* Roadmap for Sustainable Mixed Ionic-Electronic Conducting Membranes. *Adv Funct Materials* **2022**, *32*.
6. Kiebach, R.; Pirou, S.; Martinez Aguilera, L.; Haugen, A.B.; Kaiser, A.; Hendriksen, P.V.; Balaguer, M.; García-Fayos, J.; Serra, J.M.; Schulze-Küppers, F.*; et al.* A review on dual-phase oxygen transport membranes: from fundamentals to commercial deployment. *J. Mater. Chem. A* **2022**, *10*, 2152–2195.
7. Arratibel Plazaola, A.; Cruellas Labella, A.; Liu, Y.; Badiola Porras, N.; Pacheco Tanaka, D.; Sint Annaland, M.; Gallucci, F. Mixed Ionic-Electronic Conducting Membranes (MIEC) for Their Application in Membrane Reactors: A Review. *Processes* **2019**, *7*, 128.
8. Zhao, J.; Pang, Y.; Su, C.; Jiang, S.; Ge, L. Toward High Performance Mixed Ionic and Electronic Conducting Perovskite-Based Oxygen Permeable Membranes: An Overview of Strategies and Rationales. *Energy Fuels* **2023**, *37*, 7042–7061.
9. Drago, F.; Fedeli, P.; Cavaliere, A.; Cammi, A.; Passoni, S.; Mereu, R.; La Pierre, S. de; Smeacetto, F.; Ferraris, M. Development of a Membrane Module Prototype for Oxygen Separation in Industrial Applications. *Membranes* **2022**, *12*.
10. Hu, Q.; Pirou, S.; Engelbrecht, K.; Kriegel, R.; Pippardt, U.; Kiesel, L.; Sun, Q.; Kiebach, R. Testing of high performance asymmetric tubular BSCF membranes under pressurized operation – A proof-of-concept study on a 7 tube module. *Journal of Membrane Science* **2022**, *644*, 120176.
11. Sahini, M.G.; Mwankemwa, B.S.; Kanas, N. $Ba_xSr_{1-x}Co_yFe_{1-y}O_{3-\delta}$ (BSCF) mixed ionic-electronic conducting (MIEC) materials for oxygen separation membrane and SOFC

applications: Insights into processing, stability, and functional properties. *Ceramics International* **2022**, *48*, 2948–2964.

12. Gao, J.; Li, L.; Yin, Z.; Zhang, J.; Lu, S.; Tan, X. Poisoning effect of SO_2 on the oxygen permeation behavior of $La_{0.6}Sr_{0.4}Co_{0.2}Fe_{0.8}O_{3-\delta}$ perovskite hollow fiber membranes. *Journal of Membrane Science* **2014**, *455*, 341–348.

13. Yi, J.; Schroeder, M. High temperature degradation of $Ba_{0.5}Sr_{0.5}Co_{0.8}Fe_{0.2}O_{3-\delta}$ membranes in atmospheres containing concentrated carbon dioxide. *Journal of Membrane Science* **2011**, *378*, 163–170.

14. Mueller, D.N.; Souza, R.A. de; Weirich, T.E.; Roehrens, D.; Mayer, J.; Martin, M. A kinetic study of the decomposition of the cubic perovskite-type oxide $Ba_xSr_{1-x}Co_{0.8}Fe_{0.2}O_{3-\delta}$ (BSCF) (x = 0.1 and 0.5). *Physical chemistry chemical physics : PCCP* **2010**, *12*, 10320–10328.

15. Matras, D.; Vamvakeros, A.; Jacques, S.D.M.; Middelkoop, V.; Vaughan, G.; Agote Aran, M.; Cernik, R.J.; Beale, A.M. In situ X-ray diffraction computed tomography studies examining the thermal and chemical stabilities of working $Ba_{0.5}Sr_{0.5}Co_{0.8}Fe_{0.2}O_{3-\delta}$ membranes during oxidative coupling of methane. *Physical chemistry chemical physics : PCCP* **2020**, *22*, 18964–18975.

16. Waindich, A.; Möbius, A.; Müller, M. Corrosion of $Ba_{1-x}Sr_xCo_{1-y}FeyO_{3-\delta}$ and $La_{0.3}Ba_{0.7}Co_{0.2}Fe_{0.8}O_{3-\delta}$ materials for oxygen separating membranes under Oxycoal conditions. *Journal of Membrane Science* **2009**, *337*, 182–187.

17. Ramirez-Reina, T.; Santos, J.L.; García-Moncada, N.; Ivanova, S.; Odriozola, J.A. Development of Robust Mixed-Conducting Membranes with High Permeability and Stability. In *Perovskites and Related Mixed Oxides*; Granger, P., Parvulescu, V.I., Parvulescu, V.I., Prellier, W., Eds.: Wiley, 2016, pp. 719–738.

18. Ramasamy, M.; Persoon, E.S.; Baumann, S.; Schroeder, M.; Schulze-Küppers, F.; Görtz, D.; Bhave, R.; Bram, M.; Meulenberg, W.A. Structural and chemical stability of high performance $Ce_{0.8}Gd_{0.2}O_{2-\delta}$-$FeCo_2O_4$ dual phase oxygen transport membranes. *Journal of Membrane Science* **2017**, *544*, 278–286.

19. Fischer, L.; Neuhaus, K.; Schmidt, C.; Ran, K.; Behr, P.; Baumann, S.; Mayer, J.; Meulenberg, W.A. Phase formation and performance of solid state reactive sintered $Ce_{0.8}Gd_{0.2}O_{2-\delta}$-$FeCo_2O_4$ composites. *J. Mater. Chem. A* **2022**, *10*, 2412–2420.

20. Lin, Y.; Fang, S.; Su, D.; Brinkman, K.S.; Chen, F. Enhancing grain boundary ionic conductivity in mixed ionic-electronic conductors. *Nature communications* **2015**, *6*, 6824.

21. Fischer, L.; Ran, K.; Schmidt, C.; Neuhaus, K.; Baumann, S.; Behr, P.; Mayer, J.; Bouwmeester, H.J.M.; Nijmeijer, A.; Guillon, O.*; et al.* Role of Fe/Co Ratio in Dual Phase $Ce_{0.8}Gd_{0.2}O_{2-}$-$Fe_{3-x}Co_xO_4$ Composites for Oxygen Separation. *Membranes* **2023**, *13*.

22. Zeng, F.; Malzbender, J.; Baumann, S.; Krüger, M.; Winnubst, L.; Guillon, O.; Meulenberg, W.A. Phase and microstructural characterizations for $Ce_{0.8}Gd_{0.2}O_{2-\delta}$-$FeCo_2O_4$ dual phase oxygen transport membranes. *Journal of the European Ceramic Society* **2020**, *40*, 5646–5652.

23. Artini, C.; Pani, M.; Carnasciali, M.M.; Plaisier, J.R.; Costa, G.A. Lu-, Sm-, and Gd-Doped Ceria: A Comparative Approach to Their Structural Properties. *Inorganic chemistry* **2016**, *55*, 10567–10579.

24. Artini, C.; Carnasciali, M.M.; Viviani, M.; Presto, S.; Plaisier, J.R.; Costa, G.A.; Pani, M. Structural properties of Sm-doped ceria electrolytes at the fuel cell operating temperatures. *Solid State Ionics* **2018**, *315*, 85–91.

25. Luo, H.; Efimov, K.; Jiang, H.; Feldhoff, A.; Wang, H.; Caro, J. CO2-stable and cobalt-free dual-phase membrane for oxygen separation. *Angewandte Chemie (International ed. in English)* **2011**, *50*, 759–763.

26. Cheng, H.; Zhang, N.; Xiong, X.; Lu, X.; Zhao, H.; Li, S.; Zhou, Z. Synthesis, Oxygen Permeation, and CO_2-Tolerance Properties of $Ce_{0.8}Gd_{0.2}O_{2-\delta}$–$Ba_{0.95}La_{0.05}Fe_{1-x}Nb_xO_{3-\delta}$ Dual-Phase Membranes. *ACS Sustainable Chem. Eng.* **2015**, *3*, 1982–1992.

27. Samson, A.J.; Søgaard, M.; Vang Hendriksen, P. $(Ce,Gd)O_2$−-based dual phase membranes for oxygen separation. *Journal of Membrane Science* **2014**, *470*, 178–188.

28. Nigge, U. Composites of Ce0.8Gd0.2O1.9 and Gd0.7Ca0.3CoO3−δ as oxygen permeable membranes for exhaust gas sensors. *Solid State Ionics* **2002**, *146*, 163–174.

29. Kharton, V.V.; Figueiredo, F.M.; Navarro, L.; Naumovich, E.N.; Kovalevsky, A.V.; Yaremchenko, A.A.; Viskup, A.P.; Carneiro, A.; Marques, F.M.B.; Frade, J.R. Ceria-based materials for solid oxide fuel cells. *J Mater Sci* **2001**, *36*, 1105–1117.

30. Presto, S.; Artini, C.; Pani, M.; Carnasciali, M.M.; Massardo, S.; Viviani, M. Ionic conductivity and local structural features in $Ce_{1-x}Sm_xO_{2-x/2}$. *Physical chemistry chemical physics : PCCP* **2018**, *20*, 28338–28345.

31. Zhu, X.; Liu, H.; Cong, Y.; Yang, W. Novel dual-phase membranes for CO2 capture via an oxyfuel route. *Chemical communications (Cambridge, England)* **2012**, *48*, 251–253.

32. Kilner J. Fast oxygen transport in acceptor doped oxides. Solid State Ionics, 129(1-4), 13-23 **2000**.

33. Mogensen, M. Physical Properties of Mixed Conductor Solid Oxide Fuel Cell Anodes of Doped CeO_2. *J. Electrochem. Soc.* **1994**, *141*, 2122.

34. Artini, C.; Viviani, M.; Presto, S.; Massardo, S.; Carnasciali, M.M.; Gigli, L.; Pani, M. Correlations between structure, microstructure and ionic conductivity in (Gd,Sm)-doped ceria. *Physical chemistry chemical physics : PCCP* **2022**, *24*, 23622–23633.

35. Koettgen, J.; Grieshammer, S.; Hein, P.; Grope, B.O.H.; Nakayama, M.; Martin, M. Understanding the ionic conductivity maximum in doped ceria: trapping and blocking. *Physical chemistry chemical physics : PCCP* **2018**, *20*, 14291–14321.

36. Coduri, M.; Checchia, S.; Longhi, M.; Ceresoli, D.; Scavini, M. Rare Earth Doped Ceria: The Complex Connection Between Structure and Properties. *Frontiers in chemistry* **2018**, *6*, 526.

37. Koettgen, J.; Martin, M. The ionic conductivity of Sm-doped ceria. *J. Am. Ceram. Soc.* **2020**, *103*, 3776–3787.

38. Wang, S.; Kobayashi, T.; Dokiya, M.; Hashimoto, T. Electrical and Ionic Conductivity of Gd-Doped Ceria. *J. Electrochem. Soc.* **2000**, *147*, 3606.

39. Kilner, J.A, Brook., R. A study of oxygen ion conductivity in doped non-stoichiometric oxides. *Solid State Ionics* **1982**, *6*, 237–252.

40. Joo, J.H.; Park, G.S.; Yoo, C.-Y.; Yu, J.H. Contribution of the surface exchange kinetics to the oxygen transport properties in $Ce_{0.9}Gd_{0.1}O_{2-\delta}$ –$La_{0.6}Sr_{0.4}Co_{0.2}Fe_{0.8}O_{3-\delta}$ dual-phase membrane. *Solid State Ionics* **2013**, *253*, 64–69.

41. Gielen, D. and M. Lyons. Critical Materials For The Energy Transition: Rare Earth elements, *2022*.

42. Avila-Paredes, H.J.; Choi, K.; Chen, C.-T.; Kim, S. Dopant-concentration dependence of grain-boundary conductivity in ceria: A space-charge analysis. *J. Mater. Chem.* **2009**, *19*, 4837.

43. Steele, B. Appraisal of $Ce_{1-y}Gd_yO_{2-y/2}$ electrolytes for IT-SOFC operation at 500°C. *Solid State Ionics* **2000**, *129*, 95–110.

44. Malavasi, L.; Fisher, C.A.J.; Islam, M.S. Oxide-ion and proton conducting electrolyte materials for clean energy applications: structural and mechanistic features. *Chemical Society reviews* **2010**, *39*, 4370–4387.

45. Picture Thresholding Using an Iterative Selection Method. *IEEE Trans. Syst., Man, Cybern.* **1978**, *8*, 630–632.

46. Kovács, A.; Schierholz, R.; Tillmann, K. FEI Titan G2 80-200 CREWLEY. *JLSRF* **2016**, *2*.

47. Takamura, H.; Koshino, Y.; Kamegawa, A.; Okada, M. Electrode and oxygen permeation properties of (Ce, Sm)O_2–MFe_2O_4 composite thin films (M=Co and Mn). *Solid State Ionics* **2006**, *177*, 2185–2189.

48. Yousaf, M.; Mushtaq, N.; Zhu, B.; Wang, B.; Akhtar, M.N.; Noor, A.; Afzal, M. Electrochemical properties of $Ni_{0.4}Zn_{0.6}$ Fe_2O_4 and the heterostructure composites (Ni–Zn ferrite-SDC) for low temperature solid oxide fuel cell (LT-SOFC). *Electrochimica Acta* **2020**, *331*, 135349.

49. Hansson, A.N.; Linderoth, S.; Mogensen, M.; Somers, M.A. X-ray diffraction investigation of phase stability in the Co–Cr–O and the Fe–Co–Cr–O systems in air at 1323K. *Journal of Alloys and Compounds* **2005**, *402*, 194–200.

50. Neuhaus, K.; Dolle, R.; Wiemhöfer, H.-D. The Effect of Transition Metal Oxide Addition on the Conductivity of Commercially Available Gd-Doped Ceria. *J. Electrochem. Soc.* **2020**, *167*, 44507.

51. Ji, Y.; Kilner, J.; Carolan, M. Electrical conductivity and oxygen transfer in gadolinia-doped ceria (CGO)–$Co_3O_{4-\delta}$ composites. *Journal of the European Ceramic Society* **2004**, *24*, 3613–3616.

52. Zheng, Y.; Zhou, M.; Ge, L.; Li, S.; Chen, H.; Guo, L. Effect of Fe2O3 on Sm-doped ceria system solid electrolyte for IT-SOFCs. *Journal of Alloys and Compounds* **2011**, *509*, 546–550.

53. Zhang, T. Iron oxide as an effective sintering aid and a grain boundary scavenger for ceria-based electrolytes. *Solid State Ionics* **2004**, *167*, 203–207.

54. Ran, K.; Fischer, L.; Baumann, S.; Meulenberg, W.A.; Neuhaus, K.; Mayer, J. Tuning the ceria interfaces inside the dual phase oxygen transport membranes. *Acta Materialia* **2022**, *226*, 117603.

55. Joo, J.H.; Yun, K.S.; Lee, Y.; Jung, J.; Yoo, C.-Y.; Yu, J.H. Dramatically Enhanced Oxygen Fluxes in Fluorite-Rich Dual-Phase Membrane by Surface Modification. *Chem. Mater.* **2014**, *26*, 4387–4394.

56. Vives, S.; Ramel, D.; Meunier, C. Evolution of the structure with the composition and the defect arrangement in the gadolinium and samarium doped and co-doped ceria systems: A molecular dynamics study. *Solid State Ionics* **2021**, *364*, 115611.

57. Schneider, C.A.; Rasband, W.S.; Eliceiri, K.W. NIH Image to ImageJ: 25 years of image analysis. *Nature methods* **2012**, *9*, 671–675.

58. Bowman, W.J.; Zhu, J.; Sharma, R.; Crozier, P.A. Electrical conductivity and grain boundary composition of Gd-doped and Gd/Pr co-doped ceria. *Solid State Ionics* **2015**, *272*, 9–17.

59. Lee, W.; Jung, H.J.; Lee, M.H.; Kim, Y.-B.; Park, J.S.; Sinclair, R.; Prinz, F.B. Oxygen Surface Exchange at Grain Boundaries of Oxide Ion Conductors. *Adv Funct Materials* **2012**, *22*, 965–971.

60. Ran, K.; Zeng, F.; Fischer, L.; Baumann, S.; Meulenberg, W.A.; Neuhaus, K.; Mayer, J. The in situ generated emerging phase inside dual phase oxygen transport membranes. *Acta Materialia* **2022**, *234*, 118034.

61. Lei, Y.; Ito, Y.; Browning, N.D.; Mazanec, T.J. Segregation Effects at Grain Boundaries in Fluorite-Structured Ceramics. *J. Am. Ceram. Soc.* **2002**, *85*, 2359–2363.

62. Neuhaus, K.; Schmidt, C.; Fischer, L.; Meulenberg, W.A.; Ran, K.; Mayer, J.; Baumann, S. Measurement of polarization effects in dual-phase ceria-based oxygen permeation membranes using Kelvin probe force microscopy. *Beilstein journal of nanotechnology* **2021**, *12*, 1380–1391.

63. Jadhav, L.D.; Pawar, S.H.; Chourashiya, M.G. Effect of sintering temperature on structural and electrical properties of gadolinium doped ceria ($Ce_{0·9}Gd_{0.1}O_{1.95}$). *Bull Mater Sci* **2007**, *30*, 97–100.

64. Cheng, S.; Søgaard, M.; Han, L.; Zhang, W.; Chen, M.; Kaiser, A.; Hendriksen, P.V. A novel CO_2- and SO_2-tolerant dual phase composite membrane for oxygen separation. *Chemical communications (Cambridge, England)* **2015**, *51*, 7140–7143.

65. Inaba, H. Ceria-based solid electrolytes. *Solid State Ionics* **1996**, *83*, 1–16.

66. Lorenz, C.D.; Ziff, R.M. Precise determination of the critical percolation threshold for the three-dimensional “Swiss cheese” model using a growth algorithm. *The Journal of Chemical Physics* **2001**, *114*, 3659–3661.

67. Na, B.T.; Park, J.H.; Park, J.H.; Yu, J.H.; Joo, J.H. Elucidation of the Oxygen Surface Kinetics in a Coated Dual-Phase Membrane for Enhancing Oxygen Permeation Flux. *ACS applied materials & interfaces* **2017**, *9*, 19917–19924.

68. Zhu, X.; Wang, H.; Yang, W. Relationship between homogeneity and oxygen permeability of composite membranes. *Journal of Membrane Science* **2008**, *309*, 120–127.

69. Luo, H.; Jiang, H.; Efimov, K.; Caro, J.; Wang, H. Influence of the preparation methods on the microstructure and oxygen permeability of a CO_2-stable dual phase membrane. *AIChE J.* **2011**, *57*, 2738–2745.

Chapter 6

6. Thickness influence on the permeation of 60 wt. %$Ce_{0.8}Gd_{0.2}O_{2-\delta}$ – 40 wt.% $FeCo_2O_4$ composites

Abstract

The dual-phase composite 60 wt. % $Ce_{0.8}Gd_{0.2}O_{2-\delta}$ -40 wt.% $FeCo_2O_4$ (60CGO20-FCO) is an excellent Oxygen Transport Membrane (OTM) with sufficient stability and oxygen permeation performance. To study the effect of the bulk diffusion and surface exchange kinetics, the thickness of the bulk disc-shaped membrane was varied from 0.4 to 2 mm. The oxygen flux through the membrane is increased with the LSCF layer application at low temperatures, compared to the bare membranes. The characteristic thickness L_c helps to distinguish the transport-limiting regimes in the dual-phase composite. This L_c value was estimated by utilizing the modified Wagner's equation, underlying that the LSCF coating is proven to be effective to overcome the surface limitation in the CGO20-FCO composite, especially at low temperatures. The L_c=0.056 and 0.069 cm for coated and bare membrane at 800°C. Additionally, the impact of the diverse surface modifications (one-, both-side and uncoated) on the transport in dual-phase composite is discussed.

This Chapter is ready to submit to American Ceramic Society Journal in 2024

6.1 Introduction

The oxygen demand is gradually increasing from year to year since oxygen is commonly used in various industrial applications. It is widely exploited for purposes such as combustion, oxidation, and as a feed gas for various chemical reactions. Oxygen transport membranes can enable oxygen separation from mixed gases because they are designed to be selective to oxygen ions. The oxygen transport membrane technology can offer a sufficient and economically beneficial solution for different oxygen-intensive industrial sectors, due to enhanced oxygen quality [1–3]. The development of oxygen transport membranes based on mixed ionic-electronic conducting (MIEC) ceramic materials is a promising alternative to the existing methods for the intermediate operating temperature range (below 800°C). Operating at intermediate temperatures might lead to a reduction in costs and an increase in the system's durability compared to alternative high temperature membranes. Dual-phase MIEC materials are attracting much attention due to their high selectivity for oxygen and their significantly lower efficiency losses compared to the conventional cryogenic distillation. Generally, a well-mixed mixed conductor should provide a high level of ambipolar (total) conductivity and thus high ionic conductivity as well as considerable electronic conductivity. However, meeting all the requirements in a single component material is quite difficult.

Well-known examples of single-phase perovskite materials are BSCF and LSCF. Exceptional high oxygen permeability makes them a good potential oxygen transport material, [4–9]. However, the stability at intermediate temperatures is quite an issue for these materials, especially in the CO_2 or SO_x-containing atmospheres [10–15]. Operating in CO_2 and SO_2 containing atmospheres leads to irreversible reactions, i.e., carbonating reactions. In dual-phase materials on the other hand it is possible to get a chemically stable composite. Both phases in the material coexist and provide a continuous network, contributing to the different types of transport. As a rule, the ionic conductor serves as a continuous phase and the electronic conductor is uniformly dispersed, but networked in the whole membrane volume, hence facilitating oxygen permeation. This dual- or multiphase membrane concept gives rise to additional opportunities in the selection of materials and fabrication methods for oxygen transport membranes, and thus it is an interesting alternative to the known conventional materials.

Membrane thickness has generally a significant influence on the performance of inorganic dense membranes. In order to investigate the influence of the membrane thickness on the performance of dual-phase bulk membranes various gas-solid interface modifications are done. The tablets with thicknesses from 0.4 mm to 2 mm is fabricated for the investigation.

6.1.1 Transport mechanism

In general, a different partial pressure on both sides of the membrane plays a role as the driving force for the permeation process [16]. Ion transport is from the high p_{O2} side to the lower one, while the electrons are forced to move in the opposite direction to maintain charge neutrality.

Transport of the oxygen through the membrane is quite complex and accompanied by different transport mechanisms. Each of these steps might be rate limiting and can be interpreted as a resistance as shown in Figure 6.1. This resistance model is described in [17,18], and includes surface exchange reactions marked as Zones II and IV, the concentration polarisation in the gas phase in Zone I, the bulk diffusion in the thin membrane layer (Zone III) and the transport through the pores in the porous substrate (Zone V and VI).

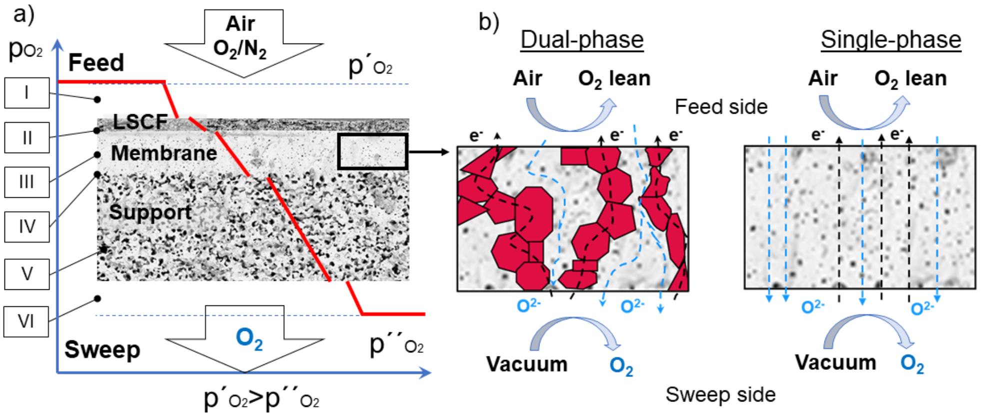

Figure 6.1 a) Oxygen transport through asymmetric membrane, including rate limiting steps and partial pressure gradient

Each zone represents the rate-limiting step or resistances, which reduces the oxygen partial pressure. The loss of partial pressure across the asymmetric membrane profile is due to oxygen depletion or accumulation in the gas phases, pores in the support as well as the catalytic activation layer. Since the resistances in the gas phase are negligible [19]. The focus in this work is on the transport in the bulk and surface exchange areas. (Zones III, II and IV) [6].

Zone III. Bulk transport

Generally, bulk diffusion is the lattice diffusion in oxides and involves some point defects such as vacancies, and interstitial atoms [19,20]. Transport in the bulk corresponds to oxygen ion diffusion from the high partial pressure side to the low pressure, while electrons move in the opposite direction to maintain charge neutrality as illustrated in Figure 6.2.

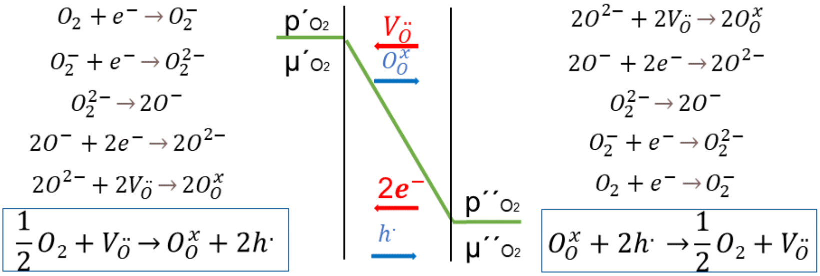

Figure 6.2 Principal overview of the ion transport through dense ion-electronic conducting membrane inclusive the reactions oxygen reduction, dissociation and incorporation into the oxide lattice at the one side and oxidation, association, and desorption of oxygen molecules on the other side of membrane

To describe the oxygen permeation process in dense membranes, a well-known model developed according to Wagner's theory of the oxygen flux in solid oxides is widely accepted. The transport in the bulk obeys the *Wagner's equation* [21]*:*

$$j_{O2} = \frac{\mathrm{RT}}{16F^2} \cdot \overline{\sigma_{amb}} \cdot \frac{1}{L} \cdot ln\frac{p'_{O2}}{p''_{O2}} \qquad \textbf{Equation 6.1}$$

with gas constant R, absolute operating temperature T, Faraday constant F, membrane thickness is L, and p'_{O2} and p''_{O2} are oxygen partial pressure at the feed and sweep gas sides, respectively. The ambipolar conductivity $\sigma_{amb} = \frac{\sigma_i \sigma_e}{\sigma_i + \sigma_e}$ is a function of the electronic $\boldsymbol{\sigma_e}$ and ionic $\sigma_{ion} = \frac{c_O D_S z_O^2 F^2}{RT}$ conductivity of the material. In the case of the composite, the ambipolar conductivity is different and should be corrected. For this case, it is assumed that ambipolar conductivity is constant across the membrane thickness. However, it should be mentioned that ambipolar conductivity represents the approximation since it is dependent on the oxygen partial pressure, which is not constant and varies significantly [17].

Zones II and IV. Surface exchange processes

At both oxygen-rich and oxygen-lean sides the MIEC undergoes a range of surface exchange reactions: oxygen adsorption, dissociation and charge transfer. It is also assumed that the same reaction takes place in opposite direction [16,19].

At the high partial pressure side, the oxygen incorporation reaction takes place $\frac{1}{2}O2 + V_{\ddot{O}} \rightarrow O_O^x + 2h^{\cdot}$, while at the low partial pressure side is the release of oxygen in the gas phase takes place: $O_O^x + 2h^{\cdot} \rightarrow \frac{1}{2}O2 + V_{\ddot{O}}$

These reactions happen to occur only in the triple phase boundary, where air, ionic, and electronic conducting phases provide molecular oxygen O_2, oxygen vacancies $V_{\ddot{O}}$, and electrons e^- respectively.

From Wagner´s equation, it can be concluded that the oxygen flux is inversely proportional to the thickness of the membrane. Based on this the performance of the membrane can be managed and the dominating transport mechanism is determined. In the MIEC with large thicknesses, bulk diffusion is dominant over surface exchange mechanisms. Interface reactions, on the other hand, are quite limiting in the case of a very thin membrane. However, both contribute equally to the resulting oxygen flux through the membrane at a certain thickness. This parameter is introduced as characteristic thickness L_c for the membranes, and since this should be considered on the both membrane sides the Wagner’s equation is corrected with $2L_c$ [16,21]. So, the equation is modified into *modified Wagner’s equation:*

$$\boldsymbol{j_{O2} = \frac{RT}{16F^2} \cdot \frac{\sigma_i \sigma_e}{\sigma_i + \sigma_e} \cdot \frac{1}{L + 2L_c} \cdot ln\frac{p'_{O2}}{p''_{O2}}} \qquad \textbf{Equation 6.2}$$

L_c is also can be found as:

$$L_c = \frac{D_s}{k_s} \qquad \textbf{Equation 6.3}$$

$$L_c(\mathrm{T}) = \frac{D_s}{k_s} = \frac{D_{s0} \cdot exp(-\frac{E_{A,D}}{RT})}{k_{s0} \cdot exp(-\frac{E_{A,k}}{RT})} = L_{c,0} \cdot exp(-\frac{E_A}{RT}) \qquad \textbf{Equation 6.4}$$

According to the inverse relationship between these two parameters in Wagner´s equation 5, the reduction of the membrane thickness leads to an increase in oxygen flux, however, it is valid only until a certain value. When L_c approaches zero or $D_s \ll k_s$, the oxygen flux, and permeation become bulk-limited. L_c is known to be a temperature-dependent value.

The characteristic membrane thickness L_c helps to differentiate the transport limiting regimes in our dual-phase material with related characteristics. L_c is known to be a temperature dependent value (equation 5).

(L_c <<L) Oxygen transport in the bulk-controlled regime generally obeys the Wagner's equation, under partial pressure gradient and written as equation 1. When L is much larger than L_c, the ratio L_c /L approaches zero, thus the resulting oxygen permeance curves are mostly showing the effect of the ionic conductivity.

(L_c >> L) L_c value in the regime, when both bulk and surface exchange kinetics are limiting the oxygen flux can be expressed as a modified Wagner equation, with the introduction of the Lc. Since this value is more significant in the case of surface limitations, we cannot neglect it.

This performance of the oxygen permeation is determined by bulk diffusion and surface exchange processes on the feed and sweep sides. On the feed side (high partial pressure side), the oxygen reduction reaction occurs, where oxygen ions are incorporated into oxygen vacancies of ceramic bulk and move to the sweep side of the membrane (low partial pressure side). After oxygen ions migrate to the permeate side, an oxygen evolution reaction takes place, where oxygen is released from the ceramic bulk phase and released from the membrane. Thus, the effects of the surface-exchange kinetics on the oxygen-permeation properties should be studied in terms of surface modification.

In this study, the oxygen flux in the CGO20-rich dual phase membrane (60 vol% CGO20: 40 vol% FCO) has been systematically investigated as a function of the thickness of the membrane by applying the catalytic activation LSCF layer at one or both sides to understand the effects of surface modification. Moreover, the surface exchange kinetics impact on the oxygen transport have been done in terms of the surface coating of the CGO20-FCO composite, by varying the membrane thickness. To the best of our knowledge, there has been no detailed and systematic study of thickness influence on the permeation in the CGO20-FCO dual-phase membrane.

6.2 Experimental

6.2.1Sample preparation

$Ce_{0.8}Gd_{0.2}O_{2-\delta}$ (CGO20) (Cerpotech, >99%, Tiller, Norway), Fe_2O_3 (FO) (Merck, 99 %) and Co_3O_4 (CO) (Merck, 99 %) powders used for the experiments were synthesized by the Solid-State Reactive Sintering method (SSRS). Fe_2O_3 and Co_3O_4 were mixed, in a 1:2 Fe: Co ratio, resulting in spinel $FeCo_2O_4$ (FCO), which was added to commercially available Gd-doped ceria. Respective amounts of powders were weighed to create $Ce_{0.8}Gd_{0.2}O_{2-\delta}$ - $FeCo_2O_4$ (CGO-FCO) compositions with a weight ratio of 60:40. The powder mixtures were ball milled in polyethylene bottles over 48 h using zirconia balls on a roller bench at a speed of 175 rpm. After drying for 48 h in ambient air at 70° C, the powder mixtures were pressed in a 20-mm stainless steel die using a uniaxial press into disc-shaped membranes, which were then sintered at 1200°C for 5h. At this sintering temperature, the spinel partially reduces into a high-temperature monoxide phase with a rock salt structure. To ensure complete reoxidation of the high-temperature Co/Fe-monoxide phase to a spinel phase that is stable at operating temperatures (600-1000°C), a slow rate of 0.5 K min^{-1} between 900 and 800 °C was implemented in the cooling cycle. This rate was determined by referring to the $Fe_{3-x}Co_xO_4$ phase diagram [22,23] After the sintering step, all samples were ground down to 0.4, 0.6, 0.8, 1,1.5- and 2-mm thick discs in 2 steps, applying SiC merge papers with different grits from P 800 to P 1200 (by WS FLEX 18C). On both sides of the discs, a porous $La_{0.58}Sr_{0.4}Co_{0.2}Fe_{0.8}O_{3-\delta}$ (LSCF) catalytic activation layer with a thickness of 5 μm was applied using a screen-printing technique. Further sample with different type of surface modification were prepared by applying LSCF layer at one or both sides, as listed in Table 6.1. Discs were then calcined in the oven at 1100 °C for 5 h.

Table 6.1 Samples for the surface modification investigation with the thickness 0.6 mm

Sample name	Surface modification
A	Both-side coated
B	Feed side coated
C	Sweep side coated
D	Bare

6.2.2 Characterization methods

Crystal structure

The crystal structure of the samples was determined using the X-ray diffraction (XRD) diffractometer D4 ENDEAVOR (Bruker, Karlsruhe, Germany). The diffraction angle was chosen in the range of 2θ from 10° to 80°, with increments of 0.02° for 2θ and 0.75 seconds of measurement time per step. Analysis of the measured data was performed with X'Pert HighScore (PANalytical B.V., version 3.0.5) software. Phase quantifications and associated crystal structure analyses were carried out by Rietveld refinement using (Version 4.2.2) software. The low error R_{wp} was held <4 % for all samples, which also indicates the good fitting. The errors of each fit were calculated individually and are reported in Table 6.2.

Microscopy

Scanning Electron Microscopy (SEM) and Energy Dispersive X-ray Spectroscopy (EDXS) were used to obtain material morphology. SEM images were taken with a Zeiss Ultra 55 and a Zeiss Supra 50 VP1 (Carl Zeiss NTS GmbH, German) SEM at different magnifications. The electronic conductivity of the samples was enhanced by sputter deposition of a thin platinum layer prior to measurement.

Oxygen permeation measurements

All composite materials were subjected to oxygen permeation experiments. The experimental setup consisted of vertical quartz glass housing, where the membrane pellets were sealed with two gold rings with an inner diameter of 13 mm. The separation of oxygen from ambient air fed with 250 $ml_N\ min^{-1}$ was performed in a temperature range between 650 °C and 1000 °C. As a sweep gas argon was used with 50 $ml_N\ min^{-1}$ flow rate using mass flow controllers (Bronkhorst, Germany).Oxygen and nitrogen concentrations in the permeate gas, i.e., oxygen enriched argon was detected by the mass spectrometer (Omnistar, Pfeiffer Vacuum GmbH, Germany). Air leakage through either membrane or the sealing was calculated based on the measured nitrogen concentration in the permeate according to

$$j_{O_2} = F_{Ar}\left(\frac{X_{O_2} - \frac{1}{4}X_{N_2}}{1 - X_{O_2} - X_{N_2}}\right)\frac{1}{A_{mem}}$$ **Equation 6.5**

Here F_{Ar} is argon flow rate, *i.e.,* 50 $ml_N\ min^{-1}$, X_{O2} and X_{N2} the oxygen and nitrogen concentration in the permeate gas, respectively, and open membrane area is

A_{mem}=1.33 mm^2. The factor $\frac{1}{4}$ reflects the O_2/N_2 ratio in the air feed assuming that the leak is not gas selective.

Since the oxygen partial pressure in the permeate gas is temperature dependent, the driving force of the permeation rate is not constant during the measurement. Additionally, the sample thickness deviation after the grinding process was ±8% from the target thickness of 1 mm. Consequently, the driving force normalized permeation rate, also referred to as permeance, was normalized to the reference thickness of L_0 = 1 mm and was calculated assuming Wagner behaviour using the following equation.

$$Permeance = \frac{j_{O_2}}{ln\frac{p'_{O_2}}{p''_{O_2}}}\frac{L_{mem}}{L_0}$$ **Equation 6.6**

Here, p'_{O_2} and p''_{O_2} are the oxygen partial pressures in the retentate and permeate gas, respectively, and L_{mem} is the actual membrane thickness. The overall experimental error is assumed to be ±10%, which is well accepted in the literature.

6.3 Results and discussion

6.3.1 Microstructure of 60CGO-FCO composite

The 60CGO-FCO composite microstructure features with the main characteristics have been investigated in detail by Fischer et.al. in [24] .

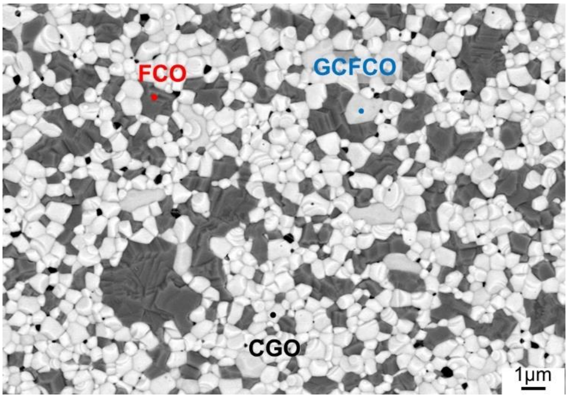

Figure 6.3 a) SEM image of the 60CGO20-FCO composite sintered at 1200°C for 5 h, fluorite grains are white, spinel grains are black, and the perovskite–grey

In all sintered samples the final microstructure consists of three phases after phase interaction: CGO a cubic fluorite structure with space group *Fm3m*, and orthorhombic donor-doped $GdFeO_3$ (GCFCO) perovskite structure with space group *Pnma*, and Fe/Co rich phases with a cubic spinel structure with space group *Fm3m*. The mean grain size of 0.64 µm as well as pore size was analysed by an image analysis-based method with ImageJ software [25,26]. In annealed pellets, the grains of each type are closely packed and uniformly distributed and can be distinguished by different grey scales, as depicted in Figure 6.3. The membrane was densified with ~6 % of porosity at a sintering temperature of 1200 °C for 5 h. The relative density of the sintered membrane is calculated to be ~94-95% from the geometry of the pellet. The sintered membrane was sufficiently dense to exclude leakage since the leaked oxygen flux calculated from the nitrogen permeance is low (10^{-12}).

6.3.2 Surface area modification

The sample without coating was tested in a permeation setup and a post-measured pellet was subjected to microstructure analysis via XRD and SEM methods since some visual differences on the surface were seen after permeation tests. The as-pressed pellet showed the presence of three used SSRS oxides: Fe_2O_3, Co_3O_4, and 20 mol. %

Gd-doped ceria. The as-sintered sample contains the following phases cubic CGO, an orthorhombic donor-doped $GdFeO_3$ (GCFCO) perovskite, and two spinel phases with a cubic structure. The FCO reflection at 36.5°2θ is split up into a broad reflection with two maxima prior to measurement, indicating Fe-rich and Co-rich spinel types. However, after the permeation measurement, the difference in the phases at both feed and sweep sides is more pronounced, emphasizing the impact of the partial pressure gradient on the phase segregation. The spinel peaks are clearly separated and placed between 36 and 37°2θ at the sweep side, as shown in Figure 6.4a.

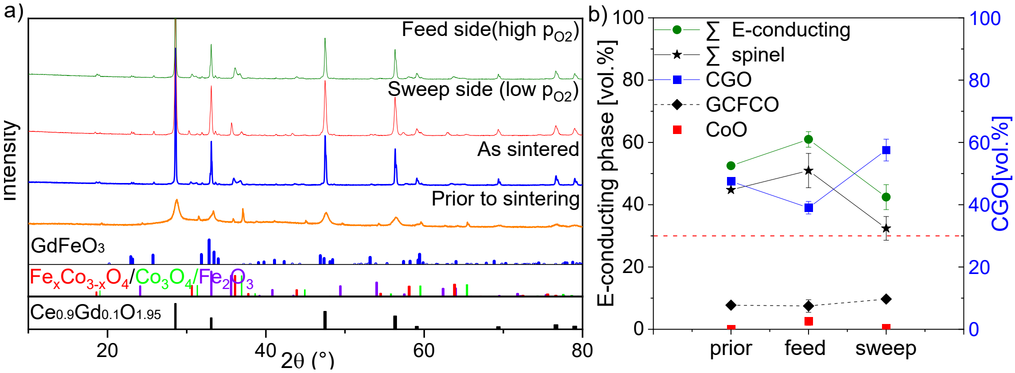

Figure 6.4 a) XRD patterns of the 60CGO-FCO as sintered and after permeation measurement membrane exposed to the feed and sweep side b) The volume fraction of the phases and b) volume fraction of the phases before and after permeation measurements (solid lines are a guide to the eye)

The post-test Rietveld refinement shows the composition of the dual-phase composites after permeation measurement on both sides (Table 6.2 and Figure 6.4b). The lattice parameter of pure CGO20 used in our composite before phase interaction was measured (a_{CGO20} =0.5425 nm) and it was found to decrease by the addition of the spinel resulting in a_{CGO}= =0.5418±0.0001 nm, compared to that of pure CGO20, however, there was no remarkable change in CGO lattice parameter before and after permeation measurement. The Fe-rich spinel lattice parameter is slightly increased after measurement, with the highest value for the sweep side, while the Co-rich spinel unit cell is decreased at the sweep side. Rietveld refinement confirmed spinel enrichment on the feed side of the membrane during permeation measurement, while the fluorite fraction is decreased. Additionally, ~1.3 wt.% of CoO is estimated on the feed side, whereas no rock salt phase is detected on the sweep side after measurement and in the sample prior to the measurement.

Table 6.2 Lattice parameter (a) and fraction (F) of the phases after quantification by Rietveld refinement of the 60CGO-FCO composites prior and post-measurement

	CGO(Fluorite), Fm***3m***		**FCO (Spinel),** Fd***3m***		**Co_3O_4(Spinel),** ***Fd3m***		**GCFCO (Perovskite),** ***Pnma***				**CoO** ***Fm3m***
Sample	F, wt.%	a=b=c, Å	F wt.%	a=b=c, Å	F, wt.%	a=b=c, Å	F, wt.%	Lattice parameter, Å			F, wt.%
								a	b	c	
CGO	100	5.424[3]	-	-	-	-	-	-	-	-	
Prior	52.1[6]	5.418[4]	22.3[4]	8.29[6]	16.61[6]	8.13[4]	9.0[1]	5.34[0]	5.608[5]	7.64[4]	-
Measured											
feed	42.18[1]	5.418[6]	28.1[6]	8.30[5]	20.62[6]	8.15[2]	6.43[9]	5.33[8]	5.61[6]	7.65[1]	1.28[1]
sweep	60.98[3]	5.419[2]	15.9[9]	8.36[6]	7.89[3]	8.10[6]	9.42[4]	5.34[1]	5.61[6]	7.65[5]	0.43[1]

Further SEM image analysis underlined the results from XRD, as shown in Figure 6.5 and Figure 6.6. Both surfaces are rough and uneven with inhomogeneous distribution of the spinel and fluorite grains. At the feed side large dark spinel grains are dominant and cover the majority of the surface, while at the sweep side, there are low fraction spinel grains but CGO. The sweep side surface is very porous with a large number of holes.

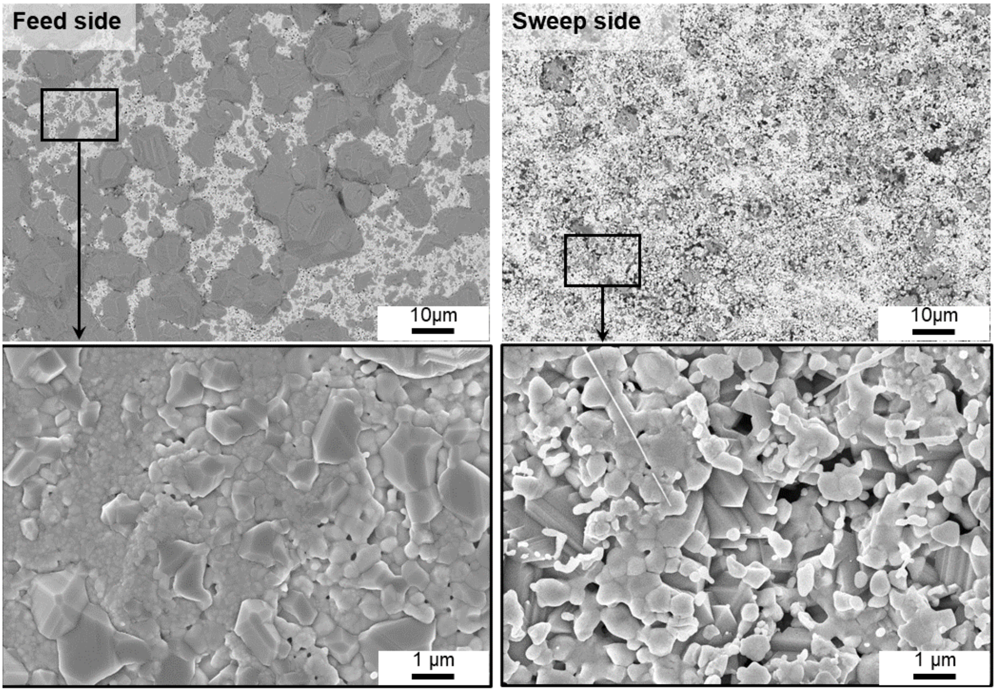

Figure 6.5 SEM of the surfaces of the 60 CGO-FCO composites on the feed (high p_{O2}) and sweep (low p_{O2}) sides post permeation measurements in the temperature range of 700-1000°C with the Air/Ar gradient

Since the fraction of the emerged GCFCO phase is almost constant for different ratios of CGO20: FCO [24,27], so the same amount of the Fe and Co cations will be taken for the GCFCO phase formation. Thus, we can assume that by reduction of the FCO in the composite, less residual FCO will be segregated at the feed side.

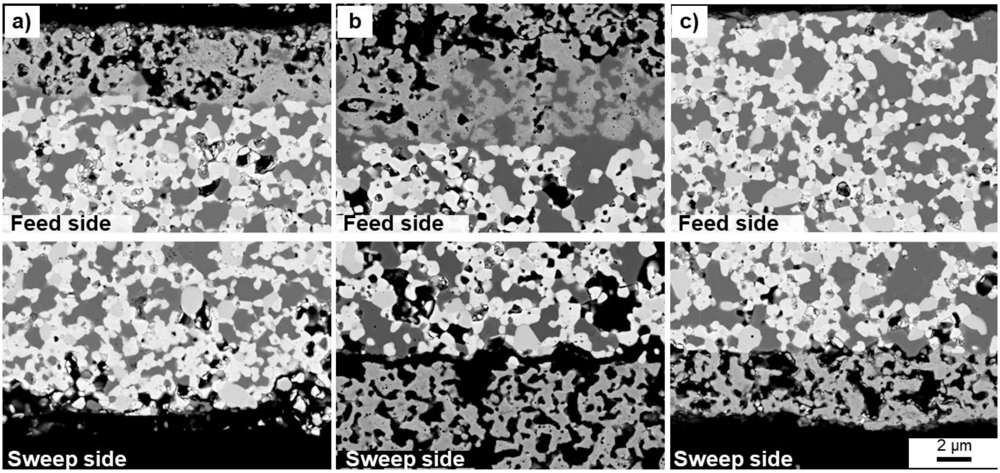

Figure 6.6 Cross-section of the measured 60CGO20-FCO membranes coated at the a) sample B feed b) sample C sweep or c) sample A on both sides

The cross-section of measured membranes shows enlarged dark crystals at the feed side of the membrane (Figure 6.6c), which is a result of the iron and cobalt cations movement towards the high oxygen partial pressure side during permeation [28–30]. The same effect was observed by Ramasamy [31] with enrichment of the spinel phase on one side with a clearly darker surface colour after permeation tests. By modification of the gas-solid interfaces, iron and cobalt cations diffuse into the LSCF layer (Figure 6.6b), forming the intermediate structure. Cobalt is known to have larger mobility than iron [32] thus it is expected that each intermediate reduction product in the Fe-Co-O system is usually initially Co-rich and then progressively increases in iron concentration [33]. Due to the higher diffusion rate of spinel cations and its resulting segregation on one side of the membrane, the transport of the charge carriers in the bulk can be negatively affected.

At the low oxygen partial pressure side, the membrane surface is quite uneven with a higher CGO grains fraction. Moreover, an additional gas layer with ~ 0.5 μm thickness between the coating and the bulk membrane is observed (Figure 6.6b) in the both side coated membrane, which nature is not clear so far. Moreover, this gap formation moment is also unknown, it could happen during the permeation test, during sample installation, or sample removal from the permeation setup. So, to make a solid conclusion further systematic investigation of this phenomenon is required.

6.3.3 Functional properties

The impact of the surface modification at the feed, sweep or both sides on the transport properties of the membrane was investigated. Four differently coated pellets were studied in context to morphology and oxygen permeation. Since the CGO20-FCO composite is a mixture of the pure ion-conducting and pure electron conducting phases, there are only two possibilities for the transport of charge carriers within the compound. FCO has high electronic conductivity and poor ionic one [27,34], providing the transport possibility for the electrons, thus the oxygen ion transport through spinel can be excluded. CGO20, on the other hand, is a pure ionic conductor, so the TPB is required for the sufficient transport of electrons and ions. To prolong the paths for both charge carriers and provide more TPB at the surfaces, a catalytic porous layer of LSCF was applied over the composite to address surface exchange limitations. The potential route for the e- and ions in the studied sample of 60CGO20-FCO dual-phase composite schematically represented in Figure 6.1b.

These routes however should be modified according to the observation after the real permeation test. Based on the SEM analysis and the resulting oxygen flux though the samples, the ionic and electronic paths could be illustrated as in Figure 6.7.

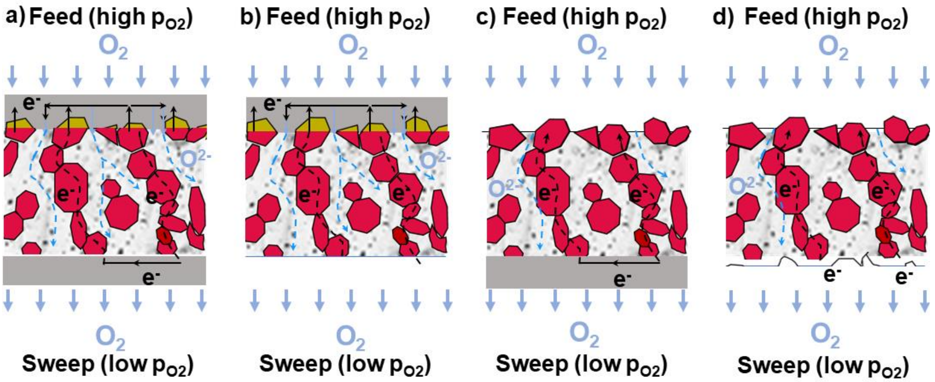

Figure 6.7 Schematic representation of the possible transport paths of e and ions during the permeation in tested a) both side coated b) feed side coated c) sweep side coated d) bare membrane; (red grains are electron conducting phase, yellow is the newly formed phase, the grey layer is coating)

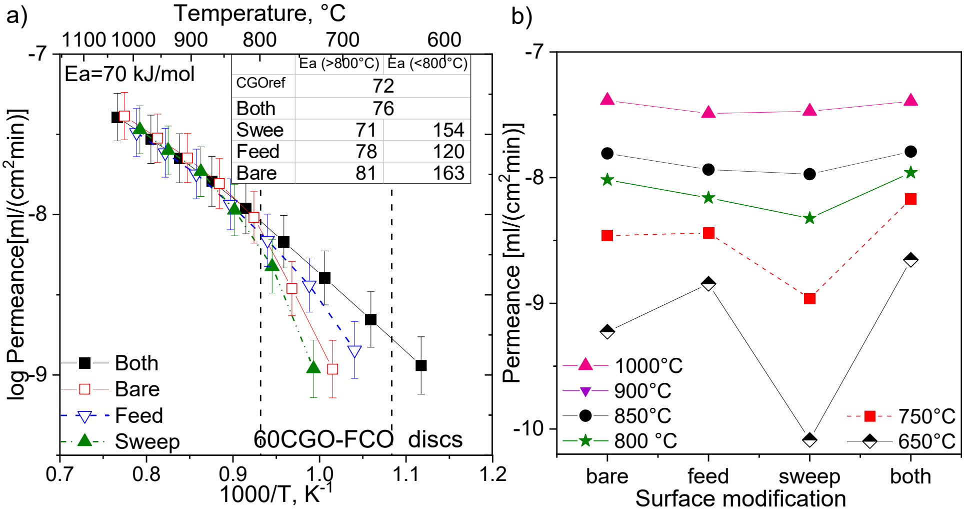

Figure 6.8 a) Comparison of the permeance in the context of the surface modification of the 0.6 mm thick bulk membrane b) Oxygen permeance at various temperatures (solid lines are a guide to the eye)

The resulting oxygen flux of the 60CGO20-FCO membranes with 0.6 mm thickness are depicted in Figure 6.8. At a high-temperature regime (>800°C) all samples exhibited a negligible difference in the oxygen flux, which is in the error range. The E_a of permeation for all four samples is similar and lies in the range of 70-85 KJ/mol, which is similar to $E_{a(CGO)}$ reported in literature [35,36]. At low temperatures, the difference in the oxygen flux is more pronounced for the samples with and without surface modification. The E_a of permeation is in the following order: both sides-activated, feed-activated, bare, and sweep-activated. The coating on both sides of the membrane reveals the largest oxygen flux at the low-temperature regime, suggesting that the surface modification significantly changes the rate-determining step in oxygen transport in ceria-based composites. It should be also mentioned that the E_a of both side-coated materials is close to the $E_{a(CGO)}$, pointing out that along the whole investigating temperature range the ionic conductivity is governing the transport process in the membrane. Since the resistances on the feed and sweep side are reported to be different, i.e., sweep side resistance is 2.5 times higher compared to the feed side in the dual-phase composite [37], the resulting permeation should be also different with respect to modified side. However, in our case the addition of the catalytic layer on the feed side (sample B) leads to the improvement of the oxygen flux, while only the sweep side-activated (sample C) reveals the lowest oxygen flux. The low electronic conductivity of the CGO and poor surface exchange kinetics on the feed side is the reason why the application of the catalytic layer only on the sweep side has not increased oxygen flux.

These results suggest that the surface-exchange kinetics on each surface is different, namely, the reaction of incorporation of the oxygen at the feed side is different than the reaction of extrapolation on the sweep side. Since the slight degradation of the oxygen flux through material is seen for the sample C it can be assumed that the rate-limiting is the incorporation reaction on the feed side for the membrane D. Thus, the application of the catalytic layer on the feed side enhanced the oxygen permeation through the composite at low temperatures, probably due to the increased continuous paths for the transport on the surface, which positively affects the oxygen incorporation reaction. Another possible explanation could be the segregation of the spinel phase at the feed side, as discussed above and shown in Figure 6.6 and Figure 6.7. Due to modification on the feed side, the newly formed structure at the interface between membrane and LSCF can still participate in the transport as TGB for example, and thus facilitate the transport of both types of charged particles, still preserving a good percolation in the material. However, by sweep side coating the spinel segregation at the high p_{O2} side (feed side) covers/ blocks the surface, which effectively participates in the oxygen-exchange reaction for oxygen incorporation. Hence, it reduces effective surface and breaks continuous particle paths, resulting in overall lower percolation in the dual-phase composite. In other words, without LSCF coating at the feed side, the spinel crystals possibly hinder the transport of charged species. Moreover, the role of the gas layer, formed at the sweep side between LSCF and a bulk membrane is not clear yet and needs to be further investigated. But since this gas gap is most likely not participate in the transport the charged species, it could be assumed to be an obstacle for the e- or ionic transport.

6.3.4 Thickness dependence

Figure 6.9 shows the temperature dependence of the permeance value for 60 CGO20-FCO composites with and without a coating layer. Generally, the oxygen flux increases with decreasing the thickness of the membranes within the investigated temperature range. All samples with both-side applied catalytic LSCF layer reveal the oxygen flux curves with no bands and constant E_a value of ~80 kJ/mol between 1000 and 700°C, emphasizing the LSCF layer effectiveness to overcome all possible surface limitations.

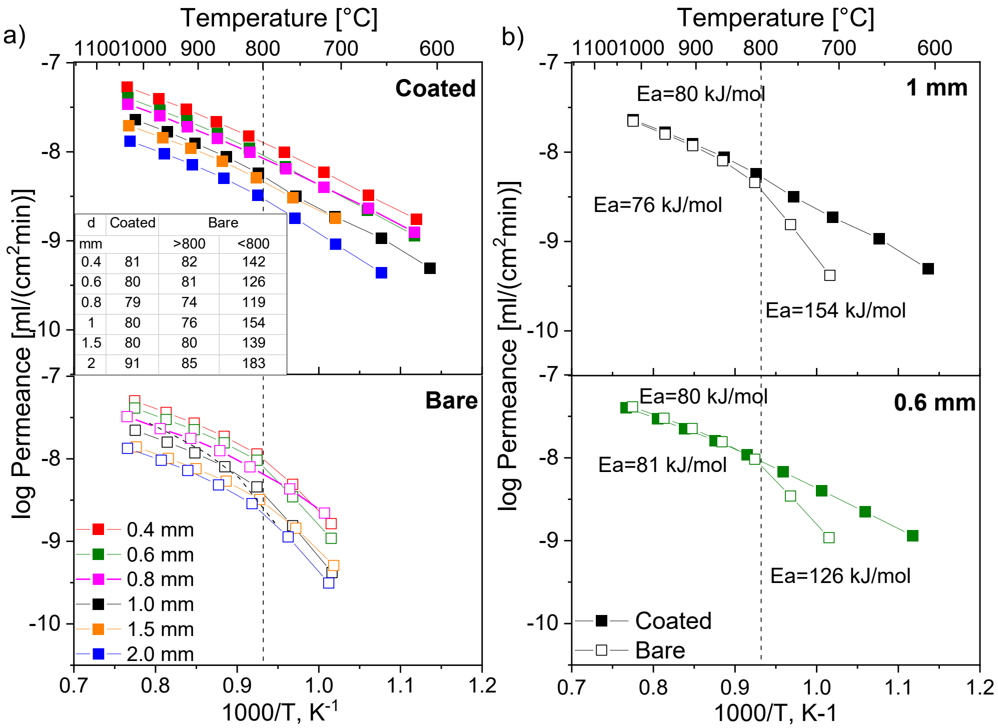

d	Coated	Bare	
mm		>800	<800
0.4	81	82	142
0.6	80	81	126
0.8	79	74	119
1	80	76	154
1.5	80	80	139
2	91	85	183

Figure 6.9 Arrhenius plots of measured permeance of bulk membranes with the thickness between 0.4- and 2-mm *a)* with applied catalytic LSCF layer and without and b) comparison of 1 mm and 0.6 mm thick membranes (solid lines are a guide to the eye)

However, an increase in oxygen flux is seen only till a certain membrane thickness, by further reduction there will be no effect of the catalytic layer [38]. Bare samples exhibit one band at ~800°C, where likely change of transport mechanisms takes place with a change of activation energy. Between 800 - 1000°C the activation energy can be accounted for the ionic conductivity of doped ceria[35,36], beneath 800°C all samples reveal the higher value of E_a (over 100 kJ/mol), due to surface exchange limitations. These results indicate that the oxygen permeation of bare dual-phase composite membrane is not only controlled by bulk diffusion but also controlled by surface-exchange kinetics, especially at low temperatures. This observation implies that the application of the activation layer plays a crucial role to build continuous paths for oxygen ion transport in the fluorite phase and thus effectively improving the oxygen flux. At temperatures beneath 650°C high leakage leads to more bands, so this temperature range will be not taken for further analysis. As an example, bare and coated 1 mm thick and 0.6 mm thick membranes were compared. The oxygen flux j_{O2}

of a 1 mm-thick pellet at 700 and 850 ◦C increased ~4 and 1.1 times respectively from that of the uncoated membrane as a result of LSCF layer application. Interestingly, the 0.6 mm thick bare membrane showed a slightly higher oxygen permeance at high temperatures compared to the coated one. However, the oxygen permeance of that sample is still in the range of the measurements error. This could be because of the limited thickness of the sample, where the surface exchange kinetics plays a more significant role. Another possible explanation could be a porous catalyst layer's contribution to oxygen transport. The bare membrane consists of a mix of CGO and two electron-conducting oxides Co_3O_4 and Fe_2O_3. Co_3O_4 is known for its high electron conductivity and in some cases, it is used as an additive to facilitate the conducting properties of materials, resulting in high permeance of the composite [39,40]. Thus, in a bare CGO20-FCO membrane, CGO provides ion-transport, while Fe_2O_3 and Co_3O_4 enable the e-transport. It has been reported that adding cobalt oxide to CGO effectively increases the surface exchange coefficient providing a higher number of electrons [39]. This Co oxide contribution could be more effective for the thinner membranes compared to the LSCF porous catalyst layer, which is known to be a mixed conductor. Thus, slightly higher oxygen permeance can be measured in the bare CGO20-FCO disc.

In order to build the Wagner´s model for our material system some parameters were estimated from the 2 mm thick membrane measurement, such as ambipolar conductivity ($\sigma_{amb}^{850°C}$=1.72*10^{-2} S/cm), oxygen partial pressure gradient at T=850°C, and the activation energy (E_a=80 kJ/mol). Assuming no surface limitations, the oxygen flux, permeance (driving force normalized permeation rate) and specific permeability (driving force and thickness normalized permeation rate) at 850°C can be modelled for dual-phase CGO20-FCO material system.

Figure 6.10 shows the experimental data with the comparison of Wagner´s equation, inclusive of assumed L_c range. According to Wagner´s theory with the absence of L_c (L_c=0), the oxygen flux should be proportional to 1/L if the permeation process is determined only by bulk diffusion. Under the given conditions of thick samples, the permeance is proportional to 1/L. Decreasing the thickness of the sample further leads to a less pronounced increase in permeance, resulting in deviation from the straight line. And from L_c in the grey field increase in oxygen flux does not follow Wagner's theory anymore, the permeation values are considerably smaller than the value extrapolated from the linear part of the line. This tendency suggests that the oxygen permeation through material is partially limited by the surface oxygen exchange process. Wagner's theory is considering only solid-state diffusion, hence to account for the growing limitation of surface exchange reactions, the equation should be accordantly modified [16,21]. For this introduction L_c is required, this value is transition thickness from bulk-limited permeation to surface exchange limited one.

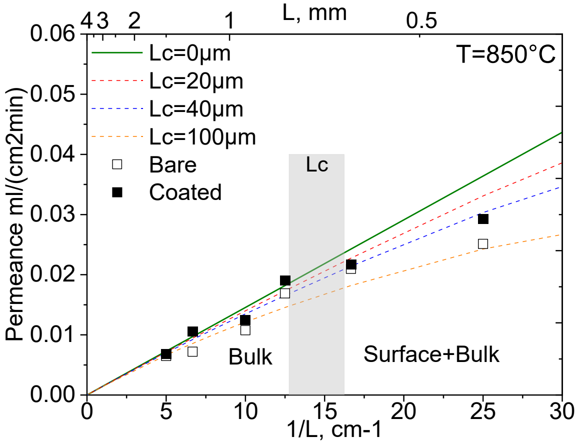

Figure 6.10 Experimental and modelled permeance with approximate L_c value range at 850°C. The dashed lines represent only approximation not model

To estimate the value of L_c at different temperatures the common used least square method is selected [41–44], so some assumptions should be made. For this we need to distinguish temperature-dependent terms from the modified Wagner equation and with the help of the least square fitting method C (specific permeability $\mathrm{C} = \mathrm{j}_{\mathrm{O2}}^{\mathrm{permeance}} \cdot \mathbf{L}$) and L_c characteristics can be estimated according to the following equation

$$\mathbf{j_{O2}} = \mathrm{C} \cdot \frac{\mathbf{1}}{\mathbf{L+2L_c}}$$

With the fixed oxygen partial pressure gradient, the values are mathematically defined, if the ionic conductivity is known. Although the exact σ_{ion} value is unknown the best fitting with the C and L_c parameters is possible. The calculation was done with the convergence tolerance of 10^{-6}.

$$(j_{O2}^{permeance} - C \cdot \frac{1}{L+2L_c})_{sum}^{2} = minimum$$ **Equation 6.7**

With the $j_{O2}^{permeance}$ is the experimentally measured oxygen flux value for pellets with the thickness from 0.4 to 2 mm.

Figure 6.11 show Wagner´s model comparison with the experimental data at 700, 850, and 950°C. By decreasing temperature, the deviation from Wagner´s model is smaller for the coated samples compared to uncoated ones, depending on thickness. By considering the L_c parameter in the modified Wagner's equation the fitted results are in agreement with the experimental data. Furthermore, the difference between the coated and uncoated pellets gets more pronounced, by lowering the temperature. These results again emphasize that the surface kinetics should be considered for the dual-phase membranes in investigated thickness range. The membrane becomes more surface limited by decreasing membrane thickness or decreasing temperature. Hence, it can be assumed that further reduction of the membrane thickness (beneath 0.4 mm) will enhance the oxygen flux in lower temperature regions.

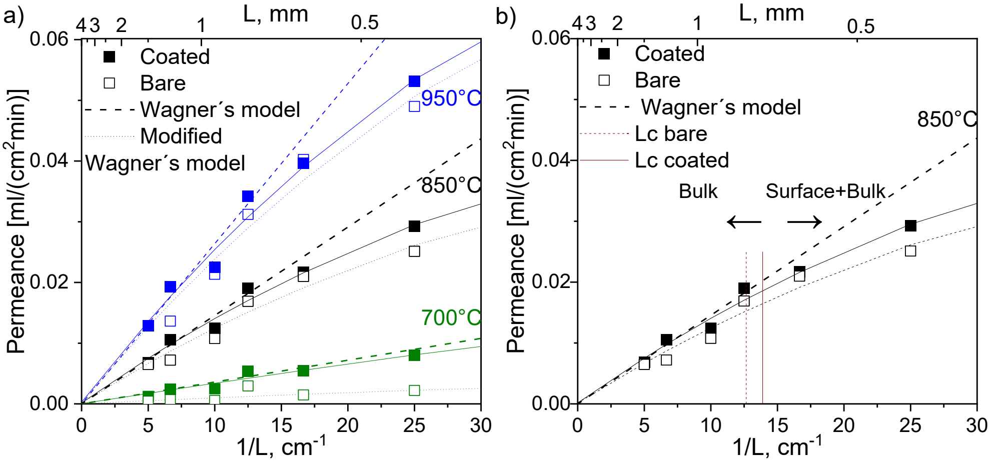

Figure 6.11 Oxygen permeation fluxes of the CGO-FCO membrane at 700, 850, and 900 °C temperatures over the inverse membrane thickness. Solid points and lines are for the coated samples and open ones for the uncoated ones (solid lines are a guide to the eye)

As an example, at 850°C the L_c illustrated for the experimental values and compared with the Wagner´s model and modified model. A decrease in thickness leads to an increase of oxygen flux however until a certain thickness, beyond which both bulk and surface exchange kinetics of the membrane at the gas/solid interfaces contribute to the oxygen transport. In our composite, we observe bulk-diffusion limited behaviour in the 1.5, 2-, 1-, and 0.8-mm thick membranes, where linear dependency between j_{O2} and 1/L is observed. The calculated L_c for both values at 850°C are close to each other, demonstrating that for both types of samples with thickness <0.8 mm, the L_c should be considered in Wagner´s model.

The estimated L_c values of both coated and bare dual-phase composite membranes are listed in Table 6.3 and plotted in Figure 6.12 over the temperature in the range between 700°C and 1000°C. Since at T<700°C for several samples the oxygen flux was not reliable due to the high leakage during measurement, thus they are not taken in the analysis. To evaluate the effectiveness of performed fitting, the value R^2 is calculated for each temperature, according to Equation 6.8. The mean R^2= 96.6 % for the coated samples, and 90 % for uncoated ones.

Table 6.3 L_c and constant values fitted by least square method for temperatures between 700 and 1000°C

	Coated		Bare	
T, °C	C*10^{-8}, mol/cm*s	L_c, cm	C*10^{-8}, mol/cm*s	L_c, cm
700	0.04	0.017	0.01	0.112
750	0.06	0.021	0.04	0.077
800	0.10	0.056	0.09	0.069
850	0.16	0.067	0.14	0.074
900	0.22	0.067	0.21	0.072
950	0.29	0.070	0.27	0.070
1000	0.39	0.066	0.37	0.067

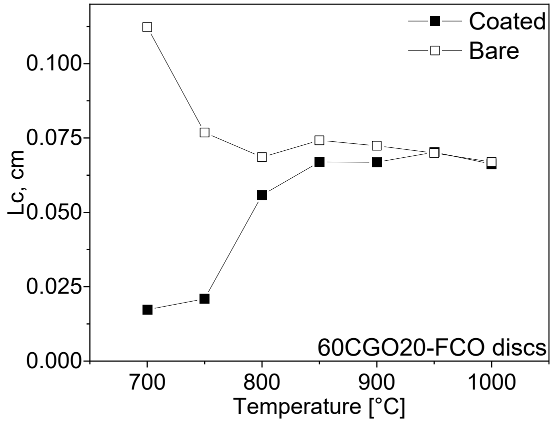

Figure 6.12 L_c value estimated in least square method over temperature for bare and coated pellets (solid lines are a guide to the eye)

$$R^2 = 1 - \frac{SQR}{RSS}$$ **Equation 6.8**

Where the RSS is residual sum of squares, and SQR is reduced Chi-square value and can be found as:

$$RSS = \sum (J_{O2}^{measured} - J_{O2}^{mean})^2$$ **Equation 6.9**

$$SQR = \sum (J_{O2}^{measured} - J_{O2}^{fit})^2$$ **Equation 6.10**

The L_c value represents the border between the transport limiting mechanisms, bulk, and mixed bulk-surface. The region above the line is bulk-limiting, and beneath the L_c the surface limiting. Based on our modelling, in general, smaller L_c values were found for the both-side coated membranes (solid symbols) than for those without coating (open symbols). With a decreasing temperature L_c value decreased for coated samples, while for bare samples decrease in temperature leads to an increase in L_c value. At temperatures, 950-1000°C there is no significant difference between L_c of coated and bare membranes, so presumably only bulk transport is dominant for the CGO20-FCO composite, independent of coating application. The surface modification reduces the L_c significantly in the ceria-based composite, especially for the T<850°C, comparting to the pure CGO, where the L_c value is in the cm range (with D=2*10^{-8}cm^2/s, k=3*10^{-9} cm/s at 800°C) [43].

From the underlying assumption that the temperature dependence of the characteristic membrane thickness follows an Arrhenius approach, statements about the activation energies can be made for bulk transport and surface exchange.

$$L_c = \frac{D_s}{k_s}$$ **Equation 6.11**

$$L_c(\mathrm{T}) = \frac{D_s}{k_s} = \frac{D_{s0} \cdot exp(-\frac{E_{A,D}}{RT})}{k_{s0} \cdot exp(-\frac{E_{A,k}}{RT})} = L_{c,0} \cdot exp(-\frac{E_A}{RT})$$ **Equation 6.12**

$$E_A = E_A^D + E_A^{ks}$$ **Equation 6.13**

For bare membranes $E_a^{ks} > E_a^D$, the difference $E_a < 0$ and an increase in L_c are expected with reducing temperatures, which is in agreement with our results. A similar trend is seen for the single-phase BSCF [45]. For coated samples the effect of the surface limitations is reduced, hence $E_a^D > E_a^{ks}$ and the difference in$E_a > 0$. In this case, the L_c value is effectively reduced with the temperature decrease, with a minimum of 0.02 cm at 700°C for the activated sample. The difference between the L_c of the bare and coated pellets gets larger by reducing the temperature. This result underlines again the importance of surface modification for the CGO20-FCO composite in particular at low temperatures.

6.4 Conclusions

MIEC composites are based on commercially available powders of 60 wt. % $Ce_{0.8}Gd_{0.2}O_{2-\delta}$ in combination with 40 wt. % spinel $FeCo_2O_4$ can be successfully synthesized by the cost-efficient solid-state reactive sintering (SSRS) technique and subjected to one-step heat treatment at 1200°C for 5h. The reduction of the membrane thickness from 2 mm down to 0.4 mm reveals the improved permeation performance of both side-coated pellets with the oxygen flux of 0.25 and 0.12 ml/cm^{2}min at 950 and 850 °C respectively. The oxygen flux of uncoated membranes at high temperatures is similar to coated ones, indicating that the transport is bulk-limited, while at low temperatures the surface exchange kinetics should be taken into account. Moreover, the L_c of the bare sample is larger compared to coated ones and it is increasing with reduced temperatures with a maximum of 1.12 mm at 700°C. At 850°C the L_c=0.74 mm for the uncoated membrane, indicating that from this value the effect of surface exchange kinetics should be considered in the dual-phase ceria-based composite. In our case, it was suitable to utilize Wagner´s equation for the 2, 1.5, 1- and 0.8-mm thick membranes. Further reduction of the thickness leads to more pronounced surface exchange limitations and does not follow Wagner’s equation anymore. Over 900 °C the L_c is almost identical for both bare and coated membranes, demonstrating that the surface limitations at high-temperature ranges are negligible for CGO-FCO composite. Further reduction in the thickness to the µm range is advisable to analyse the impact of surface exchange kinetics for the thin OTM.

Surface modification on one or both sides of the membrane is found to greatly affect the final oxygen flux at low temperatures (<850°C), while at high temperatures the difference in oxygen flux is minor. Our observations show the importance of surface modification with a catalytic layer for dual phase membranes at low temperatures. Furthermore, the application of such a catalytic layer on one side can lead to either improvement or degradation of the permeation of the CGO-FCO composite compared to the bare one at the low-temperature range, depending on which side is activated. Microstructure analysis shows the differences between the feed and sweep sides, demonstrating a higher volume of the spinel phase on the feed side of the bare membrane, while enrichment of the fluorite phase was found on the sweep side. The segregation on one side of the uncoated membrane has a negative effect on the percolation in the dual-phase material, resulting in a lower oxygen permeation.

References

1. Kiebach, R.; Pirou, S.; Martinez Aguilera, L.; Haugen, A.B.; Kaiser, A.; Hendriksen, P.V.; Balaguer, M.; García-Fayos, J.; Serra, J.M.; Schulze-Küppers, F.*; et al.* A review on dual-phase oxygen transport membranes: from fundamentals to commercial deployment. *J. Mater. Chem. A* **2022**, *10*, 2152–2195.

2. Zhu, X.; Yang, W. *Mixed Conducting Ceramic Membranes*; Springer Berlin Heidelberg: Berlin, Heidelberg, 2017.

3. Bai, W.; Feng, J.; Luo, C.; Zhang, P.; Wang, H.; Yang, Y.; Zhao, Y.; Fan, H. A comprehensive review on oxygen transport membranes: Development history, current status, and future directions. *International Journal of Hydrogen Energy* **2021**, *46*, 36257–36290.

4. Serra, J.M.; Garcia-Fayos, J.; Baumann, S.; Schulze-Küppers, F.; Meulenberg, W.A. Oxygen permeation through tape-cast asymmetric all-La0.6Sr0.4Co0.2Fe0.8O3−δ membranes. *Journal of Membrane Science* **2013**, *447*, 297–305.

5. Schulze-Küppers, F.; Baumann, S.; Tietz, F.; Bouwmeester, H.; Meulenberg, W.A. Towards the fabrication of $La_{0.98-x}Sr_xCo_{0.2}Fe_{0.8}O_{3-\delta}$ perovskite-type oxygen transport membranes. *Journal of the European Ceramic Society* **2014**, *34*, 3741–3748.

6. Baumann, S.; Serra, J.M.; Lobera, M.P.; Escolástico, S.; Schulze-Küppers, F.; Meulenberg, W.A. Ultrahigh oxygen permeation flux through supported Ba0.5Sr0.5Co0.8Fe0.2O3−δ membranes. *Journal of Membrane Science* **2011**, *377*, 198–205.

7. Zhao, J.; Pang, Y.; Su, C.; Jiang, S.; Ge, L. Toward High Performance Mixed Ionic and Electronic Conducting Perovskite-Based Oxygen Permeable Membranes: An Overview of Strategies and Rationales. *Energy Fuels* **2023**, *37*, 7042–7061.

8. Shao, Z.; Xiong, G.; Dong, H.; Yang, W.; Lin, L. Synthesis, oxygen permeation study and membrane performance of a Ba0.5Sr0.5Co0.8Fe0.2O3−δ oxygen-permeable dense ceramic reactor for partial oxidation of methane to syngas. *Separation and Purification Technology* **2001**, *25*, 97–116.

9. Tan, X.; Liu, N.; Meng, B.; Sunarso, J.; Zhang, K.; Liu, S. Oxygen permeation behavior of $La_{0.6}Sr_{0.4}Co_{0.8}Fe_{0.2}O_3$ hollow fibre membranes with highly concentrated CO_2 exposure. *Journal of Membrane Science* **2012**, *389*, 216–222.

10. Gao, J.; Li, L.; Yin, Z.; Zhang, J.; Lu, S.; Tan, X. Poisoning effect of SO_2 on the oxygen permeation behavior of $La_{0.6}Sr_{0.4}Co_{0.2}Fe_{0.8}O_{3-\delta}$ perovskite hollow fiber membranes. *Journal of Membrane Science* **2014**, *455*, 341–348.

11. Yi, J.; Schroeder, M. High temperature degradation of $Ba_{0.5}Sr_{0.5}Co_{0.8}Fe_{0.2}O_{3-\delta}$ membranes in atmospheres containing concentrated carbon dioxide. *Journal of Membrane Science* **2011**, *378*, 163–170.

12. Mueller, D.N.; Souza, R.A. de; Weirich, T.E.; Roehrens, D.; Mayer, J.; Martin, M. A kinetic study of the decomposition of the cubic perovskite-type oxide $Ba_xSr_{1-x}Co_{0.8}Fe_{0.2}O_{3-\delta}$

(BSCF) (x = 0.1 and 0.5). *Physical chemistry chemical physics : PCCP* **2010**, *12*, 10320–10328.

13. Matras, D.; Vamvakeros, A.; Jacques, S.D.M.; Middelkoop, V.; Vaughan, G.; Agote Aran, M.; Cernik, R.J.; Beale, A.M. In situ X-ray diffraction computed tomography studies examining the thermal and chemical stabilities of working $Ba_{0.5}Sr_{0.5}Co_{0.8}Fe_{0.2}O_{3-\delta}$ membranes during oxidative coupling of methane. *Physical chemistry chemical physics : PCCP* **2020**, *22*, 18964–18975.

14. Waindich, A.; Möbius, A.; Müller, M. Corrosion of $Ba_{1-x}Sr_xCo_{1-y}FeyO_{3-\delta}$ and $La_{0.3}Ba_{0.7}Co_{0.2}Fe_{0.8}O_{3-\delta}$ materials for oxygen separating membranes under Oxycoal conditions. *Journal of Membrane Science* **2009**, *337*, 182–187.

15. Ramirez-Reina, T.; Santos, J.L.; García-Moncada, N.; Ivanova, S.; Odriozola, J.A. Development of Robust Mixed-Conducting Membranes with High Permeability and Stability. In *Perovskites and Related Mixed Oxides*; Granger, P., Parvulescu, V.I., Prellier, W., Eds.: Wiley-VCH Verlag GmbH & Co. KGaA: Weinheim, Germany, 2016, pp. 719–738.

16. Bouwmeester, H.; Burggraaf, A.J. Chapter 10 Dense ceramic membranes for oxygen separation **1996**, *4*, 435–528.

17. Niehoff, P.; Baumann, S.; Schulze-Küppers, F.; Bradley, R.S.; Shapiro, I.; Meulenberg, W.A.; Withers, P.J.; Vaßen, R. Oxygen transport through supported Ba0.5Sr0.5Co0.8Fe0.2O3−δ membranes. *Separation and Purification Technology* **2014**, *121*, 60–67.

18. Baumann, S.; Niehoff, P.; Schulze-Kuppers, F.; Ramasamy, M.; Meulenberg, W.A.; Guillon, O. (Invited) The Role of Solid-Gas Electrochemical Interfaces for Mixed Ionic Electronic Conducting Oxygen Transport Membranes. *ECS Transactions* **2015**, *66*, 21–33.

19. Liu, Y.; Tan, X.; Li, K. Mixed Conducting Ceramics for Catalytic Membrane Processing. *Catalysis Reviews* **2006**, *48*, 145–198.

20. Lin, Y.-S.; Wang, W.; Han, J. Oxygen permeation through thin mixed-conducting solid oxide membranes. *AIChE J.* **1994**, *40*, 786–798.

21. Bouwmeester, H.; Kruidhof, H.; Burggraaf, A.J. Importance of the surface exchange kinetics as rate limiting step in oxygen permeation through mixed-conducting oxides. *Solid State Ionics* **1994**, *72*, 185–194.

22. Murray, P.J.; late) J.W. Linnett, (Mössbauer studies in the spinel system coxfe3−xo4. *Journal of Physics and Chemistry of Solids* **1976**, *37*, 619–624.

23. Hansson, A.N.; Linderoth, S.; Mogensen, M.; Somers, M.A. X-ray diffraction investigation of phase stability in the Co–Cr–O and the Fe–Co–Cr–O systems in air at 1323K. *Journal of Alloys and Compounds* **2005**, *402*, 194–200.

24. Fischer, L.; Neuhaus, K.; Schmidt, C.; Ran, K.; Behr, P.; Baumann, S.; Mayer, J.; Meulenberg, W.A. Phase formation and performance of solid state reactive sintered $Ce_{0.8}Gd_{0.2}O_{2-\delta}$-$FeCo_2O_4$ composites. *J. Mater. Chem. A* **2022**, *10*, 2412–2420.

25. Schneider, C.A.; Rasband, W.S.; Eliceiri, K.W. NIH Image to ImageJ: 25 years of image analysis. *Nature methods* **2012**, *9*, 671–675.

26. Picture Thresholding Using an Iterative Selection Method. *IEEE Trans. Syst., Man, Cybern.* **1978**, *8*, 630–632.

27. Fischer, L.; Ran, K.; Schmidt, C.; Neuhaus, K.; Baumann, S.; Behr, P.; Mayer, J.; Bouwmeester, H.J.M.; Nijmeijer, A.; Guillon, O.*; et al.* Role of Fe/Co Ratio in Dual Phase $Ce_{0.8}Gd_{0.2}O_{2-}$-$Fe_{3-x}Co_xO_4$ Composites for Oxygen Separation. *Membranes* **2023**, *13*.

28. Belova, I.V.; Brown, M.J.; Murch, G.E. Analysis of kinetic demixing in a mixed oxide (A,B)O in an oxygen potential gradient. *Acta Materialia* **2003**, *51*, 1821–1826.

29. Martin, M. Materials in thermodynamic potential gradients. *The Journal of Chemical Thermodynamics* **2003**, *35*, 1291–1308.

30. Hong, J.O.; Yoo, H.I. Electric Field-Induced Unmixing in Mixed Ferrite Spinel $(Co,Fe)_3O_4$. In *Mass and Charge Transport in Inorganic Materials III*: Trans Tech Publications LtdSwitzerland, 2006, pp. 11–20.

31. Ramasamy, M.; Persoon, E.S.; Baumann, S.; Schroeder, M.; Schulze-Küppers, F.; Görtz, D.; Bhave, R.; Bram, M.; Meulenberg, W.A. Structural and chemical stability of high performance $Ce_{0.8}Gd_{0.2}O_{2-\delta}$-$FeCo_2O_4$ dual phase oxygen transport membranes. *Journal of Membrane Science* **2017**, *544*, 278–286.

32. LU, F.; Dieckmann, R. Point defects and cation tracer diffusion in (CoxMn1−x)3−δO4 spinels. *Solid State Ionics* **1993**, *67*, 145–155.

33. Li, Y.; Maxey, E.R.; Richardson, J.W.; Ma, B. Structural and chemical evolution of Fe・Co・O based ceramics under reduction/oxidation—an in situ neutron diffraction study. *Materials Science and Engineering: B* **2004**, *106*, 6–26.

34. Kiefer, T. *Entwicklung neuer Schutz- und Kontaktierungsschichten für Hochtemperatur-Brennstoffzellen*; Forschungszentrum, Zentralbibliothek: Jülich, 2008.

35. Kharton, V.V.; Figueiredo, F.M.; Navarro, L.; Naumovich, E.N.; Kovalevsky, A.V.; Yaremchenko, A.A.; Viskup, A.P.; Carneiro, A.; Marques, F.M.B.; Frade, J.R. Ceria-based materials for solid oxide fuel cells. *J Mater Sci* **2001**, *36*, 1105–1117.

36. Steele, B. Appraisal of $Ce_{1-y}Gd_yO_{2-y/2}$ electrolytes for IT-SOFC operation at 500°C. *Solid State Ionics* **2000**, *129*, 95–110.

37. Na, B.T.; Park, J.H.; Park, J.H.; Yu, J.H.; Joo, J.H. Elucidation of the Oxygen Surface Kinetics in a Coated Dual-Phase Membrane for Enhancing Oxygen Permeation Flux. *ACS applied materials & interfaces* **2017**, *9*, 19917–19924.

38. Ramasamy, M. *Dual Phase Oxygen Transport Membrane for Efficient Oxyfuel Combustion*; Forschungszentrum Jülich GmbH, 2016.

39. Ji, Y.; Kilner, J.; Carolan, M. Electrical conductivity and oxygen transfer in gadolinia-doped ceria (CGO)–$Co_3O_{4-\delta}$ composites. *Journal of the European Ceramic Society* **2004**, *24*, 3613–3616.

40. Li, S.; Cheng, J.; Gan, Y.; Li, P.; Zhang, X.; Wang, Y. Enhancing the oxygen permeation rate of $Ba_{0.5}Sr_{0.5}Co_{0.8}Fe_{0.2}O_{3-\delta}$ membranes by surface loading Co_3O_4 nanorod catalysts. *Surface and Coatings Technology* **2015**, *276*, 47–54.

41. Kwon, Y.; Na, B.T.; Park, J.H.; Yun, K.S.; Hong, S.K.; Yu, J.H.; Joo, J.H. Guidelines for selecting coating materials for a high oxygen permeation flux in a fluorite-rich dual-phase membrane. *Journal of Membrane Science* **2017**, *535*, 200–207.

42. Joo, J.H.; Yun, K.S.; Lee, Y.; Jung, J.; Yoo, C.-Y.; Yu, J.H. Dramatically Enhanced Oxygen Fluxes in Fluorite-Rich Dual-Phase Membrane by Surface Modification. *Chem. Mater.* **2014**, *26*, 4387–4394.

43. Joo, J.H.; Yun, K.S.; Kim, J.-H.; Lee, Y.; Yoo, C.-Y.; Yu, J.H. Substantial Oxygen Flux in Dual-Phase Membrane of Ceria and Pure Electronic Conductor by Tailoring the Surface. *ACS applied materials & interfaces* **2015**, *7*, 14699–14707.

44. Hong, W.K.; Choi, G.M. Oxygen permeation of BSCF membrane with varying thickness and surface coating. *Journal of Membrane Science* **2010**, *346*, 353–360.

45. Engels, S.; Markus, T.; Modigell, M.; Singheiser, L. Oxygen permeation and stability investigations on MIEC membrane materials under operating conditions for power plant processes. *Journal of Membrane Science* **2011**, *370*, 58–69.

Chapter 7

7. Asymmetrical configuration of the 60 wt. % $Ce_{0.8}Gd_{0.2}O_{2-\delta}$ – 40 wt. % $FeCo_2O_4$ composite by tape casting technique

Abstract

The $Ce_{0.8}Gd_{0.2}O_{2-\delta}$ - $FeCo_2O_4$ dual-phase composite is a promising candidate for oxygen separation in a membrane reactor due to its chemical stability, mixed conducting properties, and stable oxygen flux at intermediate temperatures. According to Wagner's theory, the oxygen permeation performance of such a membrane can be enhanced by the reduction of the membrane thickness. The target membrane thickness is in the micrometre range. Such a thickness is however only possible to reach by appropriate development a supported membrane. The goal in the current work is a gas-tight 50 µm-thick membrane layer on a porous support, manufactured by a tape casting technique. The main goal of such an asymmetric membrane development is to reach a high membrane density with optimal microstructure in combination with a substrate porosity of 30%, without compromising its mechanical stability. In this chapter, the step-by-step procedure of the dual-phase composite asymmetric membrane development is described. Slurry formulation, drying process optimisation, as well as sintering profile optimization for the asymmetric configuration, is discussed. The optimisation of the slurry formulation allowed to produce defect-free tape, however further problems occurred during heat treatment, where numerous phase interactions take place. The objective of this work is to reveal possible problems during the tape casting and drying process of the cast, as well as heat treatment, suggesting the possible solutions to these problems for the future development of $Ce_{0.8}Gd_{0.2}O_{2-\delta}$ - $FeCo_2O_4$ asymmetric assembly.

This chapter is ready to submit

7.1 Introduction

Oxygen is one of the most used chemicals for application in different industry sectors and accounts for about ¼ of the world market of industrial gases [1,2]. Among others, oxygen is deployed in combustion processes and in many industrial areas, such as the steel industry, health care, and also numerous chemical processes. The continuously expanding demand for oxygen evokes interest in developing new methods for oxygen production, such as membrane technologies [3]. Oxygen transport membranes (OTM) gain considerable attention over the past decades, due to the potential reduction of the costs compared to cryogenic distillation [1,4,5].

Due to sufficient stability and permeation, MIEC materials are good candidates for application as oxygen transport membranes (OTMs) [1,6–8]. The single-phase BSCF and LSCF are potential material candidates offering high oxygen permeation performance [9–13], however, the chemical and mechanical stability showed to be an issue [14–17]. Dual-phase materials have been intensively investigated in order to overcome the limitations of single phase membranes [1,18]. $Ce_{0.8}Gd_{0.2}O_{2-\delta}$ –$FeCo_2O_4$ (CGO20-FCO) composed of acceptor-doped fluorite oxide and Fe-Co spinel has been chosen in this work because the fluorite structure materials in a composite system typically improve the overall stability of the membrane, while the spinel structure provides the necessary electron conductivity [1,7,19]. The microstructure features and transport properties of the fluorite-spinel bulk membrane were reported previously [20–23].

This study reports on sequential tape-casting employed as a processing technology to develop a two-layered asymmetric dual-phase membrane from a ceramic powder, specially designed via solid-state reactive sintering (SSRS) [24]. A thin dense membrane with a thickness in the µm range exhibits improved oxygen permeation. However, the stability of such a thin membrane layer is not sufficient, so an additional layer for mechanical stability is necessary to be applied. Tape casting is the proven method for the fabrication of a planar ceramic component, such as asymmetric and symmetric membranes for gas separation [20,25,26]. The tape casting technique offers a lot of advantages, such as precise control of the membrane thickness, is suitable for large-scale production, and can create complex configurations and shapes. For the production of the asymmetric configuration, this method is convenient due to the relatively simple procedure for manufacturing and further processing of the membranes.

7.1.1 Slurry formulation

Tape casting is the widely accepted method for the fabrication of very thin ceramic foils, with a thickness ranging from the µm to mm. The formulation of the slurry or paste is the first step in the tape-casting process. The ceramic powder should be mixed with a liquid medium (solvent) and various additives, such as pore former, binder, and plasticizer, to control the properties of the slurry and later the green tape. Each of the additives is responsible for certain properties during the slurry preparation step and its fraction should be adjusted accordantly. Lack of one or another additive leads to curative or cracking defects formation in the green tape.

The selection of the proper dispersant is an important step in the slurry preparation since the purpose of the dispersant is to disperse the primary powder particles and simultaneously hold them in a homogeneous suspension, while the binder coats them individually. Initially, Nuosperse FX9068 has been used for both layers, however, replacing the dispersant with TEGO Dispers 655 for the support layer proved to be more suitable for the dual-phase composite powder [20].

The main function of the binder is to provide the network, which holds the whole system together after the solvent evaporates. Additionally, the binder provides the necessary strength for further processing. The slurry toughness, plasticity, and viscosity are mostly affected by the binder type. Based on in-house experience, Polyvinyl butyral (PVB) is used in the current work.

The plasticizer is the next additive for tape fabrication and is responsible for the flexibility and bendability of the green tape, preventing crack nucleation and propagation. Without a plasticizer, a relatively strong, stiff, and brittle tape can be fabricated, however, such a tape might lead to problems in further processing. The plasticizers can be classified as either Type I or Type II. Type I is responsible for lowering the glass transition temperature hence making the tape more flexible, whereas type II lubricates the green tape, by partially dissolving the binder [27]. To provide the needed flexibility of the tape two types of plasticizers included in the slurry system used were 3G8 Ester and PEG400. It must be noted that not only the fraction of binder or plasticizer should be taken into account, but the binder/ plasticizer ratio as well.

For successful slurry development, the particle size and specific surface area are essential powder characteristics. To obtain the targeted value of the surface area in the range of 1-5 m^2/g, a powder with a particle size of 1-2 µm should be used to avoid precipitation of the powder particles [20]. These values are chosen based on the experience on the development of other composite systems by tape casting. The quality of the tape can be also influenced by other factors, such as technical features of the setup and environmental conditions: temperature and humidity.

7.1.2 Drying process

The casted tape undergoes some transformations during each step of fabrication, the most significant change is seen in the z-direction, which can schematically be represented as shown in Figure 7.1.

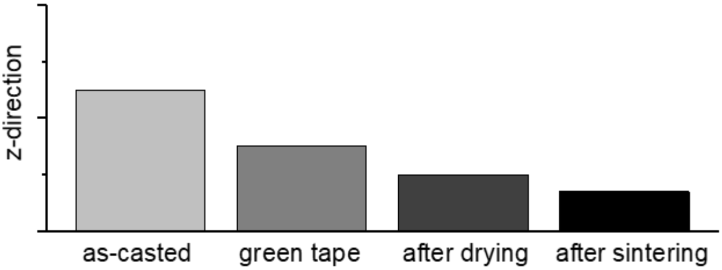

Figure 7.1 The reduction of the height of the tape at the different steps of the fabrication

After the casting, the solvent leaves the ceramic matrix with organic additives. Since the solvent removal proceeds at the top of the as-casted tape, a concentration gradient across the entire tape thickness is formed. This gradient causes uniaxial shrinkage, resulting in the reduction of the tape height and also in lateral stresses in the green body. At this stage, defects and cracks can be formed when these lateral stresses are larger than what can be compensated by the two-layered green tape [27]. The source of the cracking is usually some point defects, such as bubbles, strakes, and agglomerates. The cracking is propagated rapidly if there are a lot of such point defects. Any lateral stress is a reason for the various effect in the tape, some defects can be tolerated, whereas others completely deteriorate the quality of the green tape.

During the following sintering step, the organic additives (binder, pore former, and plasticizer) are burned out, leading to the densification of the matrix. After the sintering, the dimensional change is not only the linear in z-direction, but also radial, and strongly depends on the firing temperature. The shrinkage of the asymmetric pellet is attributed to the different sintering rates in the individual layers, which in case of a large mismatch can cause cracking and curvature of the sample [26].

The preparation of ceria-based dual-phase asymmetric membranes for oxygen separation brings many challenges concerning the shape, mechanical and chemical stability, and microstructure of the final assembly. This is quite a complex process with an issue at almost every step of the sample preparation, which is discussed in the current study in detail.

7. 2 Experimental

7.2.1 Sample preparation by tape casting

Material

$Ce_{0.8}Gd_{0.2}O_{2-\delta}$ (CGO20) (Cerpotech, >99%, Tiller, Norway), Fe_2O_3 (FO) (Merck, 99 %) and Co_3O_4 (CO) (Merck, 99 %) powders used for the experiments were synthesized by the Solid-State Reactive Sintering method (SSRS). Fe_2O_3 and Co_3O_4 were mixed in a 1:2 Fe: Co ratio, resulting in spinel $FeCo_2O_4$ (FCO), which was added to commercially available Gd-doped ceria. Respective amounts of powders were weighed to create $Ce_{0.8}Gd_{0.2}O_{2-\delta}$ - $FeCo_2O_4$ (CGO20-FCO) compositions in a with wt. % -ratio of 60:40 ratio. The powder mixtures were ball milled in polyethylene bottles over 48 h using zirconia balls on a roller bench at a speed of 175 rpm and further drying for 48 h in ambient air at 70 °C.

Slurry preparation

Prior to the casting, the slurry preparation process takes place. The slurry preparation process was carried out with 25 g composite powder for the membrane and 50 g support respectively, mixed with the binder, two types of plasticizers, solvent, and dispersant in terms of their solid content. The main steps of the sample production are shown in the form of the flow chart in Figure 7.2 [20].

Several components, such as powder, solvent, binder, and plasticizer are mixed to provide the necessary formulation and handling. Based on the properties of the investigated composite powder, such as sintering behaviour, theoretical density, particle size distribution, and the results of the previous investigation [20] the basic slurry recipe was selected. The reference recipe for both membrane and support are shown in Table 7.2the deviations from the standard recipe and results will be discussed in the Result and Discussion section.

In the very first step, mixing of the additives including solvents 34 wt. % ethanol and 66 wt. % methylethylketone (MEK) with the dispersant (NUOSPERSE FX 9086 or TEGO DISPERS 655) is performed. Followed by the addition of the 60CGO20-FCO ceramic powder, rice starch (Remy FG – Firm Remy) as pore former for the support layer, polyvinyl butyral (PVB-98) (Fa. Solutia Inc.) and two types of plasticizers 3G8 Ester (Fa. Solutia Inc.) and PEG400 (Merk, Darmstadt) are added. The slurry is ball milled in polyethylene bottles over 48 h using zirconia balls in a tumble mixer at a speed of 175 rpm with subsequently rested for 48 h.

Table 7.1 The basic slurry recipe for the dense membrane layer and porous substrate layer, the additives are given in percent of the solid content (composite powder)

Step	Material	Function	Membrane Wt.% of powder	Support Wt.% of powder
1	Milling balls ZrO2	Mixing	100	100
2	Methyl ethyl ketone/Ethanol	Solvent	46	46
3	Noospheres FX9086	Dispersant Type 1	3	-
	Disperse 655	Dispersant Type 2	-	3
		Swirl by hand for 30 seconds		
4	CGO20-FCO	Ceramic powder	100	100
	Mix using planetary mixer (1000 rpm for 3 minutes)			
5	Rice starch	Pore former	-	30
	Mix using planetary mixer (1000 rpm for 3 minutes)			
6	Polyvinyl butyral B98	Binder	7	7
7	3G8 Ester	Plasticizer Type 1	6	6
8	PEG400	Plasticizer Type 2	7	7
Mix using planetary mixer (1500 rpm for 3 minutes)				

Prior to the casting procedure, the slurry was subjected to homogenization and degassing step.

Tape casting

The tape casting technique involves the deposition of a slurry or paste onto a flat substrate, which is typically a flexible polymer film. The tape casting machine KARO cast (KARO Electronics GmbH) is used. A doctor blade (Figure 7.3a), which sets the precise thickness of ceramic slurry and enables the production very thin foils of µm range, applies the foil on the moving polymer foil. Tape casting was carried out on the micro casting machine with 5 mm/s and 2.5 mm/s speeds for support and membrane respectively. All tapes were cast at temperature and relative humidity ranging between 20 and 24 °C and 24 % and 63 %, respectively. After the tape casting the green tape was dried for approximately 12 h and stripped off the polymer tape. The film is well-connected and strong enough after drying, to be stripped off, cut, and sintered. After drying the pellets with a diameter of 20 mm were pinched off the green tape and sintered at 1200°C for 5 h.

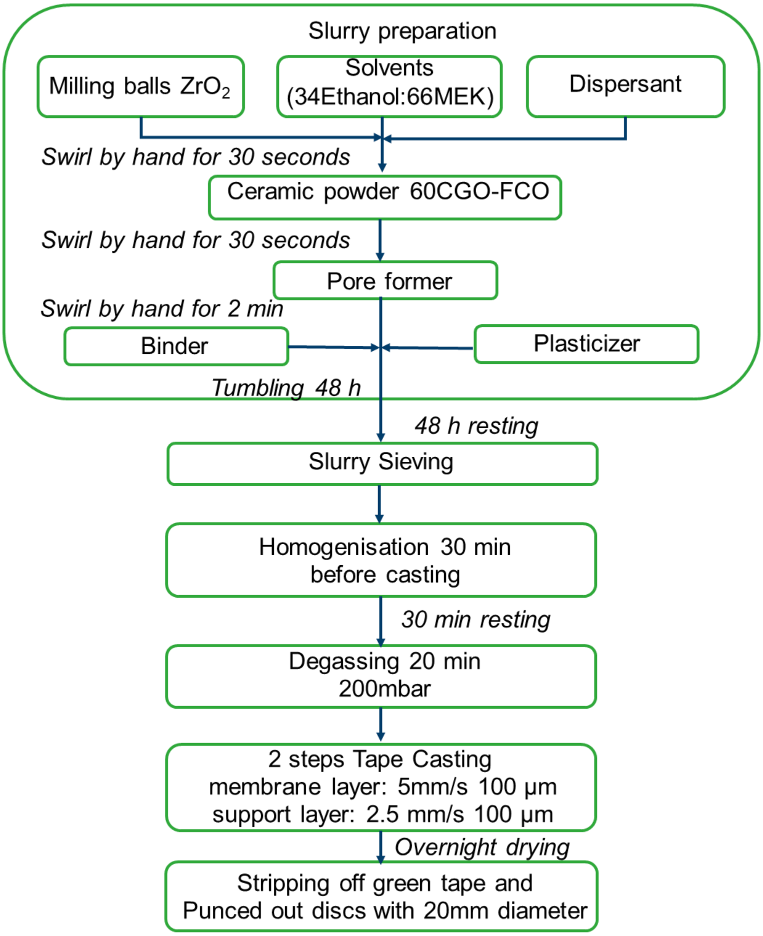

Figure 7.2 Flow chart of the asymmetric sample preparation

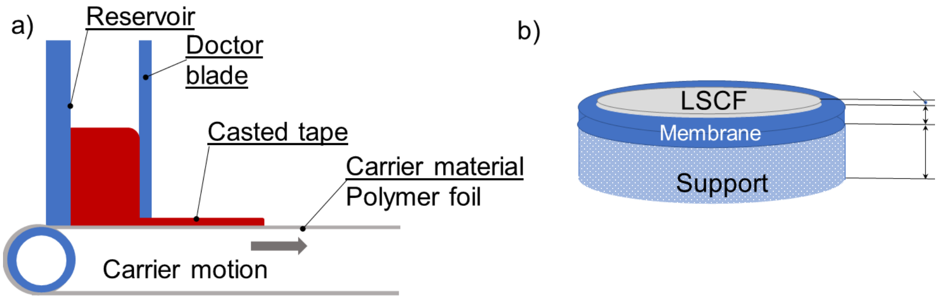

Figure 7.3 a) The schematic representation of the tape-casting process including of the doctor blade and b) resulting membrane assembly

Since surface exchange limitations are becoming more important with a decreasing thickness of the dense layer, the introduction of a catalytic LSCF layer at the membrane side and catalyst infiltration in the porous support is necessary. On the membrane side of the discs, a porous $La_{0.58}Sr_{0.4}Co_{0.2}Fe_{0.8}O_{3-\delta}$ (LSCF) catalytic activation layer with a thickness of 5 µm was applied using a screen-printing technique. Discs were then calcined in the oven at 1100 °C for 5 hours. A 50 µm dense membrane layer and a 0.7 mm support layer were chosen as the target configuration. The final asymmetric assembly is shown in Figure 7.3b.

7.2.2 Characterization methods

Crystal structure

The crystal structure was determined using an X-ray diffraction (XRD) diffractometer D4 ENDEAVOR (Bruker, Karlsruhe, Germany). The diffraction angle was chosen in the range of 2θ from 10° to 80°, with increments of 0.02° for 2θ and 0.75 seconds of measurement time per step. Analysis of the measured data was performed with X'Pert HighScore (PANalytical B.V., version 3.0.5) software. Phase quantifications and associated crystal structure analyses were carried out by Rietveld refinement using (Version 4.2.2) software. The low error R_{wp} was held <4 % for all samples, which also indicates the good fitting.

Microscopy

Scanning Electron Microscopy (SEM) and Energy Dispersive X-ray Spectroscopy (EDXS) were used to obtain material morphology. SEM images were taken with a Zeiss Ultra 55 and a Zeiss Supra 50 VP1 (Carl Zeiss NTS GmbH, German) SEM at different magnifications. The electronic conductivity of samples was enhanced by sputter deposition of a thin platinum layer prior to measurement.

7.3. Results and discussion

7.3.1 Slurry preparation

Having in mind the drying behaviour of the multi-layered assembly can be problematic due to potential expansion mismatch for both the membrane and support layer same composite material 60CGO20-FCO was used.

Membrane layer

For the membrane layer, the slurry preparation process was carried out with 25 g composite powder mixed with binder, two types of plasticizers, solvent, and dispersant as listed in Table 7.1in terms of their solid content.

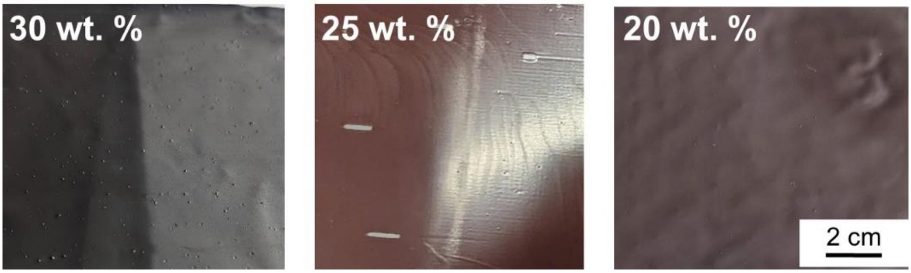

Figure 7.4 Membrane layer with various solid content of 30, 25 and 20 wt. % after drying overnight

After the first casting attempt the thin foil layer was well-connected, revealing minor defects and imperfections, such as air bubbles and clumps. The density of the slurry was an issue for the first attempt at membrane manufacturing the optimization of this layer was done by only varying the solid content. By casting 25 wt.% - and 30 wt. %-added membrane layer the clumps of the powder led to the formation of holes as seen in Figure 7.4, which resulted in an uneven surface after drying. The layer based on 20 wt. % powder in the casting mixture results in a flexible almost defect-free thin foil with some minor surface defects, which could be optimized by adjusting the additional homogenization step before casting. It helped to achieve the necessary homogeneity of the slurry and eliminate all agglomerations. However, in contact with solvent during the sequential support layer casting, the membrane layer disintegrates into cracks.

Support layer

The support layer is quite crucial for the asymmetric configuration, serving as a mechanically stabilizing layer. The fabrication of this layer is however very challenging, due to the large thickness (in our case >0.9 mm) and thus quite a complex drying process. For the thin membrane layer, the solvent removal process is not problematic, since it evaporates quite uniformly. For a thick tape (>500 μm), on the other hand, the drying process is quite critical. Drying takes much longer since the diffusion distance from the bottom to the top of the tape is larger. It leads to the formation of a concentration gradient across the entire tape thickness, with fast evaporation on the top of the tape and slow evaporation at the bottom. That in turn causes increased lateral stresses in the matrix resulting in defect formation and propagation.

To minimize mass transfer limitations in the support, about 30-40 % porosity is needed. To ensure the necessary level of porosity a pore former is needed. This pore former helps to build the microstructure of the layer with minimizing mass transfer limitations.

Based on the successful experience with this composite system, 30 wt.-% rice starch (Remy FG - firm Remy) with respect to the ceramic powder was selected in the current work [28].

Since the first attempt of the support casting resulted in many defects during casting or after the drying steps, a systematic study was performed for the optimization of the slurry recipe for 60 CGO20-FCO composites. The slurry can be optimized by means of the binder, plasticizer, and dispersant concentration. Furthermore, the ratio binder/plasticizer is critical and should be adjusted correctly to yield a good green tape quality. All the varied values and the optimised result are listed in the Table 7.2 below. The fraction of dispersant varied between 1.5 and 3 wt.%, which was experimentally found by [26] in house. The amount of the binder varied in the range of 6-11 wt.%.

Table 7.2 Supports slurry optimisation with varied parameters, wt.%

Varied parameter	Reference [20]	Fraction range	Chosen
Solid content (Powder)	20 %	18-20 %	18%
Dispersant	3 %	1.5-3 %	3 %
Binder	7 %	5-11 %	7 %
Plasticizer type I	6 %	3-9 %	6 %
Plasticizer type II	7 %	3-7 %	7 %
Binder/Plasticizer	0.54	0.54-1.3	0.54

Defects

About 20 different support slurry recipes were prepared and partly cast, helping to select the most suitable one. The most often occurring defects in the green tape were classified according to known defects, described by Mistler *et.al.* [27], and discussed with a possible way of solutions. A schematic and actual visual representation of the variety of curving or cracking defects observed in the dry tape is listed below.

Center crack

The most common defect during the tape casting attempts for the 60 CGO20-FCO composite is cracking down the centre of the tape. Generally, the nonuniformities, such as bubbles and agglomerates or any other point defects can cause crack formation and propagation along the length of the tape during drying. Although this central crack is often present, it divides the tape into 2 parts, which are in some cases defect-free. This kind of defects turned out to be related to the mixing procedure. To overcome this, the mixing procedure was adjusted with some additional homogenization and degassing steps before casting.

Crow’s-Foot cracking

The second common defect for the thick tapes (>500 µm) is the so-called crow’s-foot cracking, which is characterized by the not connected matrix in the slurry, low particle mobility, and high shrinkage during drying. The dry tape is quite brittle and cannot be stripped from the carrier without deformation and hence easily breaks into small pieces. The typical solutions to avoid this type of defect are either to decrease the solvent content, and thus the reduce the shrinkage; or to increase binder content and/or plasticizer type II, which increase matrix strength and bendability of the matrix respectively. In the current case, this defect was observed in the tapes with the binder/plasticizer ratio = 1 and 0.77 and a low amount of plasticizer type II (3 and 3.5 wt. %) This kind of cracking can possibly be avoided by adjusting the binder/plasticizer ratio or by increasing the fraction of plasticizer type II.

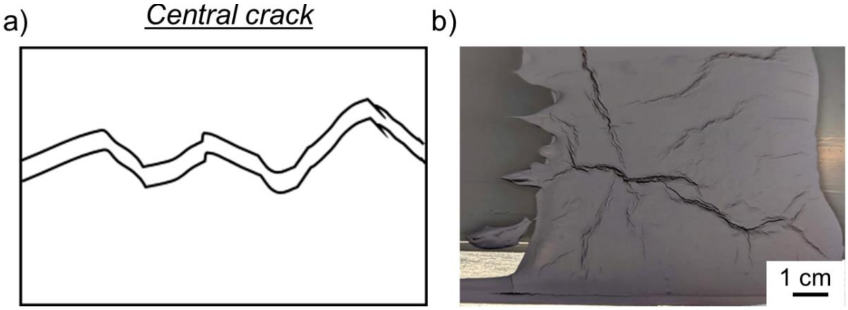

Figure 7.5 Center Crack defect a) scheme b) actual casted tape after drying

Wrinkle

Wrinkling is a very common phenomenon at the surface of just casted layers in tape casting. The solvent leaves the top of the surface quicker than the diffusion mechanism compensates it at the surface, resulting in a skin at the surface, as shown in Figure 7.7. As a rule, this skin possesses a lower diffusion rate, hence it is an obstacle for the solvent from the bottom part of the tape, slowing down its evaporation. Wrinkling is closely connected to the solvent amount in the slurry and drying rate, so to avoid wrinkling one needs to reduce the solvent fraction. Additionally, to prevent the formation of this type of defect, the cast tape is covered right after casting to perform controlled drying. It should be noted that it is often more than one defect type that occurs during the drying process, as an example Figure 7.7b illustrates the wrinkle defect accompanied by the crow´s foot defect.

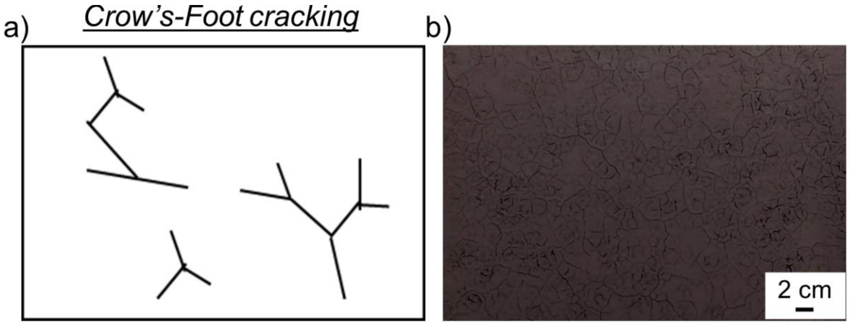

Figure 7.6 Crow´s foot defect a) scheme b) actual casted tape after drying

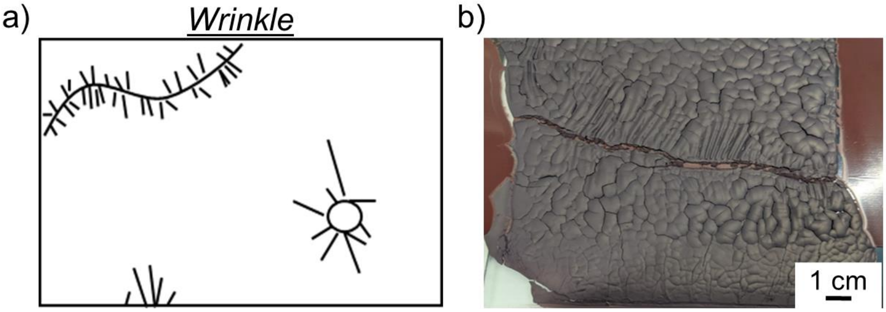

Figure 7.7 Wrinkle defect a) scheme b) actual casted tape after drying

Orange peel

One more defect is related fast evaporation of the solvent than solvent diffusion and fast drying.

There are some craters in the tape surface high degree of porosity at the foil surface. By solvent evaporating the pore channels were formed and left behind (Figure 7.8), what potentially leads to the cracking and mechanical instability by further processing. This defect can be avoided by adjusting the liquid medium content and controlling drying after casting.

Gull wing and curling

Gull wing generally happens in tapes made of very fine powder and thus quite a tight packing. In this case, the cast will bend to release stress gradients in the z-direction and shrinkage stress due to strong adhesion to the carrier and high lateral shrinkage of the top layer. This disbalance forces the tape to release stress, thus the tape undergoes a cross-cast shrinkage. Since for all attempts the same powder was used, the problem was in the formulation of the slurry. In our case, this defect was seen only for the slurries where the binder content exceeds 7 wt. % (tapes with 7, 9 and 11 wt. % of binder). In some cases, the curling of the whole tape was observed, in others only the edges curled. The addition of the plasticizer, especially type II should be done to promote plastic deformation instead of dimensional changes during drying. The increased amount of the plasticizer II has not improved tape quality, thus the lower binder content of 7 % was found suitable for the slurry.

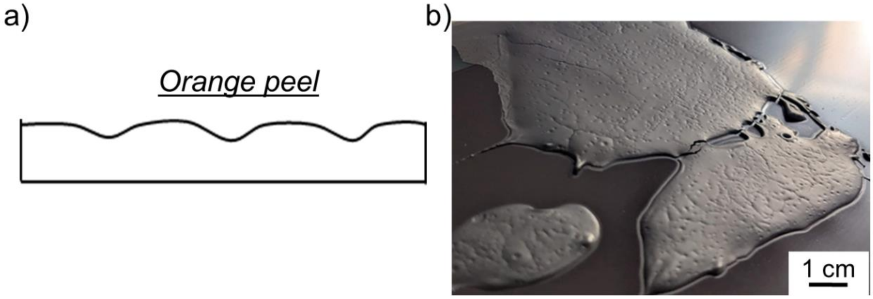

Figure 7.8 Orange peel defect a) scheme b) actual casted tape after drying

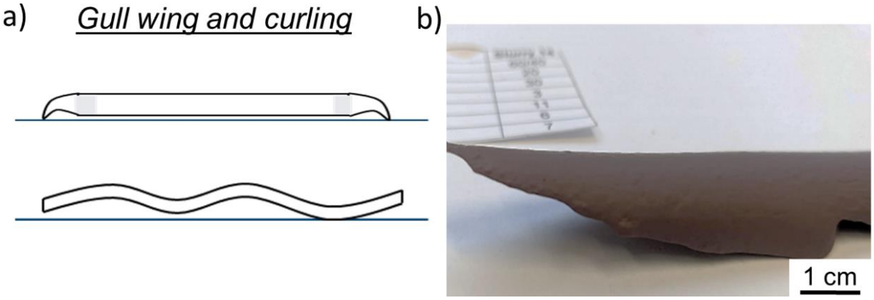

Figure 7.9 Gull wing and curling defect a) scheme b) actual casted tape after drying

All casts with reduced fraction of dispersant (1.5 %) showed cracks, hence the amount of dispersant was taken as 3%. The type of dispersant has supposedly higher impact than the fraction, since better results were obtained for the DISPERS 655 for support layer.

After all additives were adjusted, it was noted that the slurry was too dense to cast. Thus, the last varied parameter was the solid content, which was reduced to 18 %. This slurry with decreased solid content, and thus higher solvent fraction gave the best flexible and well-connected two-layered green tape with a few cracks along the edge, which could be tolerated.

7.3.2 Standard heat treatment profile

After several casting attempts, defect-free green tapes of 60CGO20-FCO-supported asymmetric membranes with optimized slurry were successfully obtained. The next issue to address is getting gas-tight membranes during the heat treatment process.

In general, the co-firing of the two layers in the asymmetric assembly is a rather complex process, due to possible mismatch of the sintering rates. The difference between the individual sintering rates of the membrane and substrate layer is large for the composite system [20]. In contrast to support layer, there is no significant mass loss in the membrane layer. A membrane layer sintered separately shows a lower shrinkage (~30 %), compared to two layered membrane (> 45 %), underlying that substrate shrinkage dominates over membrane shrinkage during heat treatment. This is also known for other ceramic materials and reported elsewhere [26]. The pore former is burning rapidly at elevated temperatures, which can lead to defects at this manufacturing step and thus should be controlled. The current sintering program includes a long heating step between 200-500 °C, to burn out the organic components (i.e., pore former, binder and plasticizer). Significant mass loss occurs in this step. As a reference to the sintering profile developed by [20], a sintering study was developed as shown in Figure 7.10.

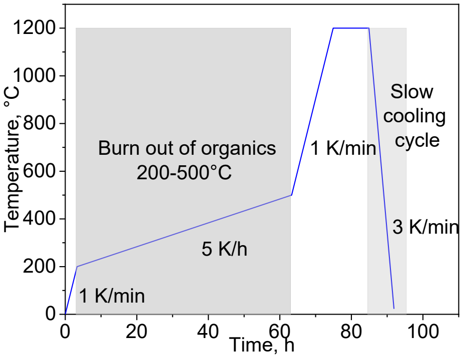

Figure 7.10 Heat treatment profile for the asymmetric CGO20-FCO membrane by tape casting

The first attempt of the sintering showed a lot of small cracks on the membrane side, pointing out that either heating or cooling rate was too high (Figure 7.11a). Some samples were broken completely (Figure 7.11b), pointing out internal stress by co-firing of two layers. Moreover, the organics burn out rapidly, consuming some oxygen and thus providing reducing conditions during the sintering process, what could be also affecting the material. Another assumption was that the phase transition in the Fe-Co system could cause internal stress, possibly leading cracks in the membrane layer. To avoid this, pre-calcination of the CGO20-FCO powder was done at 900°C, at which the FCO phase transformation starts [29]. This led to an improved sintering and no cracks were observed on the membrane surface in further experiments.

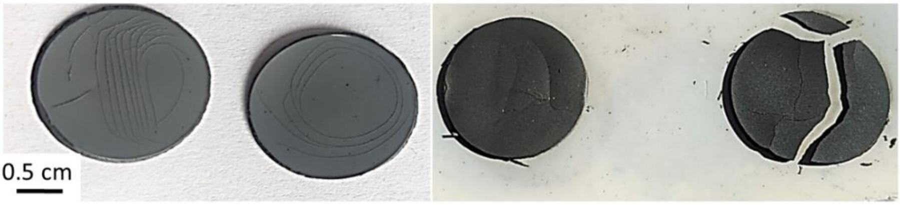

Figure 7.11 The first sintering attempt of the 60 CGO20-FCO asymmetric membrane at 1200°C for 5 h cracks on the membrane side (left) broken pellets after sintering (right)

Further SEM image analysis, shown in Figure 7.12. The sintering at 1200°C was not effective and the dense layer was not gas-tight, revealing a lot of pores at the surface as can be seen in Figure 7.12. The support side reveals also a lot of big and homogeneously distributed pores as intended. Subsequent analysis of the cross-section reveals that the membrane layer has a lot of pores, and defects such as intergranular cracks across the membrane layer, which is possible reason why this layer was not gas-tight. Zoom-in on the membrane layer reveals a large island of the spinel phase with a lot of pores trapped within the grains. Moreover, the thickness of the membrane layer is not the same along the tape and was varying in the range of 11-20 µm, which also should be further improved at the fabrication step.

According to the cross-section analysis a bimodal pore size distribution of the pores can be seen in the support layer. Generally, the ceramic powder is dispersed in a complex organic system by the slurry preparation. The spacing between particles or agglomerates and their ordering in the slurry are strongly controlled by the additives, such as chemical dispersant and polymer network. It is also affected by dynamic effects such as drying process and polymer cross-linking process. Hence, the pores can be classified by their origin nature: the small pores result from the removal of binders, whereas large pores are formed by the removal of the pore former. In the substrate layer the pores are not distributed homogeneously and there are a lot of large pores connected with each other, forming the large hollow space right under the membrane layer. This emphasizes that a longer homogenization step is required to uniformly distribute the pore former in the slurry and thus the pores in the substrate layer. Adjusting the slurry preparation with a homogenization step before casting might prevent pore accumulation.

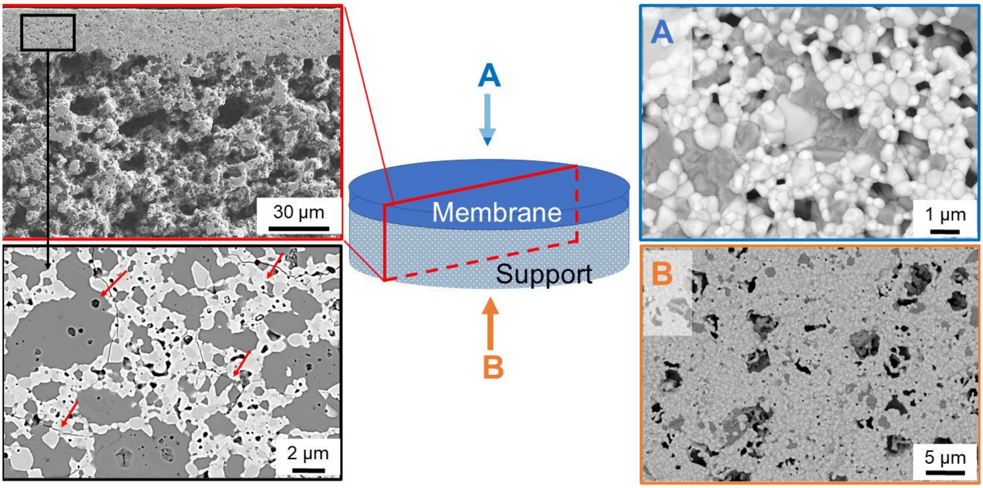

Figure 7.12 SEM investigation of the first attempt of the sintering profile at 1200°C for 5 h for 60CGO20-FCO two-layered asymmetric membrane

With the optimized slurry formulation and the fabrication process, the samples were subjected to sintering at 1200°C for 5 h. The microstructure features were improved and pore arrangement in the support layer is more homogeneous. From the microstructure point of view, the membrane layer was also slightly improved, showing the same thickness (20 µm) across the tape, lower porosity and no intergranular cracks. However, the samples were still not sufficiently dense, hence heat treatment optimisation is essential for the CGO20-FCO composite system.

7.3.3 Solution of the problems

Firstly, it was assumed that the phase interaction within the composite system, especially in the Fe-Co matrix leads to the cracks during sintering process. To prevent cracking, the phase transformation could be partly done prior the tape casting by pre-calcination of the powder. The mix of Fe_2O_3, Co_3O_4 and CGO was calcinated at 900°C, since the $FeCo_2O_4$ spinel formed at 900°C.

Two powders were characterized by XRD as shown in Figure 7.13. The 60CGO20-FCO powder showed the presence of following components: Fe_2O_3, Co_3O_4, and 20 mol. % Gd-doped ceria. Pre-calcinated powder at 900°C contains the following phases cubic CGO and two spinel phases with a cubic structure: 17.7 wt.% and 21.5 wt.% of iron-rich and cobalt-rich respectively. Moreover, about 1.5 wt.% of the Fe_2O_3 remains in the powder mixture. The FCO reflection at 36.5°2θ is split up into a broad reflection with two maxima prior to measurement, indicating iron-rich and cobalt-rich spinel types. An orthorhombic donor-doped $GdFeO_3$ (GCFCO) perovskite phase starts to form from 1050°C [29]. In the pre-calcinated powder this phase is not observed.

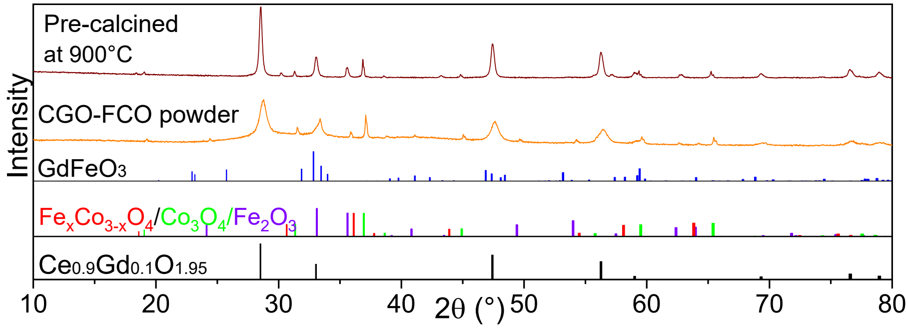

Figure 7.13 XRD patterns of two 60 CGO20-FCO powders before and after calcination. At the bottom, reference reflections are shown for the perovskite in blue, spinel in red and green, and fluorite in black

Pre-calcinated powder was further used for the manufacturing of the two layered asymmetric membrane. Due to slightly larger particle size and homogeneous particle size distribution in the powder, an improved green tape and defect-free sintered pellets were obtained.

7.3.4 Heat treatment

Although all the factors were considered and optimised, the samples were still not gas-tight, pointing out insufficient sintering parameters: 5 h dwell time at a temperature of 1200 °C. It is known that for the same material the sintering profile (dwell time and temperature) might differ depending on the fabrication method. So, the straightforward method is to adjust the sintering parameters to overcome this issue. Firstly, the dwell time was increased to 10 and 20 h. However, this has not led to any differences compared to the 5 h dwell time samples. Thus, the increase in the sintering temperature was done from 1200 °C to 1350 °C in a stepwise manner. The samples fired at 1325 and 1350 °C have a gas tightness in the range of 10^{-3} for the He-leak test, for the 1325 °C sample the value was even slightly higher. It was a slight improvement, since previously all samples were too brittle, and cracked even during the He-leak test.

In conclusion, a sintering temperature of 1350 °C was less effective than a sintering temperature of 1325 °C.

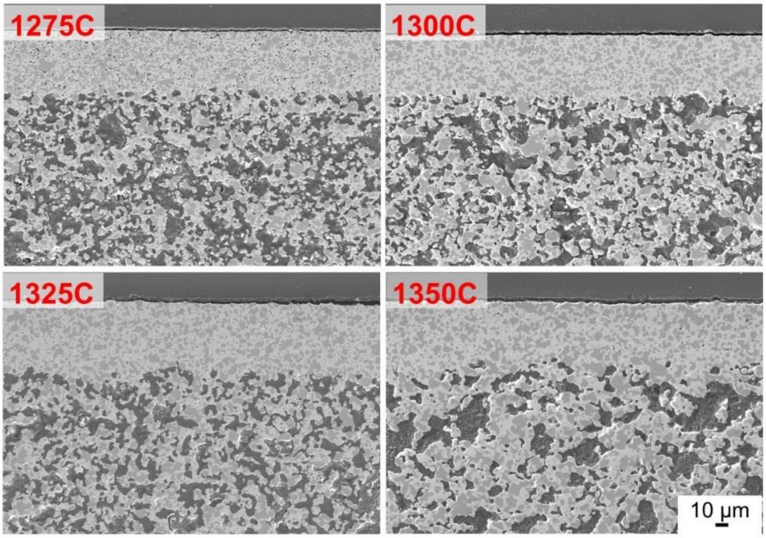

Figure 7.14 SEM images of cross-section of the asymmetric membrane sintered at 1275, 1300, 1325 and 1350 °C for 5 h

The microstructures of the samples are representative and SEM image observations over a large region showed the absence of macro-defects in both surface and cross-section images. The targeted 40 % porosity was successfully achieved by the tape casting method in all studied samples. The pores were homogenized during sintering step in the support layer and their size is growing with the elevating temperature, as depicted in Figure 7.14. An increase in the sintering temperature till 1325 °C results in a slight improvement in support layer showing a connected pore network to minimize mass transport limitations in the substrate. A further increase of the sintering temperature to 1350°C leads to agglomeration and even removal of pores, resulting in a non-continuous pore network.

The membrane layer thickness is estimated ~40 μm for all studied samples. There were no obvious pore agglomerates or microcracks, indicating a well-densified microstructure in this layer, which being a potential basis of a sufficient mechanical and transport properties. Comparison of the microstructure features of the dense membrane layer as a function of sintering temperature is shown in Figure 7.15.

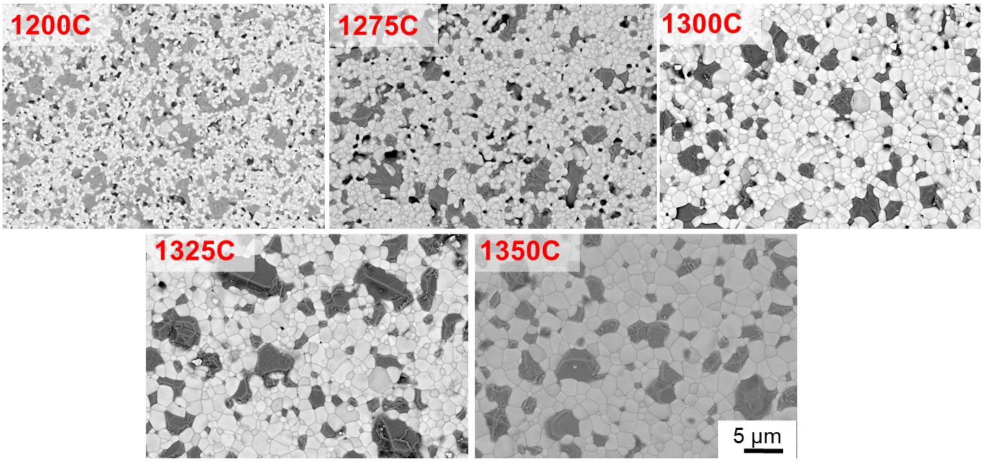

Figure 7.15 SEM images of the membrane surface of asymmetric 60 CGO20-FCO composite membrane fired at 1200, 1275, 1300, 1325 and 1350 °C

All the samples have a typical polycrystalline arrangement with fine grain sizes between 0.5 and 2 µm at the chosen sintering temperatures, as shown in Figure 7.15. The grain size of each phase as well as the pore size is analysed by an image analysis-based method with ImageJ software on all samples [30,31]. The increase in the grain size as a function of increasing sintering temperature is observed for all grains types. However, the FCO grains grow faster compared to the CGO and GCFCO grains, especially between 1325 and 1350 °C. Due to the limited number of characterized grains, there might be a large inaccuracy in the grain/pore size calculations. Densification process is usually driven by pore agglomeration and pore-removing processes and the coarsing, what is clearly seen at high dwell temperatures. The pore/grain ration should decrease, so the ceramic material experiences the densification [32,33].

The SEM analysis reveals that by increasing the sintering temperature, enhanced grain growth with simultaneous densification of the membrane layer is observed, as depicted in Figure 7.16. There are many trapped pores along the grain boundaries and in grain interior at 1200° and 1275 °C. At these temperatures only small pores can be eliminated during the coarsening process, while relatively large pores can survive. By increasing the sintering temperature to 1350°C in stepwise manner the pore size is decreasing, indicating that a significant sintering occurred at temperatures above 1300°C. Furthermore, the porosity level decreased substantially in all pellets and especially the smaller porosity among particles disappeared. Porosity decreased from

8.2 % to 1 % between 1200 and 1300°C, however further increase in sintering temperature has not much impact on the porosity. The total residual porosity was determined be around 1 % by surface and cross-section image analysis.

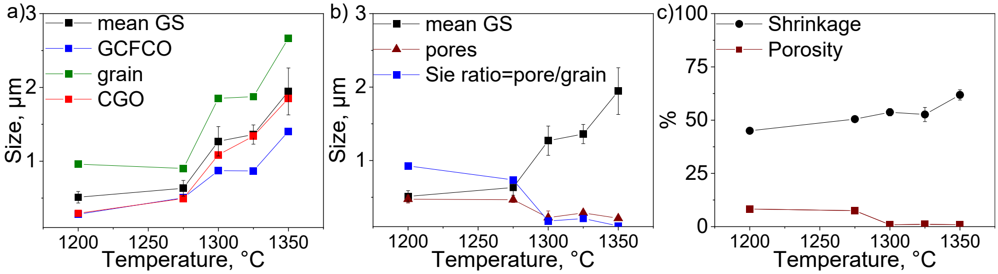

Figure 7.16 a) The pore and grain size in membrane layer dependency on the sintering temperature b) porosity grade and shrinkage of the sample as a function of sintering temperature (solid lines are a guide to the eye)

Since the significant difference in the sample's geometry was observed after the heat treatment, the shrinkage percentage was estimated. Shrinkage of the sample is increased gradually between 45 to 52 % in the sintering temperature range of 1200 to 1325°C, followed by sharp increase in shrinkage from 52 to 62 % at 1350 °C. Moreover, at 1350 °C most of samples are non-uniformly bent, what in turn is disadvantageous for further processing. At high temperatures possibly the support layer became the dominating source of shrinkage with higher strain rates than the membrane layer, what leads strong bending towards the substrate. As can be seen in Figure 7.17 a spherical shape was developed, since the bending is particularly pronounced at the edges of the disc, regardless of the membrane layer position (top side or bottom side). The curvature of the pellet is much stronger for the support layer situated on the top side, compared to membrane layer on the top side.

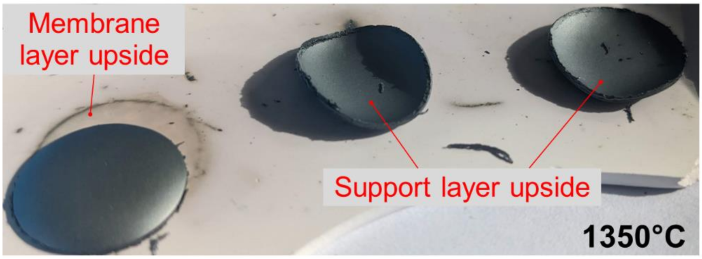

Figure 7.17 Fired samples at 1350°C for 5 h with membrane layer upside and bottom side

7.3.5 Phase analysis of the membrane layer

The presence of the fluorite, Fe-and Co-rich spinels and emerged perovskite phase was confirmed for all samples. The amount of the perovskite phase remains constant in the range of 6.4-7 wt.% for all studied samples. According to the Fe-Co-O phase diagram [34,35], the partial reduction of the spinel into a high-temperature Co/Fe monoxide phase with a rock salt structure can occur at >1200°C sintering temperature [20,21]. Generally, a slow cooling rate was implemented in the cooling cycle to avoid the formation of the rock salt phase and ensure its complete reoxidation to a spinel phase that is stable at target operating temperatures (600-1000°C). Such slow cooling helps the reoxidation process and Co/Fe monoxide is no more detectable (<1 wt. %), as can be seen for the sample sintered with the standard sintering program (1200°C for 5 h). At the temperatures above 1300°C the amount of CoO is possibly increased within the composite, which in turn has not enough time for its complete reoxidation to a spinel phase. Thus, the XRD patterns (see Figure 7.18) with Rietveld refinement reveal the additional high-temperature CoO monoxide presence from the 1300°C sintering temperature, and its fraction remains almost constant after further temperature increase (~9±0.5 vol.%). Introduction of additional step in the cooling cycle can help eliminate this phase, resulting in a higher Co-rich spinel fraction.

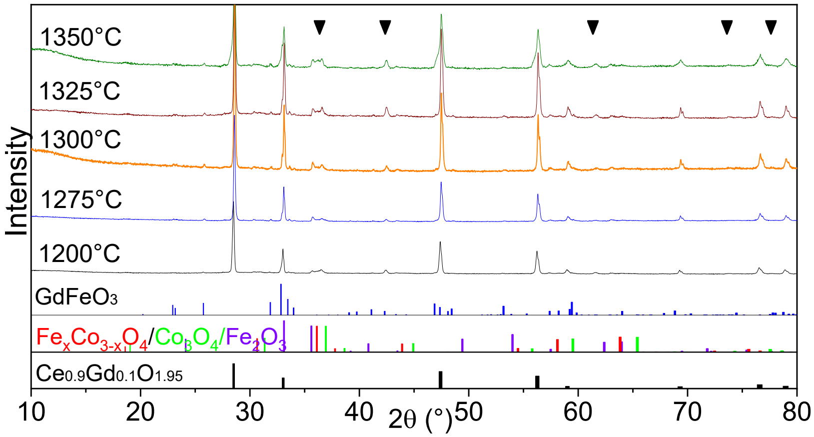

Figure 7.18 XRD patterns of 60 CGO20-FCO asymmetric membranes fired at 1275, 1300, 1325 and 1350 °C. At the bottom, reference reflections are shown for the perovskite in blue, spinel in red and green, and fluorite in black

7.3.6 Transport properties

Even after all the optimization trials and obvious improvements, some problems were not solved completely. During further processing, including the radial grinding of the pellet and application of the LSCF activation layer via a screen-printing technique, several samples were broken. Even for the successfully coated and sintered samples it was still not possible to install them into the permeation measurement setup. It underlines that the obtained pellets were still too brittle and not mechanically stable for permeation measurement. At this point, it is difficult to make a conclusion about the permeation properties of the two-layered membranes.

7.4 Conclusions

MIEC composites are based on commercially available powders of 60wt. % $Ce_{0.8}Gd_{0.2}O_{2-\delta}$ in combination with 40 wt. % spinel $FeCo_2O_4$ can be successfully synthesized by the cost-efficient solid-state reactive sintering (SSRS) technique and subjected to further tape casting techniques. Due to some challenges in the manufacturing of the asymmetric two-layered membrane, particularly the complex drying process for the support layer, optimization of the slurry formulation was done. As a result, a defect-free asymmetric tape was successfully obtained for further processing, showing the potential of the dual-phase composite material.

The next challenging step was heat treatment. The chosen heat treatment at 1200°C for 5 h was not suitable as the resulting membrane layer was cracked and not dense. Firstly, the 60CGO20-FCO powder was substituted by the powder pre-calcinated at 900°C. This measurement helped to make some phase interaction prior to the tape casting and avoid potential cracking of the casted samples during the sintering step. The heat treatment profile was optimized, by increasing the sintering temperature to 1325 °C, which leads to an improved density of the sample with an optimized microstructure with a mean grain size of 1.3 µm. The porosity of the membrane layer was reduced down to 1 %. A well-distributed pore network in the support layer was achieved minimizing mass transfer limitations in this layer.

A further increase in the sintering temperature to 1350°C is not advantageous, since it leads to new problems in each layer. The accumulation of large pores in the support layer can reduce the mechanical stability of the membrane assembly. In the membrane layer, the grain growth is different for each phase, which can lead to insufficient contiguity of the phases and hence reduced percolation. Additionally, the samples were unevenly bent and showed a high shrinkage at a sintering temperature of 1350°C, complicating further processing. Furthermore, at high sintering temperatures > 1300°C an additional CoO monoxide phase was observed. This phase is not completely oxidized during the cooling cycle. The presence of this phase might negatively affect the transport properties of the asymmetric membrane, might lead to defect formation and hence reduce the oxygen selectivity.

Due to a lot of problems at the manufacturing step, sintering step, and post-sintering processing, it was not possible to measure the oxygen permeance of the asymmetric 60 CGO20-FCO membrane. Further improvement is required to obtain the mechanically and chemically stable two-layered membrane assembled for the application as an OTM.

The following recommendations are made to overcome the listed issues and improve the process of the dual-phase material fabrication via tape casting technique and obtain a stable asymmetric membrane:

- Pre-calcination of the CGO20-FCO composite powder at 1050°C to complete the phase transformation prior to the casting, which might help to overcome the problems during heat treatment.
- Substitution of the electron-conducting phase is advisable. The donor—doped Gd FeO_3 perovskite material is chosen, based on the successful experience with the CGO-GCFCO bulk membranes, described in [22]. In this case, the fabrication process would benefit from avoiding the phase interaction during sintering and preserving the dual-phase structure.
- Use of alternative material for the support layer, i.e., the 80CGO20-FCO composite. This material can ensure the required level of mixed-conductivity and thus sufficient percolation. Moreover, it shows shrinkage close to the 60CGO20-FCO composite, which is an important factor for the tape casting technique, since both membrane and support layer materials should be compatible.

Dual-phase ceria-based composite shows potential for the application as an asymmetric membrane for the oxygen separation process. The microstructural characteristics reveal good conducting properties and thus will ensure sufficient oxygen flux through the membrane.

References

1. Kiebach, R.; Pirou, S.; Martinez Aguilera, L.; Haugen, A.B.; Kaiser, A.; Hendriksen, P.V.; Balaguer, M.; García-Fayos, J.; Serra, J.M.; Schulze-Küppers, F.*; et al.* A review on dual-phase oxygen transport membranes: from fundamentals to commercial deployment. *J. Mater. Chem. A* **2022**, *10*, 2152–2195.

2. Emsley, J. *Nature's building blocks*: *An A - Z guide to the elements*; Oxford University Press: Oxford, 2002.

3. Garcia-Fayos, J.; Serra, J.M.; Luiten-Olieman, M.W.; Meulenberg, W.A. Gas separation ceramic membranes. In *Advanced Ceramics for Energy Conversion and Storage*: Elsevier, 2020, pp. 321–385.

4. Leo, A.; Liu, S.; Costa, J.C.D.d. Development of mixed conducting membranes for clean coal energy delivery. *International Journal of Greenhouse Gas Control* **2009**, *3*, 357–367.

5. Smart, S.; Lin, C.X.C.; Ding, L.; Thambimuthu, K.; Diniz da Costa, J.C. Ceramic membranes for gas processing in coal gasification. *Energy Environ. Sci.* **2010**, *3*, 268.

6. Chen, G.; Feldhoff, A.; Weidenkaff, A.; Li, C.; Liu, S.; Zhu, X.; Sunarso, J.; Huang, K.; Wu, X.-Y.; Ghoniem, A.F.*; et al.* Roadmap for Sustainable Mixed Ionic-Electronic Conducting Membranes. *Adv Funct Materials* **2022**, *32*.

7. Bai, W.; Feng, J.; Luo, C.; Zhang, P.; Wang, H.; Yang, Y.; Zhao, Y.; Fan, H. A comprehensive review on oxygen transport membranes: Development history, current status, and future directions. *International Journal of Hydrogen Energy* **2021**, *46*, 36257–36290.

8. Zhu, X.; Yang, W. *Mixed Conducting Ceramic Membranes*; Springer Berlin Heidelberg: Berlin, Heidelberg, 2017.

9. Baumann, S.; Serra, J.M.; Lobera, M.P.; Escolástico, S.; Schulze-Küppers, F.; Meulenberg, W.A. Ultrahigh oxygen permeation flux through supported Ba0.5Sr0.5Co0.8Fe0.2O3−δ membranes. *Journal of Membrane Science* **2011**, *377*, 198–205.

10. Lane, J. Oxygen transport in La0.6Sr0.4Co0.2Fe0.8O3−δ. *Solid State Ionics* **1999**, *121*, 201–208.

11. Tan, X.; Wang, Z.; Liu, H.; Liu, S. Enhancement of oxygen permeation through $La_{0.6}Sr_{0.4}Co_{0.2}Fe_{0.8}O_{3-\delta}$ hollow fibre membranes by surface modifications. *Journal of Membrane Science* **2008**, *324*, 128–135.

12. Hoffmann, R.; Pippardt, U.; Kriegel, R. Impact of sintering temperature on permeation and long-term development of support structure and stability for asymmetric oxygen transporting BSCF membranes. *Journal of Membrane Science* **2019**, *581*, 270–282.

13. Serra, J.M.; Garcia-Fayos, J.; Baumann, S.; Schulze-Küppers, F.; Meulenberg, W.A. Oxygen permeation through tape-cast asymmetric all-La0.6Sr0.4Co0.2Fe0.8O3−δ membranes. *Journal of Membrane Science* **2013**, *447*, 297–305.

14. Gao, J.; Li, L.; Yin, Z.; Zhang, J.; Lu, S.; Tan, X. Poisoning effect of SO_2 on the oxygen permeation behavior of $La_{0.6}Sr_{0.4}Co_{0.2}Fe_{0.8}O_{3-\delta}$ perovskite hollow fiber membranes. *Journal of Membrane Science* **2014**, *455*, 341–348.

15. Waindich, A.; Möbius, A.; Müller, M. Corrosion of $Ba_{1-x}Sr_xCo_{1-y}FeyO_{3-\delta}$ and $La_{0.3}Ba_{0.7}Co_{0.2}Fe_{0.8}O_{3-\delta}$ materials for oxygen separating membranes under Oxycoal conditions. *Journal of Membrane Science* **2009**, *337*, 182–187.

16. Engels, S.; Markus, T.; Modigell, M.; Singheiser, L. Oxygen permeation and stability investigations on MIEC membrane materials under operating conditions for power plant processes. *Journal of Membrane Science* **2011**, *370*, 58–69.

17. Yi, J.; Schroeder, M. High temperature degradation of $Ba_{0.5}Sr_{0.5}Co_{0.8}Fe_{0.2}O_{3-\delta}$ membranes in atmospheres containing concentrated carbon dioxide. *Journal of Membrane Science* **2011**, *378*, 163–170.

18. Sunarso, J.; Baumann, S.; Serra, J.M.; Meulenberg, W.A.; Liu, S.; Lin, Y.S.; Diniz da Costa, J.C. Mixed ionic–electronic conducting (MIEC) ceramic-based membranes for oxygen separation. *Journal of Membrane Science* **2008**, *320*, 13–41.

19. Ramasamy, M.; Persoon, E.S.; Baumann, S.; Schroeder, M.; Schulze-Küppers, F.; Görtz, D.; Bhave, R.; Bram, M.; Meulenberg, W.A. Structural and chemical stability of high performance $Ce_{0.8}Gd_{0.2}O_{2-\delta}$-$FeCo_2O_4$ dual phase oxygen transport membranes. *Journal of Membrane Science* **2017**, *544*, 278–286.

20. Ramasamy, M. *Dual Phase Oxygen Transport Membrane for Efficient Oxyfuel Combustion*; Forschungszentrum Jülich GmbH, 2016.

21. Zeng, F. *Mechanical reliability and oxygen permeation of $Ce_{0.8}Gd_{0.2}O_{2-\delta}$-$FeCo_2O_4$ dual-phase composite*; University of Twente: Enschede, 2021.

22. Fischer, L.; Neuhaus, K.; Schmidt, C.; Ran, K.; Behr, P.; Baumann, S.; Mayer, J.; Meulenberg, W.A. Phase formation and performance of solid state reactive sintered $Ce_{0.8}Gd_{0.2}O_{2-\delta}$-$FeCo_2O_4$ composites. *J. Mater. Chem. A* **2022**, *10*, 2412–2420.

23. Fischer, L.; Ran, K.; Schmidt, C.; Neuhaus, K.; Baumann, S.; Behr, P.; Mayer, J.; Bouwmeester, H.J.M.; Nijmeijer, A.; Guillon, O.*; et al.* Role of Fe/Co Ratio in Dual Phase $Ce_{0.8}Gd_{0.2}O_{2-}$-$Fe_{3-x}Co_xO_4$ Composites for Oxygen Separation. *Membranes* **2023**, *13*.

24. Cousin, P. Ross, R.A. Preparation of mixed oxides: a review. *Mater. Sci. Eng., AMaterials Science & Engineering, A: Structural Materials: Properties, Microstructures and Processing* **1990**, 119–125.

25. Howatt, G.N.; Breckenridge, R.G.; Brownlow, J.M. FABRICATION OF THIN CERAMIC SHEETS FOR CAPACITORS. *J. Am. Ceram. Soc.* **1947**, *30*, 237–242.

26. Deibert, W.; Ivanova, M.E.; Meulenberg, W.A.; Vaßen, R.; Guillon, O. Preparation and sintering behaviour of $La_{5.4}WO_{12-}$ asymmetric membranes with optimised microstructure for hydrogen separation. *Journal of Membrane Science* **2015**, *492*, 439–451.

27. Mistler, R.E.; Twiname, E.R. *Tape casting*: *Theory and practice*; American Ceramic Society: Westerville, Ohio, 2000.

28. Schulze-Küppers, F. *Entwicklung geträgerter* $Ba_{0,5}Sr_{0,5}Co_{0,8}Fe_{0,2}O_{3-\partial}$ *Sauerstoff-Permeationsmembranen*; Forschungszentrum Jülich GmbH, 2011.

29. Zeng, F.; Malzbender, J.; Baumann, S.; Nijmeijer, A.; Winnubst, L.; Ziegner, M.; Guillon, O.; Schwaiger, R.; Meulenberg, W.A. Optimization of sintering conditions for improved microstructural and mechanical properties of dense $Ce_{0.8}Gd_{0.2}O_{2-\delta}$-$FeCo_2O_4$oxygen transport membranes. *Journal of the European Ceramic Society* **2021**, *41*, 509–516.

30. Schneider, C.A.; Rasband, W.S.; Eliceiri, K.W. NIH Image to ImageJ: 25 years of image analysis. *Nature methods* **2012**, *9*, 671–675.

31. Picture Thresholding Using an Iterative Selection Method. *IEEE Trans. Syst., Man, Cybern.* **1978**, *8*, 630–632.

32. Shi, J.L. Relation Between Coarsening and Densification in Solid-state Sintering of Ceramics: Experimental Test on Superfine Zirconia Powder Compacts. *J. Mater. Res.* **1999**, *14*, 1389–1397.

33. Shi, J.-L.; Deguchi, Y.; Sakabe, Y. Relation between grain growth, densification and surface diffusion in solid state sintering—a direct observation. *J Mater Sci* **2005**, *40*, 5711–5719.

34. Murray, P.J.; late) J.W. Linnett, (Mössbauer studies in the spinel system coxfe3−xo4. *Journal of Physics and Chemistry of Solids* **1976**, *37*, 619–624.

35. Hansson, A.N.; Linderoth, S.; Mogensen, M.; Somers, M.A. X-ray diffraction investigation of phase stability in the Co–Cr–O and the Fe–Co–Cr–O systems in air at 1323K. *Journal of Alloys and Compounds* **2005**, *402*, 194–200.

Chapter 8

8. Reflections and Conclusions

8.1 Introduction

This chapter provides a summary of the achievements and conclusions on the development of the dual-phase composite material made of the acceptor-doped ceria with the Fe-Co spinel for the potential application as an oxygen transport membrane. All findings regarding powder preparation, oxygen permeation, and associated microstructural characteristics will be reflected in the following with recommendations for future work, which should focus on the improvement of the quality and transport properties of the $Ce_{0.8}Gd_{0.2}O_{2-\delta}$ -$FeCo_2O_4$ (CGO20-FCO) composite.

Reaching an oxygen flux of 1 ml/cm^2 min is considered to be the milestone in dual-phase material development. Thus, as an initial step, the selected material system was analysed regarding its “best performance scenario”, assuming all conditions are perfect, without any limitations. By varying the parameters, such as membrane thickness and partial pressure, the temperature-related permeance level for the dual-phase composite can be estimated. It was estimated that selected dual-phase material can in theory reach the permeance required by targeted application conditions, in particular partial pressure gradient and the intermediate temperature range (<850°C)[1].

8.1.1 Sintering parameters

The heat treatment analysis was performed as an initial step in **Chapter 2**, where samples were sintered at 1200°C for various dwell times (from 0 h to 100 h). The 60 wt.% CGO20 with 40 wt.% FCO composite reveals that already at 0 h dwell time, the phase interaction was completed and all phases are present: fluorite, spinel, and perovskite. All samples were dense at various dwell times, indicating that the densification process was completed before reaching 1200°C [2].

However, under 1 h a high porosity of the pore agglomerations is seen, which negatively affects the mechanical properties of the multi-phase material. The grain size was gradually increasing with the increase of the dwell time, reaching its maximum at

100 h. The most suitable dwell time for the chosen fluorite-spinel system is 5 h, where sufficient microstructural characteristics and insignificant loss in the permeance were found.

The long dwell time (100h) was found to be not suitable since the additional undesired 2.8 vol.% of CoO phase was found, which presence indicates the problem of the selected cooling cycle. This phase transition is known for the Fe-Co system at 1200°C. Residual high-temperature CoO is identified due to the long dwell time (100 h), where a higher amount of CoO is formed and does not have enough time to oxidize completely. Thus, the control of the cooling rate can govern the process of the Co rearranging between the Co_3O_4 and CoO phases until equilibrium. By introducing a slow cooling program with an additional step at 850°C the rock salt oxidation process is facilitated and the CoO phase was eliminated. The resulting mixture of fluorite, spinel, and perovskite is preserved. These results are emphasizing the importance of slow cooling for the Fe-Co spinel for the composite system under study.

8.1.2 Composite design

Chapters 3 and 4 discuss the material design, varying the choice of the ionic and electron-conducting phases for the MIEC composite material.

Chapter 3 shows the analysis of the CGO20-FCO composite, with various FCO fractions (10-40 wt.%) [3]. The reduction of FCO fraction in the composite leads to the increase of oxygen permeance with the maximum for the 80:20 weight ratio. This dual-phase material reveals sufficient performance even at a low percentage of the electron-conducting phase in the initial composite (20 wt.%). The formation of the emerged perovskite phase obviously supported to achieve the targeted percolation threshold of 30 vol.% for the electronic conducting phases. The maximum oxygen flux was 0.1247 ml/cm^2*min for 80CGO20-FCO at 850°C in an air/Ar-gradient.

The electronic conductivity is provided by two types of spinels with donor-doped $GdFeO_3$, which is a pure electronic conductor with a similar conductivity to the spinel [4]. Further reduction of FCO (15 and 10 wt.% of FCO) leads to a drop in oxygen permeance, indicating reduced percolation and, thus, insufficient transport properties.

An alternative approach with the GCFCO perovskite material as an electron-conducting phase, synthesized separately and mixed with commercially available CGO20 was tested [3]. In this case, there is no phase interaction during the sintering of ceria-based composite membranes and indeed the dual-phase composite is obtained in Figure 8.1 a. It is expected to ensure higher chemical stability compared to FCO, in particular at lower p_{O2}. Thus, this composite represents an interesting alternative candidate for the potential application in membrane reactors and gives new direction for the development of dual-phase composite material.

A systematic study was performed to investigate electron-conducting material variation in **Chapter 4.** To do so, the choice was narrowed to the $Fe_{3-x}Co_xO_4$ spinel system with x= 0, 1, 2, and 3 [5]. The composition of spinel governs the phase interaction process, resulting in the dual- or multi-phase composite. For the Co-free composite, an emerged $Gd_5Fe_3O_{12}$ phase was found, while no third phase was found in the Fe-free composite. It was postulated that the presence of both iron and cobalt cations is necessary to form emerged $Gd_{0.85}Ce_{0.15}Fe_{0.75}Co_{0.25}O_3$ (GCFCO) phase with sufficient electron-conducting properties. A percolating network of ionic and electronic conducting phases in the investigated dual- (multi-) phase materials could only be achieved using both types of cations, iron, and cobalt, fostering tertiary phase formation in the composite and resulting in high permeance.

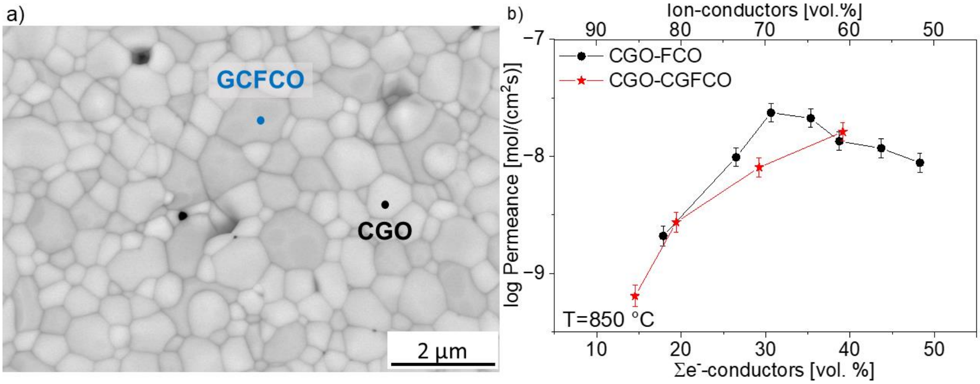

Figure 8.1 a) SEM of 60CGO20-GCFCO composite system b) Permeation of theCGO20-based composites with FCO and GCFCO as electron conducting phase

The rare-earth doped ceria materials from the system $Ce_{1-x}RE_xO_{2-\delta}$ (where RE= gadolinium or samarium and x= 0.1 or 0.2), namely $Ce_{0.9}Gd_{0.1}O_{2-\delta}$ (CGO10) and $Ce_{0.8}Sm_{0.2}O_{2-\delta}$ (CSO20) were selected as a potential candidate for the ceria-based composite, due to enhanced ionic conducting properties. The effect of its addition to the composite on the microstructural and transport properties was discussed in **Chapter 5**. For both composites a maximum oxygen permeance is seen at 20 wt.% of FCO, similar to CGO20, reaching the targeted threshold of 30 vol.% of the electron-conducting phase. The CSO20 composite shows almost identical microstructure features and performance as those in the CGO20-based composite. In addition, the mechanical properties that may impact the reliable operation of these composites are suggested for future studies.

The highest permeance among all three fluorites was measured for the 80CGO10-FCO composite. It was postulated that at the low range of the FCO in the composite (<25 wt.%) the final composite microstructure is crucial and strongly impacts the final permeance performance. Thanks to the finer microstructure in the CGO10 composite compared to CGO20, the electronic contiguity in the CGO10-based composite is improved, leading to less phase insulation.

The amount of dopant in the initial CGO-based composite system has an impact on the final microstructure, resulting in dual- or multi-phase morphology [6]. The reduction of the gadolinium in the fluorite down to 10 mol.% shows a dual-phase morphology with a fine microstructure, without formation of the perovskite GCFCO phase, due to lack of gadolinium in the fluorite. Besides, along the grain boundaries, the enrichment of gadolinium, iron and cobalt is observed, which role in the overall percolation is not clear and should be studied in detail for a solid conclusion. A thorough study of the grain boundaries is required for a comprehensive understanding of its contribution to ionic and/or electronic transport.

8.1.3 Thickness influence

Compared to the bulk disc-shaped tablets, thin dense membranes have a significantly enhanced oxygen permeation. However, by a thickness reduction, the limiting step for permeation changes, outlining the stronger surface exchange kinetics influence than bulk. Generally, to overcome the surface limitations the catalytic (i.e., LSCF) layer helps to maintain the electronic transport paths, provides continuous paths for electrons and ions; and thus, sufficient percolation.

Firstly, bare and coated pellets with a thickness in the range of 0.4 to 2 mm were investigated and discussed in **Chapter 6**. The modified Wagner´s model helped to understand the transport mechanisms and estimate the L_c for the 60CGO20-FCO. At high temperatures (850-1000°C) the LSCF coating application makes not much difference because the oxygen flux is on the same level in bare and coated materials. By temperature decrease the effect of surface limitations is more pronounced, and it is found to be eliminated by the coating of a catalytic layer for all bulk disc-shaped samples. Since the activation energy of the diffusion is much higher than for the surface exchange coefficient, the L_c was found to be significantly low (~0.02 cm) for the coated sample, emphasizing the effectiveness of the catalytic LSCF layer at low temperatures. In contrast, the L_c of the bare membranes is significantly high (0.112 cm). Further reduction in the thickness to µm range is only possible by the fabrication of the thin dense membrane layer on the porous support. For this sequential tape-casting was employed as a processing technology to develop a two-layered asymmetric dual-phase membrane, which is described in **Chapter 7** [7]**.**

The fabrication of the two-layered assembly turned out to be challenging, due to occurred problems at each fabrication step. The optimization of the slurry formulation was done to overcome problems in the drying process and finally, the stable almost defect-free green tape was obtained. The sintering profile was optimized in several steps to get a sufficiently dense membrane layer. First due to the complexity of the composite system with the phase interactions in the spinel phase during sintering, the pre-calcinated powder was exploited. The sintering temperature was increased to 1325 °C and held for 5 h to improve the density of the membrane, which however has side effects, resulting in the formation of a CoO.

It was not possible to improve the asymmetric configuration of the GCO20-FCO composite without compromising its mechanical stability, all samples turned out to be too brittle for further processing. Even for the successfully manufactured pellets it was still not possible to install them into a permeation measurement setup. Some cracked after the installation, by applying the feed gas. At this point, it is not possible to make any conclusion about the permeation properties of the two-layered asymmetric membrane.

Accordingly, the following approaches might help to improve the quality of the CGO20-FCO dual-phase tape and further by heat treatment stabilize the microstructure, resulting in the well-densified mechanically stable dual-phase membrane:

- Introduce the pre-calcination step of the CGO20-FCO composite powder at 1050°C to complete the phase transformation prior to the casting, which might help to overcome problems during heat treatment. The problems, such as the formation of the donor-doped $GdFeO_3$ perovskite phase and additional phase transformation in the spinel phase, resulted in the formation of a high-temperature Co/Fe monoxide phase with a rock salt structure.

- Use of alternative material for the support layer, such as an 80CGO20-FCO composite. This material can ensure the required level of mixed-conductivity and thus, sufficient percolation. Moreover, it shows a shrinkage level close to the 60CGO20-FCO composite, which is an important factor for the tape casting procedure, since both membrane and support layer materials should be compatible.

A further approach would be to use the emerging perovskite, i.e., donor-doped $GdFeO_3$, as the only electron-conducting phase. As shown in **Chapter 2**, the maximum permeation rate comes close to the initial composite. The fabrication process would benefit from avoiding the phase interaction during sintering and preserving a dual-phase structure. Moreover, the chemical stability is expected to be improved in particular in low p_{O2} environments.

8.2 Conclusions

In this work, CGO20-FCO dual-phase membranes are synthesized by the solid-state reactive sintering method from the commercially available $Ce_{0.8}Gd_{0.2}O_{2-\delta}$, Co_3O, and Fe_2O_3 powders.

It is shown that a well-densified (~95%) dual-phase composite with a homogeneous distribution of phases and µm range grain size can be obtained by adapting the sintering profile. The heat treatment step is crucial and strongly controls the microstructure features, resulting in the multi-phase composite material. The phase interaction is completed already at 1200°C and short or no dwell time (0 h). The most suitable sintering parameters considering the permeance and morphology characteristics are found to be 1200°C for 5 h with a slow cooling rate a slow rate of 0.5 K min^{-1} between 900 and 800 °.

The results obtained show that the key factor for maximum performance is to reduce the electron-conducting phase fraction without losing the final phase percolation, which would compromise the mixed ionic electronic conductivity. It was found that the newly formed perovskite phase effectively contributes to electronic percolation. In some cases, the enrichment of gadolinium or samarium, iron and cobalt along the grain boundaries was detected. Its effects on the transport process are not clear yet and should be further investigated.

The donor-doped $GdFeO_3$ perovskite material is found to be a promising alternative as an electron-conducting material; thus, the study of the fluorite-perovskite composite is required for a more comprehensive understanding of the mechanical and transport properties. It can potentially meet stability requirements and maintain or even improve the permeation performance at intermediate temperatures (<850°C). A further step will be the development of the CGO20-GCFCO-supported asymmetric membranes.

Summarizing, the investigated dual-phase material system is promising for application at intermediate temperatures. It shows stable oxygen flux even at relatively low driving forces. It is necessary to investigate the stability of those composites in membrane reactor conditions for potential industrial applications. Asymmetric membrane development and accordant scale-up activities have to follow.

References

1. Kiebach, R.; Pirou, S.; Martinez Aguilera, L.; Haugen, A.B.; Kaiser, A.; Hendriksen, P.V.; Balaguer, M.; García-Fayos, J.; Serra, J.M.; Schulze-Küppers, F.*; et al.* A review on dual-phase oxygen transport membranes: from fundamentals to commercial deployment. *J. Mater. Chem. A* **2022**, *10*, 2152–2195.

2. Zeng, F. *Mechanical reliability and oxygen permeation of* $Ce_{0.8}Gd_{0.2}O_{2-\delta}$*-*$FeCo_2O_4$ *dual-phase composite*; University of Twente: Enschede, 2021.

3. Fischer, L.; Neuhaus, K.; Schmidt, C.; Ran, K.; Behr, P.; Baumann, S.; Mayer, J.; Meulenberg, W.A. Phase formation and performance of solid state reactive sintered $Ce_{0.8}Gd_{0.2}O_{2-\delta}$-$FeCo_2O_4$ composites. *J. Mater. Chem. A* **2022**, *10*, 2412–2420.

4. Ran, K.; Zeng, F.; Fischer, L.; Baumann, S.; Meulenberg, W.A.; Neuhaus, K.; Mayer, J. The in situ generated emerging phase inside dual phase oxygen transport membranes. *Acta Materialia* **2022**, *234*, 118034.

5. Fischer, L.; Ran, K.; Schmidt, C.; Neuhaus, K.; Baumann, S.; Behr, P.; Mayer, J.; Bouwmeester, H.J.M.; Nijmeijer, A.; Guillon, O.*; et al.* Role of Fe/Co Ratio in Dual Phase $Ce_{0.8}Gd_{0.2}O_{2-}$-$Fe_{3-x}Co_xO_4$ Composites for Oxygen Separation. *Membranes* **2023**, *13*.

6. Ran, K.; Fischer, L.; Baumann, S.; Meulenberg, W.A.; Neuhaus, K.; Mayer, J. Tuning the ceria interfaces inside the dual phase oxygen transport membranes. *Acta Materialia* **2022**, *226*, 117603.

7. Ramasamy, M. *Dual Phase Oxygen Transport Membrane for Efficient Oxyfuel Combustion*; Forschungszentrum Jülich GmbH, 2016.

Acknowledgements

With this chapter, I take immense pleasure in acknowledging all the people who made this PhD thesis possible, and who supported and guided me through it. First, I would like to thank Prof. Dr. Wilhelm A. Meulenberg and Prof. Dr. Arian Nijmeijer for providing the opportunity to pursue a jointed PhD study of Forschungszentrum Jülich GmbH (Jülich, Germany) and the University of Twente (Enschede, the Netherlands). Prof. Dr. Wilhelm A. Meulenberg was supportive throughout my PhD journey and guided me to go through all the administrative, scientific and personal barriers during my time at IEK-1. I especially have to thank my promoter at Twente - Prof. Dr. Arian Nijmeijer for the meaningful discussions, that helped me to improve my work, and also for the meetings for project administration requirements.

I am very thankful to Dr. Stefan Baumann for being the best daily advisor throughout my PhD research work at IEK-1. His guidance and advice carried me through all the stages of designing and writing my project. He was always open to discussions and ready to help in my work life, sharing his experience and wisdom. He made himself available regardless of the time for many useful results discussions and helped me to implement basic scientific ideas and conceptualize my scientific work.

This work is primarily performed at Forschungszentrum Jülich GmbH, at the Institute of Energy and Climate Research, Materials Synthesis and Processing (IEK-1), would like to express my gratitude also to the institute director at Jülich Prof. Dr. Oliver Guillon for providing resources and facilities to develop myself as a scientist. And also, all IEK-1 colleagues for the warm and family-like atmosphere at the institute.

I also would like to thank Stefan Heinz for the lab assistance, sample preparations and permeation measurements. Many thanks to Volker Bader for all performed heat treatments and Andrea Hilgers for particle morphology measurements. During the course of the PhD, some valuable characterizations performed by Dr. Doris Sebold (SEM and EDS) and Dr. Christian Dellen (Raman) gave meaningful results. Dr. Wendelin Deibert and Dr. Falk Schulze-Küppers for sharing their experience in the tape casting field, as well as Julia Wolter. Without these experimental supports, my work would be incomplete.

I would like to acknowledge the funding for this PhD thesis by Deutsche Forschungs Gemeinschaft (DFG). And the project partners Dr. Ke Ran and Prof. Dr. rer. nat. Joachim Mayer (TEM and EFTEM, EDX, HAADF measurements) for the results, which were very helpful for deeper understanding. Dr. Kerstin Neuhaus and Christina Schmidt for performing various conductivity measurements, and Patrik Behr for Rietveld analysis.

I would also like to give special thanks to my family as a whole and especially my husband for the continuous support, encouraging and understanding when undertaking my research and writing my project.

About the Author

Liudmila Fischer is born on 12th March 1988, In Nijnii Tagil, UDSSR. After acquiring the Diploma in the field of metallurgical engineering at the Moscow State Technical University of Steel and Alloys (MISIS) in 2010, she worked for three years in a Group of companies “MetProm” in Moscow as an engineer. Afterwards, she joined the Master's program at the RWTH Aachen University (Aachen , Germany) with the speciality Process Technology of Metals.

She further started a joint PhD study of Forschungszentrum Jülich GmbH (Jülich, Germany) and the University of Twente (Enschede, the Netherlands). Under the supervision of Prof. Dr. Wilhelm A. Meulenberg and Prof. Dr. Ir. Arian Nijmeijer, she worked on the PhD project with a focus on the development of dual-phase oxygen transport membranes suitable for application at intermediate temperatures. She presented her work at two conferences (ICIM16 and ElectroceramicsXVII) and published three articles as a first author during her study.

Schriften des Forschungszentrums Jülich
Reihe Energie & Umwelt / Energy & Environment

Band / Volume 609
Mechanisches Verhalten von Polymer-Elektrolyt-Membran-Elektrolysezellen und -Stacks
S. Holtwerth (2023), x, 251 pp
ISBN: 978-3-95806-697-7

Band / Volume 610
Membrane Reactor Concepts for Power-to-Fuel Processes
H. Huang (2023), VI, 197 pp
ISBN: 978-3-95806-703-5

Band / Volume 611
Deployment of Fuel Cell Vehicles in Road Transport and the Expansion of the Hydrogen Refueling Station Network: 2023 Update
R. C. Samsun, M. Rex (2023), i, 39 pp
ISBN: 978-3-95806-704-2

Band / Volume 612
Behavior/performance of tungsten as a wall material for fusion reactors
M. Gago (2023), X, 120 pp
ISBN: 978-3-95806-707-3

Band / Volume 613
Strategieentwicklung zur Umsetzung der Klimaschutzziele im Verkehrssektor mit dem Fokus Kraftstoffe
M. Decker (2023), ix, 243 pp
ISBN: 978-3-95806-714-1

Band / Volume 614
Joining of tungsten and steel for the first wall of a future fusion reactor
V. Ganesh (2023), xxx, 142, a-v pp
ISBN: 978-3-95806-715-8

Band / Volume 615
Polluter group specific emission optimisation for regional air quality analyses using four-dimensional variational data assimilation
P. M. Backes (2023), xxi, 115 pp
ISBN: 978-3-95806-717-2

Band / Volume 616
Effect of organic soil amendments on increasing soil N retention and reducing N losses from agricultural soils
Z. Li (2023), XI, 134 pp
ISBN: 978-3-95806-721-9

Schriften des Forschungszentrums Jülich
Reihe Energie & Umwelt / Energy & Environment

Band / Volume 617
Radiolytic Stability of BTBP-, BTPhen- and DGA-based Ligands for the Selective Actinide Separation by Solvent Extraction
H. Schmidt (2023), ca. 200 pp
ISBN: 978-3-95806-723-3

Band / Volume 618
$Na_5YSi_4O_{12}$-type Na^+ superionic conductors for solid-state batteries
A. Yang (2023), X, 150 pp
ISBN: 978-3-95806-731-8

Band / Volume 619
Development of industry-scalable processes for nanocrystalline silicon oxide in silicon heterojunction solar cells
D. Qiu (2023), 202 pp
ISBN: 978-3-95806-734-9

Band / Volume 620
Photonic Sintering of Garnet-Based Solid-State Batteries
W. S. Scheld (2024), XII, 153 pp
ISBN: 978-3-95806-737-0

Band / Volume 621
Ceria-based composites for application in Oxygen transport membranes
L. Fischer (2024), xiii, 216 pp
ISBN: 978-3-95806-739-4

Weitere ***Schriften des Verlags im Forschungszentrum Jülich*** unter
http://wwwzb1.fz-juelich.de/verlagextern1/index.asp

Energie & Umwelt / Energy & Environment
Band / Volume 621
ISBN 978-3-95806-739-4

Mitglied der Helmholtz-Gemeinschaft

JÜLICH
Forschungszentrum